

2010

Application of fluorescence spectroscopy: excited-state dynamics, food-safety, and disease diagnosis

Ramkrishna Adhikary
Iowa State University

Follow this and additional works at: <https://lib.dr.iastate.edu/etd>

 Part of the [Chemistry Commons](#)

Recommended Citation

Adhikary, Ramkrishna, "Application of fluorescence spectroscopy: excited-state dynamics, food-safety, and disease diagnosis" (2010). *Graduate Theses and Dissertations*. 11904.
<https://lib.dr.iastate.edu/etd/11904>

This Dissertation is brought to you for free and open access by the Iowa State University Capstones, Theses and Dissertations at Iowa State University Digital Repository. It has been accepted for inclusion in Graduate Theses and Dissertations by an authorized administrator of Iowa State University Digital Repository. For more information, please contact digirep@iastate.edu.

Application of fluorescence spectroscopy: excited-state dynamics, food-safety, and disease diagnosis

by

Ramkrishna Adhikary

A dissertation submitted to the graduate faculty
in partial fulfillment of the requirements for the degree of

DOCTOR OF PHILOSOPHY

Major: Physical Chemistry

Program of Study Committee:
Jacob W. Petrich, Major Professor
Mark S. Gordon
Xueyu Song
Mark S. Hargrove
Theresa Windus

Iowa State University

Ames, Iowa

2011

Copyright © Ramkrishna Adhikary, 2011. All rights reserved.

Dedicated to my parents

TABLE OF CONTENTS

ACKNOWLEDGEMENT	vi
CHAPTER 1. INTRODUCTION	1
General Introduction	1
Low Density Lipoprotein	1
Hypericin	3
Micelles	6
PRODAN	9
Excited-State Intramolecular Proton/Hydrogen Atom Transfer	12
Curcumin	14
Transmissible Spongiform Encephalopathy (TSE)	18
Lipofuscin	19
Thesis Organization	21
References	22
CHAPTER 2. EXPERIMENTAL TECHNIQUES AND DATA ANALYSIS	36
Overview	36
Fluorescence Spectrophotometer	37
Ti:Sapphire Crystal	40
Optical Oscillator	41
Laser Modes	43
Mode-Locking	45
Group Velocity Dispersion	52
Prism Pair	54
Ti:Sapphire Oscillator	55
Second Harmonic Generation and Sum Frequency Mixing	57
Phase Matching	59
Tripler	63
Time-Correlated Single Photon Counting (TCSPC)	64
Fluorescence Upconversion	70
Fluorescence Quenching	75
Fluorescence Resonance Energy Transfer	80
Time-Resolved Fluorescence Anisotropy	84
Solvation Dynamics	88
Construction of Time-Resolved Emission Spectra (TRES)	93
Log-Normal Fitting Equation	94
Estimation of the Time Zero Spectrum	95
Construction of Solvation Correlation Function	97
References	97
CHAPTER 3. ACCUMULATION AND INTERACTION OF HYPERICIN IN LOW DENSITY LIPOPROTEIN (LDL) — A PHOTOPHYSICAL STUDY	106
Abstract	106
Introduction	107
Materials and Methods	108
Results and Discussion	110

Conclusions	125
Acknowledgements	125
References	126
CHAPTER 4. SOLVATION DYNAMICS OF THE FLUORESCENT PROBE, PRODAN, IN HETEROGENEOUS ENVIRONMENTS: CONTRIBUTIONS FROM THE LOCALLY EXCITED AND CHARGE-TRANSFERRED STATES	129
Abstract	129
Introduction	130
Experimental Section	134
Results and Discussion	136
Conclusions	148
References	148
CHAPTER 5. EXCITED-STATE INTRAMOLECULAR HYDROGEN ATOM TRANSFER AND SOLVATION DYNAMICS OF THE MEDICINAL PIGMENT CURCUMIN	154
Abstract	154
Introduction	155
Experimental Section	157
Results and Discussions	160
Conclusion	173
Acknowledgment	173
Appendix	174
References	181
CHAPTER 6. EXCITED-STATE INTRAMOLECULAR HYDROGEN ATOM TRANSFER OF CURCUMIN IN SURFACTANT MICELLE	186
Abstract	186
Introduction	187
Experimental Section	190
Results and Discussions	194
Conclusion	211
Acknowledgment	212
References	212
CHAPTER 7. A NEW FLUORESCENCE BASED METHOD FOR THE REAL-TIME DETECTION OF CENTRAL NERVOUS SYSTEM (CNS) TISSUES ON BOVINE CARCASSES BASED ON LIPOFUSCIN	217
Abstract	217
Introduction	218
Materials and Methods	220
Results	223
Discussion	229
Acknowledgment	235
References	235

CHAPTER 8. FLUORESCENCE SPECTROSCOPY OF THE RETINA FOR DIAGNOSIS OF TRANSMISSIBLE SPONGIFORM ENCEPHALOPATHIES	240
Abstract	240
Introduction	241
Materials and Methods	244
Results and Discussion	246
Conclusion	252
Acknowledgement	253
References	253
CHAPTER 9. GENERAL CONCLUSIONS	258
VITA	263

ACKNOWLEDGEMENT

The work described in this thesis resulted from the collaboration and contribution of a great number of people over the years. It is a great pleasure to convey my gratitude to them all in my humble acknowledgment. This is perhaps the most difficult task, but I am going to take this opportunity to write a few lines to express my gratitude and appreciation to those who have assisted and supported me in this long journey. If your name is not listed, rest assured that my gratitude is not less than for those listed below.

First and foremost, I would like to express my deeply felt thanks to my thesis advisor, Dr. Jacob W. Petrich for his unflinching encouragement, support, and guidance throughout my research. His expertise in ultrafast laser spectroscopy improved my research skills and prepared me for future challenges. I am also grateful to him for patiently going through the chapters of my thesis and for his critical comments. This thesis would not have been possible without his valuable support.

Besides my advisor, I would like to thank the members of my graduate committee, Dr. Mark S. Gordon, Dr. Xueyo Song, Dr. Mark S. Hargrove, and Dr. Theresa Windus for their helpful comments and suggestions during my study. Special thanks go to my previous committee member Dr. Hans Stauffer for all his help.

The members of our group have been a source of friendships as well as good advice and collaboration. I am indebted to Dr. Mintu Halder for sharing his knowledge with us on the Ti:Sapphire oscillator and fluorescence upconversion technique used in our laboratory. I thank Dr. Lindsay Sanders for all her help in the first year of my graduate study. My special appreciation goes to Dr. Prasun Mukherjee for his generous help on almost every aspect of research in the Petrich group. A special acknowledgement goes to Sayantan Bose who has

been a true friend since we started our M.S. in IIT Bombay. I am grateful to Charles Bernes and Philip Carlson, my other great labmates who have been supportive in every way. I have also had the opportunity to work with few undergraduate students. I would like to thank Alyse Hurd, Frank Maistrovich, Rachel Trampel and Alexandria Benson. I am grateful to Franck Maistrovich and Rachel Trampel for their hard work in the assigned project with me. I thank Dr. Govindaranjan Krishnamoorthy for his early extensive work on the sheep eye project. I feel privileged to have been able to work with all my group members.

I consider myself very fortunate to work with a number of wonderful collaborators during my research. I offer my regards to Dr. Pavol Miskovsky for educating us about the LDL-hypericin project. I am grateful to Dr. Daniel W. Armstrong and members of his group for sending us pure ionic liquids. I thank Dr. George A. Kraus and his student Aniket Thite for synthesizing (*S*)-*N*-methyl-2-pyrrolidinemethyl 2(*S*)-(6-methoxy-2-naphthyl)propionate. A special thanks goes to Dr. Mark S. Hargrove for providing the wild and mutant myoglobin proteins and allowing us to use his laboratory for making apo-proteins. I thank Dr. Xueyo Song for calculating the solvation correlation functions of Coumarin 153 in different apo-myoglobin proteins and letting us use his program for the zero-time spectrum calculation. I convey special acknowledgement to Dr. Holger Schönenbrücher for providing us tissue samples and for his helpful discussion on the CNS tissue projects. I owe my deepest gratitude to Dr. Tak W. Kee for encouragement, friendship, and numerous fruitful discussions on curcumin projects. I gratefully thank Dr. Thomas Casey, Dr. Mark Rasmussen, Dr. Jürgen Ritch, Dr. Markus Kehrl, Dr. Amir Hamir, and Dr. Robert Kunkle for all their collaborative efforts.

I would like to acknowledge Dr. Bob Doyle and Dr. Curtis Mosher for their support

in obtaining and analyzing hyperspectral fluorescence microscopy data of sheep retina. I also thank Dr. Bruce Fulton for the NMR experiment of protein samples. I am grateful to Dr. Kamal Harrata for obtaining mass spectra of cyclocurcumin. Special thanks go to Debabrata Mukherjee for performing and analyzing NMR of cyclocurcumin. I gratefully acknowledge Dr. Basudeb Saha and Dr. Feili Qin for allowing us to use the absorption spectrophotometer and pH meter in the physical and analytical chemistry laboratories. I would like to acknowledge support of all the members from department of chemistry, Iowa State University.

I am also indebted to all of my previous teachers. I am grateful to my M.S. advisor Dr. Anindya Datta for his encouragement and thoughtful guidance. I am happy to acknowledge my debt to Utpal Kundu, whose truly inspiring teaching changed my school life.

My time at Ames was enriched and enjoyable due to a number of friends. I am grateful to my roommates and friends, Sayantan Bose and Shibabrata Nandi for sharing unforgettable moments with me. I want to express my gratitude to Sayantan, not only for his friendship, but also for tolerating my erratic behavior for five years as a roommate. Special thanks go to Sbibabrata for teaching me physics and mathematics. I am grateful to all my friends in Ames especially Sumoham Misra, Biswajoy Roy Chaudhuri, Supratim Giri, Prasun Mukherjee, Sayan Ranu, Basudeb Saha, Mintu Halder, Puspita Halder, Debabrata Mukherjee, Payel Mukherjee, and Barun Jana for their wonderful company.

Lastly, I would like to thank my family for all their love and encouragement. I thank my three elder brothers for their incessant supports during this entire journey. I dedicate this thesis to my parents who unremittingly supported me during my years of study. I also thank

my relative Chanchal Das Bairagya for his support and encouragement.

CHAPTER 1. INTRODUCTION

General Introduction

Fluorescence spectroscopy has been widely used in the study of the structure and dynamics of molecules in complex systems.¹⁻⁴ Steady-state and time-resolved fluorescence methods are commonly used to characterize emissive properties of fluorophores. Time-resolved fluorescence measurements are generally more informative about the molecular environment of the fluorophore than steady-state fluorescence measurements because the competing or perturbing kinetic processes such as collisional quenching, solvent relaxation, energy transfer, and rotational reorientation, which affect the fluorescence, occur on the timescale of the fluorophore's lifetime (10^{-9} s). Thus, time-resolved fluorescence spectroscopy can be used to quantify these processes and gain insight into the chemical surroundings of the fluorophore. This thesis discusses a range of complex systems and phenomena that may fruitfully be examined by means of fluorescence spectroscopy, in particular: steady-state fluorescence, fluorescence quenching, fluorescence lifetime, time-resolved fluorescence anisotropy, fluorescence resonance energy transfer (FRET), and excited-state solvation dynamics.

Low Density Lipoprotein

Lipoproteins are complex aggregates of lipids and proteins that render the lipids compatible with the aqueous environment of body fluids and enable their transport throughout the body.⁵ In general lipoprotein is composed of an outer shell of phospholipid, which renders the particle soluble in water; a core of fats called lipid, including cholesterol and a surface apoprotein molecule that allows cells to recognize and take up the particle. Lipoproteins are characterized by their density and classified into five main groups based on

different ratio of protein to lipids as chylomicrons (CM), very low density lipoproteins (VLDL), intermediate density lipoproteins (IDL), low density lipoproteins (LDL) and high-density lipoproteins (HDL).⁵

Cholesterol is a building block of the outer layer of cells (cell membranes), and is transported through the blood as lipoprotein. LDL is the main carrier of cholesterol in the human circulatory system. It can be viewed as a spherical particle (diameter ~ 22 nm)⁶ (Figure 1.1) containing three different regions—the outer surface layer, the core region and an interfacial region between these two.^{6,7} The surface monolayer mainly consists of phospholipid molecules and a single molecule of the protein, apoB-100 (one of the largest monomeric proteins known) which consists of 4536 amino acid residues. There are 37 tryptophans among 4536 residues.^{6,7} Apo-B100 acts like a belt that surrounds the LDL and interacts with both the lipids of the LDL and with the aqueous environment as it is amphipathic in nature. The core of LDL is enriched with triglycerides and cholesteryl esters. A large LDL particle carries ~3000 lipid molecules. The interfacial layer consists of interpenetrating core and surface lipids.

In photodynamic therapy (PDT), a photosensitizing (dye molecule) agent acts against malignant tumors under the influence of light. Lipoproteins and serum albumin are the main carriers for the photosensitizers. It has been demonstrated that hydrophobic photosensitizers are carried in blood by LDLs and hydrophilic photosensitizers are largely carried by albumin and globulin.⁸ After intravenous injection of a hydrophobic photosensitizers, they are carried and accumulated to tumor cells because the hyperproliferating cells require an extra supply of cholesterol and phospholipids.⁹ Efficient transport and subsequent specific localization of photosensitizer in the body for PDT, requires detail studies on the interaction of LDL and

photosensitizer.

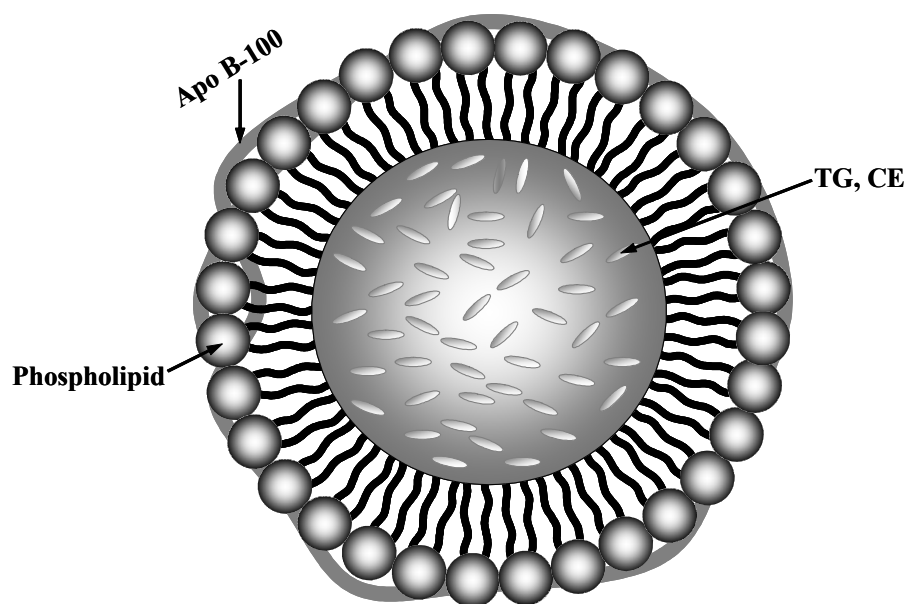


Figure 1.1. Schematic diagram of LDL particle. The surface monolayer mainly consists of phospholipids and the protein, apoB-100. The core of LDL is enriched with triglycerides (TGs) and cholesteryl esters (CEs). The interfacial layer consists of interpenetrating core and surface lipids. The diameter of a LDL particle is ~ 22 nm, including a surface monolayer ~ 2 nm.

Hypericin

Hypericin (Figure 1.2) is a naturally occurring perylene quinone pigment obtained from plants of the genus *Hypericum*.¹⁰ It is particularly the major component of the botanical dietary supplement, St. John's Wort (*Hypericum perforatum*). It displays virucidal activity against several types of viruses including the human immunodeficiency virus (HIV), as well as antiproliferative and cytotoxic effects on tumor cells.¹¹⁻²¹ It has been argued that the light is not necessary for its antiviral activity, but is enhanced in the presence of light.^{16,17,22-24} Excited state properties of hypericin have been extensively studied in order to understand the role of light on its biological activities.²⁵⁻³⁰ Several mechanisms have been proposed for the photodynamic action of hypericin including the two most common and well-known

mechanisms, type I and type II. Several reactive species such as superoxide radical anion (O_2^-), hydroxyl radical ($\cdot OH$), as well as hypericin radicals and radical ions are involved in type I mechanism.^{14,31,32} In type II oxygen-dependent photosensitization mechanism, hypericin generates singlet oxygen (1O_2) via energy transfer from triplet state of hypericin to ground triplet state of oxygen.^{21,33} Petrich and coworkers^{34,35} suggest an alternative origin of photo-induced virucidal activity that involves light-induced acidification through proton transfer in the excited state of hypericin, which is likely to precede solvent acidification.

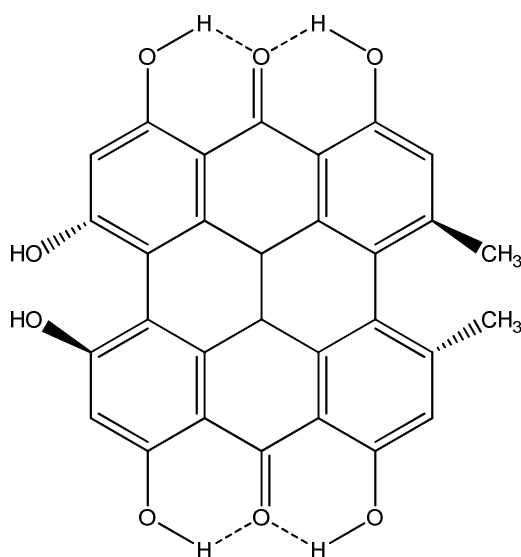


Figure 1.2. Structure of Hypericin.

Previous work from our group^{36,37} shows that hypericin strongly interacts and forms rigid complex with proteins such as human serum albumin (HSA) and two different isoforms of glutathione S-transferase (GST), HA1-1 and HP1-1. Kascakova et al.³⁸ reports hypericin binding to LDL and conclude that multiple hypericins interact with LDL. Hypericin exists as aggregates in aqueous physiological solution. The photodynamic actions of hypericin are greatly diminished when it is aggregated.³⁹ Binding with biological macromolecules helps hypericin to solubilize in its monomeric form, which is believed to be important for virucidal

action.³⁹⁻⁴¹ This lipophilic molecule interacts mainly with LDL and to a lesser extent with HSA upon its incorporation in the blood. Several studies have shown that photosensitizers mixed with LDL before administration leads to an increase in photodynamic efficiency in comparison with the administration of photosensitizers alone.⁴²⁻⁴⁵ It is important to study the interaction of hypericin with LDL in physiological condition for efficient use as photodynamic drug. More specifically, how many monomeric hypercins exist in a LDL molecule? Where do they bind (surface or core of LDL)? And how strong the binding is?

Previous binding study of hypericin with LDL by steady-state fluorescence spectroscopy showed quenching of tryptophan fluorescence emission from Apo B-100 in LDL with increase in hypericin concentration.³⁸ This observation prompted the authors to conclude that the hypericin molecules reside somewhere near the apoB-100 part of the LDL, and based on these observations, they proposed that hypericin accumulates at the interfacial region of the LDL molecule—i.e. between the surface and the core regions. In chapter 3 we continue the investigation of the location of hypericin in LDL by exploiting steady-state fluorescence quenching, fluorescence resonance energy transfer (FRET) and time-resolved fluorescence anisotropy measurements. These techniques are discussed in chapter 2. Our results indicate that multiple hypercins can penetrate considerably deeply into the LDL molecule and up to ~20 nonaggregated hypericin molecules can exist in LDL. The accommodation of multiple hypercins in LDL should not be surprising considering the diameter of LDL (~220 Å). The very inefficient quenching and single exponential rotational correlation time (~ 10.3 ns) of hypericin in 1:1 LDL:Hyp complex suggest that a single hypericin is rigidly held, and thus probably resides fairly deeply in LDL. Energy transfer from the tryptophans to hypericin is efficient, suggesting that hypericin can be moderately

close to the surface, where apoB-100 is located. All results collectively indicate that hypericin lies in an intermediate location between surface and core—i.e. the interfacial region.

Micelles

Surfactants belong to a class of molecules with surface-active properties. The surfactant molecule consists of two parts, namely, a polar head group (water-liking or hydrophilic) and a non-polar hydrophobic tail (water-hating or hydrophobic).⁴⁶ The surfactant may be anionic, cationic, zwitterionic or non-ionic depending on the charge characteristics of the head group.⁴⁷ When surfactants are dissolved in water at low concentration, they accumulate at the surface and orient themselves in such a way so that the polar head groups interact with the water and the hydrophobic regions are removed from the aqueous environment. In this arrangement at the surface, the surfactants disrupt the cohesive forces of water molecules at the surface and thus lower the surface tension. At the Critical Micelle Concentration (CMC), the surface becomes completely loaded with surfactant and any further additions of surfactants form aggregates in which the hydrophobic portions are oriented within the cluster and the hydrophilic portions are exposed to the water. Such aggregates are called micelles.⁴⁸⁻⁵⁰ The fundamental reason for micelle formation is the attainment of a minimum free energy state. The enthalpy change (ΔH) of micelles formation is very small. The primary driving force is the increase of entropy (ΔS) that occurs when the hydrophobic regions of the surfactant are removed from water and the ordered structure of the water molecules around this region of the molecule is lost.⁵¹ The average form of a micelle is often spherical because a spherical shape produces the minimum surface area-to-volume ratio. However, other geometries such as ellipsoids extended tubes are also possible.

The structure of a micelle formed by ionic surfactants (Figure 1.3a) is generally described by three regions: the core, the Stern layer, and the Gouy-Chapman double layer.⁵² The core is composed of the hydrocarbon chains of the surfactant molecule. The core is surrounded by a concentric shell consisting hydrophilic head groups together with $(1-\alpha)N$ counterions (α is the degree of ionization and N is the aggregation number) and considerable number of water molecules, known as Stern layer. The rest of the counterions (αN) require to neutralize the charge on the kinetic micelle are bound to the micelles surrounding the Stern layer as diffuse Gouy-Chapman double layer. For most ionic micelles the degree of ionization α is between 0.2 and 0.3; that is, 70–80% of the counterions are considered to be in the Gouy-Chapman double layer.⁵¹ However micelles formed by non-ionic surfactants consist of a hydrophobic core formed from the hydrocarbon chains of the surfactant molecules surrounded by a shell, known as palisade layer. The palisade layer is composed of the oxyethylene chains of the surfactant, which is heavily hydrated. Triton X-100 (TX-100), cetyl trimethyl ammonium bromide (CTAB) and sodium dodecyl sulfate (SDS) are commonly used non-ionic, cationic and anionic surfactant, respectively. These surfactants form nearly spherical micelle in water above CMC. The CMC values for TX-100, CTAB and SDS are 0.23 mM, 0.9 mM and 8 mM, respectively. Each micelle contains 100-150 surfactant molecules with a radius of ~ 50 Å for TX and CTAB and 30 Å for SDS.⁵³ Studies show that the palisade layer is ~ 25 Å thick while the Stern layers of CTAB and SDS are quite thin $\sim 6-9$ Å.⁵³⁻⁵⁶ The palisade layer is mainly composed of the oxyethylene units containing a large number of water molecules around these groups and the water molecules are hydrogen bonded, either among themselves or with the head groups of the surfactant molecules.

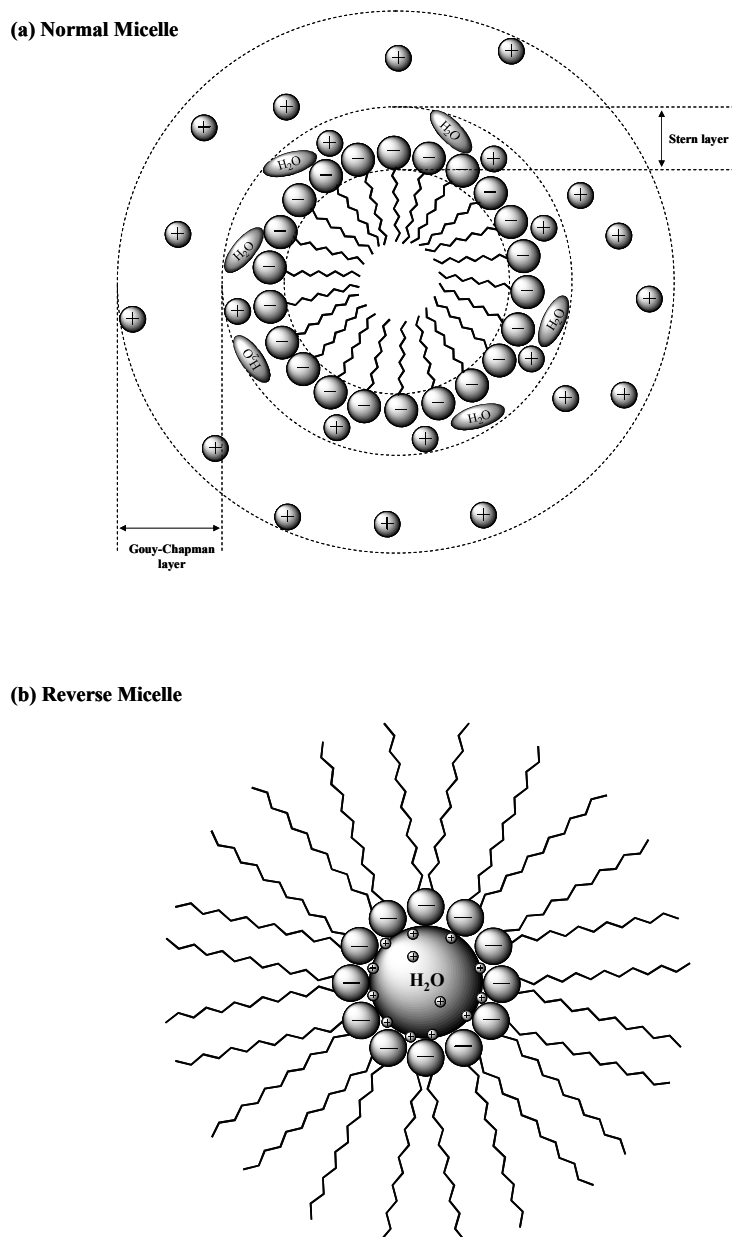


Figure 1.3. Diagrammatic representation of cross section of an anionic (a) normal micelle and (b) a reverse micelle, showing charged layers. The core of the normal micelle consists of the hydrocarbon tails of the surfactant molecules. The Stern layer consists of the head groups, bound counterions and significant amount of water. The Gouy-Chapman region is a diffuse double layer containing unbound counterions. The core of reverse micelle is composed of the hydrophilic groups around the nanometer-sized water droplet surrounded by a shell of the hydrocarbon chains.

Reverse micelles (Figure 1.3b) are formed when an amount of water and surfactants are dissolved in non-polar organic solvent.⁵⁷ It has a core composed of the hydrophilic

groups around the nanometer-sized water droplet surrounded by a shell of the hydrocarbon chains. The tiny water droplets trapped at the core of reverse micelle is known as water pool. One typical value used to characterize the reverse micelle is the ratio of water to surfactant, often described by $w_0 = [\text{H}_2\text{O}]/[\text{Surfactant}]$. If the reverse micelle is spherical, the radius of the water pool is directly proportional to w_0 .⁵⁸ Thus w_0 controls the size of the droplets and can be tuned from few nanometers to several tens of nanometers (nm). Surfactants able to form reverse micelles can also be anionic, cationic, zwitterionic and nonionic. The most widely used reverse micelle is that formed by water, an alkane, and the anionic surfactant dioctyl sodium sulphosuccinate, better known as AOT (Aerosol-OT).⁵⁹ The water inside the reverse micelle is different from bulk water, such as a structural change in the hydrogen-bonded network occurs and the scenario changes when w_0 is varied.⁶⁰

PRODAN

6-Propionyl-2-(N,N-dimethylamino)naphthalene (PRODAN) (Figure 1.4) is a highly fluorescent, hydrophobic molecule, first synthesized and characterized by Weber and Farris in 1979.⁶¹ PRODAN is a push-pull, charge-transfer chromophore that produces a substantial change in its excited-state dipole moment upon photoexcitation owing to the presence of an electron-donating dimethylamino group and electron-withdrawing propionyl group connected to the aromatic spacer by a single bond. Its absorption and emission spectra are strongly dependent upon the polarity of its environment.⁶¹ PRODAN has a single broad emission spectrum with a dramatic solvatochromatic shift (~130 nm) of its maximum, ranging from 401 nm in cyclohexane to 531 nm in water.⁶¹ The excited-state kinetics of PRODAN are complex, and the origins of its solvatochromatic nature have been debated.⁶²⁻⁶⁸ Theoretical calculations suggest a planar structure in the ground state. But the geometry of

its charge-transferred emissive state (twisted intramolecular charge transfer or planar intramolecular charge transfer) has not yet been confirmed.^{62,65-77} It is generally agreed that, PRODAN undergoes excited-state intramolecular charge-transfer following excitation from the ground state. The charge-transferred state, CT, is formed from an initially excited state referred to as the locally-excited state (LE).⁷⁸ In nonpolar environments, emission is from the LE state, while in polar environments the emission is from the CT state.⁷⁸

It has been used as an optical probe of the function and dynamics of proteins and membranes.⁷⁹⁻⁸⁶ It has also been employed to study solvation dynamics in polar liquids, ionic liquids, and supercritical fluids.⁸⁷⁻⁹¹ Fluorescent probes based upon the PRODAN chromophore, namely, DANCA⁹² and Aladan⁹³ are also used to solvation dynamics of protein. There are significant differences in the study of solvation dynamics of the same protein based on the nature of the fluorescent probes employed. More specifically DANCA⁹², aniline-2-aminonaphthalene-6-dimethylsulfonamide (ANSDMA)⁹⁴, and coumarin 153⁹⁵ were used to study the solvation response of myoglobin replacing the heme. DANCA yielded a complicated solvation response with significant contributions into the nanosecond regime. ANSDMA provided a single-exponential response of ~ 9 ns (although rapid components might have been neglected because of the time resolution of the experiment). Using coumarin 153 Petrich and coworkers⁹⁵ showed that almost 60 % of the solvation is complete within the time resolution of the experiment (300 fs) and that this initial response is followed by a slower one. Most importantly, there was excellent agreement between the solvation correlation function, $C(t)$, from fluorescence upconversion experiments and those obtained from molecular dynamics simulations. It is important to note that DANCA and ANSDMA are both capable of charge transfer in the excited state and can emit from dual

excited states. However, coumarin 153 is exquisitely inert, which is one of the reasons it has been so extensively employed as a probe of solvation.⁹⁵⁻¹⁰⁷

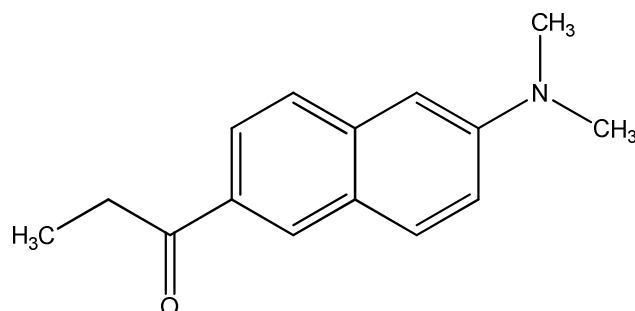


Figure 1.4. Chemical structure of PRODAN.

Recently Boxer and coworkers¹⁰⁸ have incorporated Aladan at different buried and exposed sites of the immunoglobulin binding domain, B1, of protein G (GB1) and measured the time-dependent Stokes shift. All the sites showed a bimodal relaxation with an inertial ultrafast response of ~80-140 fs followed by a much slower relaxation on the timescale of several picoseconds to several nanoseconds, depending upon the location of the probe. They also found an interesting observation. The time-resolved emission spectra of Aladan at fully and partially exposed sites of the protein showed a blue shift at long times (> 1 ns). The authors suggested that this blue shift could be attributed either to different chromophore populations having different lifetimes and solvation dynamics or to aggregation effects. Aladan is a PRODAN based probe, it can emit from both LE and CT states depending upon the polarity of the environment. The coexistence of different excited states with different properties of the same chromophores could have significant consequences for the accurate characterization of solvation dynamics in a heterogeneous environment, such as a protein. If there is a ground-state conformational change or aggregation of the protein that can perturb the environment of the chromophore in such a manner that both the excited state can exist

which can also lead to a blue shift in time-resolved emission spectra. Novaira et al.^{109,110} have already reported dual fluorescence from both LE and CT of PRODAN in reverse micelles. In order to resolve this discrepancy, in chapter 4 we study the contributions of LE and CT states of PRODAN to its solvation dynamics, in particular, in reverse micelles formed by sodium 1,4-bis-(2-ethylhexyl) sulfosuccinate (AOT)/n-heptane/water. We have found that the LE and CT states of PRODAN solvate on different time scales and conclude that PRODAN's use as a probe of heterogeneous environments must be used with caution.

Excited-State Intramolecular Proton/Hydrogen Atom Transfer

Intramolecular proton (H^+) or hydrogen atom (H) transfer occurs most commonly within molecules containing an intramolecular hydrogen bond between the hydrogen-atom donor and acceptor group in the electronic ground state.¹¹¹ Absorption of photon in these kind of molecules cause the intramolecular redistribution of electronic charge that induces fast reorganization of the molecular structure that involves motion of H or H^+ is generally referred as excited-state intramolecular hydrogen atom (ESIHT) or proton transfer (ESIPT).¹¹² It can be named "hydrogen atom" or "proton" transfer depending upon the degree of charge transfer.¹¹³ Since this process involves the transfer of a hydrogen atom over a small distance, it is ultrafast and occurs in the subpicosecond time scale.^{112,114-123} Proton or hydrogen atom transfer reactions are one of the simplest chemical transformations. Despite the chemical simplicity, subtleties in the shapes of the relevant potential energy surfaces, quantum mechanical tunneling, and extremely high reaction rates have made these reactions difficult to understand.^{113,117}

Excited-state proton transfer (ESPT) has been attracting considerable attention because it plays a crucial role in photochemistry and photobiology.¹²⁴⁻¹³⁰ H/D isotope effect

on the proton (or H-atom) transfer reaction is usually used as a probe for the existence or non-existence of a barrier on the potential energy surface.¹¹² Herek et al.¹¹⁴ studied the dynamics of H-atom (and D-atom) motion in methyl salicylate (MS), and reported that both the process takes place within 60 fs with no isotope effect, unlike the structurally related 1-hydroxy-2-acetonaphthone (HAN), which exhibit a prominent isotope effect. The absence of isotope effect in MS was attributed to a barrierless reaction. The ESIPT reaction in 2-(2'-hydroxyphenyl)-5-phenyloxazole (HPPO) occurs in the femtosecond time scale with a time constant of ~ 220 fs.¹¹⁵ Deuteration of HPPO (OH/OD) leads to a decrease in ESIPT rate by a factor of 4 to 6. The isotope effect was attributed to proton tunneling. Elsaesser and coworkers¹¹⁶ studied intramolecular proton and deuterium transfer in the excited state of 2-(2'-hydroxyphenyl)benzothiazole (HBT). In nonpolar solvent, proton and deuterium transfer time of 160 fs and 150 fs were found, respectively. They suggested a barrierless potential energy surface of the excited-state reaction with a rate determined by the period of low-frequency vibrations of large amplitude because the measured time constants correspond to the period of molecular vibrations of low frequency. Schwartz et al.¹¹⁷ reported a proton transfer time of 240 fs for 3-hydroxyflavone in methycyclohexane. No significant changes in the fast ESPT dynamics upon deuteration were found. Petrich and coworkers^{15,118-123} reported ESIHT in hypericin and hypocrellin A. A ~ 10 ps for hypericin and 10-250 ps for hypocrellin A were assigned as the ESIHT time. The 10 ps component neither in hypericin nor hypocrellin A exhibited a deuterium isotope effect. Interestingly, the long-lived component (50-250 ps) of hypocrellin A showed an isotope effect of 1.4. The absence of isotope effect in hypericin was explained in term of adiabatic limit of proton transfer where the vibrational energy levels of the proton stretch mode lie well above a small barrier. The

similar adiabatic limit of proton transfer model was applied for hypocrellin, which leads to an isotope effect due to tunneling or activated crossing of the barrier when deuteration lowers the ground vibrational energy below the top of the barrier.¹²³

Curcumin

Curcumin (Figure 1.5), 1,7-bis(4-hydroxy-3-methoxyphenyl)-1,6-heptadiene-3,5-dione, is a naturally occurring yellow-orange pigment derived from the rhizomes of *Curcuma longa* (turmeric). Turmeric has been traditionally used as a spice and food coloring in Indian cooking and medicine.¹³¹ Its yellow color is primarily caused by a group of structurally related polyphenols collectively known as curcuminoids, which are composed of curcumin (77%), as the major bioactive component, and two of its derivatives, demethoxycurcumin (17%) and bismethoxycurcumin (3%). Currently, curcumin is the subject of a large number of investigations in the fields of biology, medicine, and pharmacology owing to its profound effects on human health. It exhibits a variety of biological and photochemical properties, including antioxidant, anti-inflammatory, and anticancer activity.¹³²⁻¹³⁶ Recently, it is also established that curcumin has the ability to prevent protein aggregation in debilitating diseases such as Alzheimer's and Parkinson's.^{137,138}

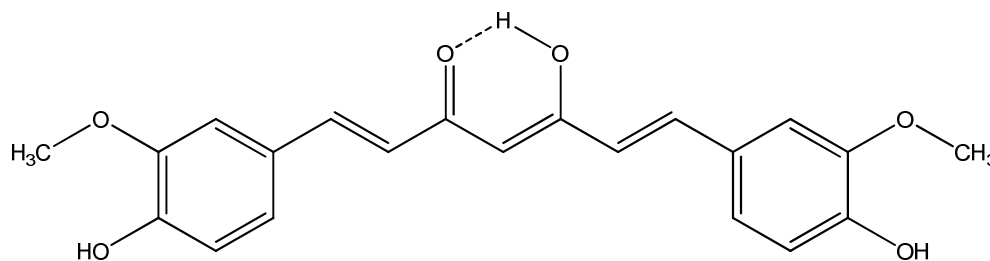


Figure 1.5. Chemical structure of curcumin.

Curcumin has great potential to be an effective photodynamic agent.¹³⁹⁻¹⁴⁶ In particular, studies have demonstrated the use of curcumin to treat melanoma.¹⁴⁷⁻¹⁵³ It has

been shown that the photodynamic action is greatly enhanced in the presence of light for destruction of tumor cells.¹⁴⁴⁻¹⁴⁶ Photolytically produced active oxygen species such as singlet oxygen, hydroxyl radical, superoxide or hydrogen peroxide are mainly suggested for its activity.^{139,140,154-158} In addition, Slobodan et al. demonstrated that H-atom transfer is a preferred antioxidant mechanism of curcumin by laser flash photolysis and pulse radiolysis.¹⁵⁹ Currently, there is much interest in developing a detailed level of understanding in the photophysics and photochemistry of curcumin in order to further exploit its medicinal effects. It has been proposed that the presence of a labile hydrogen as a result of ESIHT plays a role in the medicinal effects of other naturally occurring pigments such as hypericin and hypocrellin.^{119-121,123,160} Curcumin has two tautomeric forms, namely the β -diketone and keto-enol. It has been shown that curcumin exists predominantly as a keto-enol tautomer in a number of solvents with various polarities.¹⁶¹ It follows that strong intramolecular hydrogen bonding is present in the keto-enol tautomer of curcumin, which provides a favorable interaction for stabilization of this tautomeric form. Thus, there is a high probability that curcumin may undergo excited state intramolecular hydrogen atom transfer (ESIHT) that results in partial deprotonation, which induces fragmentation to yield the medicinal degradation products mentioned earlier.

In chapter 5 the excited state photophysics of curcumin is studied by means of ultrafast fluorescence upconversion spectroscopy. The results show two decay components in the excited-state kinetics with time scales of 12-20 ps and \sim 100 ps in methanol and ethylene glycol. The resulting prominent isotope effect in the long component upon deuteration indicates that curcumin undergoes ESIHT in these solvents. The short component (12-20 ps) is insensitive to deuteration, and study of solvation dynamics of

curcumin in these solvents show that this decay component is due to solvation of excited-state curcumin.

Two major challenges in the application of curcumin as an effective treatment agent are lack of bioavailability and severely limited stability in aqueous environments. Because of the low aqueous solubility, curcumin tends to aggregate and precipitate in water, limiting its bioavailability.¹⁶²⁻¹⁶⁵ In addition, curcumin undergoes rapid degradation in water and buffer solutions, with a reaction half-life of 9.5 minutes at pH 7.2.¹⁶⁶ It has been demonstrated that the degradation is mostly due to deprotonation of curcumin, producing the degradation products: vanillin, ferulic acid, and feruoyl methane.^{166,167} It is interesting that most of these products have medicinal properties as well. Previous studies have shown that encapsulation of curcumin in surfactant micelles and binding to proteins resolve these two major issues.¹⁶²⁻¹⁶⁴ Micellar systems may potentially play an important role in leading to improved clinical use of curcumin. It is established that micelle-captured curcumin is well dispersed in aqueous solutions, thereby increasing the bioavailability significantly.^{162,163,165} Moreover, curcumin is trapped in the regions of the micelle where the presence of free water molecules is relatively limited, preventing alkaline hydrolysis, which is the major mechanism for degradation.^{166,167} It is therefore plausible that association to micelles plays a considerable role in enabling curcumin to exhibit its medicinal characteristics. Apart from preventing degradation, micelles also serve as well defined model systems for biomembranes. It has been shown that a large portion of curcumin is membrane bound in a biological environment.¹⁶⁸ Investigations on the behavior of curcumin in micelles may provide valuable insight into the properties of curcumin in biomembranes.

It is known that intra- and intermolecular proton transfer processes are affected in

confined environment due to the structure, various interfaces and dynamics of the environment.¹⁶⁹⁻¹⁷² Fleming and coworkers found nearly two to three fold increase in the rate of ESPT of protonated 1-aminopyrene in β -cyclodextrin as compared to bulk water.¹⁶⁹ A higher basicity of water molecules in the immediate vicinity of cyclodextrin has been suggested. Zewail and coworkers have also reported appreciable reduction in the ESIPT rate of 2-(2'-hydroxyphenyl)-4-methyloxazole from 300 fs in bulk aprotic solvents to pico and nanosecond timescales when encapsulated in β -cyclodextrin.¹⁷⁰ Macanita and coworkers have observed two orders decrease in rate constant for deprotonation of the 4-methyl-7-hydroxyflavylium cation (HMF) upon going from water (10^{-6} s range) to anionic sodium dodecyl sulfate (SDS) micelles (10^{-4} s range).¹⁷¹ The decrease in the rate constant was attributed to the preferential stabilization of the flavylium cation by the anionic micelle relative to the neutral anhydrobase form. Analogous effects of SDS micelles on deprotonation rate constants have also been observed for the naturally occurring anthocyanin oenin.¹⁷²

In chapter 6 we have investigated the ESIHT of curcumin in sodium dodecyl sulfate (SDS), dodecyl trimethyl ammonium bromide (DTAB) and triton X-100 (TX-100), which are anionic, cationic and nonionic in nature, respectively. By comparing the excited-state decay kinetics obtained by fluorescence upconversion spectroscopy, we show that the time constant of ESIHT of curcumin in these micelles ranges from 50 – 80 ps. This slow component exhibits a pronounced isotope effect, producing a decay time constant of 80 – 130 ps in the micelles, which is assigned to ESIHT. In addition to ESIHT, a fast component of 3 – 8 ps is also observed. Results from the study of solvation dynamics of curcumin in the micellar media confirm that the faster component is due to solvation dynamics. The ESIHT

rate of curcumin in the TX-100 micelle is lower than those in the other two micellar system. The intermolecular hydrogen bonding between curcumin and the TX-100 surfactant may contribute to this effect.

Transmissible Spongiform Encephalopathy (TSE)

Transmissible spongiform encephalopathies (TSEs) are slowly progressive, insidiously degenerative diseases that affect the central nervous system (CNS) of both humans and animals.¹⁷³⁻¹⁷⁶ TSEs are transmissible because they are capable of being transferred from one animal to another, spongiform because they create sponge-like texture in the brain of the affected animal and encephalopathies because they are neurodegenerative diseases of the brain.¹⁷⁷ TSEs are believed to be transmitted by abnormally shaped protein lacking nucleic acid, which are resistant to enzymatic degradation, called prion (**proteinacious infectious particle**).¹⁷⁸ This prion protein (PrP) exists in two forms, normal (PrP^c) and its pathological isoform (PrP^{res}).^{177,178} PrP^{res} is resistant to protease digestion. The PrP^c becomes PrP^{res} when the tertiary structure of PrP^c changes from a normal α -helix to a misfolded β -pleated sheet, resulting in altered function.^{177,178} PrP^c is expressed most abundantly in the CNS tissue of mammals. Researchers believe that TSE disease is initiated when PrP^{res} interact with PrP^c and precipitate a shape change in the protein itself.¹⁷⁷ The structural malformation of this protein alters its function and ultimately results in cell damage.

Bovine spongiform encephalopathy (BSE) of cattle (“mad-cow disease”) is a fatal, neurodegenerative transmissible spongiform encephalopathy (TSE). In human, the new variant Creutzfeldt-Jakob disease (vCJD) is believed to be transmitted BSE from cattle through human food chain.¹⁷⁹ BSE is infectious but not contagious because it is not excreted, thereby

preventing transmission from cow to cow. It can be transmitted orally, for example, spread through BSE contaminated food. Clinical tests shows that prion protein, the causative agent of BSE, accumulates in the brain, spinal cord, eyes, tonsils, trigeminal ganglia, dorsal root ganglion, distal ileum of the small intestine and 3rd eyelid of the BSE affected cows. It has been also shown that ruminant brain and spinal cord contain highest infectivity of prion protein.^{180,181} As the oral route of infection is most probable way of transmission of BSE to human, it is important to prohibit the use of BSE risk material (e.g, brain and spinal cord) of cattle in human food chain.^{182,183}

Among other animals, scrapie is the most widespread TSE affecting sheep and goats worldwide. It is characterized by a gradual onset; and advanced cases show typical disease characteristics including unthriftiness, compulsive itching, balance and ambulatory abnormalities, convulsions, and eventual death. The disease has been observed for centuries. Scrapie is contagious and thought to be easily spread via contact with placenta and placental fluids or environmental contamination.¹⁷⁷ At present, it is incurable and the most common form of control is quarantine, euthanasia, and proper disposal of the carcass. Scrapie is not considered to be infectious to humans. However, there is evidence that scrapie was transmitted to cattle and thereby initiated the European “mad-cow” disease.

Lipofuscin

Lipofuscin is a yellow-brown, granular, heterogeneous, high-molecular weight intracellular complex aggregate of material that undergoes age-related progressive accumulation mainly in postmitotic cells, such as neurons, cardiac muscle and retinal epithelium.¹⁸⁴⁻¹⁹⁰ Although extensive studies have been carried out for more than a century, the biochemistry, formation mechanisms, fluorescence emission and composition of

lipofuscin are still a matter of debate and controversy.¹⁸⁵ Even though lipofuscin can be produced from different types of biological materials due to different side reactions of essential biology, the cross linking of carbonyl-amino compound is recognized as a common process during their formation.¹⁸⁵ One of the most pronounced characteristics of lipofuscin is its yellowish-orange autofluorescence when excited with UV or blue light.

It is known that the amount of fluorescent lipofuscin in CNS tissue increases as a result of spontaneous and experimentally induced Creutzfeldt-Jakob's disease (CJD). Boellaard et al. have demonstrated a relationship between lipofuscin production, a decline in autophagocytosis activity, and the experimental induction of CJD in mice.¹⁹¹ Furthermore, there is substantial documentation linking neurological disease produced by TSEs to eye damage and the accumulation of lipofuscin.¹⁹¹⁻¹⁹⁹

Since lipofuscin has been characterized as highly fluorescent pigment of cell, fluorescence spectroscopy can be used to characterize and differentiate the autofluorescence from different type of tissues. The introduction of specified risk materials (SRM), such as central nervous system (CNS) tissues, during the processing of foods destined for human consumption has become a concern because of bovine spongiform encephalopathy (BSE). There are no sufficiently rapid methods for detecting CNS tissue. In chapter 7 we have investigated the applicability of fluorescence spectra and signal intensities from CNS (brain and spinal cord) and non-CNS tissues of cattle for real-time detection of SRM, brain and spinal cord in human food chain. We have shown that fluorescence intensity from brain and spinal cord is higher than that of non-CNS tissues and small quantities of bovine spinal cord can be reliably detected in the presence of raw bovine skeletal muscle, fat, and vertebrae. There are no current methods which can detect TSE disease in live animals. Only post-

mortem examinations and laboratory tests can confirm if the animal has been suffering from TSE disease. Any technique which is capable of testing a live animal for TSE disease is of great interest. CNS tissues are mostly affected by TSE disease and eye is the direct entry point to reach CNS tissues. In chapter 8, we investigate the use of fluorescence signatures of sheep eye to identify scrapie, which we use as a model for TSEs. Our data indicate that the fluorescence spectra from scrapie-positive retinas are more structured and intense compared to the scrapie-negative retinas. We suggest that the eye, in particular the retina, is a useful tissue for noninvasive examination of some neurological pathologies such as scrapie.

Thesis Organization

General introductions on essential topic are discussed briefly in **chapter 1**. The rest of this thesis is organized into the following chapters

Chapter 2 provides basic principles and outlines of steady-state and time-resolved fluorescence techniques that are used throughout this thesis along with analysis of experimental data.

Chapter 3 describes interaction of hypericin with biologically important macromolecule, low-density lipoprotein (LDL).

Chapter 4 discusses the contributions of the locally excited (LE) and charge-transferred (CT) states of the fluorescent probe molecule PRODAN to its solvation dynamics in the heterogeneous environment.

Chapter 5 establishes excited-state intramolecular hydrogen atom transfer (ESIHT) of the medicinal pigment curcumin in bulk solvent.

Chapter 6 presents excited-state intramolecular hydrogen atom transfer (ESIHT) of the medicinal pigment curcumin in cationic, anionic and neutral micellar environments.

Chapter 7 demonstrates real-time detection of central nervous system tissues on bovine carcasses exploiting fluorescence signatures of the tissues.

Chapter 8 provides the feasibility for diagnosis of transmissible spongiform encephalopathies (TSEs) exploiting retinal fluorescence spectra.

Chapter 9 summarizes this thesis and discusses future work.

References

- (1) Lakowicz, J. R. *Principles of fluorescence spectroscopy*, 3rd ed.; Springer: New York, 2004.
- (2) Fleming, G. R. *Chemical Applications of Ultrafast Spectroscopy*; Oxford University Press: London, 1986.
- (3) Birks, J. B. *Photophysics of Aromatic Molecules*; Wiley-Interscience: London, 1970.
- (4) Valeur, B. *Molecular fluorescence: principles and applications* Wiley-VCH: Weinheim, 2002.
- (5) Vance, D. E.; Vance, J. E. *Biochemistry of Lipids, Lipoproteins and Membranes*; Elsevier, 2002.
- (6) Hevonoja, T.; Pentikäinen, M. O.; Hyvönen, M. T.; Kovanen, P. T.; Ala-Korpela, M. *Biochim. Biophys. Acta.* **2000**, *1488*, 189.
- (7) Esterbauer, H.; Gebicki, J.; Puhl, H.; Jürgens, G. *Free Radical. Biol. Med.* **1992**, *13*, 341.
- (8) Jori, G. In vivo transport and pharmacokinetic behaviour of tumour photosensitizers. In *Photosensitizing Compounds: Their Chemistry, Biology and Clinical Use*; John Wiley & Sons Inc., 1989; Vol. 146; pp 78.

- (9) Maiya, B. G. *Resonance* **2000**, 5, 6.
- (10) Pace, N.; Mackinney, G. *J. Am. Chem. Soc.* **1941**, 63, 2570.
- (11) Durán, N.; Song, P. S. *Photochem. Photobiol.* **1986**, 43, 677.
- (12) Lown, J. W. *Can. J. Chem.* **1997**, 75, 99.
- (13) Diwu, Z. *Photochem. Photobiol.* **1995**, 61, 529.
- (14) Diwu, Z.; Lowen, J. W. *Free Rad. Biol. Med* **1993**, 14, 209.
- (15) Kraus, G. A.; Zhang, W. J.; Fehr, M. J.; Petrich, J. W.; Wannemuehler, Y.; Carpenter, S. *Chem. Rev.* **1996**, 96, 523.
- (16) Meruelo, D.; Lavie, G.; Lavie, D. *Proc. Natl. Acad. Sci. USA* **1988**, 85, 5230.
- (17) Lenard, J.; Rabson, A.; Vanderoef, R. *Proc. Natl. Acad. Sci. USA* **1993**, 90, 158.
- (18) Lopez-Bazzocchi, I.; Hudson, J. B.; G. H. N. Towers, G. H. N. *Photochem. Photobiol.* **1991**, 54, 95.
- (19) Couldwell, W. T.; Gopalakrishna, R.; Hinton, D. R.; He, S.; Weiss, M. H.; Law, R. E.; Apuzzo, M. L. *Neurosurgery* **1994**, 35, 705.
- (20) Anker, L.; Gopalakrishna, R.; Jones, K. D.; Law, R. E.; Couldwell, W. T. *Drugs Fut.* **1995**, 20, 511.
- (21) Thomas, C. P. R. S. *Photochemistry* **1992**, 55, 831.
- (22) Hudson, J. B.; Lopez-Bazzocchi, I.; Towers, G. H. N. *Antiviral Res.* **1991**, 15, 101.
- (23) Degar, S.; Prince, A. M.; Pascual, D.; Lavie, G.; Levin, B.; Mazur, Y.; Lavie, D.; Ehrlich, L. S.; Carter, C.; Meruelo. *AIDS Res. Hum. Retroviruses* **1992**, 8, 1929.
- (24) Carpenter, S.; Kraus, G. A. *Photochem. Photobiol.* **1991**, 53, 169.

- (25) Bouirig, H.; Eloy, D.; Jardon, P. *J. Chim. Phys. Phys.-Chim. Biol.* **1992**, *89*, 1391.
- (26) Bouirig, H.; Eloy, D.; Jardon, P. *J. Chim. Phys. Phys.-Chim. Biol.* **1993**, *90*, 2021.
- (27) Yamazaki, T.; Ohta, N.; Yamazaki, I.; Song, P. S. *Journal of Physical Chemistry* **1993**, *97*, 7870.
- (28) Gai, F.; Fehr, M. J.; Petrich, J. W. *J. Am. Chem. Soc.* **1993**, *115*, 3384.
- (29) Gai, F.; Fehr, M. J.; Petrich, J. W. *J. Phys. Chem.* **1994**, *98*, 5784.
- (30) Gai, F.; Fehr, M. J.; Petrich, J. W. *J. Phys. Chem.* **1994**, *98*, 8352.
- (31) Weiner, L.; Mazur, Y. *J. Chem. Soc. Perkin Trans.* **1992**, *2*, 1439.
- (32) Redepenning, J.; Tao, N. *Photochem. Photobiol.* **1993**, *58*, 532.
- (33) Jardon, P.; Lazortchak, N.; Gautron, R. *J. Chim. Phys. Phys.-Chim. Biol.* **1987**, *84*, 1141.
- (34) Carpenter, S.; Fehr, M. J.; Kraus, G. A.; Petrich, J. W. *Proc. Natl. Acad. Sci. USA* **1994**, *91*, 12273.
- (35) Fehr, M. J.; McCloskey, M. A.; Petrich, J. W. *J. Am. Chem. Soc.* **1995**, *117*, 1833.
- (36) Das, K.; Smirnov, A. V.; Wen, J.; Miskovsky, P.; Petrich, J. W. *Photochem. Photobiol.* **1999**, *69*, 633.
- (37) Halder, M.; Chowdhury, P. K.; Das, R.; Mukherjee, P.; Atkins, W. M.; Petrich, J. W. *J. Phys. Chem. B* **2005**, *109*, 19484.
- (38) Kascakova, S.; Refregiers, M.; Jancura, D.; Sureau, F.; Maurizot, J.-C.; Miskovsky, P. *Photochem. Photobiol.* **2005**, *81*, 1395.

- (39) Burel, L.; Jardon, P. *J. Chim. Phys. Phys.-Chim. Biol.* **1996**, *93*, 300.
- (40) Senthil, V.; Longworth, J. W.; Ghiron, C. A.; Grossweiner, L. I. *Biochem. Biophys. Acta.* **1992**, *1115*, 192.
- (41) Senthil, V.; Jones, L. R.; Senthil, K.; Grossweiner, L. I. *Photochem. Photobiol.* **1994**, *59*, 40.
- (42) Jori, G.; Reddi, E. *Int. J. Biochem.* **1993**, *25*, 1369.
- (43) Maziere, J. C.; Moliere, P.; Santus, R. *J. Photochem. Photobiol. B* **1991**, *8*, 351.
- (44) Morliere, P.; Kohen, E.; Reyftmann, J. P.; Santus, R.; Cohen, C.; Maziere, J. C.; Goldstein, S.; Mangel, W. F.; Dubertret, L. *Photochem. Photobiol.* **1987**, *46*, 183.
- (45) Chowdhary, R. K.; Sharif, I.; Chansarkar, N.; Dolphin, D.; Ratkay, L.; Delaney, S.; Meadows, H. *J. Pharm. Pharm. Sci.* **2003**, *6*, 198.
- (46) Everett, D. H. *Basic Principles of Colloid Science*; The Royal Society of Chemistry: Cambridge, U.K., 1988.
- (47) *Colloid Science: Principles, Methods and Applications*; Wiley-Blackwell: Oxford, U.K., 2005.
- (48) Tanford, C. *The Hydrophobic Effect: Formation of Micelles and Biological Membranes*; Wiley: New York, 1973.
- (49) Hayter, J. B. *Physics of Amphiphiles: Micelles, Vesicles and Microemulsion*; North Holland: Amsterdam, 1985.
- (50) Moulik, S. P. *Curr. Sci.* **1996**, *71*, 368.
- (51) Florence, A. T.; Attwood, D. *Physicochemical principles of pharmacy*, 4th ed.; Pharmaceutical Press: London : Macmillan, 2006.

- (52) Kalyanasundram, K. *Photochemistry in Microheterogeneous Systems*; Academic Press: New York, 1987.
- (53) Paradies, H. H. *J. Phys. Chem.* **1980**, *84*, 599.
- (54) Berr, S. S.; Coleman, M. J.; Jones, R. R. M.; Johnson, J. S. *J. Phys. Chem.* **1986**, *90*, 6492.
- (55) Berr, S. S.; Caponetti, E.; Jones, R. R. M.; Johnson, J. S.; Magid, L. J. *J. Phys. Chem.* **1986**, *90*, 5766.
- (56) Berr, S. S. *J. Phys. Chem.* **1987**, *91*, 4760.
- (57) Paul, B. K.; Moulik, S. P. *J. Dispers. Sci. Technol.* **1997**, *18*, 301.
- (58) Zulauf, M.; Eicke, H. F. *J. Phys. Chem.* **1979**, *83*, 480.
- (59) De, T. K.; Maitra, A. *Adv. Colloid Interface Sci.* **1995**, *59*, 95.
- (60) D'Aprano, A.; D'Arrigo, G.; Paparelli, A.; Goffredi, M.; Liveri, V. T. *J. Phys. Chem.* **1993**, *97*, 3614.
- (61) Weber, G.; Farris, F. J. *Biochemistry* **1979**, *18*, 3075.
- (62) Nowak, W.; Adamczak, P.; Balter, A.; Sygula, A. *J. Mol. Struct. THEOCHEM* **1986**, *32*, 13.
- (63) Marks, D.; Proposito, P.; Zhang, H.; Glasbeek, M. *Chem. Phys. Lett.* **1998**, *289*, 535.
- (64) Balter, A.; Nowak, W.; Pawelkiewicz, W.; Kowalczyk, A. *Chem. Phys. Lett.* **1988**, *143*, 565.
- (65) Catalan, J.; Perez, P.; Laynez, J.; Garcia Blanco, F. *J. Fluoresc.* **1991**, *1*, 215.
- (66) Parusel, A. B. J.; Schneider, F. W.; Kohler, G. *J. Mol. Struct. THEOCHEM* **1997**, *398-399*, 341.

- (67) Parusel, A. B. J.; Nowak, W.; Grimme, S.; Koehler, G. *J. Phys. Chem. A* **1998**, *102*, 7149.
- (68) Parusel, A. *J. Chem. Soc., Faraday Trans.* **1998**, *94*, 2923.
- (69) Ilich, P.; Prendergast, F. G. *J. Phys. Chem.* **1989**, *93*, 4441.
- (70) Heisel, F.; Miehe, J. A.; Szemik, A. W. *Chem. Phys. Lett.* **1987**, *138*, 321.
- (71) Bunker, C. E.; Bowen, T. L.; Sun, Y. P. *Photochem. Photobiol.* **1993**, *58*, 499.
- (72) Pal, S. K.; Mandal, D.; Bhattacharyya, K. *J. Phys. Chem. B* **1998**, *102*, 11017.
- (73) Lobo, B. C.; Abelt, C. J. *J. Phys. Chem. A* **2003**, *107*, 10938.
- (74) Samanta, A.; Fessenden, R. W. *J. Phys. Chem. A* **2000**, *104*, 8972.
- (75) Davis, B. N.; Abelt, C. J. *J. Phys. Chem. A* **2005**, *109*, 1295.
- (76) Mennucci, B.; Caricato, M.; Ingrosso, F.; Cappelli, C.; Cammi, R.; Tomasi, J.; Scalmani, G.; Frisch, M. J. *J. Phys. Chem. B* **2008**, *112*, 414.
- (77) Bakalova, S. M.; Kaneti, J. *Spectrochim. Acta Part A, Mol. Biomol. Spectrosc.* **2009**, *72*, 36.
- (78) Rollinson, A. M.; Drickamer, H. G. *J. Chem. Phys.* **1980**, *73*, 5981.
- (79) Moreno, F.; Cortijo, M.; Gonzalez-Jimenez, J. *Photochem. Photobiol.* **1999**, *69*, 8.
- (80) Lasagna, M.; Vargas, V.; Jameson, D. M.; Brunet, J. E. *Biochemistry* **1996**, *35*, 973.
- (81) Rottenberg, H. *Biochemistry* **1992**, *31*, 9473.
- (82) Bondar, O. P.; Rowe, E. S. *Biophys. J.* **1999**, *76*, 956.
- (83) Bondar, O. P.; Rowe, E. S. *Biophys. J.* **1996**, *71*, 1440.
- (84) Sommer, A.; Paltauf, F.; Hermetter, A. *Biochemistry* **1990**, *29*, 11134.

- (85) Krasnowska, E. K.; Gratton, E.; Parasassi, T. *Biophys. J.* **1998**, *74*, 1984.
- (86) Zeng, J. W.; Chong, P. L. *Biochemistry* **1991**, *30*, 9485.
- (87) Chapman, C. F.; Fee, R. S.; Maroncelli, M. *J. Phys. Chem.* **1990**, *94*, 4929.
- (88) Chapman, C. F.; Maroncelli, M. *J. Phys. Chem.* **1991**, *95*, 9095.
- (89) Betts, T. A.; Zagrobelny, J.; Bright, F. V. *J. Supercrit. Fluids* **1992**, *5*, 48.
- (90) Karmakar, R.; Samanta, A. *J. Phys. Chem. A* **2002**, *106*, 6670.
- (91) Betts, T. A.; Zagrobelny, J.; Bright, F. V. *J. Am. Chem. Soc.* **1992**, *114*, 8163.
- (92) Pierce, D. W.; Boxer, S. G. *J. Phys. Chem.* **1992**, *96*, 5560.
- (93) Cohen, B. E.; McAnaney, T. B.; Park, E. S.; Jan, Y. N.; Boxer, S. G.; Jan, L. *Y. Science* **2002**, *296*, 1700.
- (94) Bashkin, J. S.; Mclendon, G.; Mukamel, S.; Marohn, J. *J. Phys. Chem.* **1990**, *94*, 4757.
- (95) Halder, M.; Mukherjee, P.; Bose, S.; Hargrove, M. S.; Song, X.; Petrich, J. W. *J. Chem. Phys.* **2007**, *127*, 055101/1.
- (96) Changenet-Barret, P.; Choma, C. T.; Gooding, E. F.; DeGrado, W. F.; Hochstrasser, R. M. *J. Phys. Chem. B* **2000**, *104*, 9322.
- (97) Maroncelli, M.; Fleming, G. R. *J. Chem. Phys.* **1987**, *86*, 6221.
- (98) Horng, M. L.; Gardecki, J. A.; Papazyan, A.; Maroncelli, M. *J. Phys. Chem.* **1995**, *99*, 17311.
- (99) Lewis, J. E.; Maroncelli, M. *Chem. Phys. Lett.* **1998**, *282*, 197.
- (100) Muhlfordt, A.; Schanz, R.; Ernsting, N. P.; Farztdinov, V.; Grimme, S. *Phys. Chem. Chem. Phys.* **1999**, *1*, 3209.
- (101) Jiang, Y.; McCarthy, P. K.; Blanchard, D. J. *Chem. Phys.* **1994**, *183*, 249.

- (102) Flory, W. C.; Blanchard, D. J. *Appl. Spectrosc.* **1998**, *52*, 82.
- (103) Palmer, P. M.; Chen, Y.; Topp, M. R. *Chem. Phys. Lett.* **2000**, *318*, 440.
- (104) Chen, Y.; Palmer, P. M.; Topp, M. R. *Int. J. Mass Spectrom.* **2002**, *220*, 231.
- (105) Agmon, N. *J. Phys. Chem.* **1990**, *94*, 2959.
- (106) Chowdhury, P. K.; Halder, M.; Sanders, L.; Arnold, R. A.; Liu, Y.; Armstrong, D. W.; Kundu, S.; Hargrove, M. S.; Song, X.; Petrich, J. W. *Photochem. Photobiol.* **2004**, *79*, 440.
- (107) Mukherjee, P.; Halder, M.; Hargrove, M.; Petrich, J. W. *Photochem. Photobiol.* **2006**, *82*, 1586.
- (108) Abbyad, P.; Shi, X.; Childs, W.; McAnaney, T. B.; Cohen, B. E.; Boxer, S. G. *J. Phys. Chem. B* **2007**, *111*, 8269.
- (109) Novaira, M.; Biasutti, M. A.; Silber, J. J.; Correa, N. M. *J. Phys. Chem. B* **2007**, *111*, 748.
- (110) Novaira, M.; Moyano, F.; Biasutti, M. A.; Silber, J. J.; Correa, N. M. *Langmuir* **2008**, *24*, 4637.
- (111) Kosower, E. M. H., D. *Annu. Rev. Phys. Chem.* **1986**, *37*, 127.
- (112) Douhal, A.; Lahmani, F.; Zewail, A. H. *Chem. Phys.* **1996**, *207*, 477.
- (113) Barbara, P. F.; Walsh, P. K.; Brus, L. E. *J. Phys. Chem.* **1989**, *93*, 29.
- (114) Herek, J. L.; Pedersen, S.; Banares, L.; Zewail, A. H. *J. Chem. Phys.* **1992**, *97*, 9046.
- (115) Douhal, A.; Lahmani, F.; Zehnacker-Rentien, A.; Amat-Guerri, F. *J. Phys. Chem.* **1994**, *98*, 12198.
- (116) Frey, W.; Laermer, F.; Elsaesser, T. *J. Phys. Chem.* **1991**, *95*, 10391.

- (117) Schwartz, B. J.; Peteanu, L. A.; Harris, C. B. *J. Phys. Chem.* **1992**, *96*, 3591.
- (118) English, D. S.; Das, K.; Ashby, K. D.; Park, J.; Petrich, J. W.; Castner, E. W. *J. Am. Chem. Soc.* **1997**, *119*, 11585.
- (119) English, D. S.; Zhang, W.; Kraus, G. A.; Petrich, J. W. *J. Am. Chem. Soc.* **1997**, *119*, 2980.
- (120) Das, K.; English, D. S.; Petrich, J. W. *J. Am. Chem. Soc.* **1997**, *119*, 2763.
- (121) Das, K.; English, D. S.; Petrich, J. W. *J. Phys. Chem. A* **1997**, *101*, 3241.
- (122) Das, K.; Dertz, E.; Paterson, J.; Zhang, W.; Kraus, G. A.; Petrich, J. W. *J. Phys. Chem. B* **1998**, *102*, 1479.
- (123) Petrich, J. W. *Int. Rev. Phys. Chem.* **2000**, *19*, 479.
- (124) Arnaut, L. G. F., S. J. *J. Photochem. Photobiol. A: Chem.* **1993**, *75*, 1.
- (125) Formosinho, J. S.; Arnaut, G. L. *J. Photochem. Photobiol. A* **1993**, *75*, 21.
- (126) Waluk, J. *Acc. Chem. Res.* **2003**, *36*, 832.
- (127) Douhal, A.; Kim, S. K.; Zewail, A. H. *Nature* **1995**, *378*, 260.
- (128) Tanner, C.; Manca, C.; Leutwyler, S. *Science* **2003**, *302*, 1736.
- (129) Rini, M.; Magnes, B.-Z.; Pines, E.; Nibbering, E. T. *Science* **2003**, *301*, 349.
- (130) Geissler, P. L.; Dellago, C.; Chandler, D.; Hutter, J.; Parrinello, M. *Science* **2001**, *291*, 2121.
- (131) Goel, A.; Kunnumakkara, A. B.; Aggarwal, B. B. *Biochem. Pharmacol.* **2008**, *75*, 787.
- (132) Ruby, A. J.; Kuttan, G.; Babu, K. D.; Rajasekharan, K. N.; Kuttan, R. *Cancer Lett.* **1995**, *94*, 79.

- (133) Lantz, R. C.; Chen, G. J.; Solyom, A. M.; Jolad, S. D.; Timmermann, B. N. *Phytomedicine* **2005**, *12*, 445.
- (134) Aggarwal, B. B.; Kumar, A.; Bharti, A. C. *Anticancer Res.* **2003**, *23*, 363.
- (135) Shi, M.; Cai, Q.; Yao, L.; Mao, Y.; Ming, Y.; Ouyang, G. *Cell Biol. Int.* **2006**, *30*, 221.
- (136) Surh, Y.-J. *Food Chem. Toxicol.* **2002**, *40*, 1091.
- (137) Yang, F.; Lim, G. P.; Begum, A. N.; Ubeda, O. J.; Simmons, M. R.; Ambegaokar, S. S.; Chen, P. P.; Kaye, R.; Glabe, C. G.; Frautschy, S. A.; Cole, G. M. *J. Biol. Chem.* **2005**, *280*, 5892.
- (138) Masuda, M.; Suzuki, N.; Taniguchi, S.; Oikawa, T.; Nonaka, T.; Iwatsubo, T.; Hisanaga, S.-i.; Goedert, M.; Hasegawa, M. *Biochemistry* **2006**, *45*, 6085.
- (139) Tonnesen, H. H.; De Vries, H.; Karlsen, J.; Beijersbergen van Henegouwen, G. *J. Pharm. Sci.* **1987**, *76*, 371.
- (140) Dahl, T. A.; McGowan, W. M.; Shand, M. A.; Srinivasan, V. S. *Arch. Microbiol.* **1989**, *151*, 183.
- (141) Gorman, A. A.; Hamblett, I.; Srinivasan, V. S.; Wood, P. D. *Photochem. Photobiol.* **1994**, *59*, 389.
- (142) Chignell, C. F.; Bilski, P.; Reszka, K. J.; Motten, A. G.; Sik, R. H.; Dahl, T. A. *Photochem. Photobiol.* **1994**, *59*, 295.
- (143) Dahl, T. A.; Bilski, P.; Reszka, K. J.; Chignell, C. F. *Photochem. Photobiol.* **1994**, *59*, 290.
- (144) Chan, W.-H.; Wu, H.-J. *J. Cell. Biochem.* **2004**, *92*, 200.

- (145) Koon, H.; Leung, A. W. N.; Yue, K. K. M.; Mak, N. K. *J. Environ. Pathol. Toxicol. Oncol.* **2006**, *25*, 205.
- (146) Park, K.; Lee, J.-H. *Oncol. Rep.* **2007**, *17*, 537.
- (147) Menon, L. G.; Kuttan, R.; Kuttan, G. *Cancer Lett.* **1995**, *95*, 221.
- (148) Iersel, M. L.; Ploemen, J.-P.; Struik, I.; Amersfoort, C. v.; Keyzer, A. E.; Schefferlie, J. G.; Bladeren, P. J. v. *Chem. Biol. Interact.* **1996**, *102*, 117.
- (149) Odot, J.; Albert, P.; Carlier, A.; Tarpin, M.; Devy, J.; Madoulet, C. *Int. J. Cancer* **2004**, *111*, 381.
- (150) Zheng, M.; Ekmekcioglu, S.; Walch, E. T.; Tang, C.-H.; Grimm, E. A. *Melanoma Res.* **2004**, *14*, 165.
- (151) Siwak, D. R.; Shishodia, S.; Aggarwal, B. B.; Kurzrock, R. *Cancer Lett.* **2005**, *104*, 879.
- (152) Lao, C. D.; Demierre, M.-F.; Sondak, V. K. *Expert Rev. Anticancer Ther.* **2006**, *6*, 1559.
- (153) Marin, Y. E.; Wall, B. A.; Wang, S.; Namkoong, J.; Martino, J. J.; Suh, J.; Lee, H. J.; Rabson, A. B.; Yang, C. S.; Chen, S.; Ryu, J.-H. *Melanoma Res.* **2007**, *17*, 274.
- (154) Sharma, O. P. *Biochem. Pharmacol.* **1976**, *25*, 1811.
- (155) Priyadarsini, K. I. *Free Radical Biol. Med.* **1997**, *23*, 838.
- (156) Khopde, S. M.; Priyadarsini, K. I.; Venkatesan, P.; Rao, M. N. A. *Biophys. Chem.* **1999**, *80*, 85.
- (157) Kunchandy, E.; Rao, M. N. A. *Int. J. Pharm.* **1989**, *57*, 173.
- (158) Kunchandy, E.; Rao, M. N. A. *Int. J. Pharm.* **1990**, *58*, 237.

- (159) Jovanovic, S. V.; Steenken, S.; Boone, C. W.; Simic, M. G. *J. Am. Chem. Soc.* **1999**, *121*, 9677.
- (160) Smirnov, A. V.; Das, K.; English, D. S.; Wan, Z.; Kraus, G. A.; Petrich, J. W. *J. Phys. Chem. A* **1999**, *103*, 7949.
- (161) Payton, F.; Sandusky, P.; Alworth, W. L. *J. Nat. Prod.* **2007**, *70*, 143.
- (162) Tonnesen, H. H. *Pharmazie* **2002**, *57*, 820.
- (163) Leung, M. H. M.; Colangelo, H.; Kee, T. W. *Langmuir* **2008**, *24*, 5672.
- (164) Leung, M. H. M.; Kee, T. W. *Langmuir* **2009**, *25*, 5773.
- (165) Bisht, S.; Feldmann, G.; Soni, S.; Ravi, R.; Karikar, C.; Maitra, A.; Maitra, A. *J. Nanobiotechnol.* **2007**, *5*, 1.
- (166) Wang, Y.-J.; Pan, M.-H.; Cheng, A.-L.; Lin, L.-I.; Ho, Y.-S.; Hsieh, C.-Y.; Lin, J.-K. *J. Pharm. Biomed. Anal.* **1997**, *15*, 1867.
- (167) Tonnesen, H. H.; Karlsen, J. Z. *Lebensm.-Unters. Forsch.* **1985**, *180*, 402.
- (168) Kunwar, A.; Barik, A.; Pandey, R.; Priyadarsini, K. I. *Biochim. Biophys. Acta, Gen. Subj.* **2006**, *1760*, 1513.
- (169) Hansen, J. E.; Pines, E.; Fleming, G. R. *J. Phys. Chem.* **1992**, *96*, 6904.
- (170) Zhong, D. P.; Douhal, A.; Zewail, A. H. *Proc. Natl. Acad. Sci. USA* **2000**, *97*, 14056.
- (171) Vautier-Giongo, C.; Yihwa, C.; Moreira, P. F. J.; Lima, J. C.; Freitas, A. A.; Alves, M.; Quina, F. H.; Macüanita, A. L. *Langmuir* **2002**, *18*, 10109.
- (172) Lima, J. C.; Vautier-Giongo, C.; Lopes, A.; Melo, E. C.; Quina, F. H.; Macüanita, A. L. *J. Phys. Chem. A* **2002**, *106*, 5851.
- (173) Kelly, J. W. *Structure* **1997**, *5*, 595.

- (174) Tan, S. Y.; Pepys, M. B.; Hawkins, P. N. *Am. J. Kidney Dis.* **1995**, *26*, 267.
- (175) Sunde, M.; Serpell, L. C.; Bartlam, M.; Fraser, P. E.; Pepys, M. B.; Blake, C. C. F. *J. Mol. Biol.* **1997**, *273*, 729.
- (176) Conway, K. A.; Harper, J. D.; Lansbury, P. T. J. *Biochemistry* **2000**, *39*, 2552.
- (177) Hueston, W.; Bryant, C. M. *J. Food. Sci.* **2005**, *70*, R77.
- (178) Prusiner, S. B. *Proc. Natl. Acad. Sci. USA* **1998**, *95*, 13363.
- (179) Ironside, J. W. *Brain Pathol.* **1996**, *6*, 379.
- (180) (EFSA), E. F. S. A. “Quantitative Assessment of the Residual BSE Risk in Bovine-Derived Products, EFSA QRA Report 2004 - working document,” 2005.
- (181) Evaluation of the Potential for Bovine Spongiform Encephalopathy in the United States, 2001; Harvard Center of Risk Analysis, Harvard School of Public Health, and Center of Computational Epidemiology, College of Veterinary Medicine, Tuskegee University, 2001; Vol. 2001; pp available at http://www.fsis.usda.gov/Science/Risk_Assessments/.
- (182) Cousens, S.; Smith, P. G.; Ward, H.; Everington, D.; Knight, R. S.; Zeidler, M.; Stewart, G.; Smith-Bathgate, E. A.; Macleod, M. A.; Mackenzie, J.; Will, R. G. *Lancet* **2001**, *357*, 1002.
- (183) Comer, P. J.; Huntly, P. J. *Stat. Methods Med. Res.* **2003**, *12*, 279.
- (184) Sohal, R. S. *Age Pigments*; Elsevier: Amsterdam, 1981.
- (185) Yin, D. *Free Radical Biol. Med.* **1996**, *21*, 871.
- (186) Terman, A.; Brunk, U. T. *Acta Pathol., Microbiol., Immunol.* **1998**, *106*, 265.
- (187) Terman, A. *Redox Rep.* **2001**, *6*, 15.
- (188) Tsuchida, M.; Miura, T.; Aibara, K. *Chem. Phys. Lipids* **1987**, *44*, 297.

- (189) Strehler, B. L. *Time, Cells, and Aging*; Academic Press: San Diego, 1977.
- (190) Sundelin, S. P.; Nilsson, S. E. G. *Free Radical Biol. Med.* **2001**, *31*, 217.
- (191) Boellaard, J. W.; Schlote, W.; Tateishi, J. *Acta Neuropathol.* **1989**, *78*, 410.
- (192) Foncin, J. F.; Gaches, J.; Le Beau, J. *Rev. Neurol. (Paris)* **1964**, *111*, 507.
- (193) Kirschbaum, W. R. *Jakob-Creutzfeldt disease*; Elsevier: Amsterdam, New York, 1968.
- (194) Jacobson, S.; Koenig, H.; Ross, E. *J. Neuropathol. Exp. Neurol.* **1967**, *22*, 152.
- (195) Miyashita, M.; Stierstorfer, B.; Schmahl, W. *J. Vet. Med. B* **2004**, *51*, 209.
- (196) Smith, J. D.; Greenlee, J. J.; Hamir, A. N.; Richt, J. A.; Greenlee, M. H. W. *Vet. Pathol.* **2009**, *46*, 810.
- (197) Smith, J. D.; Greenlee, J. J.; Hamir, A. N.; Greenlee, M. H. W. *Vet. Rec.* **2009**, *165*, 179.
- (198) Hortells, P.; Monzon, M.; Monleon, E.; Acin, C.; Vargas, A.; Bolea, R.; Lujan, L.; Badiola, J. J. *Brain Res.* **2006**, *1108*, 188.
- (199) Rubenstein, R.; Gray, P. C.; Wehlburg, C. M.; Wagner, J. S.; Tisone, G. C. *Biochem. Biophys. Res. Commun.* **1998**, *246*, 100.

CHAPTER 2. EXPERIMENTAL TECHNIQUES AND DATA ANALYSIS

Overview

Spectroscopy has made an outstanding contribution to the present state of atomic and molecular physics and lasers have always played an important role in this area. Fluorescence spectroscopy has been widely applied for probing structure and properties molecules or environments in chemical and biological systems.¹⁻³ The information on molecular structure and on the interaction of molecules with their surroundings may be derived in various ways from the absorption and fluorescence spectra generated when electromagnetic radiation interacts with matter. Although steady-state techniques have always played important roles in fluorescence spectroscopy, a thorough knowledge of dynamical processes is of fundamental importance for many branches of physics, chemistry, or biology. The investigation of ultrafast processes, such as electron transfer, proton transfer, energy transfer, rotational motion and isomerization of excited molecules of an optically pumped system opens the way to study in detail the dynamic properties of excited molecules. In order to study these processes experimentally, one needs a high-time resolution of the instrument so that the resolvable minimum time interval is shorter than the time scale of the process under investigation. Recent development of ultrashort mode-locked lasers that deliver intense short light pulses with width down to femtosecond range and of new detection techniques allow a very high time resolution, which has made impressive progress in the study of fast processes. This chapter focuses on steady-state and time-resolved fluorescence techniques used in the research described in this thesis, as well as some fundamental concepts associated with the physical processes being studied and the data analysis involved.

Fluorescence Spectrophotometer

A diagram of a typical fluorimeter is shown in Figure 2.1.⁴ It consists of a 150 W continuous ozone-free xenon lamp generating a continuum of visible and ultra-violet light, a monochromator to select the required wavelength for excitation, a sample compartment, and a second monochromator coupled with a photomultiplier tube (PMT) to analyze the fluorescence signal. The grating in the excitation and emission monochromator can disperse light from 200 to 900 nm. The entrance and exit slits of each monochromator control the intensity and wavelength spread (bandpass) of the light. Illumination from the Xe-lamp is collected by an elliptical mirror and directed toward the entrance slit of the excitation monochromator. The excitation monochromator selectively delivers a narrow band of wavelengths of excitation light that strikes the sample. A portion of the incident light is absorbed by the sample, and some of the molecules in the sample fluoresce. The emitted light enters the emission monochromator, which is positioned at 90° angle (right angle geometry) with respect to excitation light path in order to minimize the risk of transmitted or reflected incident light reaching the detector. No monochromator is perfect and it will transmit some stray light, that is, light with other wavelength than targeted. The emitted light is transmitted in a narrow range of centered about the specified emission wavelength and exits through the adjustable slits, and finally striking the detector. The signal is amplified and generates a voltage that is proportional to the measured emitted intensity. The right angle geometry is used when the sample is transparent. There is geometry for collecting fluorescence, known as front faced geometry. In this geometry the fluorescence is collected from the sample from the same surface at which the sample is illuminated by excitation light. The front face geometry is used primarily when the sample is opaque or solid.

A fluorescence spectrum of a sample is recorded by scanning the emission monochromator for a constant wavelength of the excitation light (λ_{ex}). Similarly, an excitation spectrum is acquired by scanning the excitation monochromator at a fixed emission wavelength (λ_{em}). The source light has different intensities at all wavelengths, and it may vary over time during each experiment or between each experiment. This can distort the spectrum and corrections are necessary to get a instrument-independent spectrum. In order to correct this, fluorimeter is equipped with an additional reference photodiode (PD) which measures a fraction of source light (~8%) separated using a beam splitter (BS) after the exit slit of excitation monochromator before it enters the sample compartment. By rationing the fluorescence signal to the reference signal, correction is made for variation in excitation light intensity as a function of wavelength. Additionally, the transmission efficiency of the grating, and detection efficiency of PMT varies with wavelength. A correction factor file is supplied from the company; automatically correct the response characteristics of grating and PMT-tube. The correction factor $\gamma(\lambda)$ is a number by which the experimental intensity (I_{exp}) be multiplied to get corrected intensity (I_{corr}).⁵

$$I_{\text{corr}}(\lambda) = \gamma(\lambda)I_{\text{exp}}(\lambda) \quad (2.1)$$

It is important to check if the excitation and emission monochromator are properly calibrated before acquiring any spectra from sample. For this purpose, Xe-lamp and water Raman spectra are obtained everyday after turning on the system. A maximum at 467.125 nm in Xe-lamp spectrum and a maximum at 467 ± 0.5 nm in water Raman ($\lambda_{\text{ex}} = 350$ nm) confirm the calibration of the excitation and emission monochromator, respectively.

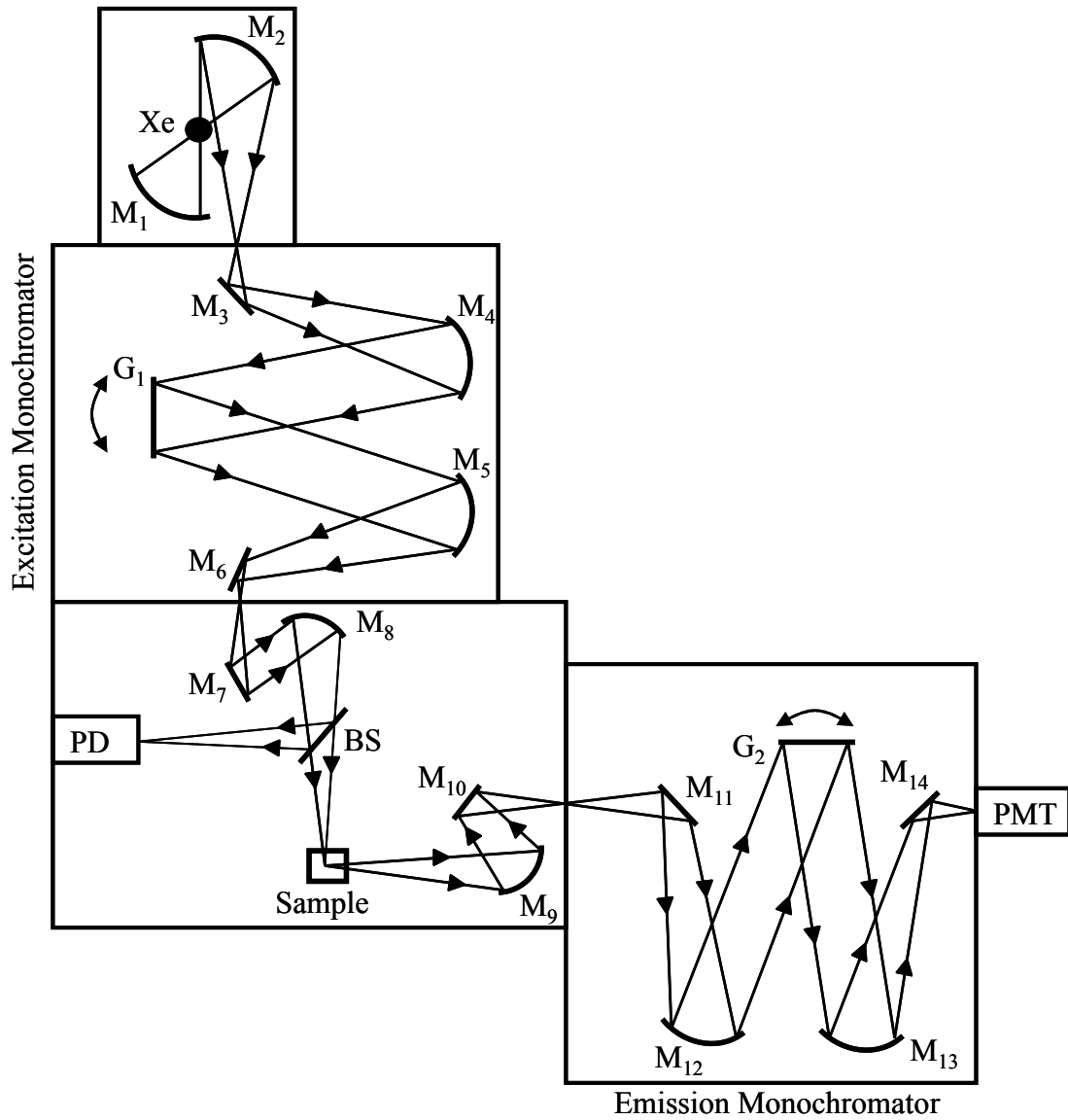


Figure 2.1. Schematic representation of fluorescence spectrophotometer. Xe - Xe-lamp, M - mirror, G - grating, BS - beam splitter, PD - photodiode and PMT - photomultiplier tube.

Ti:Sapphire Crystal

The titanium sapphire, $\text{Ti:Al}_2\text{O}_3$, is the most widely used tunable solid-state laser. The sapphire crystal has a hexagonal structure with aluminum at the center and oxygen atoms at the vertices.^{6,7} $\text{Ti:Al}_2\text{O}_3$ crystal is grown by doping 0.1-0.5% (by weight) of Ti_2O_3 with Al_2O_3 , where some of the Al^{+3} ions are replaced by Ti^{+3} ions. Ti^{+3} ion possesses only one electron in the 3d shell. Crystalline field perturbs the electronic energy level of Ti^{+3} ion producing a triply degenerate 2T_2 ground state and a doubly degenerate 2E excited state. A schematic energy level diagram of $\text{Ti:Al}_2\text{O}_3$ is shown in Figure 2.2a. There are no d-state energy level above the upper 2E level due to simplest electronic configuration ($3d^1$) of Ti^{+3} ion, eliminating the possibility of excited state absorption of the laser radiation, that is important for the efficiency and tunability of the laser. $\text{Ti:Al}_2\text{O}_3$ is a four level laser medium. At room temperature only the lowest vibrational level of 2T_2 is populated as spacing between two vibrational energy levels is larger than kT . Optical pumping excites the electron of Ti^{+3} to $({}^2E, \nu_n)$, then relaxes quickly to the bottom of the vibronic band due collision before making the laser action. Laser action happens during the transition from $({}^2E, \nu_0)$ to $({}^2T_2, \nu_m)$. The cycle is close by fast vibration relaxation to the $({}^2T_2, \nu_0)$. The fluorescence lifetime is 3.2 μs . Strong interaction of the 3d electron with the crystal field results in the large equilibrium Ti-O distance for upper state compared to lower level. This causes a wide separation between emission and absorption band with large width. The absorption band centered at 490 nm makes it suitable for pumping with a number of sources such as argon laser, frequency-doubled Nd:YAG, Nd:YLF lasers. We use frequency-doubled diode-pumped Nd:YAG laser from Spectra Physics. This laser provides high power (up to 10 W) stable pumping radiation at 532 nm in TEM_{00} spatial mode. The fluorescence peaks at 780

nm with a 180 nm band width (FWHM). Therefore Ti:sapphire laser output is tunable from 675 nm to 1110 nm. Absorption and emission spectra of Ti:sapphire crystal is shown in Figure 2.2b. In order to prevent accumulation of heat in the crystal, the supporting mount is cooled by running continuous flow water.

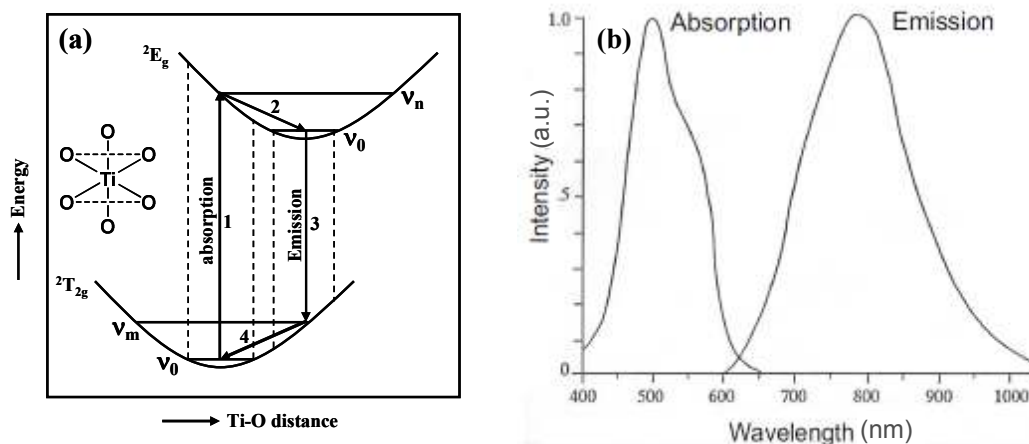


Figure 2.2. Schematic energy level diagram of Ti:Sapphire (a). Absorption and emission spectra of Ti:Sapphire crystal (b).⁶

Optical Oscillator

A laser consists of at least three components: a gain medium, a pump source and two mirrors that form an optical cavity.^{6,8} The pump source creates a population inversion in the gain medium; the gain medium amplifies light by stimulated emission and the optical cavity traps the light and makes them oscillate back and forth between the two mirrors. The mirror R_1 , is fully reflective with reflectivity $\sim 100\%$ for the radiation inside the cavity, called high reflector. The mirror R_2 has some transmission to allow a fraction of light trapped in the cavity, known as output coupler. The entire system consisting of mirrors and the gain medium is called optical resonator or laser oscillator (Figure 2.3). The intensity of stimulated emission increases when it propagates along the cavity axis and passes through the pumped laser medium and reflected back through it, stimulating further emission in the same

direction. This means that laser photons undergo multiple reflections within the cavity, being amplified at each pass through the laser medium. If the amplification is large enough to overcome various losses (such as diffraction losses from the edges of the mirrors, absorption and scattering by the mirrors and in the laser medium etc.), a single photon can be amplified by several orders of magnitude to produce a huge number of coherently generated photons trapped inside the resonator.

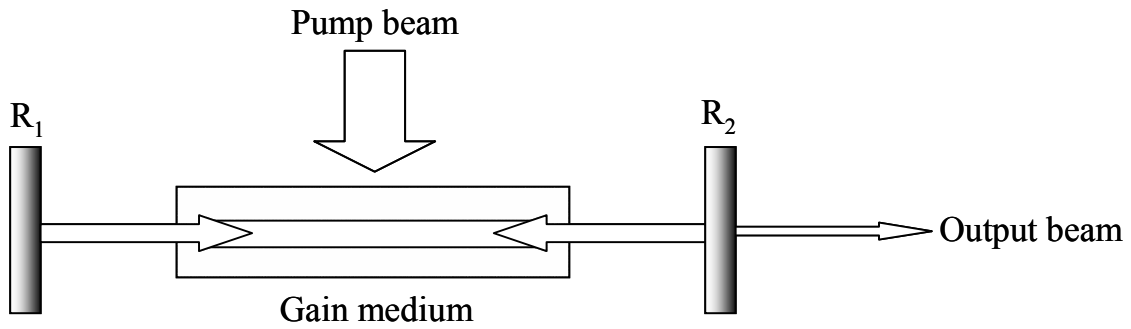


Figure 2.3. Schematic arrangement of a resonator. R_1 is the total reflector and R_2 is the partial reflector (output coupler).⁹

Let us assume that the stimulated light intensity increases from I_0 to I_l after traveling from one end mirror to the other with a cavity length of L . In case of no loss and a gain coefficient of k , I_l can be expressed as¹⁰

$$I_l = I_0 e^{kL} \quad (2.2)$$

If we define a single loss coefficient by γ for all the losses, then the I_l can be written as

$$I_l = I_0 e^{(k-\gamma)L} \quad (2.3)$$

The final intensity after a round trip including the reflectance of two mirrors, r_1 and r_2 , is given by

$$I_l = r_1 r_2 I_0 e^{2(k-\gamma)L} \quad (2.4)$$

The round trip gain, G , is defined as the ratio of the intensity I_l and the initial intensity I_0 is

written as

$$G = \frac{I_l}{I_0} = r_1 r_2 e^{2(k-\gamma)L} \quad (2.5)$$

If the gain in the resonant cavity is <1 , the cavity will cause cessation of the oscillation. It is important that the gain, G , must be ≥ 1 to initiate and sustain of oscillation. The threshold gain coefficient k_{th} while $r_1 r_2 e^{2(k-\gamma)L} = 1$ is obtained from eq 2.5, and expressed as

$$k_{th} = \gamma + \frac{1}{2L} \ln \frac{1}{r_1 r_2} \quad (2.6)$$

Laser Modes

Lasers oscillate in both longitudinal and transverse modes. One can observe an intensity distribution not only along the laser resonator axis, but also in the plane perpendicular to the direction of the laser beam propagation. The origin of these modes can be understood when the boundary condition of the laser cavity is considered. One boundary condition is that the electromagnetic field must be able to self-replicate in phase after one round trip of the laser cavity. This gives rise to the longitudinal mode structure of the laser. For a two-mirror linear cavity of length L , the operating wavelength, λ , must satisfy

$$n\left(\frac{\lambda}{2}\right) = L \quad (2.7)$$

where the n is an positive integer, known as the mode order. Using $\nu = c/\lambda$, eq 2.7 yields

$$\nu = \frac{nc}{2L} \quad (2.8)$$

The frequency separation $\Delta\nu$ between adjacent modes ($\Delta n = 1$) is

$$\Delta\nu = \nu_{n+1} - \nu_n = \frac{c}{2L} \quad (2.9)$$

This indicates that total number of longitudinal modes depend on the spontaneous emission band width. If we assume, λ_0 as peak and $\Delta\lambda$ as half width at half height of the spontaneous emission band (Figure 2.4), then we can write¹¹

$$n_{\max}(\lambda_0 - \Delta\lambda) = 2L \quad (2.10)$$

$$n_{\min}(\lambda_0 + \Delta\lambda) = 2L \quad (2.11)$$

The total numbers of modes (N) is given by

$$N = n_{\max} - n_{\min} = \frac{2L}{\lambda_0^2 - \Delta\lambda^2} [(\lambda_0 + \Delta\lambda) - (\lambda_0 - \Delta\lambda)] \cong \frac{4L\Delta\lambda}{\lambda_0^2} \quad (2.12)$$

where $\lambda_0^2 \gg \Delta\lambda^2$. If the stimulated emission from Ti:Sapphire laser has a band width of ~300 nm, then a cavity of 30 cm may potentially support ~250,000 modes.

The second boundary condition explains the transverse nature of the laser beam.¹² In free space, electromagnetic field falls to zero away from resonator axis. This condition predicts the transverse mode structure and the observed intensity profiles of the laser output. The cross section the laser beam exhibits the nature of the transverse electromagnetic mode, TEM_{nm}, where m and n are integers representing the number of nodes in the direction orthogonal to the direction of propagation beam. If the light is propagates in the z direction, the x, y dependence of the beam is given by^{6,11,13}

$$E_{mn}(x, y) = E_0 H_m \left(\frac{\sqrt{2}x}{w} \right) H_n \left(\frac{\sqrt{2}y}{w} \right) e^{-\frac{x^2+y^2}{w^2}} \quad (2.13)$$

where H_m and H_n are the Hermite polynomials. The $H_0 = 1$ at zero order. This leads to TEM₀₀, known as the fundamental mode, which has Gaussian spatial distribution. This is the most common mode in almost all the laser, and is expressed as

$$E_{mn}(x, y) = E_0 e^{-\frac{x^2+y^2}{w^2}} \quad (2.14)$$

The intensity distribution in the Gaussian beam can be written as

$$I(r) = I_0 e^{-\frac{2r^2}{w^2}} \quad (2.15)$$

where r is the radius of the beam, I_0 is the intensity of the beam at $r = 0$, and w is the radius of the beam at $I = I_0 e^{-2}$.

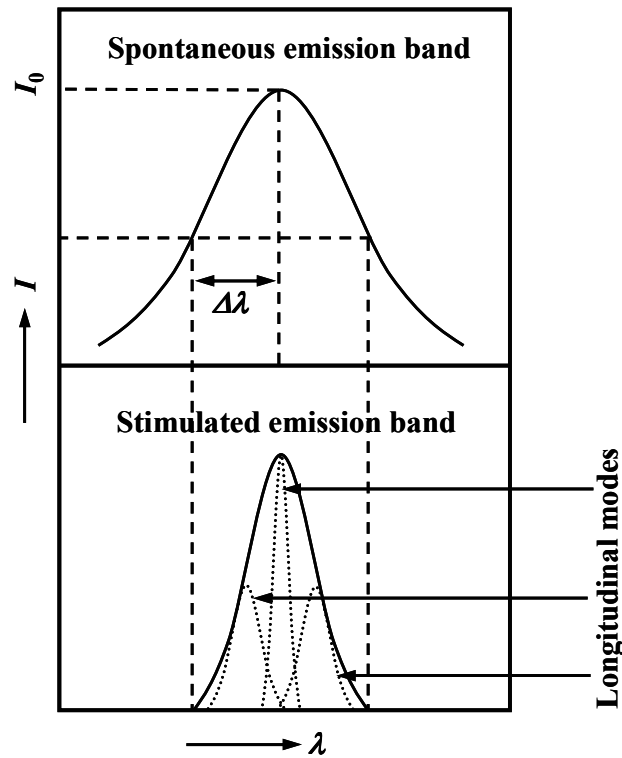


Figure 2.4. Schematic demonstration of the number of longitudinal modes.¹¹

Mode-Locking

In a free-running laser, both longitudinal and transverse mode oscillate simultaneously without any fixed mode-to-mode phase and amplitude relationship.^{6,11} We will assume that the laser oscillates in fundamental transverse, TEM_{00} . In a Ti:Sapphire laser cavity, there is over 100,000 longitudinal modes exist within the frequency region as long as

the gain remains greater than the cavity losses. When laser operates in multi-mode regime, there is generally a strong competition among the modes to be amplified by the stimulated emission of the same atoms, molecules or ions in the gain medium. This competition causes big fluctuations in the relative phases and amplitudes of the modes, resulting in big fluctuations of the instantaneous intensity. The purpose of mode-locking is to organize the competition between modes in such a way that the relative phases stay constant. Mode-locking is a laser operation in which many longitudinal modes of the cavity are simultaneously forced to oscillate with a precise phase relation. If the phases of multi-longitudinal modes are locked, then the modes constructively interfere at some point in the cavity and destructively interfere elsewhere, resulting in a single circulating pulse. Each time this pulse reaches the output coupler, part of it escapes the laser cavity and the output thus consists of a train of pulses separated by the circulating time of the cavity (Figure 2.5).¹⁴

In order to get very short pulses, it is better to get as many longitudinal modes oscillating as possible with all their phases locked together in the mode-locked operation. The minimum pulse duration, $\Delta\tau_p$, is limited by the Fourier transform of the spectrum. From the uncertainty principle, we get

$$\Delta\tau_p \Delta\nu \geq \frac{1}{2\pi} \quad (2.16)$$

This principle indicates that to obtain very short pulses we need a wide gain bandwidth. For example, the gain bandwidth of Ti:Sapphire is $\sim 10^{14}$ Hz, and pulses as short as 10 fs can be produced from this laser. This corresponds to the oscillation of millions of longitudinal modes oscillating.¹⁵

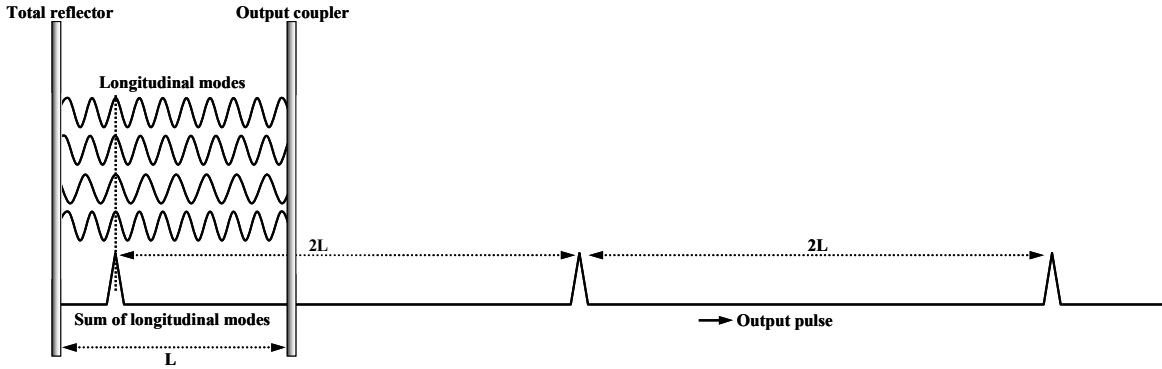


Figure 2.5. In a mode-locked laser, the longitudinal cavity modes interfere constructively with each other at one point in the cavity because of their slightly different wavelengths, producing a short pulse of light, which travels around the cavity.¹⁴

Let us consider that a laser is oscillating with $N = 2m+1$ longitudinal modes. The modes can be assumed as plane wave, $E(t) = E_0 e^{i\omega t}$. The mode at the center of the gain bandwidth has angular frequency ω_0 . Above and below of this frequency, there are $\pm m$ additional modes with an angular frequency separation of $\Delta\omega$. The total electric field resulting from $N = 2m+1$ modes is represented as¹¹

$$E(t) = \sum_{n=-m}^m E_n e^{i(\omega_0 + \Delta\omega)t + \Delta\phi_n} \quad (2.17)$$

where $\Delta\phi$ is the phase difference between the neighboring modes. The summation for a finite series is expressed as

$$E(t) = E_0 e^{i\omega_0 t} \frac{\sin N \frac{(\Delta\omega t + \Delta\phi_n)}{2}}{\sin \frac{(\Delta\omega t + \Delta\phi_n)}{2}} \quad (2.18)$$

The total intensity is written as

$$I(t) = E(t)E^*(t) = E_0^2 \frac{\sin^2 N \frac{(\Delta\omega t + \Delta\phi_n)}{2}}{\sin^2 \frac{(\Delta\omega t + \Delta\phi_n)}{2}} \quad (2.19)$$

If $\Delta\phi_n$ changes with time in a random way, the resultant intensity, $I(t)$, also changes randomly with time as shown in Figure 2.6a. When $\Delta\phi_n$ between modes is constant, the oscillator is mode-locked and very short pulse is obtained as a result of the interference of N synchronized longitudinal modes. This situation is shown in Figure 2.6b.

It is clear from eq 2.19, that the first maximum of the pulse at time t_1 , when

$$\Delta\omega t_1 + \Delta\phi_n = 0 \quad (2.20)$$

The next maximum occur at time t_2 when

$$\Delta\omega t_2 + \Delta\phi_n = 2\pi \quad (2.21)$$

Subtraction of eq 2.20 from eq 2.21 yields

$$\Delta\omega(t_2 - t_1) = 2\pi \quad (2.22)$$

The separation between two pulses, $T_R = t_2 - t_1$, is given by

$$T_R = \frac{2\pi}{\Delta\omega} = \frac{1}{\Delta\nu} = \frac{2L}{c} \quad (2.23)$$

Mode-Locking Methods

The methods of mode-locking can be divided into two categories: active and passive mode-locking. We will restrict our discussions on the passive mode-locking methods that are our interest. There are two types of passive mode-locking techniques: saturable absorber mode-locking and Kerr-lens mode-locking.

Saturable Absorption Mode-Locking. Saturable absorber mode-locking is achieved by placing a saturable absorber (such as a dye solution or semiconductor saturable absorber mirror) with saturation at low light intensity and relaxation time of the upper state population shorter than the duration of the mode-locked pulse close to one of the end mirror.¹⁶⁻¹⁸ This method is based on intensity dependent transmission property of the

saturable absorber. It allows transmission of high intensity light and absorbs low intensity light. In an unlocked laser, there is random sequence of light burst as shown in Figure 2.6a. The most intense fluctuation preferentially suffers the lowest absorption losses and thus experiences the largest net gain. It therefore grows faster than other large number of small intensity fluctuations which encounter larger absorption in the saturable absorber and are effectively suppressed. After a few resonator round trips, the higher intense peak becomes so powerful that it depletes the inverted population of the active laser medium almost completely. This means all the energy of the cavity is concentrated in one single pulse. This is the mode-locked situation because selecting a single intensity maximum in the time domain is equivalent to establishing a phase relation among the longitudinal modes in frequency domain.

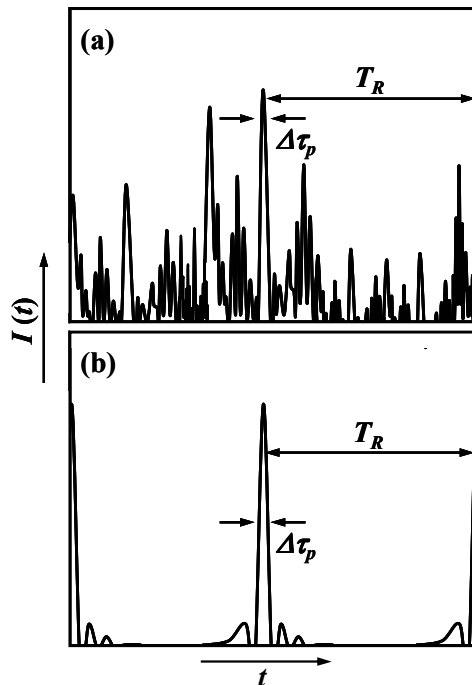


Figure 2.6. Example of time behavior of the total intensity, $I(t)$ for many longitudinal oscillating cavity modes in (a) free-running regime, corresponding to random phases $\Delta\phi_n$ and (b) mode-locking regime, corresponding to constant $\Delta\phi_n$.¹⁷

Kerr-Lens Mode-Locking. The field of ultrafast pulse generation has been revolutionized by the development of the Kerr-lens mode-locking technique. In saturable absorber mode-locking method, the duration of the mode-locked pulse is limited by the recovery time of the saturable absorber, usually ~ 1 ps. Pulses of much shorter duration (~ 6 fs) can be produced using Kerr-lens mode-locking because it is based on the nonlinear refractive index at high intensity that arises from distortions of the atom's electron cloud whose response being on the femtosecond timescale. The optical Kerr effect is a third order, non-linear phenomenon that is based on the intensity-dependent refractive index change of a material at high-intensity electric fields. The behavior of the refractive index under the Kerr effect can be described as^{6,11,17-19}

$$n(r,t) = n_0 + n_2 I(r,t) \quad (2.24)$$

where n_0 is the linear refractive index, n_2 is the nonlinear refractive index coefficient, and I is the instantaneous beam intensity. A laser operate in TEM₀₀ mode has a Gaussian intensity distribution, eq 2.15, is more intense in center than edges. This means that the strong intensity maxima at the center of the beam will be much more strongly focused than edges, as velocity of light (v) through the matter is speed of light (c) divided by the refractive index (n) of the medium (Figure 2.7a). If an aperture is placed at a suitable distance from the Kerr medium in a laser cavity so that a higher fraction of focused beam is transmitted and low intense (CW) part of the beam is blocked, then the Kerr medium with an aperture acts like an effective fast saturable absorber, which introduces low losses when instantaneous pulse intensity is increased and leads to mode-locking condition of the laser (Figure 2.7b). The Kerr-lens mode-locking can also be achieved by making a narrower pump beam exciting the gain medium so that there is better overlap between the pump beam and the mode-locked

beam, than that of CW beam (Figure 2.7c).⁸ This is because pump beam exciting gain medium always forms an intrinsic aperture, known as soft aperture, and cavity modes that have the largest overlap with the excited gain medium experience the largest gain.

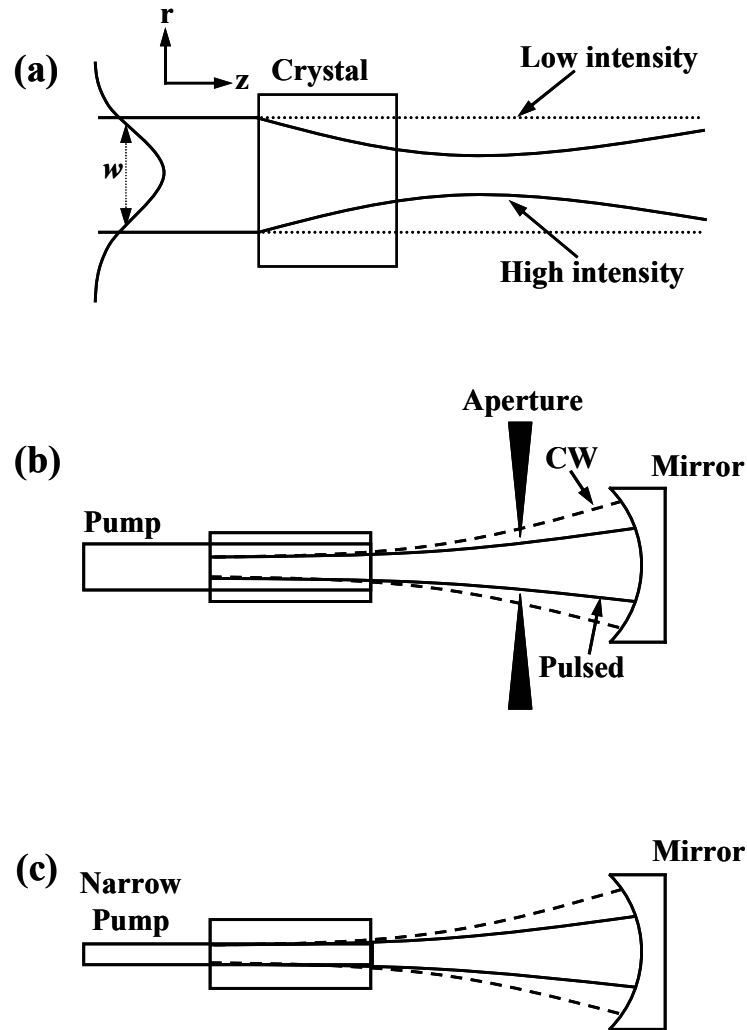


Figure 2.7. Schematic representation of (a) Kerr-lens or self-focusing, (b) hard-aperture mode-locking and (c) soft-aperture mode-locking.⁸

The Kerr nonlinearity is usually not strong enough to self-start the mode-locking when the laser runs freely. In order to initiate Kerr-lens mode-locking, a strong intensity fluctuation must be induced by perturbing the cavity. The simplest method in our laboratory setup is to slightly tap one of the resonator mirrors. Perturbation of a cavity mirrors allows

sweeping the frequencies of competing longitudinal modes, and produce a strong amplitude modulation due to mode beating. The most intense mode-beating pulse will be strong enough to initiate mode-locking. It is also noticed that our Ti:Sapphire laser runs in pulse regime from continuous wave output when the laser table (where the laser is mounted) is banged on. The output is then comprised of very short pulses and maintains itself once it has been initiated.

Group Velocity Dispersion

We have discussed in the previous section that any pulse of light can be viewed as a superimposition of many waves having different frequencies. Generally, duration of pulse is inversely proportional to the range of frequencies of waves that are superposed to form the pulse. Electromagnetic waves of different frequencies travel with different velocities through a medium. This is known as dispersion.^{20,21} Dispersion plays a critical role broadening an optical pulse while propagating through a medium as its spectral components travel with different velocities. In order to understand the effect of dispersion on pulse broadening, let us consider a monochromatic plane optical wave is propagating in the x direction. The electric field can be written as

$$E = E_0 e^{i(kx - \omega t)} \quad (2.25)$$

Here $k = 2\pi / \lambda$ is known as the propagation constant. If a pulse is composed of a number of this kind of waves with different ω , then the superimposed envelope or the pulse propagates with group velocity (v_g). The group velocity is defined as $v_g = \frac{d\omega}{dk}$, whereas the carrier waves propagate with $v_p = \frac{\omega}{k}$, known as phase velocity. If the refractive index of the

medium, n , depends on ω , then k is expressed as

$$k(\omega) = \frac{\omega n(\omega)}{c} \quad (2.26)$$

When an optical pulse propagates through a medium with refractive index $n(\omega)$, its time profile will change because the group velocity with which pulse moves, shows dispersion

$$\frac{dv_g}{d\omega} = \frac{dv_g}{dk} \frac{dk}{d\omega} = \frac{1}{v_g} \frac{d^2\omega}{dk^2} \quad (2.27)$$

If $\frac{d^2\omega}{dk^2} \neq 0$, different frequency components of the pulse face different velocities, and change

the shape of the pulse during traveling through the medium. The quantity, $\frac{d^2k}{d\omega^2}$, is a

measure of variation of the group velocity with frequency and, is defined as group velocity

dispersion (GVD), β . It is expressed in term of ω and λ as²²

$$\beta = \frac{d^2k}{d\omega^2} = \frac{1}{c} \left(2 \frac{dn}{d\omega} + \omega \frac{d^2n}{d\omega^2} \right) = \frac{\lambda^3}{2\pi c^2} \frac{d^2n}{d\lambda^2} \quad (2.28)$$

where $\omega = 2\pi c/\lambda$. In order to analyze the effect of dispersion, let us consider the phase (ϕ)

shift with frequency. When a pulse passes through a medium of length L , the time delay

produced by the medium is

$$\tau_d = \frac{L}{v_g} = L \left(\frac{dk}{d\omega} \right)_{\omega_L} = \left(\frac{d\phi}{d\omega} \right)_{\omega_L} = \phi' \quad (2.29)$$

The phase of a wave passing through a material of length L is characterized by the refractive

index of the medium, and is given by

$$\phi(\omega) = \frac{\omega n(\omega)}{c} L = k(\omega)L \quad (2.30)$$

The phase, $\phi(\omega)$ can be expanded in a Taylor series^{6,11} around the center frequency ω_0 of the

pulse spectrum assuming the phase varies slowly with frequency as

$$\phi(\omega) = \phi(\omega_0) + \phi'(\omega - \omega_0) + \frac{1}{2}\phi''(\omega - \omega_0)^2 + \dots \quad (2.31)$$

where $\phi' = \left(\frac{\partial\phi}{\partial\omega}\right)_{\omega=\omega_0}$ is the group delay and $\phi'' = \left(\frac{\partial^2\phi}{\partial\omega^2}\right)_{\omega=\omega_0}$ is the group delay dispersion

(GDD). A Gaussian pulse with center frequency ω_0 and width (FWHM) τ_0 is represented by^{13,23}

$$E_{in}(t) = E_0 e^{-\left(\frac{2\ln 2t^2}{\tau_0}\right) + i\omega_0 t} \quad (2.32)$$

This pulse after passing through a material of length L and adding the phase delay on its components according to eq 2.31 is represented by

$$E_{out}(t) = E_0 e^{i(\omega_0 t - \phi) - \left(\frac{\tau_0^2}{2\ln 2} + 2i\phi''\right)(t - \phi')^2} \quad (2.33)$$

By comparing eqs 2.32 and 2.33, it can be shown that the pulse width broaden as^{13,23,24}

$$\tau = \tau_0 \sqrt{1 + \frac{\phi''^2}{\tau_0^4} 16(\ln 2)^2} \quad (2.34)$$

Prism Pair

In a Ti:Sapphire oscillator a pulse travels back and forth through the Ti:Sapphire crystal and receives slight chirp for each round-trip due to GVD. The pulse broadening by the Ti:Sapphire crystal is caused by the positive GVD ($\beta > 0$), which means longer wavelengths travel faster than shorter ones. In order to obtain the shortest possible pulses from the laser cavity, the overall GVD has to be minimized by using optical components that intentionally produce negative GVD ($\beta < 0$). In our Ti:Sapphire oscillator, we use the prism pair to minimize GVD. The glass material in prism itself produces positive dispersion but

the arrangement of the two prisms (P_1 and P_2) is such that it creates a longer path through the prism material for red wavelengths compared to blue, and introduces a negative GVD (Figure 2.8).^{22,25} The chirped pulse enters the P_1 and is spatially dispersed. The blue wavelengths bend more than red after P_1 because the red components of the pulse travel faster through the prism material than blue component and therefore experience less refraction. The red components are delayed with respect to blue components by having traversed more glass of P_2 . A high reflecting mirror is placed after P_2 in order to double pass through the prism pairs. The degree of negative GDV can be tuned by changing the distance between the two prisms, L , or the distance d , as it changes the optical path difference between red and blue components.

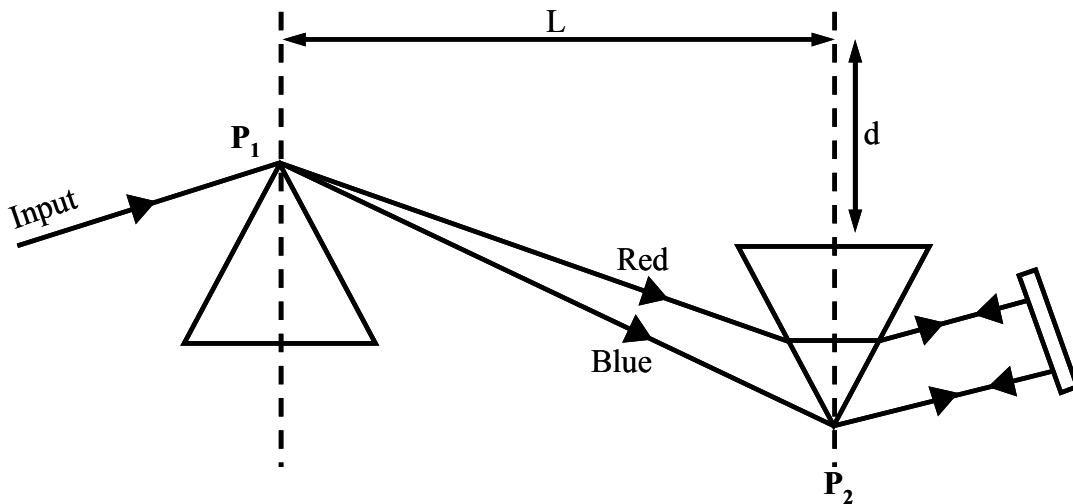


Figure 2.8. A prism pair arrangement for group velocity dispersion (GVD) compensation.²²

Ti:Sapphire Oscillator

Ti:Sapphire oscillator is a Kerr-lens mode-locked laser that produces femtosecond pulses. The design of our oscillator is shown in Figure 2.9, and is based on the design by Murnane and coworkers.²⁶ The cavity consists of two curve mirrors (M_1 , M_2), three flat

mirrors (M_3 , M_4 and OC), a Ti:sapphire rod, and a pair of intracavity prisms (P_1 and P_2). Ti:Sapphire crystal is the lasing medium, which is cut at the Brewster angle to minimize the losses. The oscillator is pumped with 5 W power at 532 nm of a diode-pumped frequency-doubled Nd:YAG CW laser from Spectra Physics, Millennia. A lens (L) is used to focus the pump beam inside the crystal collinearly with the laser axis. Two curve mirrors are placed in such a way so that it can form a telescope with the crystal in the focal plane in order to achieve the Kerr-lens effect. The prisms used in this laser are made of fused silica and cut to an apex angle (69°) such that the angle of incidence corresponds to the Brewster angle at minimum deviation. The prism pair is used to compensate for the dispersion introduced in the crystal. The spectrum is dispersed by the first prism (P_1), collimated by the second prism (P_2) and redirected by high reflector (M_4) back into the resonator. The Ti:Sapphire emits in the range from 675 to 1110 nm but the laser operates most effectively at ~ 800 nm. Tuning in this laser is accomplished by placing an adjustable slit in front of the high reflector where the beam is spectrally and spatially dispersed. The slit is oriented vertically, and translated horizontally to adjust the wavelength. The cavity is asymmetric, i.e., the side with the dispersion-compensating prisms is longer than the other arm of the laser. The asymmetric cavity arrangement is critical for operating the laser in high-power TEM_{00} mode-locked mode. Total length of this cavity is 170 cm, corresponding to a pulse repetition rate of 88 MHz. The output from the oscillator is obtained from the end mirror with transmission of 10% at ~ 790 nm, known as output coupler (OC), situated opposite to the dispersion-compensating prisms side. The average output power is ~ 500 mW depending upon the alignment. In order to initiate mode-locking, we first align the laser for maximum power in a continuous mode of operation. Then a slight tap on one of the curved mirrors initiates the

mode-locking, with a TEM₀₀ pulsed mode.

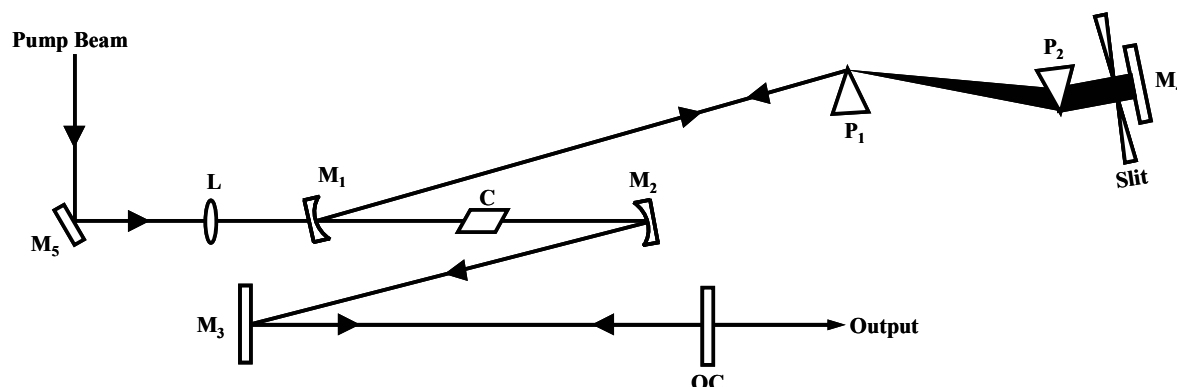


Figure 2.9. Schematic diagram of Ti:Sapphire oscillator. M – mirror, L – lens, C – crystal, P – prism, OC – output coupler.

Second Harmonic Generation and Sum Frequency Mixing

Nonlinear optical phenomena arise owing to the inability of the induced dipoles in the medium to respond in a linear fashion to the alternating electric field E associated with a light beam.²¹ When light wave propagates through a medium, the alternating electric field E produces a change in the spatial and temporal electric charge distribution mainly to outer electron cloud of atom's in the material, resulting an induced dipole whose macroscopic manifestation is known as induced polarization. The oscillation of the induced dipoles in response to weak electric field is small, and the polarization is proportional to the electric field E . However, as the strength of the electric field increases, the proportionality begins to fail, resulting a nonlinear response of the material in the presence of strong electric field.

The magnitude of induced polarization per unit volume P of a material is dependent on the magnitude of the applied electric field E .^{21,27} In the presence of weak electric field, the linear polarization P_1 , is represented by $P_1 = \epsilon_0 \chi^{(1)} E$, where ϵ_0 is the permittivity of free space and $\chi^{(1)}$ is the linear susceptibility representing linear response of the material. But

when the electric field is very strong, P is no longer linear and can be expanded as a power series of E

$$P = P_1 + P_2 + P_3 + \dots = \varepsilon_0 \chi^{(1)} E + \varepsilon_0 \chi^{(2)} E^2 + \varepsilon_0 \chi^{(3)} E^3 + \dots \quad (2.35)$$

Let us assume that two oscillating electric fields of frequencies ω_1 and ω_2 incident upon a material. The total field can be written as⁸

$$E(t) = (E_1 e^{-i\omega_1 t} + E_1^* e^{i\omega_1 t}) + (E_2 e^{-i\omega_2 t} + E_2^* e^{i\omega_2 t}) \quad (2.36)$$

The second order nonlinear polarization ($P_2 = \varepsilon_0 \chi^{(2)} E^2$) can be expressed as⁸

$$P_2 = \varepsilon_0 \chi^{(2)} [E_1^2 e^{-i(2\omega_1)t} + (E_1^*)^2 e^{-i(2\omega_1)t} + E_2^2 e^{-i(2\omega_2)t} + (E_2^*)^2 e^{-i(2\omega_2)t} + 2E_1 E_1^* + 2E_2 E_2^* + 2E_1 E_2 e^{-i(\omega_1 + \omega_2)t} + 2E_1^* E_2^* e^{-i(\omega_1 + \omega_2)t} + 2E_1 E_2 e^{-i(\omega_1 - \omega_2)t} + 2E_1^* E_2^* e^{-i(\omega_1 - \omega_2)t}] \quad (2.37)$$

The results include frequencies that are exactly twice the frequency of the fundamental waves, $2\omega_1$ and $2\omega_2$. It is obvious that if the two waves have the same frequency of ω , then an output at 2ω can be obtained, is referred as second harmonic generation (SHG). The other new terms (from eq 2.37) involving $\omega_1 + \omega_2$ and $\omega_1 - \omega_2$ lead to sum and difference frequency generation, respectively. This qualitatively indicates that coupling of two light waves is possible in a material if the intensity of the light is high enough. One wave changes the properties of the medium in such a way that the other wave is affected by the changed properties of the medium.²⁷ Pulsed lasers generating short pulses can achieve laser beam intensity greater than 10^{12} W/cm, and nonlinear effects become easily feasible with pulse laser.

Second-order nonlinear polarization is responsible for the second harmonic, sum and difference frequency generation. A crystal having a center of symmetry makes no contribution to second-order polarization, P_2 . In this crystal, reversing the applied electric

field does not change its polarization, as the new lattice encountered by the reverse electric field is physically the same.^{21,27} More specifically, upon inversion, $E \rightarrow -E$. Since the E -field is squared in $P_2 = \varepsilon_0 \chi^{(2)} E^2$, $P_2 = -P_2$ is true if $P_2 = 0$ for crystal with center symmetry. For P_2 to be nonzero, the crystal must lack of symmetry.

Phase Matching

The velocity of any plane wave with frequency ω through a medium is determined by phase velocity $v_p = \omega/k = c/n(\omega)$, and is characterized by the refractive index $n(\omega)$. Since the interacting waves in a nonlinear process have different frequencies, i.e., different phase velocities in the nonlinear material, it is important to maintain a proper phase velocity relation among them to maximize the efficiency of nonlinear output. This relation is known as phase matching.^{11,28-30} The phase matching condition can be realized from the energy and momentum conservation of photons. Energy ($\hbar\omega$) and momentum ($\hbar k$) conservation for three-wave mixing in dispersion free media is given by

$$\omega_1 + \omega_2 = \omega_3 \quad (2.38)$$

$$k_1 + k_2 = k_3 \quad (2.39)$$

From eq 2.26 and 2.39, the phase matching condition for collinear propagation can be summarized as

$$\omega_1 n(\omega_1) + \omega_2 n(\omega_2) = \omega_3 n(\omega_3) \quad (2.40)$$

This condition (eq 2.40) can not be satisfied for normal dispersive materials because the index of refraction increases with frequency, i.e., $n(\omega_3) > n(\omega_2), n(\omega_1)$. However, it is possible to satisfy the phase matching condition in birefringent medium.

Phase Matching Angle

In a birefringent crystal, the index of refraction of the medium is not constant in all propagation directions.³¹ There are two orthogonally polarized modes of propagation for each wave. One of these waves called ordinary wave which experiences index of refraction, n_o , that does not depend on the direction of propagation, whereas the extraordinary wave whose index of refraction, n_e , is dependent on its direction of propagation. The refractive indices (n_o , n_e) and their dependence on the propagation direction in a uniaxial birefringent crystal can be depicted by the index ellipsoid. The index ellipsoid is written as²⁸⁻³⁰

$$\frac{x^2}{n_x^2} + \frac{y^2}{n_y^2} + \frac{z^2}{n_z^2} = 1 \quad (2.41)$$

For a uniaxial crystal, $n_x = n_y = n_o$ and $n_z = n_e$. The eq 2.41 becomes³⁰

$$\frac{x^2 + y^2}{n_o^2} + \frac{z^2}{n_e^2} = 1 \quad (2.42)$$

For positive uniaxial crystal $n_o < n_e$, and for negative $n_e < n_o$. For example, β -barium borate (BBO), a negative uniaxial birefringence crystal, is used for sum frequency mixing in our fluorescence upconversion technique. In this section, we will limit our discussion to negative uniaxial crystal. An arbitrary point on ellipsoid can be expressed in polar coordinate. The dependence of $n_e(\theta)$ when extraordinary wave propagates at an angle θ with the optical axis can be easily derived if we insert $x = n_e(\theta)\sin\theta\cos\phi$, $y = n_e(\theta)\sin\theta\sin\phi$, and $z = n_e(\theta)\cos\phi$ in eq 2.42, and is given by^{6,31-34}

$$\frac{1}{n_e^2(\theta)} = \frac{\cos^2\theta}{n_o^2} + \frac{\sin^2\theta}{n_e^2} \quad (2.43)$$

where $n_e(\theta) = n_o$ at $\theta = 0^\circ$ and $n_e(\theta) = n_e$ at $\theta = 90^\circ$. There are two types of phase matching,

type I and type II, depending upon which of the three waves ω_1 , ω_2 , ω_3 propagates as an ordinary or as an extraordinary wave. Type I corresponds to $o + o \rightarrow e$ and type II corresponds to $e + o \rightarrow e$ for negative uniaxial crystal.

In collinearly phase-matched SHG, there is only fundamental wave with frequency ω i.e., $\omega_1 = \omega_2 = \omega$ and $\omega_3 = 2\omega$. A schematic representation of phase matching condition for SHG in a negative uniaxial crystal is shown in Figure 2.10. For SHG, Type I phase matching condition is $n_o^\omega = n_e^{2\omega}(\theta_{pm})$, according to eq 2.40. This leads to a phase matching angle³¹ based on eq 2.43

$$\sin^2 \theta_{pm} = \frac{(n_e^{2\omega})^2}{(n_o^\omega)^2} \left[\frac{(n_o^{2\omega})^2 - (n_o^\omega)^2}{(n_o^{2\omega})^2 - (n_e^{2\omega})^2} \right] \quad (2.44)$$

For type II phase matching the polarization of the fundamental wave is not on the plane defined by the optical axis and the propagation vector. Therefore, the fundamental wave consists of two components, one in the plane, travels with $v_p = c/n_o$, and another perpendicular to the plane, travels with $v_p = c/n_e$. According to type II phase matching, we can write the phase matching condition from eq 2.40 as

$$\frac{1}{2} [n_e^\omega(\theta_{pm}) + n_o^\omega] = n_e^{2\omega}(\theta_{pm}) \quad (2.43)$$

The phase matching angle can be derived from eq 2.43, and is expressed as³¹

$$\frac{n_o^{2\omega}}{\sqrt{1 + \left[\frac{(n_o^{2\omega})^2}{(n_e^{2\omega})^2} - 1 \right] \sin^2 \theta_{pm}}} - \frac{\frac{1}{2} n_o^\omega}{\sqrt{1 + \left[\frac{(n_o^\omega)^2}{(n_e^\omega)^2} - 1 \right] \sin^2 \theta_{pm}}} = \frac{1}{2} n_o^\omega \quad (2.44)$$

Similarly, condition for sum frequency generation in type I and type II phase matching are

given as

$$\omega_1 n_o^{\omega_1} + \omega_2 n_o^{\omega_2} = \omega_3 n_e^{\omega_3}(\theta_{pm}) \quad (\text{type I}) \quad (2.45)$$

$$\omega_1 n_e^{\omega_1}(\theta_{pm}) + \omega_2 n_o^{\omega_2} = \omega_3 n_e^{\omega_3}(\theta_{pm}) \quad (\text{type II}) \quad (2.46)$$

and the phase matching angles are expressed as³¹

$$\sin^2(\theta_{pm}) = \frac{(n_e^{\omega_3})^2}{\left[(\lambda_3 / \lambda_1) n_o^{\omega_1} + (\lambda_3 / \lambda_2) n_o^{\omega_2} \right]^2} \left(\frac{(n_o^{\omega_3})^2 - \left[(\lambda_3 / \lambda_1) n_o^{\omega_1} + (\lambda_3 / \lambda_2) n_o^{\omega_2} \right]^2}{(n_o^{\omega_3})^2 - (n_e^{\omega_3})^2} \right) \quad (\text{type I}) \quad (2.47)$$

and

$$\frac{\frac{n_o^{\omega_3}}{\sqrt{1 + \left[\frac{(n_o^{\omega_3})^2}{(n_e^{\omega_3})^2} - 1 \right] \sin^2 \theta_{pm}}} - \frac{(\lambda_3 / \lambda_1) n_o^{\omega_1}}{\sqrt{1 + \left[\frac{(n_o^{\omega_1})^2}{(n_e^{\omega_1})^2} - 1 \right] \sin^2 \theta_{pm}}}}{=} = (\lambda_3 / \lambda_2) n_o^{\omega_2} \quad (\text{type II}) \quad (2.48)$$

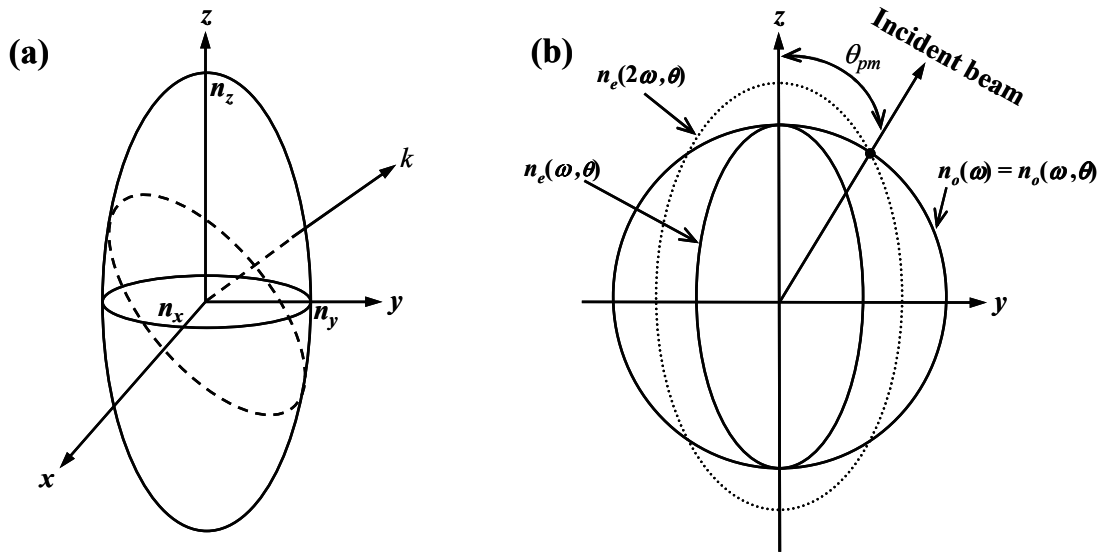


Figure 2.10. Schematic representation of (a) index ellipsoid as described by eq 2.41 and (b) phase matching condition for SHG in a negative uniaxial crystal.^{28,29} In figure (a), for a given direction, the intersection curve of a plane perpendicular to k and the ellipsoid is an ellipse. The lengths of the axes of this ellipse correspond to their respective indices. For a uniaxial crystal, the index ellipsoid is an ellipsoid of revolution about the optical axis. Figure (b) describes phase matching angle for SHG when fundamental light with frequency ω propagates as ordinary wave and second harmonic (2ω) light propagates as extraordinary wave.

Tripler

The output from the Ti:Sapphire oscillator is frequency tripled by a tripler from U-Oplaz Technologies, Inc. The optical layout of the tripler is shown in Figure 2.11. The output polarization of Ti:Sapphire oscillator is parallel to the laser table. The input beam (ω) is polarized vertically by the first half wave plate (WP₁) and focused onto the type I phased matched SHG crystal using a lens (L₁). The residual of fundamental (ω) and second harmonic (2ω) beam after the SHG crystal are polarized vertically and horizontally, respectively. After SHG, there is a time delay between ω and 2ω pulses due to the GVD by the crystal. This time delay is ~ 100 fs for 1 mm crystal. It is very important to compensate the time delay for efficient generation of femtosecond (fs) third harmonic pulses. The time delay is compensated using a specially designed birefringent crystal, known as time plate (TP). The n_o axis of refractive index of the crystal is along z -axis and n_e axis in the x - y plane. In this configuration, ω and 2ω propagate through the crystal as ordinary and extraordinary waves respectively, and the time delay is overcome depending upon the rotation angle, thickness, cutting angle and indices of refraction of the crystal because the ordinary and extraordinary wave travels with different speed. The tripler uses a type I BBO crystal to generate the third harmonic pulse. Since type I phase matching demands parallel polarization of the two different frequencies light, a half wave plate (WP₂) before third harmonic crystal is used to make both ω and 2ω polarized horizontally. The output third harmonic beam is vertically polarized. The output frequencies are separated using high reflecting dichroic mirrors (M₃, M₄, M₅ and M₆).

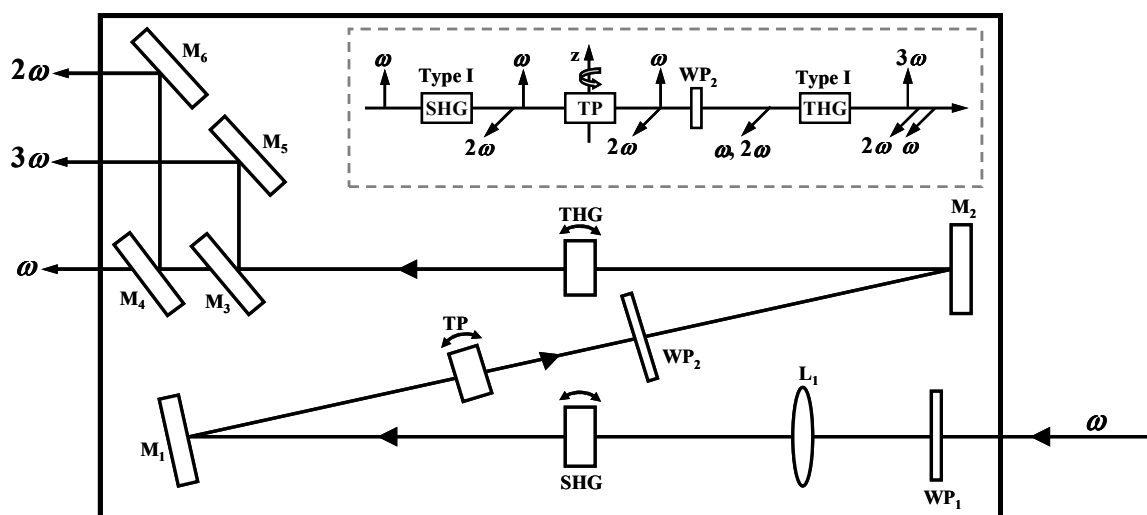


Figure 2.11. Schematic diagram of the tripler. WP - wave plate, L - lens, SHG - second harmonic generation, M - mirror, TP - time plate, THG - third harmonic generation.

Time-Correlated Single Photon Counting (TCSPC)

Principle

Let us consider that a dilute solution of fluorescent species is excited with a short pulse of light at time, $t = 0$. A certain number of molecules get excited to S_1 and some of them relax back to ground state (S_0) from S_1 . The rate of relaxation of the population, n , of excited molecules is given by first-order differential equation^{35,36}

$$\frac{dn}{dt} = -kn \quad (2.49)$$

Integration of eq 2.49 yields an exponential decay of the excited state population

$$n_t = n_0 e^{-\frac{t}{\tau}} \quad (2.50)$$

where n_t and n_0 represent excited state population at time t and $t = 0$, respectively. The τ is the excited state lifetime, which is related to k by

$$\tau = \frac{1}{k} \quad (2.51)$$

The fluorescence intensity, I , is proportional to the excited state population and also decays exponentially

$$I_t = I_0 e^{-\frac{t}{\tau}} \quad (2.52)$$

In order to measure the intensity of emitted light at a particular time t , one needs to count the number of photons that are being emitted at that time. One cannot predict when a photon will be emitted following an excitation pulse due to random nature of the emission of photons. If we excite a single molecule with a short pulse, the probability (P) of emitting a photon after a time delay Δt with respect to the time of excitation is given by³⁵

$$P(\Delta t) \sim e^{-\frac{\Delta t}{\tau}} \quad (2.53)$$

This indicates that the statistics for the detection of single photon emission time following excitation can reproduce excited population decay instead of measuring light intensity, which is a cooperating effect of many photons. Time-correlated single photon counting (TCSPC) detects only one photon at a time as it is based on the above hypothesis that the probability distribution for the emission of a single photon is equivalent to the actual intensity versus time distribution for all photons detected.^{7,37} A schematic diagram of TCSPC is presented in Figure 2.12. A pulsed light excites the sample at a high repetition rate. The sample emits fluorescence photons, which are detected by very sensitive detector, usually micro-channel plate (MCP) that is capable of responding to a single photon with a defined and measurable electric output pulse. A reference photodiode (PD) triggered by the excitation pulse is usually used to start the time-to-amplitude converter (TAC). TAC can be viewed as very precise stopwatch. The role of TAC is to measure the delay time between the excitation pulse and the pulse produced from the MCP by the emitted photon. TAC after

being started by the reference PD charges a capacitor with constant current and generates linearly rising voltage. The output pulse created by the first fluorescence photon in MCP is used to stop the clock (i.e., charging of the capacitor is stopped). The single-photon output pulse from MCP may have considerable amplitude jitter due to random amplification mechanism in the detector. The reference pulse from PD may also change because of intensity fluctuation of the laser source. The exact positions in time of a pulse from MCP (representing time of the photon event) or the timing of the reference signal are crucial. In order to avoid timing jitter arising from amplitude jitter of the detectors, the out put pulses are directed to constant fraction discriminator (CFD) before they start-stop TAC. The accumulated voltage in the TAC is proportional to the time delay between excitation pulse (start pulse) and the pulse produce by the photon (stop pulse). The amplitude of the voltage from TAC is measured by an analog-to-digital converter (ADC) to determine into which of the time slot on the time axis of the decay curve this photon should be recorded. It sends the time slot number to multi-channel analyzer (MCA). This number is then interpreted as a channel number in MCA. MCA has a memory—a multichannel array, which divided into N channels. Each channel corresponds to a short voltage interval in increasing order. For example, if the intervals are 0.1V and the input signal is 1.0 V, the signal is attributed to channel 10 and the value in this channel is incremented by one.³⁵ Of course, the measurement of a single photon does not contain any information about the fluorescence time course. If the sample is repeatedly excited by pulses and single photons are counted, then a histogram, which corresponds to the decay curve, is built up in the MCA with increasing numbers of events.

TCSPC deals with single photon detection. It is important that during the detection

cycle only one photon is detected, since all other photon but the first will be lost. This is the case when many molecules are excited at the same time. The lost photons could induce a nonlinear distortion in the histogram, known as pile-up.^{7,37,38} In order to avoid pile-up, the average count rate at the detector should be 1-5% of the excitation rate. Low excitation pulse energy (<1 nJ) and low sample concentration are also recommended to ignore pile-up.

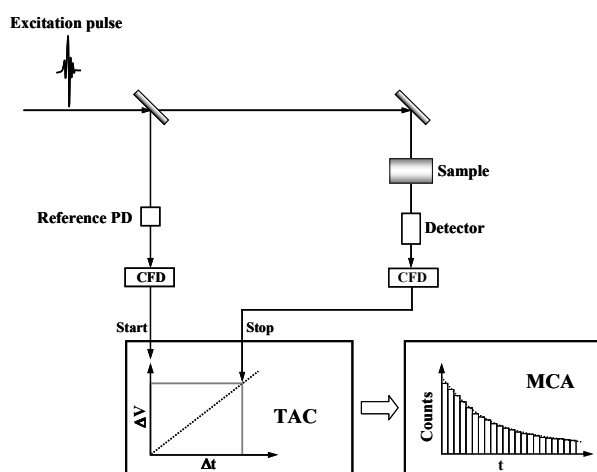


Figure 2.12. Illustration of basic principle of time-correlated single photon counting method. PD - photodiode, CFD - constant fraction discriminator, TAC - time to amplitude converter, MCA - multi-channel analyzer.⁹

The time resolution of this technique is limited by the transit time spread of the electron response pulse of the detector. Transit time spread reflects how much the timing of the response pulse varies from one pulse to another. For example, the transit time spread of MCP detector (Model R3809U-50) from Hamamatsu is 25 ps. One can get ≤ 40 ps instrument response function using this detector in TCSPC.^{7,37,38}

The recorded fluorescence profile $f(t)$ is the convolution of instrument response function $i(t)$ and the sample's response to delta pulse excitation $g(t)$, is given by²

$$f(t) = \int_0^{\infty} i(t-t')g(t')dt' \quad (2.54)$$

The instrument response function, $i(t)$, is measured by scattering the excitation pulse using nondairy coffee creamer. The $g(t)$ can be obtained by deconvolution of $f(t)$ using known $i(t)$.

Let us assume that the actual fluorescence, $g(t)$, is represented by sum of exponential decays as

$$g(t) = \sum_i a_i e^{-\frac{t}{\tau_i}} \quad (2.55)$$

where a_i and τ_i are the amplitude and decay time, respectively, of the i th decay component.

In order to extract $g(t)$, one generally start with trial values of a_i and τ_i and a calculated $f_c(t)$ is obtained after convoluting with the instrument response function, $i(t)$, according to eq 2.54.

The difference between $f_c(t)$ and $f(t)$ is then minimized by least square fitting, in which a_i and τ_i are varied. The goodness of the fit is represented by χ^2 , is expressed as

$$\chi^2 = \sum_i \frac{[g(t) - g_c(t)]^2}{g(t)^2} \quad (2.56)$$

TCSPC Setup

An optical layout of the TCSPC instrument used for the experiments is shown in Figure 2.13. A homebuilt mode-locked Ti:sapphire oscillator pumped by a Nd:VO₄ laser (Millennia, Spectra Physics) producing femtosecond pulses tunable from 780 to 900 nm with a repetition rate of 88 MHz is used as the laser source. The fundamental wavelength at 814 nm from the Ti-sapphire oscillator is modulated by a Pockels cell (Model 350-160, Conoptics Inc.) to reduce the repetition rate to approximately 8.8 MHz and is subsequently frequency doubled or tripled by using a harmonic generator (Model TP-2000B, U-Oplaz Technologies). The resulting blue (~ 407 nm) or UV (~ 266 nm) light provides the excitation source. The excitation pulses are passed through a half-wave plate and a polarizer before reaching the

sample in order to make the polarization of the excitation light vertical with respect to the laser table. The fluorescence is collected at a 90° geometry, and passes through an analyzer set at the magic angle (54.7°) with respect to excitation polarization. The fluorescence is generally collected at the magic angle in order to avoid the influence of orientational motions of the fluorophores on the temporal behavior of the fluorescence. A microchannel plate, MCP (Hamamatsu) is used for the fluorescence detection. The detector output is amplified and fed to the Becker & Hickl photon counting module Model SPC-630. The module contains the usual building blocks (CFDs, TAC, ADC) together with a large histogram memory integrated on one board. The full-width-at-half-maximum (FWHM) of the instrument response function is $\sim 40 - 45$ ps.

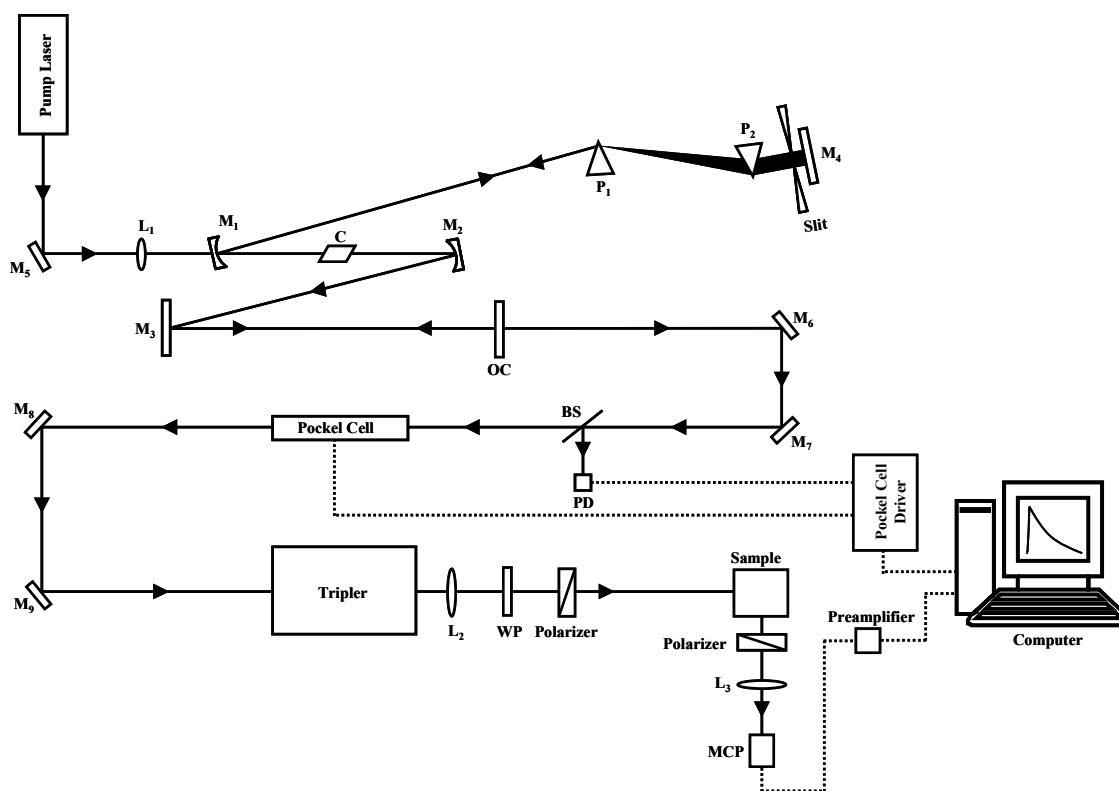


Figure 2.13. Schematic diagram of TCSPC instrument. M - mirror, L - lens, C - crystal, OC - output coupler, P - prism, BS - beam splitter, PD - photodiode, WP - wave plate, MCP - microchannel plate.

Fluorescence Upconversion

Ultrafast dynamics in the femtosecond time range cannot be resolved using TCSPC owing to the limiting factor of the detector response, even if femtosecond excitation pulses are used. But fluorescence spectroscopy can be performed in the ultrafast regime by optical gating of the fluorescence emission using a nonlinear crystal with a technique popularly known as fluorescence upconversion. With this method, time resolution comparable to laser pulse width is obtained.

Principle

The fluorescence upconversion technique^{2,35,36,38-42} is based on nonlinear effect of sum frequency mixing in a nonlinear birefringent crystal. Typically, the sample is excited with femtosecond light pulses and the emitted fluorescence (ν_f) is collected, and focused along with the gate pulses (ν_g) onto a nonlinear crystal. The combined electric fields of the two pulses interact with electrons of the nonlinear crystal to generate a new radiation field at the sum frequencies (ν_s) of the incident radiation. Since the output photons, $\nu_s = \nu_f + \nu_g$, are upconverted to a higher frequency by the gate pulse, this technique is known as fluorescence upconversion (Figure 2.14a). The upconverted signal (ν_s) is separated with a monochromator and sent to subsequent light detection and data acquisition devices. The detector response may be slow because it only measures the signal intensity at sum frequency, not its time course. A necessary condition for upconversion is that the two fields (gate pulse and fluorescence) be present in the crystal at the same time because polarization of electrons is essentially instantaneous. If the gate pulse is not present, the fluorescence alone cannot produce a sum signal (ν_s). Thus the gate pulse opens an optical gate to measuring the

fluorescence intensity at a certain instant after excitation. Usually, the arrival time of the gate pulse is controlled with a motorized delay stage consists of a retro-reflecting mirror, and is swept across the time profile of the fluorescence. The reverse method can also be carried out, i.e., the arrival time of fluorescence photons is controlled by delaying the excitation pulse and scanned with respect to the gate pulse that is fixed in time. Our upconversion instrument follows this method. Based on the speed of light (c) in air and folded path of excitation beam along the delay stage, a delay of $\Delta t = 1$ fs is generated by a displacement $d = c\Delta t/2 = 1.5 \mu\text{m}$ in translation line. Moving the translational line with small steps, one can scan the whole decay profile.

The important point here is the width of pulse because the time resolution of this method is limited by the width of gate and excitation pulse. Both the pulses get broaden when they pass through the solvent, sample cell window, detection optics and nonlinear crystal because of group velocity dispersion (GDV). In order to achieve good time resolution it is better to use the sample cell, crystal and lenses in the optical scheme as thin as possible.^{35,38}

The intensity output photons (I_s) at sum frequency is proportional to the product of intensity of gating (I_g) and fluorescence (I_f) photons, and is given by^{2,41}

$$I_s(t') = \int_{-\infty}^{t'} I_f(t - t') I_g(t) dt \quad (2.57)$$

Eq 2.57 also clearly indicates that the signal at sum frequency is not obtained when the gate and fluorescence photons are simultaneously coincident on the crystal. The gate photons slice out only those photons of fluorescence, which are overlapped with the gate photons (Figure 2.14b). Thus the time course of the fluorescence at a particular frequency, ν_s , is

mapped out by scanning the delay line for excitation pulse causing fluorescence from sample.

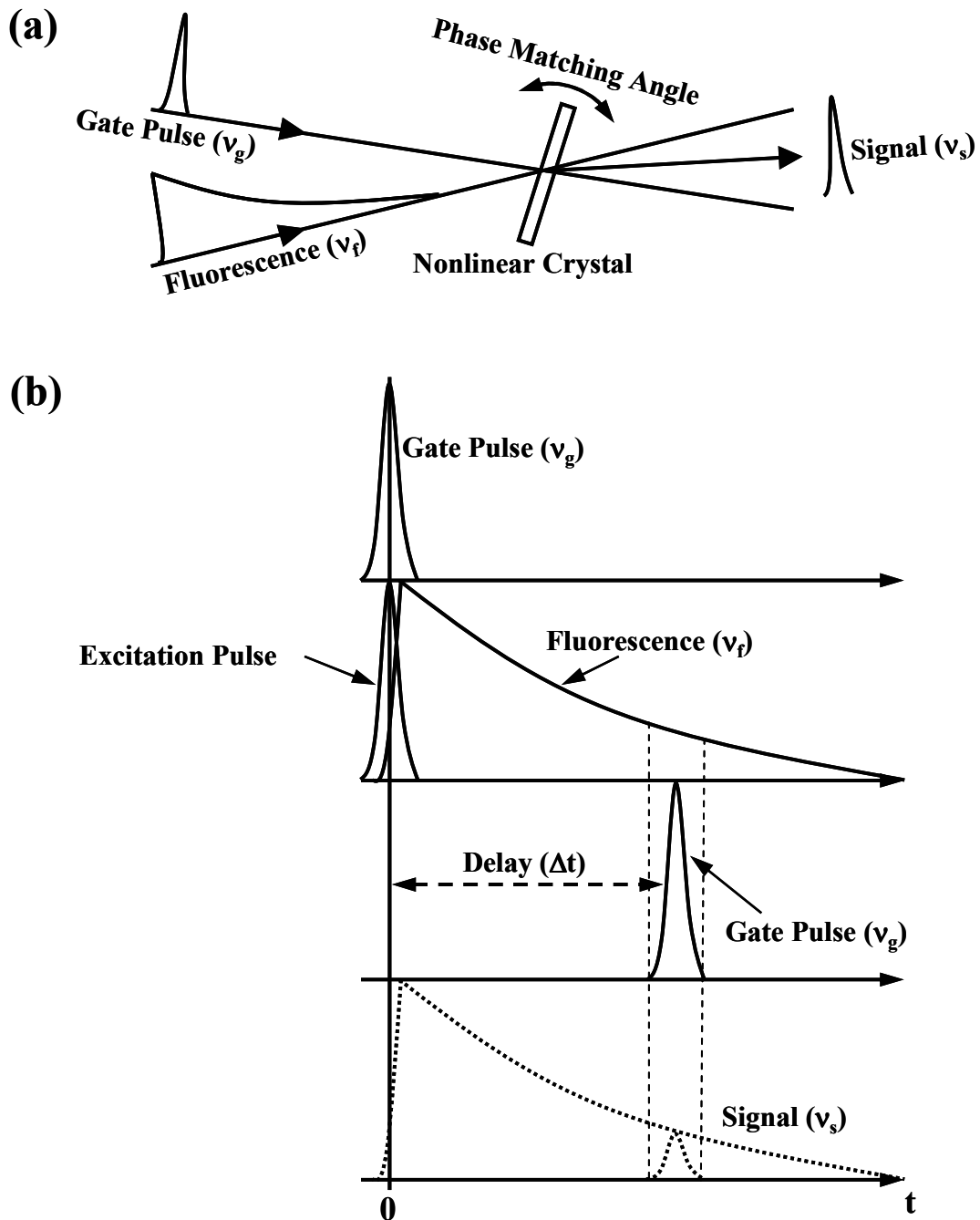


Figure 2.14. Principle of fluorescence upconversion. (a) The sum frequency signal is generated in the crystal when both the gate pulse and fluorescence is present at the same time. (b) The intensity of sum frequency signal is proportional to the product of gate pulse and fluorescence intensity. Thus, sum frequency signal obtained with delay time is accurate representation of time-resolved fluorescence decay.^{38,40,42,43}

The instrument response function is obtained from cross-correlation function of gate pulse $I_g(t)$ and excitation pulse $I_{ex}(t)$ using the same optics and crystal that are used for the sample. The cross-correlation function (C') is given by³⁹

$$C'(t') = \int_{-\infty}^{t'} I_{ex}(t-t') I_g(t) dt \quad (2.58)$$

The cross-correlation function is used for the deconvolution of optically gated fluorescence data because experimentally measured fluorescence intensity is the convolution of true fluorescence decay and excitation pulse.

Fluorescence Upconversion Setup

A schematic diagram of fluorescence upconversion setup is displayed in Figure 2.15. The laser source is a homebuilt mode-locked Ti:sapphire oscillator. The fundamental wavelength and repetition rate of the femtosecond output are 814 nm and 88 MHz, respectively. The fundamental output from the oscillator is frequency-doubled by a type-I LBO crystal (2 mm). The frequency-doubled pulses (407 nm) are separated from residual fundamental light using a dichroic mirror, and used to excite the sample. The residual of the fundamental is used as the gate pulse to upconvert the fluorescence signal. A filter is used to block trace 407 nm light with the fundamental. The gate pulses pass through a $\lambda/2$ plate, turning the polarization by 90° with to plane of laser table. The exciting pulses also pass through a $\lambda/2$ plate, which is adjusted at the magic angle (54.7°). In our upconversion system, the excitation pulse is delayed with respect to gate pulse using a motorized delay stage.

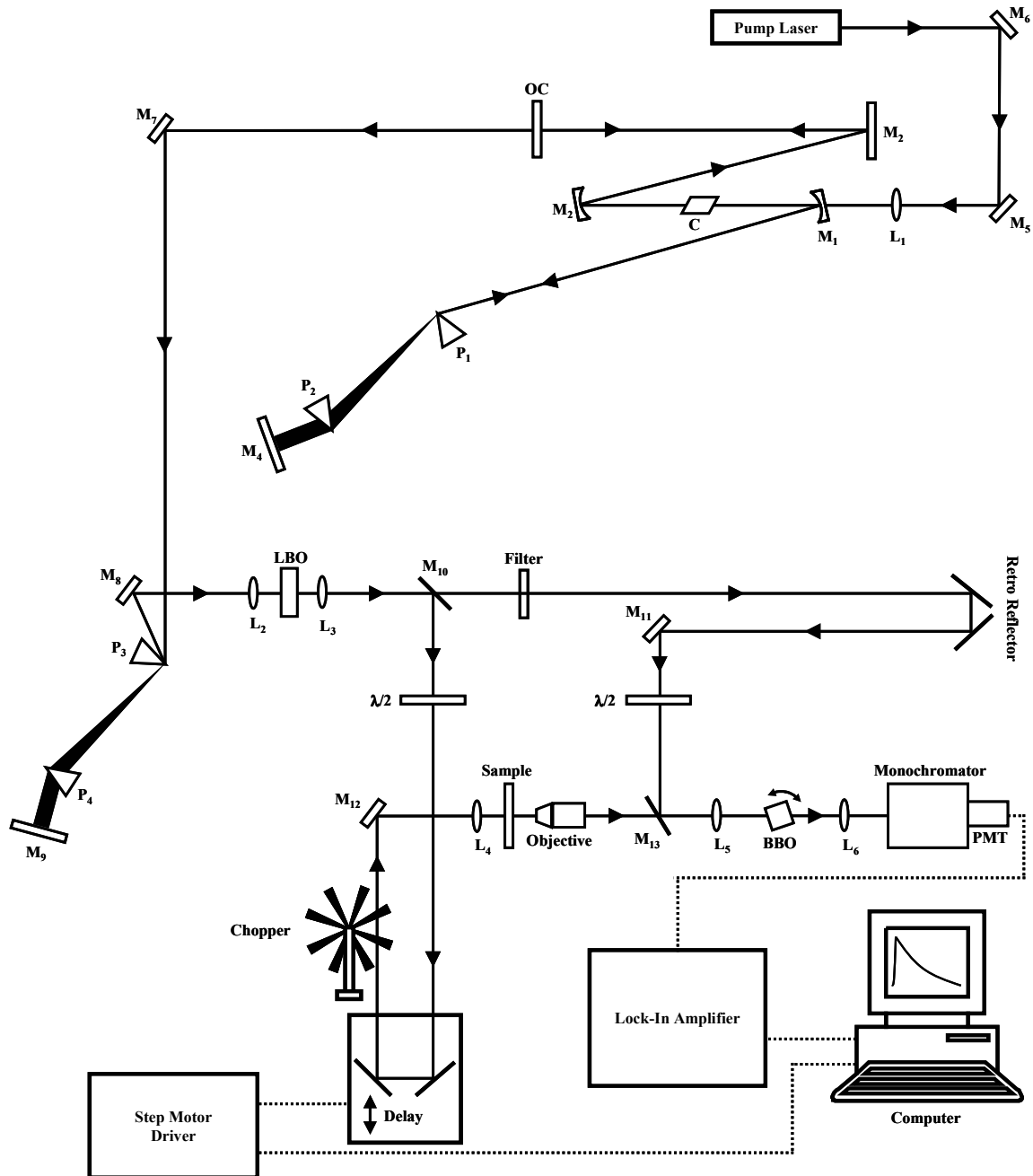


Figure 2.15. Schematic diagram fluorescence upconversion system. M - mirror, L - lens, C - crystal, OC - output coupler, P - prism, BS - beam splitter, BBO - β -barium borate, PMT - photomultiplier tube.

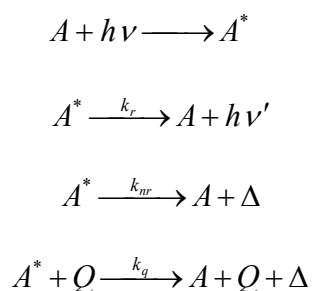
The sample is contained in a glass rotating cell of path length 1 nm mounted perpendicularly to the exciting beam and spins about an axis parallel to the beam. First, the frequency-doubled blue pulses (407 nm) are focused on the sample and the fluorescence signal is collected using a 10x objective lens. Then, the gate pulse and fluorescence signal are focused onto a 0.4 mm type-I BBO crystal to generate the sum frequency light, which is detected by a photomultiplier tube mounted on a monochromator. The upconverted signal is usually weak. In order to pick up the upconverted signal from the background noise, an optical light chopper is settled in the excitation beam line. The light is chopped at 1000 Hz, and the signal is counted at this rate using a lock-in amplifier connected to the PMT. The full-width-at-half-maximum (FWHM) of the instrument response function is 300 fs, obtained by the cross-correlation function of the frequency doubled and the fundamental light.

Fluorescence Quenching

Fluorescence quenching refers to any process that decreases the fluorescence intensity or lifetime of a sample. Fluorescence quenching has been a common experiment to determine the location of fluorescent probes in macromolecules based on the accessibility of fluorophores to quenchers.¹ There are two basic types of quenching: static and dynamic (collisional). Both types of quenching mechanism require an interaction between the fluorophore and the quencher. In the case of static quenching, a ground-state nonfluorescent complex is formed between the fluorophore and the quencher. In the case of dynamic quenching, the quenchers diffuse to fluorophores during its excited-state lifetime. The fluorophore returns to the ground state without emission of a photon after a diffusive encounter with a quencher during its excited-state lifetime. It is known that the fluorescence of dyes is quenched by a wide variety of external quenchers. Excited-state electron transfer,

energy transfer, proton transfer, exciplex formation (excited-state complex) and spin-orbit coupling (heavy atom effect) have been proposed as possible quenching mechanisms for various quenchers.^{1,44} Mechanism of quenching varies with the fluorophore-quencher pair. For example, for halide ions such as Br^- and I^- , fluorescence quenching are thought to be a result of enhanced intersystem crossing to an excited triplet state because of efficient spin-orbit coupling of the excited (singlet) fluorophore and the halide upon contact.⁴⁵ Since molecules usually have a longer triplet state lifetime, the triplet emission is quenched by collisions with surrounding solvents at room temperature. Acrylamide is a quencher that quenches fluorescence of tryptophan possibly due to electron transfer from tryptophan in excited state to acrylamide.¹ Other quenchers, such as Cu^{2+} , Pb^{2+} are thought to cause the donation of an electron from the fluorophore in the excited state.

Bimolecular fluorescence quenching mechanism can usually be described by the following kinetic scheme⁴⁶



In the absence of quenchers, the rate of relaxation of an excited fluorophore, A^* , can be written as⁴⁷

$$\frac{d[A^*]}{dt} = -(k_r + k_{nr})[A^*] \quad (2.59)$$

Solution of eq 2.59 with respect to initial conditions, at $t = 0$, $[A^*] = [A^*]_0$ is

$$[A^*] = [A^*]_0 e^{-t/\tau_0} \quad (2.60)$$

where $\tau_0 = 1/(k_r + k_{nr})$, is the fluorescence lifetime in the absence of any quencher. If a quenching agent (Q) is present in solution, the rate of relaxation of A^* becomes

$$\frac{d[A^*]}{dt} = -(k_r + k_{nr} + k_q[Q])[A^*] \quad (2.61)$$

If $[Q] \gg [A^*]$, which means $[Q]$ can be treated as a constant (the quencher concentration is orders of magnitude larger than $[A^*]$ in practice), then eq 2.61 can be integrated to obtain

$$[A^*] = [A^*]_0 e^{-t/\tau} \quad (2.62)$$

with $\tau = 1/(k_r + k_{nr} + k_q[Q])$. From the ratio of lifetimes in absence and presence of quencher, we have

$$\frac{\tau_0}{\tau} = 1 + k_q \tau_0 [Q] \quad (2.63)$$

The fluorescence quantum yield in the absence of quencher is

$$\Phi_0 = \frac{k_r}{k_r + k_{nr}} = k_r \tau_0 \quad (2.64)$$

whereas in the presence of quencher, it is given by

$$\Phi = \frac{k_r}{k_r + k_{nr} + k_q[Q]} = \frac{k_r}{1/\tau_0 + k_q[Q]} \quad (2.65)$$

Eqs 2.63, 2.64 and 2.65 can be grouped together to obtain

$$\frac{\Phi_0}{\Phi} = \frac{F_0}{F} = \frac{\tau_0}{\tau} = 1 + k_q \tau_0 [Q] = 1 + K_{SV} [Q] \quad (2.66)$$

where F_0 and F are the steady-state fluorescence intensities in the absence and presence of quencher, respectively. The relation (eq 2.66) between fluorescence intensity and quencher concentration is known as Stern-Volmer equation. If the fluorescence intensity (F) (or lifetime, τ) in the absence of quencher and in the presence of incremental amounts of

quencher are measured, and then the resulting ratio of fluorescence intensities (F_0/F) (or τ_0/τ) is plotted as a function of quencher concentration, $[Q]$, the resulting graph (a Stern-Volmer plot) will have an intercept of one, and a slope known as Stern-Volmer constant, K_{SV} . Since $K_{SV} = k_q \tau_0$, knowing the slope and the lifetime in the absence of quencher, τ_0 , it allows easy calculation of the quenching rate constant k_q .

For dynamic quenching, all fluorophore are affected by the quenching process as there is the possibility of collision with a quencher during the excited state lifetime. Thus, both fluorescence intensity (F) and lifetime (τ) are reduced with increasing concentration of the quencher. For static quenching, only fluorophore-quencher associations result in reduction in fluorescence intensity because unassociated fluorophores are free to fluoresce. Increasing quencher concentration affects fluorescence intensity, because there are more associations, but not the fluorescence lifetime because the unassociated fluorophores can fluoresce with its normal fluorescence lifetime. Therefore, the diagnostic test for assigning if a quenching mechanism is dynamic or static is to compare how the fluorescence intensity and lifetime change as a function of increasing quencher concentration. In the case of dynamic quenching, plots of F_0/F and τ_0/τ with $[Q]$ will be the same. For static quenching, only a plot of F_0/F will change with $[Q]$ whereas τ_0/τ plot will have slope close to zero (Figure 2.16).

Modified form of Stern-Volmer equation is often used when there are two types of populations of fluorophores present in the system, one being accessible to quenchers, a , and the other inaccessible or buried, b .¹ The total fluorescence intensity in the absence of quencher can be written as

$$F_0 = F_0^a + F_0^b \quad (2.67)$$

The quenchers affect only fluorescence intensity of accessible fluorophore according to Stern-Volmer equation. This leads to observed fluorescence intensity, F , as

$$F = \frac{F_0^a}{1 + K_{SV}^a [Q]} + F_0^b \quad (2.68)$$

where K_{SV}^a is the Stern–Volmer quenching constant of the accessible fraction. Substraction of eq 2.68 from eq 2.67 results

$$F_0 - F = \Delta F = F_0^a \left(\frac{K_{SV}^a [Q]}{1 + K_{SV}^a [Q]} \right) \quad (2.69)$$

The eq 2.69 can also be expressed as

$$\frac{F_0}{\Delta F} = \frac{1}{f_a K_{SV}^a [Q]} + \frac{1}{f_a} \quad (2.70)$$

with fraction of initial fluorescence accessible to the quencher, $f_a = F_0^a / (F_0^a + F_0^b)$. Plot of $F_0/\Delta F$ against $1/[Q]$ produces the intercept as $1/f_a$ and slope $1/f_a K_{SV}^a$.

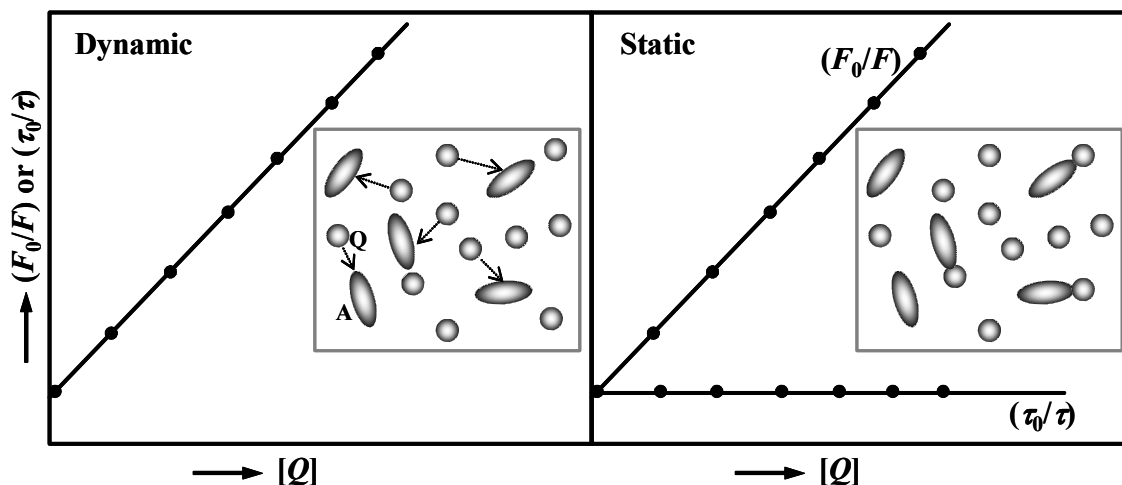


Figure 2.16. Model plots to distinguish between dynamic and static quenching. In dynamic quenching, increasing quencher concentration increases the probability of collisions with fluorophore during its fluorescence lifetime while incase of static quenching increasing quencher concentration increases probability of association with the fluorophore in the ground state.

Fluorescence Resonance Energy Transfer

Resonance energy transfer (RET) is an important mechanism by which an excited molecule (donor) can return to its ground state by transferring the excitation energy to another molecule (acceptor). If the donor molecule is fluorescent, then RET is referred to as fluorescence resonance energy transfer, FRET. The acceptor however may or may not be fluorescent. FRET is the non-radiative transfer of energy from a donor molecule to the acceptor molecule, therefore the signature of FRET is quenching of the high energy donor emission followed by emission from the acceptor of relatively low frequency of light. When donor and acceptor are too close ($< 10 \text{ \AA}$), energy transfer occurs by exchange of electrons due to overlapping of their electron cloud known as Dexter mechanism of energy transfer.⁴⁸ In this thesis we will deal with Förster energy transfer.⁴⁹ In principle for Förster energy transfer to occur several major criteria must be satisfied. First, the donor emission spectrum must overlap with the absorption spectrum of acceptor. A second criterion that needs to be satisfied is that the donor to acceptor distance must be within 10-100 \AA of each other. The third criterion that must be met is that the excited state lifetime of the donor molecule must be of sufficient duration to allow energy transfer to occur.

Theodore Förster provided a quantitative idea in 1946 by developing non-radiative transfer rate equation that relates to the inter-chromophore distance and the spectroscopic properties of the chromophores, known as “Förster theory of energy transfer”.⁴⁹ He showed that the efficiency of energy transfer decreases with sixth power of the distance between donor and acceptor. Stryer and Haugland have verified this theory critically in 1967.⁵⁰ Förster theory is based on very weak dipole-dipole interaction between the donor and acceptor. Thus spectroscopic properties like absorption of donor and acceptor should not be

altered in the presence of each other. In resonance energy transfer process; first the donor (D) molecule gets excited by absorbing light energy. As a consequence of this, an induced dipole is formed in the donor molecule. When D^* (excited donor) and A (acceptor) molecules come close to each other in solution, they feel each other's presence due to long-range Coulomb forces. As D^* and A approach, the D^* dipole starts interacting with the A dipole. As a result of this dipole-dipole interaction, the electron in the HOMO (highest occupied molecular orbital) of A will also be induced to oscillate more violently. This violent oscillation can cause the excitation of the electron into the LUMO (lowest unoccupied molecular orbital) of A, along with a de-excitation of the excited electron on D. The ultimate result of this interaction is that D^* has become de-excited to the ground electronic state with simultaneous excitation of A to A^* (Figure 2.17).⁵¹ This dipoles interaction and exchange of energy is similar to two oscillating pendulums that are mechanically coupled. If two pendulums have a spring connecting their rods then when one pendulum is set swinging (the donor molecule absorbs a photon) the other pendulum of couple will begin swinging (the acceptor molecule emits a photon).⁵²

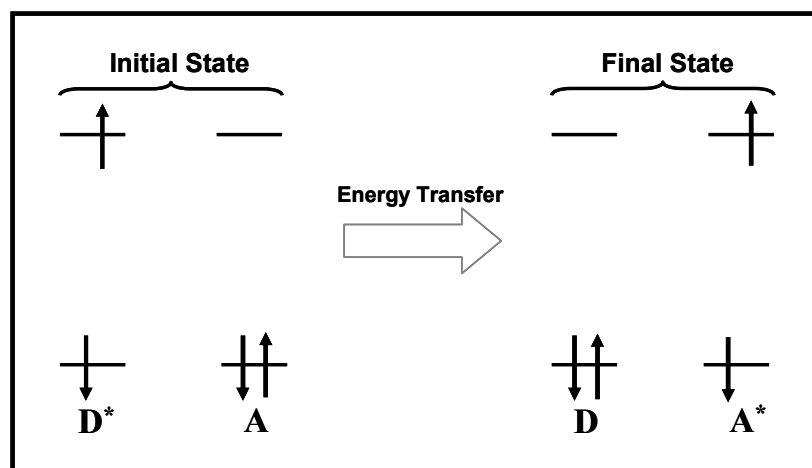


Figure 2.17. Energy level diagram showing electron movements in long-range Coulombic energy transfer.

The rate of energy transfer from the donor to an acceptor is given by

$$k_{ET} = \frac{9000\kappa^2 (\ln 10)\phi_D c^4}{128\pi^5 n^4 N\tau_D R^6} \int_0^\infty f_D(\tilde{\nu})\varepsilon_A(\tilde{\nu}) \frac{d\tilde{\nu}}{\tilde{\nu}^4} \quad (2.71)$$

where N is the Avogadro's number, c is the velocity light, ϕ_D is the quantum yield of donor in the absence of acceptor, τ_D is the donor lifetime in the absence of acceptor, n is the refractive index of the medium, R is the distance between donor and acceptor, f_D is the fluorescence emission spectrum of donor normalized to unity, ε_A is the absorption spectrum of the acceptor, and $\tilde{\nu}$ is the wavenumber in cm^{-1} . The integrated part of eq 2.71 is known as overlap integral (Figure 2.18). κ is known as orientation factor which is expressed as

$$\kappa = \sin\theta_1 \sin\theta_2 \cos\phi_{12} - 2\cos\theta_1 \cos\theta_2 \quad (2.72)$$

θ_1 , θ_2 and ϕ_{12} are the angles designated in Figure 2.19. The maximum, minimum and the average value of κ^2 are 4, 0 and $2/3$.

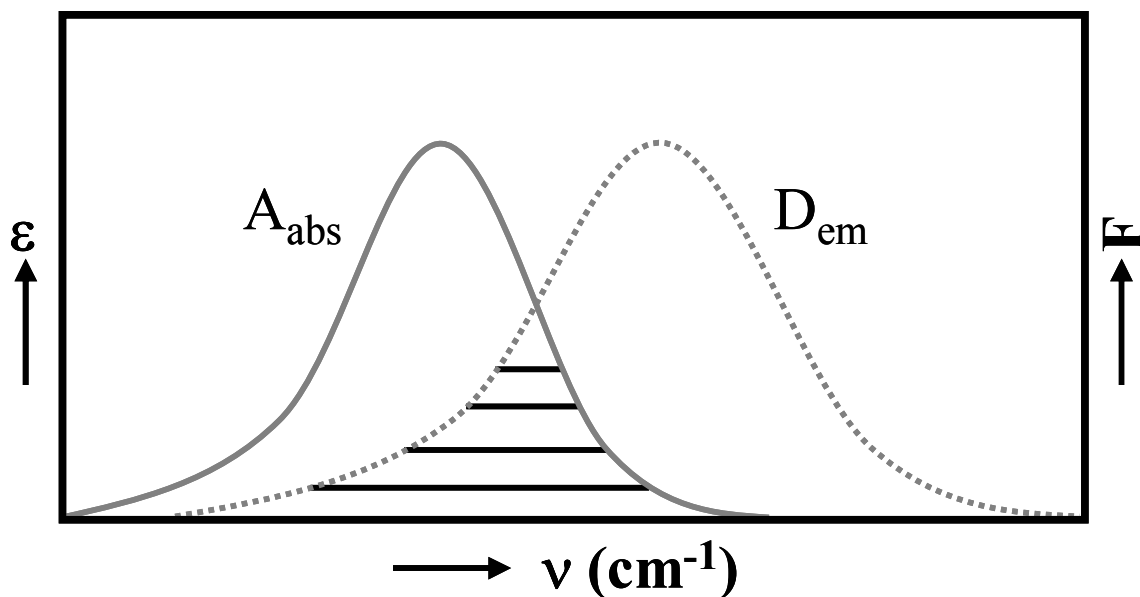


Figure 2.18. Overlap integral of donor emission and absorption spectra is shown by series of horizontal lines.

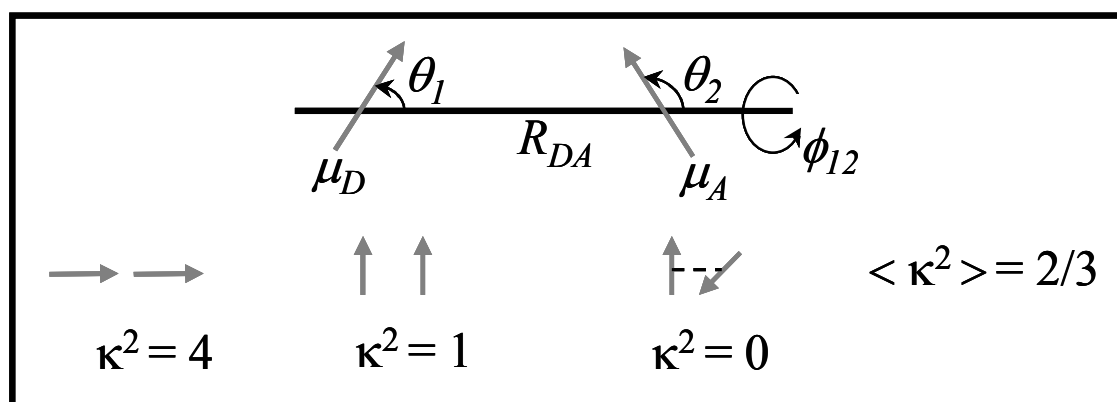


Figure 2.19. Orientation for dipole-dipole coupling.

From eq 2.71 it is clear that rate of energy transfer energy decreases with sixth power of the distance between donor and acceptor. k_{ET} is expressed as

$$k_{ET} = \frac{1}{\tau_D} \left(\frac{R_0}{R} \right)^6 \quad (2.73)$$

R_0 is known as Förster distance that represents the distance at which the efficiency of energy transfer is 50%, and is expressed as

$$R_0^6 = \frac{9000\kappa^2(\ln 10)\phi_D c^4}{128\pi^5 n^4 N} \int_0^\infty f(\tilde{\nu})\varepsilon(\tilde{\nu}) \frac{d\tilde{\nu}}{\tilde{\nu}^4} \quad (2.74)$$

In an alternative way at $R = R_0$, k_{ET} is equal to the decay rate of the donor (τ_D^{-1}) in the absence of acceptor. At this distance, one half of the donor molecules decay by energy transfer and the other half decay by the usual radiative and non-radiative processes.

The efficiency can be defined in many ways like in term of lifetime of donor, fluorescence intensity of donor and also in term of D-A distance. τ_{DA} and τ_D are the lifetime donor in presence and absence of acceptor respectively. Similarly, f_{DA} and f_D are the fluorescence of donor in presence and absence of acceptor

$$E = 1 - \frac{\tau_{DA}}{\tau_D} = 1 - \frac{f_{DA}}{f_D} = \frac{R_0^6}{R_0^6 + R^6} \quad (2.75)$$

The distance dependence of resonance energy transfer process provides the basis of its usefulness in the study of molecular interactions. Förster distance 10-100 Å is especially convenient of studying interactions biological macromolecules. These distances are comparable to the diameter of many proteins, the thickness of biological membrane and distance between the sites on multi-subunits proteins. Any phenomenon, which affects the D-A distance, will also affect the rate of energy transfer, allowing the phenomenon to be quantified. Also this technique is important because measurement can be done under physiological (or other) with near angstrom resolution. For this reason resonance energy transfer has found to be widely useful in polymer science, biochemistry and structural biology.⁵³⁻⁵⁹

Time-Resolved Fluorescence Anisotropy

Absorption of a photon by a molecule takes place on the order of 10^{-15} s. The average fluorescence lifetime is in the range of 10^{-9} s for many fluorophores.¹ Therefore, there is a significant time delay between absorption and fluorescence, and a molecule or its constituent parts can undergo significant angular displacement in the time between absorption and emission.⁶⁰ In the time-resolved fluorescence anisotropy experiment (Figure 2.20), an ensemble of dyes is excited using a polarized laser pulse. In a solution of randomly oriented fluorophores (isotropic solution), an incident beam of polarized light preferentially excites molecules with a probability proportional to $\cos^2\theta$, where θ is the angle between the transition dipole moment of the dye and the polarization of the incident light. This process is known as photoselection.⁶¹ The orientational anisotropic distribution of the excited dye

molecules relaxes by rotational diffusion during their fluorescence lifetime and emits the fluorescence in a possibly changed orientation. The resulting rotation in the plane of fluorescence polarization is usually detected by using a polarizer before the detector at parallel and perpendicular orientation with respect to excitation polarization. This yields two fluorescence intensity signals; $I_{\parallel}(t)$ and $I_{\perp}(t)$ as the parallel and perpendicular part of the fluorescence, respectively. The $I_{\parallel}(t)$ and $I_{\perp}(t)$ of the same sample are different because the time evolution of fluorescence intensity at a fixed plane of polarization is the superposition of rotational diffusion and excited state population decay. For a single rotational correlation time, τ_r , $I_{\parallel}(t)$ and $I_{\perp}(t)$ can be written as³⁷

$$I_{\parallel}(t) = e^{-t/\tau_f} (1 + 2r_0 e^{-t/\tau_r}) \quad (2.76)$$

$$I_{\perp}(t) = e^{-t/\tau_f} (1 - r_0 e^{-t/\tau_r}) \quad (2.77)$$

τ_f is fluorescence lifetime of the probe. The r_0 is anisotropy value at $t = 0$, and is related to the θ by the relation given as^{1,37}

$$r_0 = \frac{1}{5} \left(\frac{3 \langle \cos^2 \theta \rangle - 1}{2} \right) \quad (2.78)$$

The value of r_0 varies between 0.4 and -0.2 because the angle θ changes between 0° to 90° . When the $\theta = 54.7^\circ$, there is a complete loss of anisotropy. The total fluorescence intensity, $F(t)$, according to eq 2.76 and 2.77 is

$$F(t) = I_{\parallel}(t) + 2I_{\perp}(t) = 3e^{-t/\tau_f} = F_0 e^{-t/\tau_f} \quad (2.79)$$

The fluorescence anisotropy $r(t)$ at time t after the excitation of the fluorophore is defined as^{2,37,62}

$$r(t) = \frac{I_{\parallel}(t) - I_{\perp}(t)}{I_{\parallel}(t) + 2I_{\perp}(t)} = r_0 e^{-t/\tau_r} \quad (2.80)$$

If the fluorophore behaves in solution as a rigid rotator, the τ_r depends mainly on the size and shape of the molecule. The Stokes-Einstein-Debye^{1,63} relation can estimate the τ_r for a fluorophore in solution

$$\tau_r = \frac{\eta V}{k_B T} \quad (2.81)$$

where η is the solvent viscosity, k_B is the Boltzmann constant, T is temperature, and V is the molecular volume of the fluorophore. This equation is based on classical hydrodynamics and requires the hypothesis of a continuous and homogeneous solvent. If the rotational motion of a fluorophore is restricted in an environment in such way that the anisotropy $r(t)$ never (on the time scale of fluorescence) decays to zero, then a residual anisotropy r_{∞} is observed as given by⁶⁴

$$r(t) = (r_0 - r_{\infty})e^{-t/\tau_r} + r_{\infty} \quad (2.82)$$

For more complex motions or nonspherical molecules, the $r(t)$ must be described by multi-exponential functions. In this case, a general description of the anisotropy is given by¹

$$r(t) = \sum_i r_i e^{-t/\tau_{r(i)}} \quad (2.83)$$

Time-resolved depolarization of fluorescence of dye molecules in liquids is one of the powerful techniques for the investigation of the tumbling or rotational motion of the molecule on the picosecond to nanosecond time scale.² Information about the microscopic motions is contained in the time-dependent fluorescence anisotropy $r(t)$. The fluorescence anisotropy decay for a number of organic dye molecules in pure solvents is usually single

exponential, and the rotational dynamics of the molecule resembles that of an ellipsoid or a sphere.⁶⁵⁻⁶⁹ There are also a few reports where the anisotropy decay of dye molecules in liquids is biexponential.⁷⁰⁻⁷² In microheterogeneous media such as micelles and membranes, the rotational dynamics of the dye is different from that in homogeneous media due to the existence of an aqueous/nonaqueous interface that leads to an orientationally nonrandom equilibrium distribution of the molecules, and highly restricted dynamics of the molecules.⁷³ For example, the fluorescence anisotropy decay of a dye molecule in a spherical micelle is best described by a model of restricted rotational motion of the dye (wobbling-in-cone) coupled with the rotational motion of the whole micelle (tumbling motion of the micelle), leads to a biexponential anisotropy decay with two widely separated rotational correlation time constants.⁷³

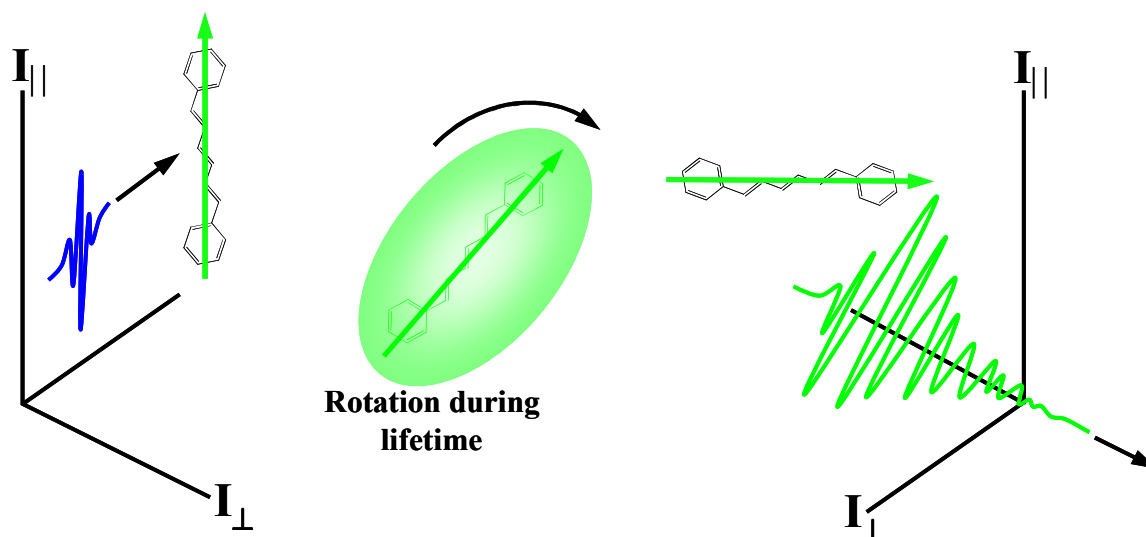


Figure 2.20. Schematic model of fluorescence anisotropy. The dye is first excited by a polarized laser pulse. During fluorescence lifetime the dye undergoes rotational diffusion. Finally, the dye emits a photon in a possibly changed orientation. A polarizer (before the detector) at the parallel (I_{\parallel}) and perpendicular (I_{\perp}) orientation with respect to polarization of excitation yields ($I_{\parallel}(t)$) and $I_{\perp}(t)$, respectively.

Solvation Dynamics

The area of solvation dynamics has attracted much attention in the past several years because of its influence on various chemical reactions, especially on charge transfer processes.⁷⁴⁻⁷⁸ The time scale of the response of surrounding solvent to electronic rearrangement of solute molecule can play a deterministic role in the rates of chemical reaction.^{75,79-82} In particular, for a reaction, if the solvents cannot respond quickly enough to the electronic rearrangement as the reactant passes through the transition state, the evolving product may re-cross the free-energy barrier; hence rate of the reaction is reduced.⁸³⁻⁸⁷ Theoretical, experimental and molecular dynamic simulation studies reveal that the rates of both activated and activationless electron transfer are most affected by the fastest part of the solvent response, hence the dynamics of solvation on a femtosecond timescale is critical.⁸⁸⁻⁹³

The central question in liquid-phase chemistry is: how do solvents affect the rate, mechanism and outcome of chemical reactions? The term “solvation” refers to the thermodynamically stable state of the local system consisting of a solute and its surrounding solvents. Understanding the rate of solvent reorganization in response to a perturbation in solute-solvent interactions (solvation dynamics) is an essential step in answering this central question. Time-resolved fluorescence spectroscopy has been of great importance probing the dynamics of the solvent.^{80,81,94-99} The dynamics of solvent relaxation around the solute molecules, which are perturbed from equilibrium solvation is often followed by measuring the time-dependent fluorescence Stokes shift of the solute molecule. In a typical solvation dynamics experiment, a chromophore that is in equilibrium with surrounding solvent molecules is electronically excited with ultrafast optical pulse. An abrupt change of electronic charge distribution of the probe molecule is induced by the electronic excitation

from the electronic ground state to the excited state. The formation of the excited state occurs on 10^{-15} s time scale much faster than any nuclear rearrangement of the environment according to Franck-Condon principle. This indicates that the nuclear solvent coordinates are “frozen” (although the solvent’s electronic charge distribution can follow the photo-induced change in the chromophore’s electronic charge distribution). As a result, the excited-state solute-solvent configuration is in highly non-equilibrium situation. Usually the fluorescence lifetime of the probe molecule is long compared to solvation time scale. Consequently, the solvent molecules around the new excited-state charge distribution of the solute respond by reorientation in order to minimize the free energy of the system (Figure 2.21). During this process of adjustment of free energy, the energy of excited state is lowered. This results in a red shift of the fluorescence spectrum as the solvation proceeds, known as dynamic Stokes shift.^{81,100}

It is important to use a relatively structurally rigid chromophore, so that most of the changes in the fluorescence spectrum can be ascribed to changes in the solvent environment rather than changes in the molecular geometry. Selection of the probe is crucial in order to obtain correct information from solvation dynamics experiment. For example, Coumarin 153 (C153) is a standard fluorescence probe that has been used in solvation dynamics studies.^{80,94,96,101} C153 is a reasonably rigid molecule with high fluorescence quantum yield and undergoes a large change in its dipole moment on photoexcitation.⁹⁴ Only a single excited state (S_1 state) of intramolecular charge transfer character is responsible for the fluorescence of this dye.⁹⁴ Thus, complications arising due to the participation of multiple fluorescent states, as happens with many probe molecules, can be avoided with C153.

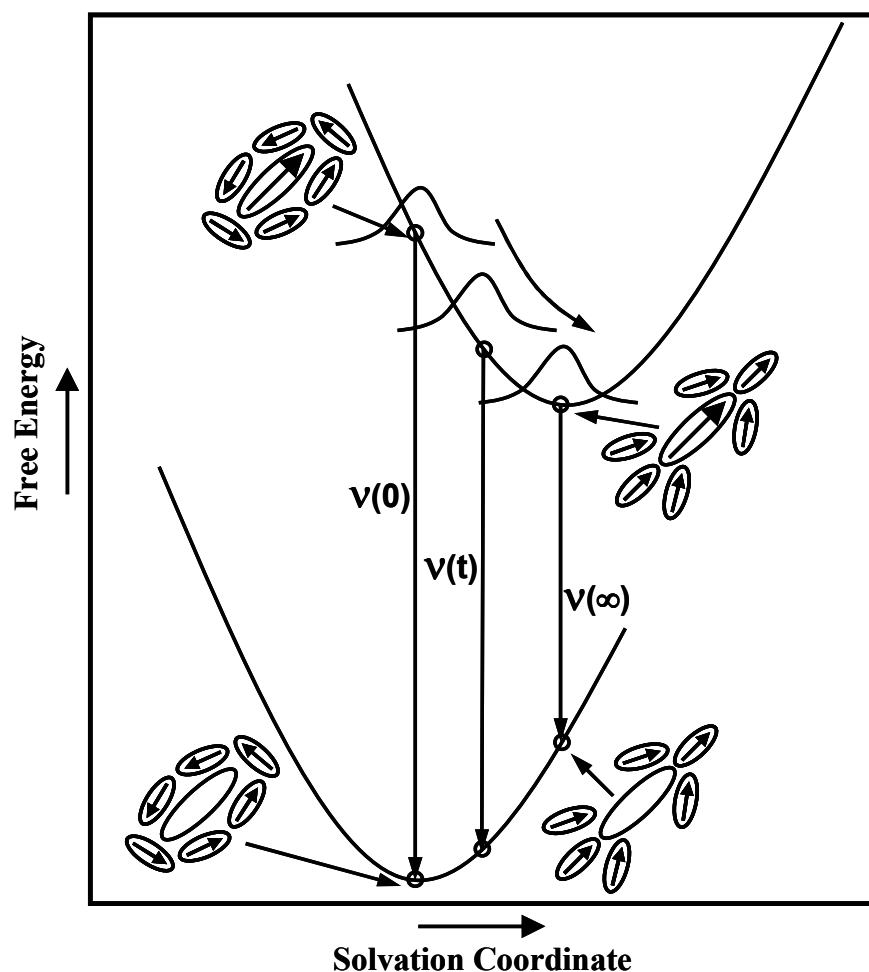


Figure 2.21. A schematic representation of electronic transition involved in a typical time-resolved fluorescence experiment measuring solvation dynamics. A short laser pulse excites the probe molecule from S_0 to S_1 . Since the electronic transition is fast compared to nuclear motions of the solvent, an excited state with a solvent environment that is characteristic of equilibrium in S_0 is initially prepared. The solvents reorganize over time along the solvation coordinate in order to lower the solvation energy in the excited state. This relaxation can be followed by measuring the fluorescence of the probe as a function of time after excitation.

The observed dynamic Stokes shift is represented by a correlation function, $C(t)$, defined as⁸¹

$$C(t) = \frac{\nu(t) - \nu(\infty)}{\nu(0) - \nu(\infty)} \quad (2.84)$$

where $\nu(t)$, $\nu(0)$ and $\nu(\infty)$ are the emission maxima at time t , zero and infinity, respectively.

It is clear from eq 2.84 that $C(t)$ equals to 1 at $t = 0$ and decays to 0 as $t \rightarrow \infty$. Thus, the time-dependent behavior of $C(t)$ provides a means of quantifying the relaxation of the surrounding environment on a microscopic level. The solute-solvent interaction energy as function of time, $E(t)$, fluctuates rapidly about some average value $\langle E \rangle$. The time dependence of these fluctuations is $\delta E(t) = E(t) - \langle E \rangle$. Thus, one can follow the “solvation dynamics” by calculating the time correlation function, $\langle \delta E(0) \delta E(t) \rangle$, which is the ensemble averaged (“ $\langle \dots \rangle$ ”) behavior of these fluctuations. When the solvent response is linear to the external perturbation, the non-equilibrium correlation function, $C(t)$, is equivalent equilibrium correlation function, $C_{\Delta E}(t)$:⁹⁷

$$C(t) \cong C_{\Delta E}(t) = \frac{\langle \delta \Delta E(0) \delta \Delta E(t) \rangle}{\langle \delta \Delta E^2 \rangle} = \frac{\langle \delta v(0) \delta v(t) \rangle}{\langle \delta v^2 \rangle} \quad (2.85)$$

The solvation correlation function, $C(t)$ is typically not a single exponential. Details of molecular motions are important in order to understand the multi-exponential relaxation. Solvation of newly created charge distribution in the excited state of a solute molecule surrounding dipolar molecules involves primarily librational (hindered rotation, a high frequency mode), rotational and translational motion (including intermolecular vibrations) of the dipolar solvent molecules. All these motions generally determine the final organized structure of solvent molecules around the excited dipole of solute. Contribution from electronic polarization that can be estimated from polarizability of the solvent molecules may also be significant part of the total solvation energy. Therefore, the time scales of solvation dynamics can be very wide. For example, the electronic, high frequency vibration and libration motions are very fast (≤ 100 fs). However, translational (low frequency vibration, diffusive translation) and rotational (diffusive rotation) motions can be significantly

slower.¹⁰²

Jimenez et al.⁹⁵ reported excited-state solvation dynamics of Coumarin 343 (dye) in water. The experimental $C(t)$ in water is fitted by $C(t) = a_g e^{-\frac{1}{2}\omega_g^2 t^2} + a_1 e^{-\frac{t}{\tau_2}} + a_2 e^{-\frac{t}{\tau_3}}$ with a Gaussian component ($\omega_g = 38.5 \text{ ps}^{-1}$, 48% of the total amplitude) and a slower biexponential decay with $\tau_2 = 126 \text{ fs}$ (20%) and $\tau_3 = 880 \text{ fs}$ (35%). The ultrafast solvation is attributed to the high frequency intermolecular vibrational or librational motions of water. The solvation dynamics of methanol is also nonexponential and shows an ultrafast component of 30 fs with a contribution of 20% to $C(t)$.¹⁰³ It was concluded that the O—H librational motion is responsible for the initial 30 fs decay. Molecular dynamic simulations of solvation dynamics water and methanol have also shown that the relaxation contains a large contribution (~50%) from a very rapid (sub ~100 fs) underdamped, inertial response.^{83,103}

$C(t)$ can also be calculated theoretically using the frequency-dependent dielectric response $\varepsilon(\omega)$ of the solvent. Briefly, in dielectric continuum model, the solvent is treated as structureless fluids with a frequency-dependent dielectric constant, $\varepsilon(\omega)$, represented in the Debye equation¹⁰⁴⁻¹⁰⁶ as

$$\varepsilon(\omega) = \varepsilon_\infty + \frac{\varepsilon_0 - \varepsilon_\infty}{1 + i\omega\tau_D} \quad (2.86)$$

where ε_0 and ε_∞ are the static and optical frequency dielectric constants of the liquid, respectively. τ_D is Debye relaxation time, which is a measure of the time it takes for the polarization of a macroscopic sample of liquid to decay to zero after the electric field has been turned off. In this model the $C(t)$ is given by⁹⁴

$$C(t) = e^{-t/\tau_L} \quad (2.87)$$

This shows that $C(t)$ decays single-exponentially with a lifetime of $\tau_L = \varepsilon_\infty \tau_D / \varepsilon_0$. The assumption of Debye form of the frequency-dependent dielectric response $\varepsilon(\omega)$ may over simplify the solvent. Majority of the solvents show complex dielectric response than given in eqs 2.88 to 2.90. In practice, one can use one of the following three forms of $\varepsilon(\omega)$ to describe the experimental data.⁴²

$$\varepsilon(\omega) = \varepsilon_\infty + \sum_j^n \frac{\varepsilon_{0j} - \varepsilon_{\infty j}}{1 + i\omega\tau_{Dj}} \quad \text{Multiple Debye} \quad (2.88)$$

$$\varepsilon(\omega) = \varepsilon_\infty + \frac{\varepsilon_0 - \varepsilon_\infty}{(1 + i\omega\tau_0)^\beta} \quad \text{Davidson-Cole} \quad (2.89)$$

$$\varepsilon(\omega) = \varepsilon_\infty + \frac{\varepsilon_0 - \varepsilon_\infty}{1 + (i\omega\tau_D)^{1-\alpha}} \quad \text{Cole-Cole} \quad (2.90)$$

For instance, dielectric response of normal alcohols is generally expressed in terms of multiple Debye form⁹⁴ and $C(t)$ is represented by multi-exponential decay function

$$C(t) = \sum_j a_j e^{-t/\tau_{Fj}} \quad (2.91)$$

with $\tau_{Fj} = \left(\frac{2\varepsilon_{\infty j} + \varepsilon_c}{2\varepsilon_{0j} + \varepsilon_c} \right) \tau_{Dj}$ and relative amplitude, $a_j \propto \frac{(\varepsilon_{0j} - \varepsilon_{\infty j})}{(2\varepsilon_{\infty j} + \varepsilon_c)(2\varepsilon_{0j} + \varepsilon_c)}$. Here ε_c is

dielectric constant of the cavity surrounding the probe.

Data Analysis

Construction of Time-Resolved Emission Spectra (TRES)

Determination of time-resolved emission spectra (TRES) is the most general and precise way to quantitatively describe the solvation response function, $C(t)$. The TRES at a given time t is calculated from wavelength-dependent time-resolved fluorescence decays by relative normalization to the steady-state spectrum. Deconvoluted fluorescence decay using

instrument response function at each wavelength is represented by multiexponential function^{107,108}

$$D(\lambda, t) = \sum_i a_i(\lambda) e^{-\frac{t}{\tau_i(\lambda)}} \quad (2.92)$$

where $a(\lambda)$ and $\tau(\lambda)$ are the pre-exponential factor and time constant at a particular wavelength λ . The wavelength-dependent steady-state normalized fluorescence decay function, $S(\lambda, t)$ is defined as

$$S(\lambda, t) = A(\lambda) D(\lambda, t) \quad (2.93)$$

where $A(\lambda)$ is the normalization constant. The pre-exponential factors (a_i) in eq 2.92 are relative to each other, but not absolute. Absolute pre-exponential factor is obtained when they are normalized to steady-state intensity $S_0(\lambda)$. $S_0(\lambda)$ is given by

$$S_0(\lambda) = \int_0^{\infty} S(\lambda, t) dt = A(\lambda) \int_0^{\infty} D(\lambda, t) dt = A(\lambda) \sum_i a_i(\lambda) \tau_i(\lambda) \quad (2.94)$$

This leads to the normalization constant, $A(\lambda)$

$$A(\lambda) = \frac{S_0(\lambda)}{\sum_i a_i(\lambda) \tau_i(\lambda)} \quad (2.95)$$

Thus, the fluorescence emission intensity at any wavelength (λ) and time (t) can easily be calculated using the eq 2.96.^{83,94}

$$S(\lambda, t) = \frac{S_0(\lambda)}{\int_0^{\infty} D(\lambda, t) dt} D(\lambda, t) = \frac{S_0(\lambda)}{\sum_i a_i(\lambda) \tau_i(\lambda)} \sum_i a_i(\lambda) e^{-\frac{t}{\tau_i(\lambda)}} \quad (2.96)$$

Log-Normal Fitting Equation

The emission maximum frequencies, $\nu(t)$ are usually determined by fitting the points

in TRES at different times to the log-normal line shape function, $G(\nu)$. The $G(\nu)$ is defined as⁹⁴

$$G(\nu) = \begin{cases} G_0 \exp\left\{-\ln(2)\left(\frac{\ln[1+\alpha]}{b}\right)^2\right\} & \text{for } \alpha > 1 \\ 0 & \text{for } \alpha \leq 1 \end{cases} \quad (2.97)$$

where $\alpha = \frac{2b(\nu - \nu_p)}{\Delta}$. Here, G_0 , b and ν_p denote the peak height, asymmetry factor and peak frequency, respectively. The full width at half maximum (FWHM) Γ , and the width, Δ of this function are related by

$$\Gamma = \Delta \left(\frac{\sinh(b)}{b} \right) \quad (2.98)$$

Estimation of the Time Zero Spectrum

The time-zero spectrum is the hypothetical spectrum that would be observed for a solute that has completely relaxed vibrationally but before any relaxation of the solvent has occurred.¹⁰⁹ This is based on the fact that intramolecular vibrational relaxation occurs on much faster time scale (sub 100 fs) compared to solvent relaxation. This indicates that the shift between absorption and emission spectra of a solute before solvation takes place should be equal to the Stokes shift of the same solute in a non-polar solvent.

The basic idea is that a molecule has an intrinsic spectral absorption $g(\nu)$ and an emission line-shape $f(\nu)$. These line shapes are related to the absorption (A_{np}) and emission spectra (F_{np}) of the molecule in a non-polar solvent by

$$g(\nu) \propto \nu^{-1} A_{np}(\nu) \quad (2.99)$$

$$f(\nu) \propto \nu^{-3} F_{np}(\nu) \quad (2.100)$$

These line shapes functions can be used to calculate the absorption and emission spectra of the molecules in an inhomogenously broadened environment. The solvent molecules, distributed around the solute molecule, cause a broadening (σ) and a shift (δ_0) of the line shape function due to solvent-solute interactions. Assuming a Gaussian distribution $p(\delta)$ of solvent molecules, these effects can be described as a convolution of the line shape function $g(\nu)$ with the solvent distribution function $p(\nu)$. Based on this assumption, the absorption spectrum in a polar solvent can be written as

$$A_p(\nu) \propto \nu \int g(\nu - \delta)p(\delta)d\delta \quad (2.101)$$

where $p(\delta) = (2\pi\sigma^2)^{-1/2} \exp[-(\delta - \delta_0)^2 / 2\sigma^2]$. Similarly, the time-zero emission spectrum immediately after monochromatic excitation (ν_{ex}) in a polar solvent can be expressed as

$$F_p(\nu, t = 0; \nu_{ex}) \propto \nu^3 \nu_{ex} \int g(\nu_{ex} - \delta)p(\delta)f(\nu - \delta)k_{rad}(\delta)d\delta \quad (2.102)$$

Here, $\nu_{ex}g$ is essentially proportional to the measured absorption spectrum; ν^3f is proportional to the emitted quantum distribution over wavenumbers. The k_{rad} is the radiative constant. The terms, $f(\nu - \delta)k_{rad}(\delta)$ leads to emission intensity function and $g(\nu - \delta)p(\delta)$ to convolution of the solvent distribution initially transferred to the excited state. $g(\nu)$ and $f(\nu)$ are obtained from the absorption and emission spectra in a non-polar solvent. The broadening and shift by the solvent which define distribution function, $p(\delta)$, are determined as a set that yields closest match with the absorption spectra in an polar solvent of interest when convoluted with $g(\nu)$.

The radiative rate function is calculated with shift using

$$k_{rad}(\delta) \propto \frac{\int f(\nu - \delta)\nu^3 d\nu}{\int f(\nu - \delta)d\nu} \quad (2.103)$$

Construction of Solvation Correlation Function

Solvation dynamics are analyzed and quantified by means of the solvation correlation function, $C(t)$,

$$C(t) = \frac{\nu(t) - \nu(\infty)}{\nu(0) - \nu(\infty)} \quad (2.104)$$

where $\nu(0)$, $\nu(t)$ and $\nu(\infty)$ denote the peak frequency of the emission spectra at time zero, t and infinity. The “zero time” emission spectrum is obtained according to the method of Fee and Maroncelli.¹⁰⁹ The $\nu(\infty)$ is taken as the peak frequency of the steady-state fluorescence spectrum. The $\nu(t)$ is determined by taking the maxima from the log-normal fits as the time-resolved emission maximum which is constructed according to the procedure described by eq 2.96 using steady-state emission spectrum and fitting parameters from wavelength-resolved decay traces. In most cases, however, the broad spectra result in uncertainty in the exact position of the emission maxima. Thus, using the signal-to-noise ratio and width of the spectrum (including “zero-time”, steady-state, or time-resolved emission spectrum) as guides, we have determined the typical uncertainties as follows: time-resolved emission $\sim \pm 200 \text{ cm}^{-1}$, “zero-time” and steady-state $\sim \pm 100 \text{ cm}^{-1}$. These uncertainties are used to compute error bars for the $C(t)$. The fractional solvation at any time, t is calculated using $f_t = 1 - C(t)$.

References

- (1) Lakowicz, J. R. *Principles of fluorescence spectroscopy*, 3rd ed.; Springer: New York, 2004.
- (2) Fleming, G. R. *Chemical Applications of Ultrafast Spectroscopy*; Oxford University Press: London, 1986.

- (3) *Fluorescence Spectroscopy in Biology: Advanced Methods and their Applications to Membranes, Proteins, DNA, and Cells* Hof, M.; Hutterer, R.; Fidler, V.; Fidler, V., Eds.; Springer: Berlin, 2005; Vol. 3.
- (4) *Floromax Spectrophotometer: Operation and Maintenance*; SPEX Industries Inc.: Edison, N.J., 1990.
- (5) Wgger, S. W.; Ghiggino, K. P.; Meilak, G. A.; Verity, B. *J. Chem. Edu.* **1992**, *69*, 675.
- (6) Svelto, O. *Principles of lasers*, 4th ed.; Plenum Press: New York, 1998.
- (7) Becker, W. *Advanced time-correlated single photon counting techniques*; Springer: Berlin ; New York, 2005.
- (8) Silfvast, W. T. *Laser fundamentals*, 2nd ed.; Cambridge University Press: Cambridge, UK ; New York, 2005.
- (9) Optical Properties. In *Springer handbook of materials measurement methods*; Czichos, H., Saito, T., Smith, L., Eds.; Springer, 2006; pp 531.
- (10) Wilson, J.; Hawkes, J. F. B. *Lasers, principles and applications*; Prentice Hall: New York, 1987.
- (11) Abramczyk, H. *Introduction to laser spectroscopy*; Elsevier: Amsterdam & Boston, 2005.
- (12) *Optical Angular Momentum* Allen, L.; Barnett, S. M.; Padgett, M. J., Eds.; Institute of Physics Pub.: Bristol 2003.
- (13) Siegman, A. E. *Lasers*; University Science Books: Mill Valley, CA, 1986.
- (14) The Diversification of Ultrafast Lasers: The “one-box” concept takes hold. In *Photonics Tech Briefs*, 2001.

- (15) Diels, J.-C.; Rudolph, W. *Ultrashort laser pulse phenomena: fundamentals, techniques, and applications on a femtosecond time scale* 2nd ed.; Academic Press: Burlington, MA, 2006.
- (16) Haus, H. A. *J. Appl. Phys.* **1975**, *46*, 3049.
- (17) Lasers and Coherent Light Sources. In *Springer Handbook of Lasers and Optics*; Träger, F., Ed.; Springer, 2007; pp 586.
- (18) Keller, U. *Nature* **2003**, *424*, 831.
- (19) Steinmeyer, G.; Sutter, D. H.; Gallmann, L.; Matuschek, N.; Keller, U. *Science* **1999**, *286*, 1507.
- (20) Hecht, E. *Optics*, 4th ed.; Addison-Wesley: Reading, Massachusetts, 2002.
- (21) Pedrotti, F. L.; Pedrotti, L. S.; Pedrotti, L. M. *Introduction to optics*, 3rd ed.; Pearson Prentice Hall: Upper Saddle River, N.J., 2007.
- (22) Milonni, P. W.; Eberly, J. H. *Laser Physics* John Wiley & Sons Inc., 2010.
- (23) Reid, G. D.; Wynne, K. Ultrafast Laser Technology and Spectroscopy. In *Encyclopedia of Analytical Chemistry*; John Wiley & Sons Inc.: Chichester, 2000; pp 13644.
- (24) *Femtosecond Laser Pulses*; Rulliere, C., Ed.; Springer: Berlin ; Heidelberg, 2003.
- (25) Martinez, O. E.; Gordon, J. P.; Fork, R. L. *J. Opt. Soc. Am. A* **1984**, *1*, 1003.
- (26) Huang, C. P.; Asaki, M. T.; Backus, S.; Murnane, M. M.; Kapteyn, H. C. *Opt. Lett.* **1992**, *17*, 1289.
- (27) Quimby, R. S. *Photonics and lasers : an introduction*; Wiley-Interscience: ken, N.J., 2006.

- (28) Ghatak, A.; Thyagarajan, K. *Optical electronics*; Cambridge University Press: Cambridge ; New York 1989.
- (29) Rosencher, E.; Vinter, B. *Optoelectronics*; Cambridge University Press: Cambridge; New York, 2002.
- (30) Zhang, K.; Li, D. *Electromagnetic theory for microwaves and optoelectronics*, 2nd ed.; Springer: Berlin ; New York, 2008.
- (31) Sutherland, R. L. *Handbook of nonlinear optics*, 2nd ed.; Marcel Dekker, Inc.: New York, 2003.
- (32) Gou, Y.; Kao, C. K.; Li, E. H.; Chiang, K. S. *Nonlinear photonics : nonlinearities in optics, optoelectronics, and fiber communications*; Chinese University Press/Springer: Hong Kong ; Berlin ; New York, 2002.
- (33) Liu, J.-M. *Photonic devices*; Cambridge University Press: Cambridge ; New York 2005.
- (34) Demtröder, W. *Laser spectroscopy : basic concepts and instrumentation*, 3rd ed.; Springer: Berlin ; New York, 2003.
- (35) Tkachenko, N. V.; Lemmetyinen, H. *Springer Ser. Fluoresc.* **2008**, 5, 195.
- (36) Holzwarth, A. R. *Meth. Enzymol.* **1995**, 246, 334.
- (37) O'Connor, D. V.; Phillips, D. *Time-correlated single photon counting*; Academic Press: Orlando, Florida, 1984.
- (38) Tkachenko, N. V. *Optical spectroscopy : methods and instrumentations*, 1st ed.; Elsevier: Amsterdam ; Boston 2006.
- (39) Ruggiero, A. J.; Todd, D. C.; Fleming, G. R. *J. Am. Chem. Soc.* **1990**, 112, 1003.

- (40) Shah, J. *IEEE J. Quantum Electron.* **1999**, *24*, 276.
- (41) Kahlow, M. A.; Jarzeba, W.; DuBruil, T. P.; Barbara, P. F. *Rev. Sci. Instrum.* **1988**, *59*, 1098.
- (42) Simon, J. D. *Ultrafast dynamics of chemical systems*; Kluwer Academic: Dordrecht ; Boston 1994.
- (43) *Fluorescence spectroscopy*; Brand, L.; Johnson, M. L., Eds.; Elsevier/Academic Press: Amsterdam ; Boston, 2008.
- (44) Eftink, M. R. Fluorescence quenching: theory and applications. In *Topics in Fluorescence Spectroscopy*; Lakowicz, J. R., Ed.; New York: Plenum, 1991; Vol. 2; pp 53.
- (45) Geddes, C. D. *Meas. Sci. Technol.* **2001**, *12*, R53.
- (46) Parker, C. A. *Photoluminescence of solutions*; Elsevier: New York, 1968.
- (47) Valeur, B. *Molecular fluorescence: principles and applications* Wiley-VCH: Weinheim, 2002.
- (48) Dexter, D. L. *J. Chem. Phys.* **1953**, *21*, 836.
- (49) Förster, T. *Ann. Phys.* **1948**, *2*, 55.
- (50) Stryer, L.; Haugland, P. R. *Proc. Nat. Acad. Sci.* **1967**, *58*, 719.
- (51) Gilbert, A.; Baggott, J. *Essentials of molecular Photochemistry*, 3rd ed.; CRC Press: Boca Raton 1991.
- (52) Clegg, R. Fluorescence Resonance Energy Transfer. In *Fluorescence Imaging Spectroscopy and Microscopy*; Wang, X. F., Herman, B., Eds.; John Wiley & Sons Inc, 1996.
- (53) Matyus, L. *J. Photochem. Photobiol. B* **1992**, *12*, 323.
- (54) Bottiroli, G.; Croce, A. C.; Ramponi, R. *J. Photochem. Photobiol. B* **1992**, *12*, 413.

- (55) Stryer, L.; Thomas, D. D.; Meares, C. F. *Annu. Rev. Biophys. Bioeng.* **1982**, *11*, 203.
- (56) Herman, B. *Methods Cell Biol.* **1989**, *30*, 219.
- (57) Jovin, T. M.; Arndt-Jovin, D. J. *Annu. Rev. Biophys. Biophys. Chem.* **1989**, *18*, 271.
- (58) Matayoshi, E. D.; G.T., W.; A., K. G.; Ericson, J. *Science* **1990**, *247*, 954.
- (59) Taylor, D. L.; Reidler, J.; Spudich, J. A.; Stryer, L. *J. Cell Biol.* **1981**, *89*, 363.
- (60) Mann, T. L.; Krull, U. J. *Analyst* **2003**, *128*, 313.
- (61) Jameson, D. M.; Seifreid, S. E. *Methods* **1999**, *19*, 222.
- (62) Fleming, G. R.; Morris, J. M.; Robinson, G. W. *Chem. Phys.* **1976**, *17*, 91.
- (63) Van Holde, K. E.; Johnson, W. C.; Ho, P. S.; Prentice Hall: New Jersey, 1998.
- (64) Schröder, G. F.; Alexiev, U.; Grubmuller, H. *Biophys. J.* **2005**, *89*, 3757.
- (65) Fleming, G. R.; Knight, A. E. W.; Morris, J. M.; Robbins, R. J.; Robinson, G. W. *Chem. Phys. Lett.* **1977**, *51*, 399.
- (66) Sadkowski, P. J.; Fleming, G. R. *Chem. Phys. Lett.* **1978**, *57*, 526.
- (67) Dutt, G. B.; Doraiswamy, S.; Periasamy, N.; Venkataraman, B. *J. Chem. Phys.* **1990**, *93*, 8498.
- (68) Dutt, G. B.; Doraiswamy, S.; Periasamy, N. *J. Chem. Phys.* **1991**, *94*, 5360.
- (69) Roy, M.; Doraiswamy, S. *J. Chem. Phys.* **1993**, *98*, 3213.
- (70) Weber, G. *J. Chem. Phys.* **1977**, *66*, 4081.
- (71) Kim, Y. R.; Hochstrasser, R. M. *J. Phys. Chem.* **1992**, *96*, 9595.
- (72) Christensen, R. L.; Drake, R. C.; Phillips, D. *J. Phys. Chem.* **1986**, *90*, 5960.

- (73) Maiti, N. C.; Krishna, M. M. G.; Britto, P. J.; Periasamy, N. *J. Phys. Chem. B* **1997**, *101*, 11051.
- (74) Fleming, G. R.; Wolynes, P. G. *Phys. Today* **1990**, *43*, 36.
- (75) Barbara, P. F.; Jarzeba, W. Ultrafast Photochemical Intramolecular Charge Transfer and Excited State Solvation. In *Advances in Photochemistry*; Volman, D. H., Hammond, G. S., Gollnick, K., Eds.; John Wiley & Sons Inc., 1990.
- (76) Kahlow, M. A.; Jarzeba, W.; Kang, T. J.; Barbara, P. F. *J. Chem. Phys.* **1989**, *90*, 151.
- (77) Barbara, P. F.; Jarzeba, W. *Acc. Chem. Res.* **1988**, *21*, 195.
- (78) Hynes, T. J. *Annu. Rev. Phys. Chem.* **1985**, *36*, 573.
- (79) Hynes, J. T. Charge Transfer Reactions and Solvation Dynamics. In *Ultrafast Dynamics of Chemical Systems*, 1994; Vol. 7; pp 345.
- (80) Maroncelli, M.; Macinnis, J.; Fleming, G. R. *Science* **1989**, *243*, 1674.
- (81) Maroncelli, M. *J. Mol. Liq.* **1993**, *57*, 1.
- (82) Bagchi, B.; Chandra, A. *Adv. Chem. Phys.* **1991**, *80*, 1.
- (83) Maroncelli, M.; Fleming, G. R. *J. Chem. Phys.* **1988**, *89*, 5044.
- (84) Bader, J. S.; Chandler, D. *Chem. Phys. Lett.* **1989**, *157*, 501.
- (85) Bader, J. S.; Chandler, D. *Chem. Phys. Lett.* **1989**, *157*, 501.
- (86) Maroncelli, M. *J. Chem. Phys.* **1991**, *94*, 2084.
- (87) Carter, E. A.; Hynes, J. T. *J. Chem. Phys.* **1991**, *94*, 5961.
- (88) Hynes, T. J. *J. Phys. Chem.* **1986**, *90*, 3701.
- (89) Zusman, L. D. *Chem. Phys.* **1988**, *119*, 51.

- (90) Tominaga, K.; Walker, G. C.; Jaxzeba, W.; Barbara, P. F. *J. Phys. Chem.* **1991**, *95*, 10475.
- (91) Weaver, M. J.; McManis, G. E.; Jarzeba, W.; Barbara, F. P. *J. Phys. Chem.* **1990**, *94*, 1715.
- (92) Zichi, D. A.; Ciccotti, G.; Hynes, J. T.; Ferrario, M. *J. Phys. Chem.* **1989**, *93*, 6261.
- (93) Hynes, J. T.; Carter, E. A.; Ciccotti, G.; Kim, H. J.; Zichi, D. A.; Ferrario, M.; Katpral, R. In *Perspectives in Photosynthesis*; Jortner, J., Pullnan, B., Eds.; Kluwer Academic: Dordrecht, the Netherlands, 1990.
- (94) Maroncelli, M.; Fleming, G. R. *J. Chem. Phys.* **1987**, *86*, 6221.
- (95) Jimenez, R.; Fleming, G. R.; Kumar, P. V.; Maroncelli, M. *Nature* **1994**, *369*, 471.
- (96) Horng, M. L.; Gardecki, J. A.; Papazyan, A.; Maroncelli, M. *J. Phys. Chem.* **1995**, *99*, 17311.
- (97) Stratt, R. M.; Maroncelli, M. *J. Phys. Chem.* **1996**, *100*, 12981.
- (98) Kahlow, M. A.; Kang, T. J.; Barbara, F. P. *J. Chem. Phys.* **1988**, *88*, 2372.
- (99) Nagarajan, V.; Brearley, A. M.; Kang, T. J.; Barbara, F. P. *J. Chem. Phys.* **1987**, *86*, 3183.
- (100) Simon, J. D. *Acc. Chem. Res.* **1988**, *21*, 128.
- (101) Chapman, C. F.; Maroncelli, M. *J. Phys. Chem.* **1991**, *95*, 9095.
- (102) Bagchi, B.; Jana, B. *Chem. Soc. Rev.* **2010**, *39*, 1936.
- (103) Rosenthal, S. J.; Jimenez, R.; Fleming, G. R.; Kumar, P. V.; Maroncelli, M. *J. Mol. Liq.* **1994**, *60*, 25.

- (104) Fröhlich, H. *Theory of Dielectrics*, 2nd ed.; Oxford University Press: New York, 1986.
- (105) Kivelson, D.; Madden, P. A. *Annu. Rev. Phys. Chem.* **1980**, *31*, 523.
- (106) Debye, P. *Polar Molecules*; Chemical Catalog Co.: New York, 1929.
- (107) Lakowicz, J. R.; Laczko, G.; Cherek, H.; Gratton, E.; Limkeman, M. *Biophys. J.* **1984**, *46*, 463.
- (108) Lakowicz, J. R.; Gratton, E.; Cherek, H.; Maliwal, B. P.; Laczko, G. *J. Biol. Chem.* **1984**, *259*, 10967.
- (109) Fee, R. S.; Maroncelli, M. *Chem. Phys.* **1994**, *183*, 235.

CHAPTER 3. ACCUMULATION AND INTERACTION OF HYPERICIN IN LOW DENSITY LIPOPROTEIN (LDL) — A PHOTOPHYSICAL STUDY

A paper published in the *Photochemistry and Photobiology*

Prasun Mukherjee¹, Ramkrishna Adhikary¹, Mintu Halder^{1,2}, Jacob W. Petrich^{1,*},
and Pavol Miskovsky^{3,*}

Abstract

The accumulation and interaction of hypericin with the biologically important macromolecule, LDL, is investigated using various steady-state and time-resolved fluorescence measurements. It is concluded that multiple hypericins can penetrate considerably deeply into the LDL molecule. Up to ~ 20 nonaggregated hypericin molecules can enter LDL; but upon increasing the hypericin concentration, the fluorescence lifetime of hypericin decreases drastically, suggesting most likely the self quenching of aggregated hypericin. There is also evidence of energy transfer from tryptophans of the constituent protein, apoB-100, to hypericin in LDL. The results demonstrate the ability of LDL to solubilize hypericin (a known photosensitizer) in nonaggregated form, which has

Reprinted with permission from *Photochemistry and Photobiology*, 2008, 84(3), 706-712.

¹Department of Chemistry, Iowa State University, 50011 USA.

²Department of Chemistry, Indian Institute of Technology, Kharagpur, West Bengal, 721302, India.

³Department of Biophysics, P. J. Safarik University, Jesenna 5, 04154 Kosice and International Laser Center, Ilkovicova 3, Bratislava, Slovak Republic.

*To whom correspondence should be addressed.

implications for the construction of drug delivery systems.

Introduction

Hypericin (Figure 3.1) is a major component of the botanical dietary supplement, St. John's Wort. It is a widely spread, naturally occurring perylene quinone pigment that is of great interest because of its broad spectrum of light-induced biological activities.¹⁻⁴ Here, we investigate the interaction of hypericin with the biologically important complex, low density lipoprotein (LDL). LDL is the main carrier of cholesterol in the human circulatory system. It can be characterized as a spherical particle having three different regions: the outer surface layer, the core region, and an interfacial region between these two. The surface monolayer mainly consists of phospholipid molecules and a single molecule of the protein, apoB-100, (one of the largest monomeric proteins known) which consists of 4536 amino acid residues, and the core of LDL is enriched with triglycerides and cholesteryl esters.^{5,6} The biological activity of hypericin and its analogs depends on light. This activity and the underlying photophysics have been the subject of numerous reviews.^{1,4,7-12}

In the biological context, we have extensively studied the interaction of hypericin with proteins such as human serum albumin (HSA)¹³ and two different isoforms of glutathione S-transferase (GST), HA1-1 and HP1-1.¹⁴ These studies reveal that hypericin forms a rigid complex with these proteins. Upon its incorporation in the blood, it interacts mainly with LDL and to a lesser extent with HAS.¹⁵ There are also numerous examples of interactions of photosensitizers with serum proteins and LDL.¹⁶⁻²⁴ Miskovsky and coworkers have studied hypericin binding to LDL using steady-state fluorescence measurements.²⁵ They concluded that multiple hypericins interact with LDL, most likely through a nonspecific interaction with the lipid part of LDL. The quenching of tryptophan fluorescence

emission with increase in hypericin concentration prompted the authors to conclude that the hypericin molecules reside somewhere near the apoB-100 part of the LDL; and, based on these observations, they proposed that hypericin accumulates at the interfacial region of the LDL molecule: i.e., between the surface and the core regions. In this work, we continue the investigation of the location of hypericin in LDL by exploiting fluorescence quenching and time-resolved fluorescence measurements. Our results are consistent with theirs.

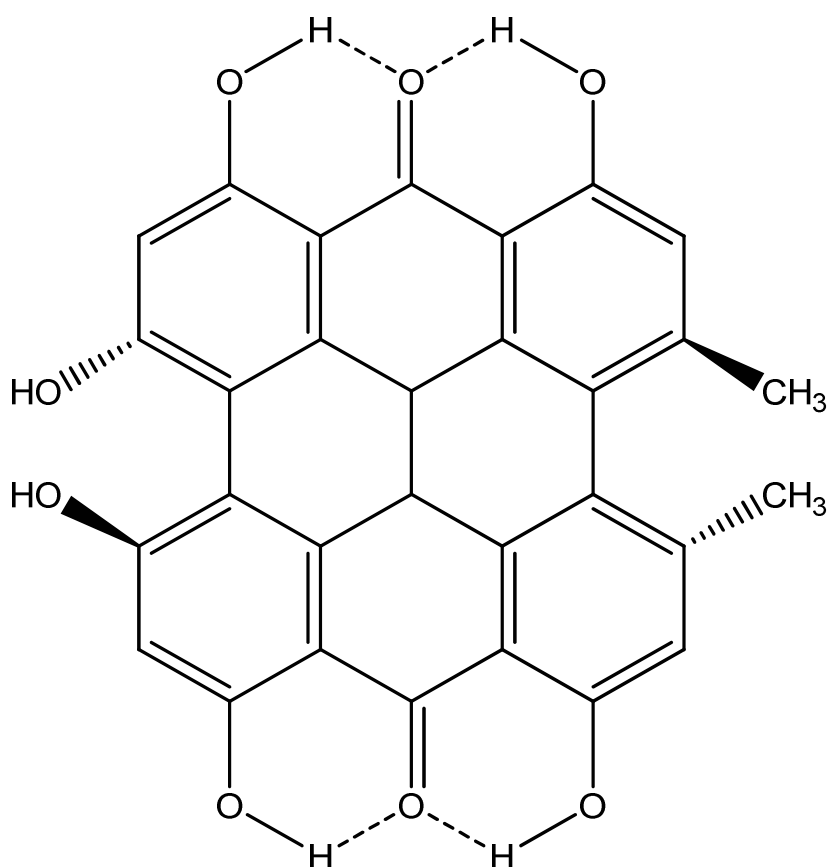


Figure 3.1. Structure of hypericin (7,14 normal form).

Materials and Methods

Hypericin was purchased from Molecular Probes (Eugene, Oregon, USA) and used without further purification. Low density lipoprotein (LDL) (purity > 95 % of total lipoprotein content by electrophoresis) was purchased from Calbiochem.

Steady-State and Time-Resolved Measurements. Steady-state absorption spectra were obtained on Hewlett Packard 8453 UV-visible spectrophotometer with 1-nm resolution. Steady state fluorescence spectra were obtained on a Spex Fluoromax-2 with a 3-nm bandpass and corrected for lamp spectral intensity and detector response. For both fluorescence and absorption measurements, a 3-mm path-length quartz cuvette was used. All experiments were done at room temperature.

The apparatus for time correlated single photon counting is described elsewhere.²⁶ Briefly, the fundamental from the home-made mode-locked Ti-sapphire oscillator was modulated by a Pockels cell (Model 350-160, Conoptics Inc) to reduce the repetition rate. The excitation source (266 nm) was generated by sum frequency generation of the fundamental red light (~ 800 nm) and the second harmonic blue light (~ 400 nm) using U-Oplaz Technologies (Model TP-2000B). Fluorescence decay traces were recorded by exciting the sample at 266 nm or at 407 nm and collecting the emission of tryptophan or hypericin using appropriate cut-off filters. For fluorescence lifetime measurements typically ~ 3000 - 5000 counts were collected at the peak channel. The polarized fluorescence traces of hypericin were used to obtain fluorescence anisotropy decay parameters collected to a maximum of ~ 10000 counts at the peak channel. For LDL/buffer system ~ 6000 counts were collected at the peak channel. Fits were considered acceptable for $\chi^2 \leq 1.3$.

Sample preparation. A hypericin stock solution in DMSO was used for sample preparation. The total organic content of the final sample solution was kept < 1% for all solutions containing LDL in phosphate buffer (pH 7.0). The hypericin/LDL solutions were equilibrated for about 12 hours in the dark prior to steady state and time resolved experiments. For steady state fluorescence measurements, the solutions were prepared

having [LDL] $\sim 1 \times 10^{-7}$ M with varying amounts of hypericin corresponding to [Hyp] $\sim 1 \times 10^{-7}$ M (1:1 LDL to hypericin) - 3×10^{-6} M (1:30 LDL to hypericin). For time-resolved fluorescence studies, [LDL] was maintained at $\sim 5 \times 10^{-7}$ M and [Hyp] was varied from $\sim 5 \times 10^{-7}$ (corresponding to 1:1 LDL to hypericin) to 1.5×10^{-5} M (corresponding to 1:30 LDL to hypericin).

Preparation of solutions for Stern-Volmer quenching experiments. For quenching of hypericin in DMSO, two stock solutions were prepared of concentrations 1×10^{-5} M hypericin in DMSO and 2 M potassium iodide in DMSO. For all measurements, hypericin concentrations were kept constant at 1×10^{-7} M. Nine solutions were prepared with increasing quencher concentration from 0 to 1.2 M. Similar quenching experiments were performed in LDL:Hyp = 1:1 complex by preparing three stock solutions of concentrations 1×10^{-5} M, 1×10^{-5} M and 2 M, of hypericin in DMSO, LDL in pH 7 phosphate buffer and potassium iodide in water. For experiments with LDL:Hyp = 1:30 complex the concentration of stock solution of hypericin in DMSO was changed to 3×10^{-4} M. For all measurements, hypericin and LDL concentrations were kept constant at 1×10^{-7} M (for the 1:1 complex) or 3×10^{-6} M (for the 1:30 complex) and 1×10^{-7} M. Six or seven solutions were prepared with increasing quencher concentration from 0 to 1.6 M for LDL:Hyp = 1:1 and from 0 to 1 M for LDL:Hyp = 1:30. Samples were excited at 550 nm for taking the emission spectra.

Results and Discussion

Steady-state experiments

Hypericin in aqueous physiological solution is aggregated^{27,28}, and binding with

biological macromolecules helps to solubilize it in monomeric form, which is believed to be important for virucidal action. For example, Burel and Jardon have noted that the photodynamic properties of hypericin are greatly diminished when it is aggregated.²⁹ Upon interacting with LDL, the emission intensity of hypericin increases drastically and the emission spectrum closely resembles that of hypericin in bulk organic solvents—e.g., the peak maximum is only ~2 nm blue shifted with respect to that of DMSO. In the following sections we discuss the results obtained from different experiments which help us to predict the possible location of hypericin in LDL.

Stern-Volmer quenching by Γ^- ion

The quenching of hypericin fluorescence by Γ^- is shown in Figure 3.2. The very inefficient quenching in LDL/Hyp = 1:1 complex ($K_{sv} = 0.25 \text{ M}^{-1}$) as compared to Hyp/DMSO ($K_{sv} = 5 \text{ M}^{-1}$) indicates that hypericin is not exposed to the surface of LDL and is buried sufficiently deeply inside the LDL molecule so as to become inaccessible by Γ^- ion. To evaluate the possibility of incorporation of multiple hypericin inside one LDL molecule we undertook similar quenching experiment in LDL:Hyp = 1:30 complex. Most interestingly for this complex the K_{sv} value was found to be 0.75 M^{-1} , larger than that for the 1:1 complex, suggesting that some of the accumulated hypericins are nearer to the surface than in the 1:1 complex. To the extent that the data for the 1:30 complex are genuinely nonlinear, as they seem to be from Figure 3.2, they may be analyzed in terms of a nonlinear Stern-Volmer plot³⁰ which provides the fraction of fluorophores, which are initially accessible to the quencher, f_a , and the intrinsic Stern-Volmer quenching constant. Using such an approach, we obtain 0.42 and 9.2 M^{-1} , respectively, which is consistent with our analysis since the

quenching constant obtained in this manner is similar to that obtained in bulk DMSO.

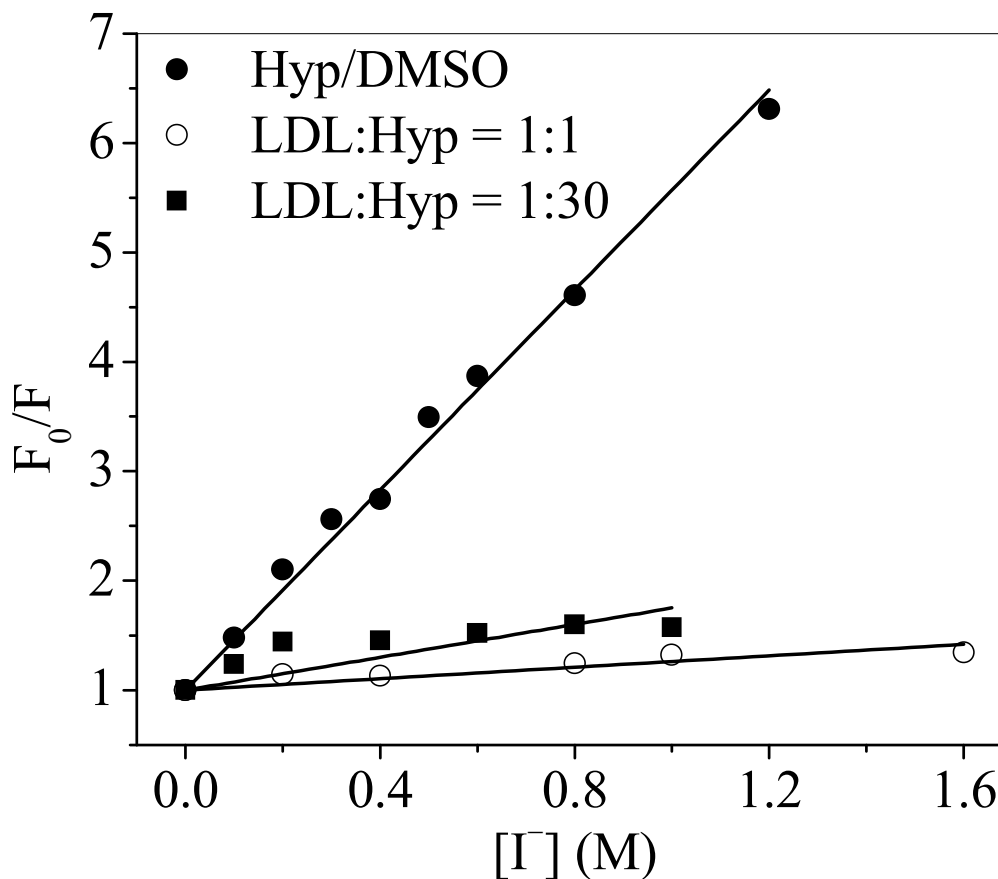


Figure 3.2. Stern-Volmer quenching plot of hypericin in DMSO (solid circles), LDL:hypericin = 1:1 complex (open circles) and LDL:hypericin = 1:30 complex (solid squares) by I^- ion. K_{SV} values for hypericin/DMSO, LDL:hypericin = 1:1 and LDL:hypericin = 1:30 complexes were found to be $5 M^{-1}$, $0.25 M^{-1}$ and $0.75 M^{-1}$, respectively. The very inefficient quenching in LDL/hypericin complexes indicates that hypericin is not located at the LDL surface and that it is inaccessible to iodide. All samples were excited at 550 nm.

Energy transfer from tryptophan to hypericin

There is significant overlap of tryptophan emission and hypericin absorption spectra (Figure 3.3). This facilitates energy transfer from tryptophan to hypericin molecules. Energy

transfer is well-documented for the HSA-hypericin complex.¹³ There are 37 tryptophan molecules in LDL, clearly rendering such a process plausible in this system as well. To evaluate the relative position of hypericin molecules with respect to apoB-100, we studied the energy transfer from tryptophan molecules in apoB-100 to hypericin molecules. With increasing hypericin concentration (going from 0 to 30 molecules of hypericin for each LDL molecule), there is a decrease in tryptophan emission. Consequently, it is reasonable to conclude that there is efficient energy transfer between tryptophan and hypericin. In order to quantify this observation, however, it is necessary to correct the tryptophan emission spectra since hypericin's absorption spectrum overlaps that of tryptophan. Corrected steady-state fluorescence emission spectra of tryptophan and hypericin are shown in Figure 3.4. The decrease of the tryptophan fluorescence quantum yield (10 % decrease in the 1:10 LDL:Hyp complex) and corresponding increase in the hypericin quantum yield (20 % increase in 1:10 LDL:Hyp complex) points toward energy transfer from tryptophan to hypericin molecules. However, for the 1:20 complex the decrease in tryptophan fluorescence quantum yield is more pronounced (20 % decrease for tryptophan). We observe a corresponding increase in hypericin emission when complexed to LDL in LDL:Hyp = 1:20 complex (37 % increase in hypericin emission with respect to that of in DMSO). This suggests that the efficiency of energy transfer increases with increasing hypericin content. The fluorescence quantum yields of tryptophan and hypericin in different systems are shown in Figures 3.4a and 3.4b respectively. Its value in the 1:30 complex is smaller than in the 1:20 complex, suggesting self quenching among hypericin aggregates.

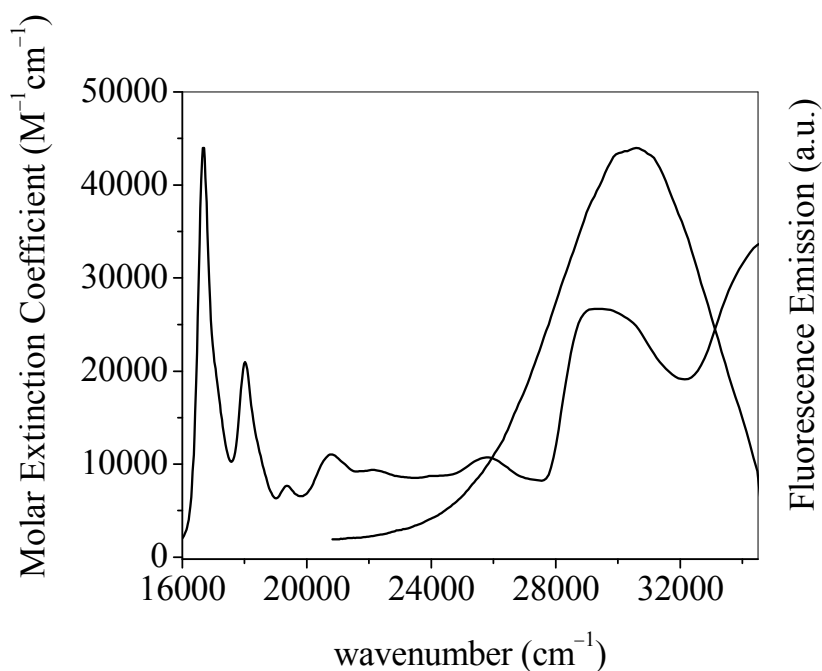


Figure 3.3. Spectral overlap between hypericin absorption and tryptophan emission in the LDL-hypericin complex, suggesting the possibility of energy transfer from tryptophan to hypericin. The calculated R_0 for LDL-hypericin complex is 27 Å (see text). The corresponding value for HSA-hypericin complex is 28 Å, which was incorrectly calculated elsewhere.¹³ The donor spectrum was obtained using a solution of LDL in buffer and its fluorescence quantum yield (for the computation of R_0) was obtained in the absence of hypericin. For the acceptor spectrum we have used the excitation spectrum of hypericin in DMSO, converted to molar extinction coefficient.

Time-resolved fluorescence measurements

Fluorescence lifetime parameters of tryptophan and hypericin with an excitation wavelength of 266 nm are compiled in Tables 3.1 and 3.2. Representative decays are shown in Figure 3.5. There is a decrease in tryptophan fluorescence lifetime with increasing hypericin concentration. This effect is more pronounced in the LDL:Hyp = 1:20 complex than in LDL in buffer (1.2 ns as opposed to 2.3 ns). The decrease in tryptophan lifetime in the presence of hypericin is consistent with energy transfer from tryptophan to hypericin.

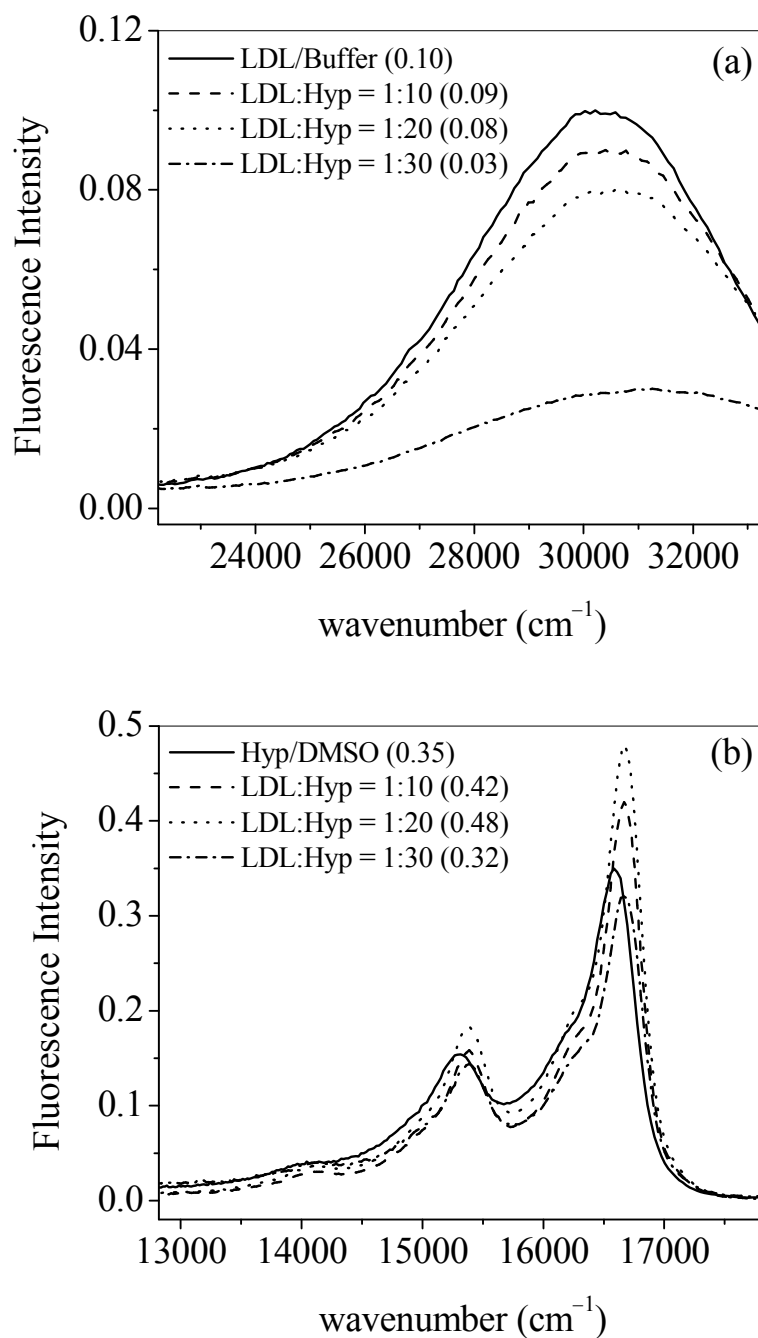


Figure 3.4. Corrected steady-state fluorescence emission spectra of (a) tryptophan and (b) hypericin in different systems. The decrease in tryptophan emission and the corresponding increase in hypericin emission suggest energy transfer from tryptophan to hypericin. For all experiments, samples were excited at 266 nm. The fluorescence quantum yield of tryptophan and hypericin are given in parentheses in the figure.

Table 3.1. Fluorescence lifetime parameters of tryptophan in different systems

System ^a	a ₁	τ ₁ (ps)	a ₂	τ ₂ (ps)	τ ₃ (ps) ^b	⟨τ⟩ (ps) ^c
LDL/Buffer	0.44 ± 0.02	600 ± 100	0.56 ± 0.02	3600 ± 300	----	2300 ± 300
LDL:Hyp = 1:10	0.47 ± 0.01	560 ± 100	0.53 ± 0.01	3200 ± 200	----	2000 ± 200
LDL:Hyp = 1:20	0.23 ± 0.02	130 ± 20	0.46 ± 0.03	620 ± 100	3000 ± 300	1200 ± 400
LDL:Hyp = 1:30	0.32 ± 0.02	120 ± 20	0.40 ± 0.03	600 ± 100	2800 ± 200	1100 ± 300

^aλ_{ex} = 266 nm, λ_{em} = 300-410 nm.

^bThe absence of τ₃ indicates that the decay was fit to two decaying exponentials.

^cThe average lifetime was calculated according to $\langle\tau\rangle = \sum_i a_i \tau_i$. The pre-exponential factors sum to unity. The error bars are based on the average of three measurements.

Table 3.2. Fluorescence lifetime parameters of hypericin in different systems

System ^a	a ₁	τ ₁ (ps)	τ ₂ (ps) ^b	⟨τ⟩ (ps) ^c
Hyp/DMSO	1.0	----	5600 ± 200	5600 ± 200
LDL:Hyp = 1:10	1.0	----	7400 ± 300	7400 ± 300
LDL:Hyp = 1:20	1.0	----	7600 ± 300	7600 ± 300
LDL:Hyp = 1:30	0.20 ± 0.01	1200 ± 100	5400 ± 200	4600 ± 300

^aλ_{ex} = 266 nm, λ_{em} ≥ 500 nm.

^bThe absence of τ₁ indicates that the decay was fit to a single decaying exponential.

^cThe average lifetime was calculated according to $\langle \tau \rangle = \sum_i a_i \tau_i$. The pre-exponential factors sum to unity. The error bars are based on the average of three measurements.

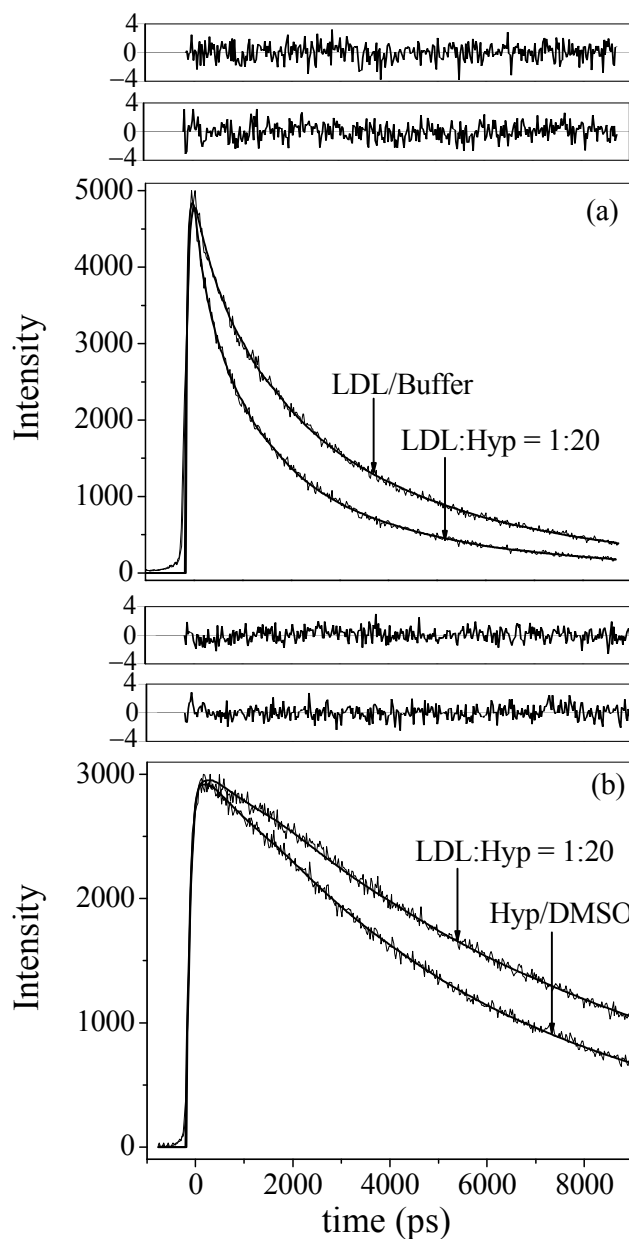


Figure 3.5. Representative fluorescence lifetime decays of (a) tryptophan and (b) hypericin. All samples were excited at 266 nm. There is a decrease in fluorescence lifetime of tryptophan and an increase in hypericin lifetime when complexed to LDL. Fitting parameters are given in Tables 3.1 and 3.2. Data on the 11.9-ns time scale are collected with a resolution of 23.3 ps/chan.

Hypericin absorbs light directly at 266 nm and, as indicated above, is also an acceptor for energy transfer from tryptophan. Thus, 266-nm excitation will induce hypericin

fluorescence: the lifetime decay of hypericin is single exponential up to LDL:Hyp = 1:20. Also, there is an increase in fluorescence lifetime of hypericin compared to that of in bulk solvents (~ 7.5 ns in LDL as opposed to ~ 5.6 ns in DMSO). The question then arises whether this lengthening of the hypericin lifetime is a result of interactions with tryptophan or induced by local environment of hypericin in LDL. To attempt to differentiate between these two possibilities we measured the lifetimes exciting hypericin directly. Lifetime parameters are given in Table 3.3. Here too, a similar trend is observed.

This lifetime lengthening is clearly a result of multiple hypericins in the LDL molecule. There are two explanations that seemed likely for its presence. There is the possibility that it arises from energy transfer from the tryptophans: the latter acting as a relatively long-lived pulse source that artificially seems to lengthen the hypericin lifetime. This idea was tested by convoluting tryptophan lifetimes from 100 ps to 3 ns with the “standard” hypericin lifetime of ~ 5.6 ns. This clearly induced a rise-time in the simulated hypericin transient, but it did not produce any significant lengthening of the lifetime and produced nothing like that we measured experimentally. This possibility can definitively be eliminated by noting that direct excitation into hypericin produces similar effects (Figure 3.6). Consequently, it seems most likely to us that the observed lifetime is a result of hypericin-hypericin interactions, possibly excimer-like interactions. We note that similar fluorescence lifetimes (i.e., longer than that observed in bulk solvent) have been observed in other systems as well.³¹ We also note that our earlier investigation of hypericin in reverse micelles in heptane indicated that there is a slight lengthening of the fluorescence lifetime to ~ 5.9 ns.³²

Table 3.3. Fluorescence lifetime parameters of hypericin in different system

System ^a	a ₁	τ ₁ (ps)	τ ₂ (ps) ^b	<τ> (ps) ^c
Hyp/DMSO	1.0	-----	5600 ± 200	5600 ± 200
LDL:Hyp = 1:10	1.0	-----	6600 ± 300	6600 ± 300
LDL:Hyp = 1:10	0.14 ± 0.01	200 ± 50	7000 ± 200	6000 ± 600
LDL:Hyp = 1:20	0.09 ± 0.01	600 ± 100	6500 ± 200	6000 ± 700
LDL:Hyp = 1:30	0.24 ± 0.02	900 ± 100	4800 ± 200	3900 ± 500

^aλ_{ex} = 407 nm, λ_{em} ≥ 500 nm.

^bThe absence of τ₁ indicates that the decay was fit to a single decaying exponential.

^cThe average lifetime was calculated according to $\langle \tau \rangle = \sum_i a_i \tau_i$. The pre-exponential factors sum to unity. The error bars are based on the average of three measurements.

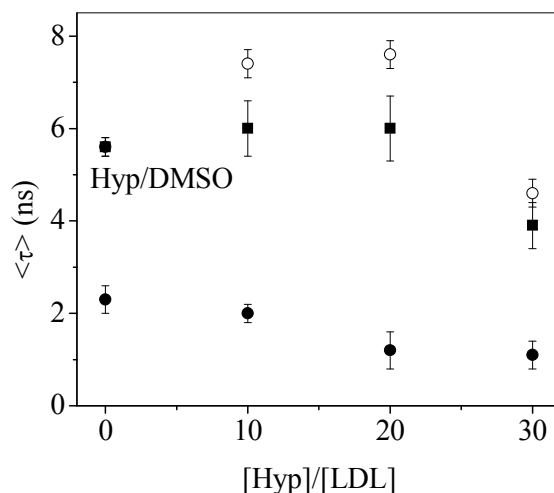


Figure 3.6. Plot of average fluorescence lifetime of tryptophan with 266 nm excitation (solid circles), hypericin with 266 nm excitation (open circles) and hypericin with 407 nm excitation (solid squares) with respect to the ratio of concentration of LDL to hypericin in different LDL-hypericin complexes studied.

In order to determine the efficiency of the tryptophan-hypericin energy transfer, we estimated the critical distance for the LDL-hypericin complex. The efficiency of the nonradiative energy transfer in a Förster energy transfer mechanism is given by, among other things, R_0 , the critical distance at which the rate of energy transfer is equal to the inverse of fluorescence lifetime of the donor.

$$k_{ET} = \frac{1}{\tau_F} \left(\frac{R_0}{R} \right)^6$$

$$R_0^6 = \frac{9000(\ln 10)\Phi_D}{128\pi^5 n^4 N} \frac{2}{3} \frac{\int_0^\infty F_D(\bar{\nu}) \epsilon_A(\bar{\nu}) \bar{\nu}^{-4} d\bar{\nu}}{\int_0^\infty F_D(\bar{\nu}) d\bar{\nu}}$$

In the above equations k_{ET} is the rate of energy transfer, τ_F is the average lifetime of the tryptophan donor, R is the distance between the donor and acceptor, n is the refraction index

of the medium (considered as 1.4), N is Avogadro's number, Φ_D is the fluorescence quantum yield of the tryptophan donor (0.10) which was calculated with respect to standard value for tryptophan in pH 7 buffer (0.18)^{13,33,34}, $F_D(\bar{\nu})$ is the donor emission spectrum on a wavenumber scale and $\epsilon_A(\bar{\nu})$ is the molar extinction coefficient of the acceptor (in $M^{-1}cm^{-1}$) on a wavenumber scale. The calculated R_0 for LDL-hypericin complex is 27 Å. Considering the apoB-100 is mainly located on the surface of LDL this distance might indicate that the hypericin molecules are mainly localized near the apoB-100.

The presence of multiple donors and acceptors in LDL-hypericin complex (37 tryptophans and 10-30 hypericins), however, clearly obviates any concrete interpretation of this "distance," since with the current experiments it is impossible to specify which of the donor-acceptor pairs are participating in the energy transfer process.

Time resolved anisotropy measurements

Fluorescence anisotropy decay parameters are given in Table 3.4. Representative polarized fluorescence decays are presented in Figure 3.7. Tryptophan molecules in LDL show two rotational time constants, which are widely separated. The shorter component (~ 400 ps) can be attributed to local motion of tryptophan molecules; the very long component (> 40 ns), to the tumbling motion of the LDL molecule.

For LDL:Hyp = 1:1 complex, exciting hypericin directly at 407 nm, we observed a single rotational time constant of ~ 10 ns for hypericin, indicating that it is rigidly bound and consequently, probably not attached to the LDL surface, where more flexibility might be expected. Similar behavior is observed in other hypericin/protein systems that we have investigated (Table 3.4).

Table 3.4. Fluorescence Anisotropy Decay Parameters in Different Systems^a

System	r_0^b	r_F	$\tau_F^{(r)}$ (ns)	r_S	$\tau_S^{(r)}$ (ns)	$\langle \tau \rangle$ (ns)
LDL/buffer ^c	0.22 ± 0.02	0.08 ± 0.02	0.4 ± 0.1	0.14 ± 0.02	> 40	-----
LDL:Hyp = 1:1 ^d	-0.07 ± 0.01^f	-----	-----	-0.07 ± 0.01	10.3 ± 0.5	10.3 ± 0.5
LDL:Hyp = 1:10 ^d	-0.06 ± 0.01^f	-0.02 ± 0.01	0.9 ± 0.2	-0.04 ± 0.01	10.3^g	7.2 ± 1.2
LDL:Hyp = 1:30 ^d	-0.06 ± 0.01^f	-0.03 ± 0.01	1.6 ± 0.3	-0.03 ± 0.01	10.3^g	6.0 ± 1.0
HSA:Hyp ₁₃ = 1:1 ^e	0.32	-----	-----	0.32	31	31
GST (HA1-1/HP1-1):Hyp = 1:1 ^{e 14}	0.30	-----	-----	0.30	≥ 20	≥ 20

^aThe subscripts “F” and “S” denote the fast and slow depolarizing events, the latter which is attributed to overall protein tumbling.

^bThe error bars are based on the average of three measurements. An average anisotropy decay time is not computed for the LDL/buffer system, since the longer decay component could not be accurately determined on the time scale used, 24-ns full scale. For all systems $\chi^2 \leq 1.3$.

^c $\lambda_{ex} = 266$ nm, $\lambda_{em} \geq 300$ nm. ^d $\lambda_{ex} = 407$ nm, $\lambda_{em} \geq 500$ nm. ^e $\lambda_{ex} = 580$ nm, $\lambda_{em} \geq 610$ nm.

^fThe negative r_0 value for hypericin is due to excitation at 407 nm. See Das et al. ³⁵ for a discussion of the wavelength dependence of the limiting anisotropy of hypericin and related pigments.

^gFor LDL complexes with multiple hypericins, the longer rotational time component was considered as a fixed global parameter.

For complexes having multiple hypericins, we have fit the polarized fluorescence decays to two decaying exponentials. Here we take the longer time component as a fixed global parameter having a 10.3-ns rotational time constant, as determined for the LDL:Hyp = 1:1 complex. Shorter “nontumbling” time constants are observed: ~ 900 ps and ~ 1600 ps for 1:10 and 1:30 complexes, respectively. The possibility of surface exposure of hypericin is unlikely given the results of the Stern-Volmer experiments cited above. Two possibilities thus present themselves: some hypericins are nearer to the surface (i.e., farther to the surface in the interfacial zone, but not surface exposed) and have more latitude of movement; all hypericins are bound rigidly, but there are depolarizing events due to energy transfer (self-quenching) among hypericin molecules, whose presence seems likely given the data in Tables 3.3 and 3.4. Most likely, a combination of both is possible.

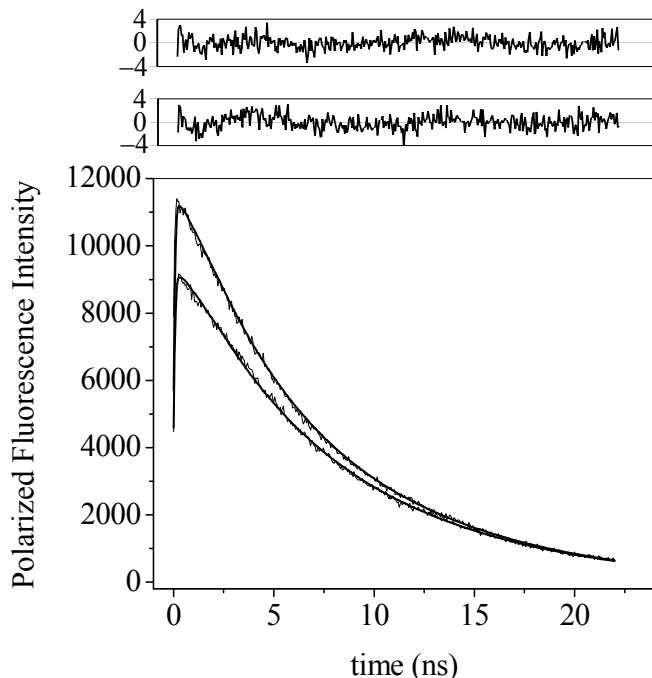


Figure 3.7. Representative polarized fluorescence decay of hypericin in 1:1 LDL:Hyp complex. $\lambda_{\text{ex}} = 407$ nm, $\lambda_{\text{em}} \geq 500$ nm. Anisotropy parameters indicate that hypericin is rigidly bound to LDL (see the text and Table 3.4).

Conclusions

We have studied the interaction of hypericin with the biologically important macromolecule, LDL. Based on various steady-state and time-resolved fluorescence measurements, we conclude that multiple hypericins can penetrate considerably deeply into the LDL molecule and most likely span the interfacial region. In particular, the anisotropy data indicate that a single hypericin is rigidly held, and thus probably resides fairly deeply in LDL. Energy transfer is efficient, suggesting that hypericin can be moderately close to the surface, where apoB-100 is located. Both results taken together suggest that the hypericin lies in an intermediate location between surface and core—i.e., the interfacial region. The accommodation of multiple hypericins in LDL should not be surprising considering the diameter of LDL ($\sim 220 \text{ \AA}$) and the dimensions of hypericin: major axis, 10.5 \AA ; minor axis, 9.6 \AA .

Up to ~ 20 nonaggregated hypericin molecules can enter one LDL; but upon increasing the hypericin concentration, the fluorescence lifetime of hypericin decreases drastically, suggesting most likely the self quenching of aggregated hypericin. The ability of LDL to solubilize hypericin is significant because hypericin has been reported to be most active in its monomeric form.³⁶

Acknowledgements

J. W. Petrich was supported by grant number P01 ES012020 from the National Institute of Environmental Health Sciences (NIEHS) and the Office of Dietary Supplements (ODS), NIH. Its contents are solely the responsibility of the authors and do not necessarily represent the official views of the NIEHS, NIH. P. Miskovsky was supported by the Fulbright scholarship program and the Slovak Science and Technology Assistance Agency

under the contract APVT-20-036104. We thank Dr. Kaustuv Das for helpful discussions.

References

- (1) Lown, J. W. *Can. J. Chem.* **1997**, *75*, 99.
- (2) Diwu, Z. *Photochem. Photobiol.* **1995**, *61*, 529.
- (3) Kraus, G. A.; Zhang, W. J.; Fehr, M. J.; Petrich, J. W.; Wannemuehler, Y.; Carpenter, S. *Chem. Rev.* **1996**, *96*, 523.
- (4) Falk, H. *Angew. Chem., Int. Ed.* **1999**, *38*, 3117.
- (5) Esterbauer, H.; Gebicki, J.; Puhl, H.; Jürgens, G. *Free Radical. Biol. Med.* **1992**, *13*, 341.
- (6) Hevonoja, T.; Pentikäinen, M. O.; Hyvönen, M. T.; Kovanen, P. T.; Ala-Korpela, M. *Biochim. Biophys. Acta.* **2000**, *1488*, 189.
- (7) Durán, N.; Song, P. S. *Photochem. Photobiol.* **1986**, *43*, 677.
- (8) Diwu, Z.; Lown, J. W. *Photochem. Photobiol.* **1990**, *52*, 609.
- (9) Petrich, J. W. *Int. Rev. Phys. Chem.* **2000**, *19*, 479.
- (10) Halder, M.; Chowdhury, P. K.; Gordon, M. S.; Petrich, J. W.; Das, K.; Park, J.; Alexeev, Y. *Adv. Photochem.* **2005**, *28*, 1.
- (11) Lobban, C. S.; Hallam, S.; Mukherjee, P.; Petrich, J. W. *Photochem. Photobiol.* **2007**, *83*, 1074.
- (12) Miskovsky, P. *Curr. Drug Targets* **2002**, *3*, 55.
- (13) Das, K.; Smirnov, A. V.; Wen, J.; Miskovsky, P.; Petrich, J. W. *Photochem. Photobiol.* **1999**, *69*, 633.
- (14) Halder, M.; Chowdhury, P. K.; Das, R.; Mukherjee, P.; Atkins, W. M.; Petrich, J. W. *J. Phys. Chem. B* **2005**, *109*, 19484.

- (15) Chen, B.; Xu, Y.; Roskams, T.; Delaey, E.; Agostinis, P.; Vandenneede, J. R.; de Witte, P. *Int. J. Cancer* **2001**, *93*, 275.
- (16) Derycke, A. N. L.; de Witte, P. *Adv. Drug Delivery Rev.* **2004**, *56*, 17.
- (17) Jori, G. *J. Photochem. Photobiol. B.* **1996**, *36*, 87.
- (18) Konan, Y. N.; Gurny, R.; Alleman, E. *J. Photochem. Photobiol. B.* **2002**, *66*, 89.
- (19) Reddi, E. *J. Photochem. Photobiol. B.* **1997**, *37*, 189.
- (20) Sherman, W. M.; van Lier, J. E.; Allen, C. M. *Adv. Drug Delivery Rev.* **2004**, *56*, 53.
- (21) Morliere, P.; Kohen, E.; Reyftmann, J. P.; Santus, R.; Cohen, C.; Maziere, J. C.; Goldstein, S.; Mangel, W. F.; Dubertret, L. *Photochem. Photobiol.* **1987**, *46*, 183.
- (22) Reyftmann, J. P.; Morliere, P.; Goldstein, S.; Santus, R.; Dubertret, L.; Lagrange, D. *Photochem. Photobiol.* **1984**, *40*, 721.
- (23) Candide, C.; Reyftmann, J. P.; Santus, R.; Maziere, J. C.; Morliere, P.; Goldstein, S. *Photochem. Photobiol.* **1988**, *48*, 137.
- (24) Mishra, P. P.; Patel, S.; Datta, A. *J. Phys. Chem. B* **2006**, *110*, 21238.
- (25) Kascakova, S.; Refregiers, M.; Jancura, D.; Sureau, F.; Maurizot, J.-C.; Miskovsky, P. *Photochem. Photobiol.* **2005**, *81*, 1395.
- (26) Chowdhury, P. K.; Halder, M.; Sanders, L.; Calhoun, T.; Anderson, J. L.; Armstrong, D. W.; Song, X.; Petrich, J. W. *J. Phys. Chem. B* **2004**, *108*, 10245.
- (27) Senthil, V.; Longworth, J. W.; Ghiron, C. A.; Grossweiner, L. I. *Biochem. Biophys. Acta.* **1992**, *1115*, 192.
- (28) Senthil, V.; Jones, L. R.; Senthil, K.; Grossweiner, L. I. *Photochem.*

Photobiol. **1994**, *59*, 40.

(29) Burel, L.; Jardon, P. *J. Chim. Phys. Phys.-Chim. Biol.* **1996**, *93*, 300.

(30) Lakowicz, J. R. *Principles of fluorescence spectroscopy*, 3rd ed.; Springer: New York, 2004.

(31) Lenci, F.; Angelini, N.; Ghetti, F.; Sgarbossa, A.; Losi, A.; Veccli, A.; Viappiani, C.; Taroni, P.; Pifferi, A.; Cubeddu, R. *Photochem. Photobiol.* **1995**, *62*, 199.

(32) Chowdhury, P. K.; Ashby, K. D.; Datta, A.; Petrich, J. W. *Photochem. Photobiol.* **2000**, *72*, 612.

(33) Rich, R. L.; Gai, F.; Lane, J. W.; Petrich, J. W.; Schwabacher, A. W. *J. Am. Chem. Soc.* **1995**, *117*, 733.

(34) Avouris, P.; Yang, L. L.; El-Bayoumi, M. A. *Photochem. Photobiol.* **1976**, *24*, 211.

(35) Das, K.; Dertz, E.; Paterson, J.; Zhang, W.; Kraus, G. A.; Petrich, J. W. *J. Phys. Chem. B* **1998**, *102*, 1479.

(36) Lavie, G.; Mazur, Y.; Lavie, D.; Prince, A. M.; Pascual, D.; Liebes, L.; Levin, B.; Meruelo, D. *Transfusion* **1995**, *35*, 392.

**CHAPTER 4. SOLVATION DYNAMICS OF THE FLUORESCENT PROBE,
PRODAN, IN HETEROGENEOUS ENVIRONMENTS: CONTRIBUTIONS FROM
THE LOCALLY EXCITED AND CHARGE-TRANSFERRED STATES**

A paper published in *The Journal of Physical Chemistry B*

Ramkrishna Adhikary, Charles A. Barnes, and Jacob W. Petrich*

Abstract

The coexistence of different excited states with different properties of the same chromophores could have significant consequences for the accurate characterization of solvation dynamics in a heterogeneous environment, such as a protein. The purpose of this work is to study the contributions of the locally-excited (LE) and charge-transferred (CT) states of the fluorescent probe molecule, 6-propionyl-2-(N,N-dimethylamino)naphthalene (PRODAN), PRODAN to its solvation dynamics in the heterogeneous environment provided by reverse micelles formed by sodium 1,4-bis-(2-ethylhexyl) sulfosuccinate (AOT)/n-heptane/water. We have found that the LE and CT states of PRODAN solvate on different time scales in reverse micelles (2 and ~ 0.4 ns, respectively), consistent with results suggested in the literature, and have concluded that PRODAN's use as a probe of heterogeneous

Reprinted with permission from *The Journal Physical Chemistry B* 2009, 113(35), 11999-12004. Copyright (2009) American Chemical Society.

Department of Chemistry, Iowa State University, Ames, Iowa 50011.

*To whom correspondence should be addressed.

environments must be used with caution and that, more importantly, the same caution must be exercised with any chromophore capable of emitting from different excited states.

Introduction

Fluorescent molecules sensitive to environmental polarities have been used extensively as probes in the studies of physicochemical properties of solvents, surfaces, proteins, membranes, cells etc.¹⁻⁵ It is critical to understand the photophysical properties of the fluorescent probe molecule, especially if it can emit from more than one state. 6-Propionyl-2-(N,N-dimethylamino)naphthalene (PRODAN) (Figure 4.1) is a highly fluorescent, hydrophobic molecule, first synthesized and characterized by Weber and Farris in 1979.⁶ Its absorption and emission spectra are strongly dependent upon the polarity of its environment⁶, and it has a long history of use in probing biological systems.⁷⁻¹⁴ It has been used as an optical probe of the function and dynamics of proteins and membranes.⁷⁻¹⁴ Recently it has also been used to study solvation dynamics in polar liquids, ionic liquids, and supercritical fluids.¹⁵⁻¹⁹

PRODAN is a push-pull, charge-transfer chromophore that produces a substantial change in its excited-state dipole moment upon photoexcitation owing to the presence of an electron-donating dimethylamino group and electron-withdrawing propionyl group connected to the aromatic spacer by a single bond. The excited-state kinetics of PRODAN are complex, and the origins of its solvatochromatic nature have been debated.²⁰⁻²⁶ Theoretical calculations suggest a planar structure in the ground state. But the geometry of its charge-transferred emissive state has not yet been confirmed.^{20,27} Several theoretical studies have been performed to determine the possible conformational changes in its excited-state geometry: for example, whether the emissive state is twisted intramolecular charge

transfer (TICT) or planar intramolecular charge transfer (PICT).^{20,23-35}

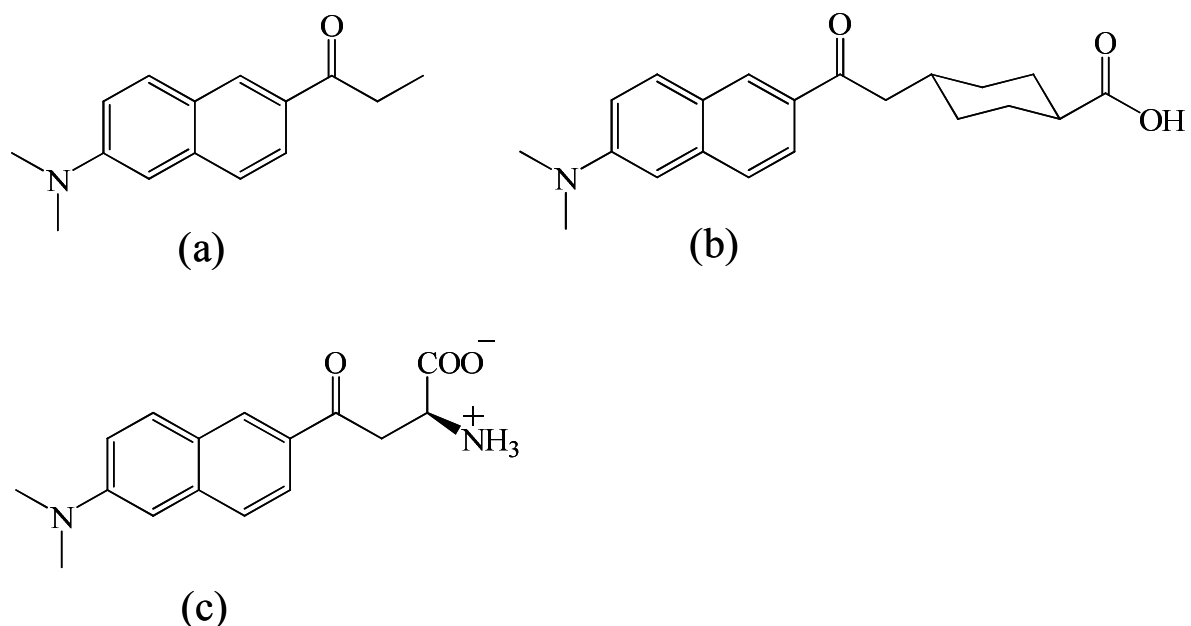


Figure 4.1. Structure of (a) 6-Propionyl-2-(N,N-dimethylamino)naphthalene (PRODAN), (b) 2'-(N,N-dimethylamino)-6-naphthoyl-4-trans-cyclohexanoic acid (DANCA) and (c) Aladan.

Lakowicz and Balter^{36,37} studied PRODAN in n-butanol and suggested that its spectral relaxation requires at least two steps. Later Heisel et al.²⁸ explained the time-resolved fluorescence experimental results of PRODAN in n-butanol in terms of a nonradiative intramolecular reaction from a locally-excited state to an energetically lower charge-transferred state and to solute-solvent interactions. Chapman et al.¹⁵ and Chapman and Maroncelli¹⁶ discussed the spectral relaxation of PRODAN in terms of a continuous solvation process. It is generally agreed that, PRODAN undergoes excited-state intramolecular charge-transfer following excitation from the ground state. The charge-transferred state, CT, is formed from an initially excited state referred to as the locally-excited state (LE).³⁸ In nonpolar environments, emission is from the LE state, while in polar environments the emission is from the CT state (Figure 4.2).³⁸

PRODAN has a single broad emission spectrum with a dramatic solvatochromatic shift (~ 130 nm) of its maximum, ranging from 401 nm in cyclohexane to 531 nm in water.⁶ Weber and Farris⁶ first reported a change in dipole moment, $\Delta\mu \sim 20$ D, upon excitation, and concluded that this was responsible for its large Stokes shift. Balter et al. modified this value to 10 D and suggested that solvent-specific interactions (e.g., hydrogen bonding) may cause a large Stokes shift in polar protic solvents.²⁹ Recently Samanta et al.³² have suggested this value to be 4.4-5.0 D based on transient dielectric loss measurements. Recently ground and excited Frank-Condon state dipole moment of PRODAN was also reported from electrooptical absorption measurements.³⁹

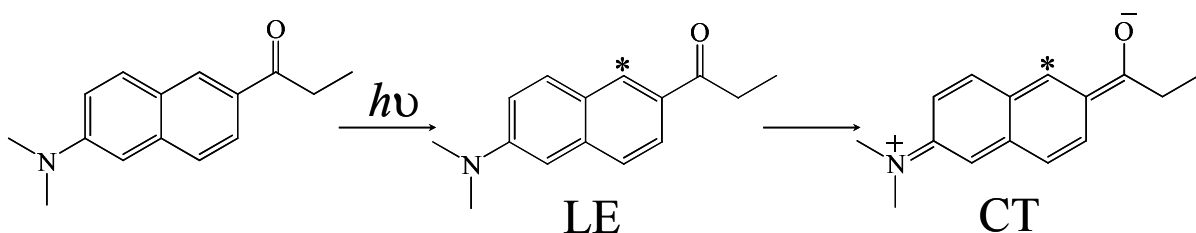


Figure 4.2. The charge-transferred (CT) state is created via the locally-excited (LE) state in polar environments.

PRODAN has a single-exponential fluorescence lifetime decay in nonpolar solvents (e.g., cyclohexane: ~ 0.2 ns; heptane: ~ 0.14 ns) and in polar aprotic solvents (e.g., acetonitrile: ~ 3.3 ns).^{22,40} However, it exhibits a biexponential lifetime in polar protic solvents such as methanol and water. The reported lifetime components in methanol are ~ 2.0 ns (75%) and 3.4 ns (25%).²² The fluorescence behavior is more complex in water than in other solvents: Balter et al.²² observed an additional, weak emission band around 430 nm. They also reported a biexponential fluorescence lifetime ($\tau_1 \sim 0.5$ ns and $\tau_2 \sim 1.9$ ns) with an additional small contribution from a long-lived component of ~ 13 ns at the blue edge of

emission spectrum, exciting at 337 nm. The faster lifetime component in protic solvent was interpreted in terms of a solute-solvent complex formation via hydrogen bonding. Later, Bunker et al.²⁹ noticed a stronger blue emission band exciting at 280 nm, and they suspected that the blue emission was the consequence of water-soluble impurities present in commercial PRODAN. Sun and coworkers⁴¹ resolved this ambiguity. They showed that the extra blue-edge shoulder and the small contribution from the additional long-lived component (~ 13 ns) in the fluorescence decay were the result of PRODAN-PRODAN intermolecular interactions in a supersaturated solution of PRODAN in water.

Our work here is motivated by previous studies using PRODAN to study the environments of reverse micelle.^{40,42-48} While most of these studies attributed PRODAN fluorescence to only the LE state and rationalized the observed emission to partitioning of the fluorophore in different regions of the reverse micelle⁴²⁻⁴⁷, Novaira et al.^{40,48} have reported dual fluorescence from both LE and CT in reverse micelles arising from both the LE and CT states by using time-resolved area normalized emission spectroscopies.

The coexistence of different excited states with different properties of the same chromophores could have significant consequences for the accurate characterization of solvation dynamics in a heterogeneous environment, such as a protein. Therefore, the purpose of this work is to study the contributions of LE and CT states of PRODAN to its solvation dynamics, in particular, in reverse micelles formed by sodium 1,4-bis-(2-ethylhexyl) sulfosuccinate (AOT)/n-heptane/water (Figure 4.3). We have found that the LE and CT states of PRODAN solvate on different time scales and concluded that PRODAN's use as a probe of heterogeneous environments must be used with caution.

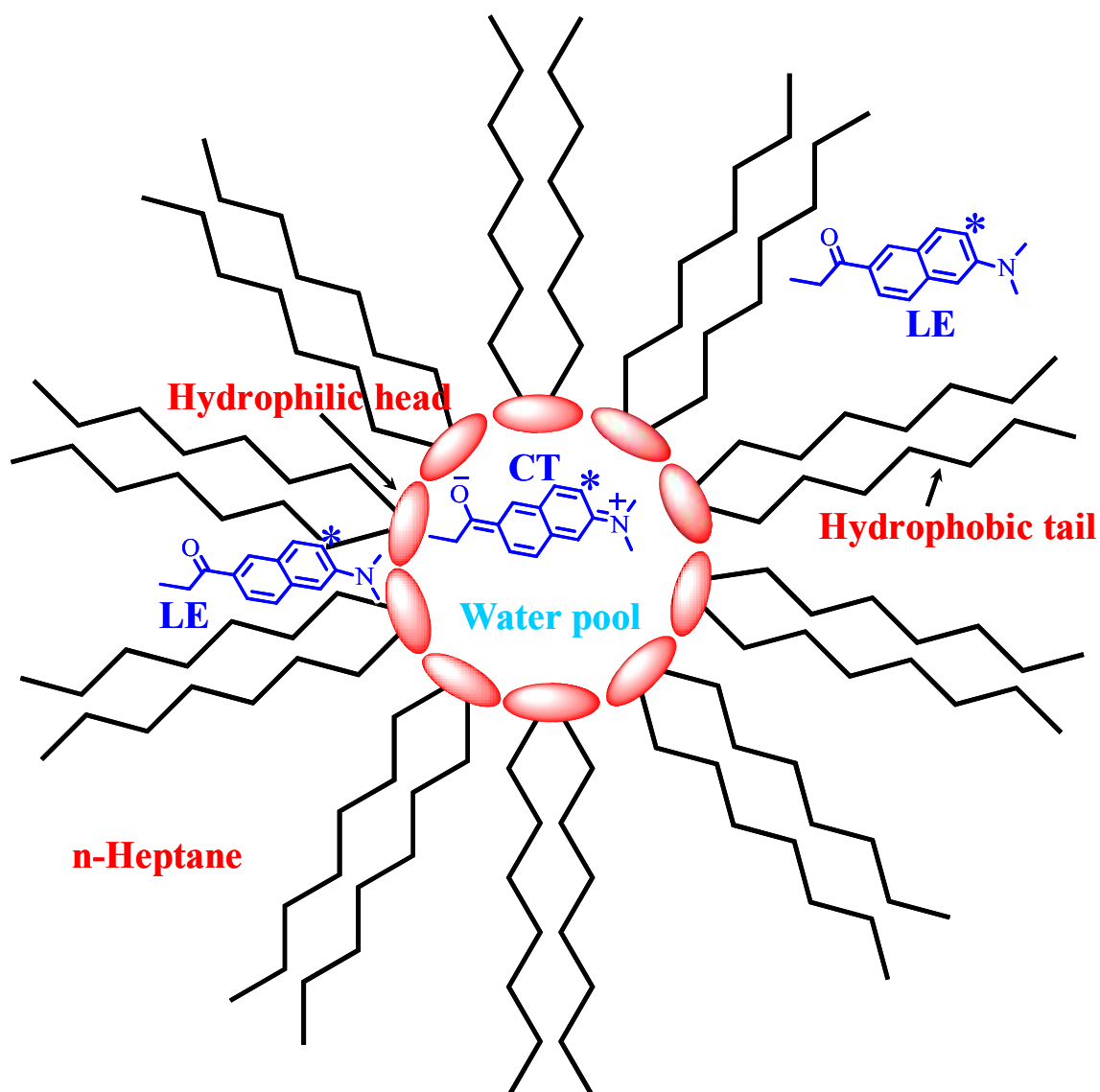


Figure 4.3. PRODAN in the 1,4-bis-(2-ethylhexyl) sulfosuccinate (AOT)/n-heptane/water reverse micellar environment. LE and CT are the locally-excited and charge-transferred emissive states of PRODAN, respectively.

Experimental Section

Materials. 6-Propionyl-2-(N,N-dimethylamino)naphthalene (PRODAN) (purity \geq 98%) and sodium 1,4-bis-(2-ethylhexyl) sulfosuccinate (AOT) (purity $>$ 99%) were obtained from Sigma-Aldrich and used as received. n-Heptane was obtained from Acros, Spectrargrade. Methanol and acetonitrile (purity 99.9%) were purchased from Fisher

Scientific and used without further purification.

Sample Preparation. Stock solutions of PRODAN (0.05 M) in acetonitrile and AOT (0.8 M) in n-heptane were prepared. The reverse micelle system was prepared through volumetric dilution from the stock solutions. The final AOT concentration was 0.2 M. The concentrated PRODAN in acetonitrile solution was used to introduce the probe into the system. The final concentration of PRODAN was 5×10^{-5} M with an organic content of < 0.1%. An appropriate amount of nanopure water was then added to obtain $w = 20$ ($w = [\text{H}_2\text{O}]/[\text{AOT}]$). All samples were allowed to equilibrate for 24 hrs before subsequent steady-state and time-resolved measurements. To prepare a PRODAN/water solution, 45 μL of a solution of 1×10^{-3} M PRODAN in methanol (Fisher Scientific, HPLC) was added to 5 mL of water: i.e., 9×10^{-6} M PRODAN/water was prepared with an organic content < 0.9%. This freshly prepared solution was then used for the steady-state and time-resolved measurements.

Steady-State Measurements. Steady-state absorption spectra were obtained on a Hewlett Packard 8453 UV-visible spectrophotometer with 1-nm resolution. Steady-state emission spectra were obtained on a Spex Fluoromax-4 with a 3- or 4-nm bandpass and corrected for lamp spectral intensity and detector response. For absorption and emission measurements, 5-mm and 1-cm path-length quartz cuvettes were used, respectively. All experiments were done at room temperature.

Time-Resolved Measurements. Measurements of excited-state lifetimes were performed with the time-correlated single-photon counting (TCSPC) technique. The apparatus for time-correlated single-photon counting is described elsewhere.⁴⁹ The fundamental from a home-made mode-locked Ti-sapphire oscillator was modulated by a Pockels cell (Model 350-160, Conoptics Inc) to reduce the repetition rate to 8.8 MHz. All

experiments were performed using either the 407-nm or 266-nm excitation obtained from the 814 nm fundamental by means of a U-Oplaz Technologies (Model TP-2000B) doubler/tripler. Recent modifications in the experimental set-up include the replacement of NIM-style electronics by a Becker & Hickl photon counting module (Model SPC-630). With this modified system, the full-width at half-maximum of the instrument-response function is ~40 – 50 ps. A cuvette of 5-mm or 1-cm path length was used for the time resolved measurement depending upon the system.

To construct the time-resolved spectra, a series of decays were collected typically from 370 nm to 560 nm at 10 nm intervals. Transients were fit to sums of exponentials, and time-dependent spectra were reconstructed from these fits by normalizing to the steady-state spectra:

$$S(\lambda, t) = D(\lambda, t) \frac{S_0(\lambda)}{\int_0^{\infty} D(\lambda, t)} \quad (4.1)$$

$D(\lambda, t)$ is the wavelength-resolved fluorescence decay, and $S_0(\lambda)$ is the steady-state emission intensity at a given wavelength. We have employed the traditional approach of fitting the time-resolved spectra to a log-normal function, from which we extract the peak frequency, $\nu(t)$, as a function of time.

Results and Discussion

The absorption and emission spectra of PRODAN in AOT/n-heptane/water ($w = 20$) are shown in Figure 4.4. The emission spectrum of PRODAN in AOT/n-heptane/water exciting at 266 nm consists of two bands. This result is consistent with the dual emission obtained previously exciting at 330 nm in AOT/n-heptane/water reverse micelles⁴⁰ from a

locally-excited state (LE) at $\lambda^{\text{em}}_{\text{max}} = 411 \text{ nm}$ and from a charge-transferred state (CT) at $\lambda^{\text{em}}_{\text{max}} = 507 \text{ nm}$. Upon excitation at 407 nm, only one emission band was obtained, with $\lambda^{\text{em}}_{\text{max}} = 508 \text{ nm}$. Thus, it is possible to observe PRODAN emission from both the LE and CT states in the same sample; and its emission can be tuned with excitation energy.

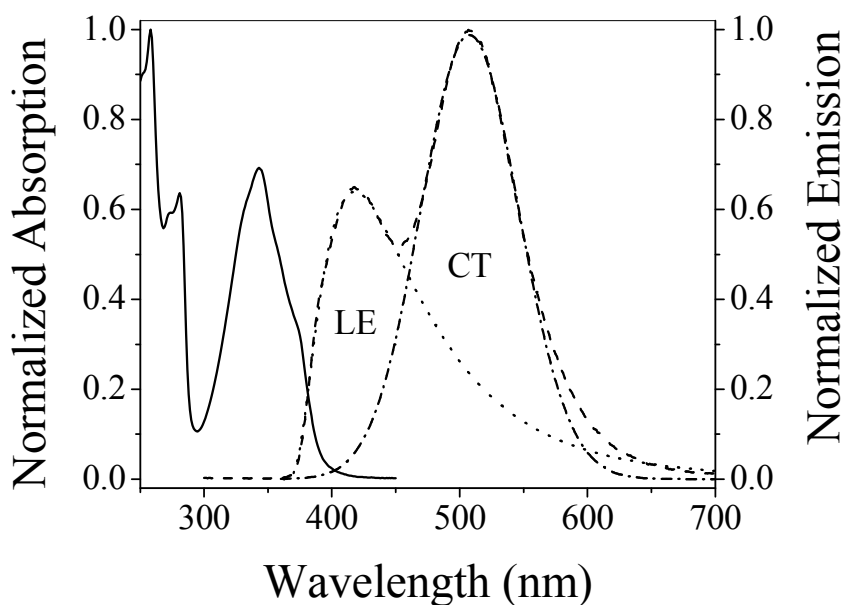


Figure 4.4. Normalized absorption (solid line) and emission spectra (dashed line) of PRODAN in AOT/n-heptane/water ($w = 20$). The emission spectrum was fit with two log-normal equations to obtain individual emission spectra for the CT (dashed-dotted line) and LE states (dotted line). The sample was excited at 266 nm and emission was collected using a 345 nm long-pass filter.

Fluorescence lifetime decays of PRODAN in water, n-heptane and AOT/n-heptane/water ($w = 20$) at different excitation wavelengths are displayed in Figure 4.5. Figure 4.5A presents the decay traces of PRODAN in n-heptane and water exciting at 266 nm. The lifetime parameters are given in Table 4.1. PRODAN has a single-exponential lifetime with a time constant of 0.15 ns in n-heptane. The decay of PRODAN in water is well described by a biexponential function with time constants of 0.70 ns (60%) and 2.0 ns

(40%). There is a significant change in the decay kinetics of PRODAN in AOT/n-heptane/water ($w = 20$) depending on whether the excitation wavelength is 266 or 407 nm (Figure 4.5B). The trace obtained with 266 nm excitation was best fit with a biexponential function with time constants of 0.16 ns (70%) and 2.3 ns (30%). The trace obtained with 407 nm, however, was best fit by a single exponential with a time constant of 2.6 ns. The absence of a risetime of the CT emission band (Table 4.1, Figure 4.5B) suggests that in such a polar environment the LE \rightarrow CT reaction rate of PRODAN is too fast to be resolved under the present experimental conditions. 4-*N,N*-dimethylaminobenzonitrile (DMABN) is a well studied molecule which emits from both LE and CT states and shows dual emission bands in polar solvents.^{50,51} It is important to note that DMABN also leads to a complete cutoff of the LE emission band and shows only the CT emission band upon red-edge excitation of its absorption spectrum in polar solvent.⁵² The charge-transferred time found for DMABN in a polar acetonitrile solution was ~ 4 -6 ps.^{53,54}

To investigate the solvation of the LE and CT states, wavelength-resolved lifetime measurements were carried out at 20 different wavelengths from 370 to 560 nm for PRODAN in AOT/n-heptane/water ($w = 20$) and were fit to a sum of two decaying exponentials. Representative wavelength-resolved fluorescence decay traces are displayed in Figure 4.6. To evaluate the spectra and dynamics of the LE and CT states separately, the emission spectrum in Figure 4.4 was decomposed into two bands using log-normal functions. Time-resolved emission spectra were constructed according to eq 4.1 for each using the fitting parameters for the 20 wavelength-resolved decay traces. Representative time-resolved emission spectra for the LE and the CT states are given in Figure 4.7. Plots of peak frequencies as a function of time are given in Figure 4.8 for the LE and CT states. The peak

shift was fit to a single exponential of time constant 2.0 ns for LE and to two exponentials with time constants of 0.40 ns (91%) and 4.0 ns (9%) for CT.

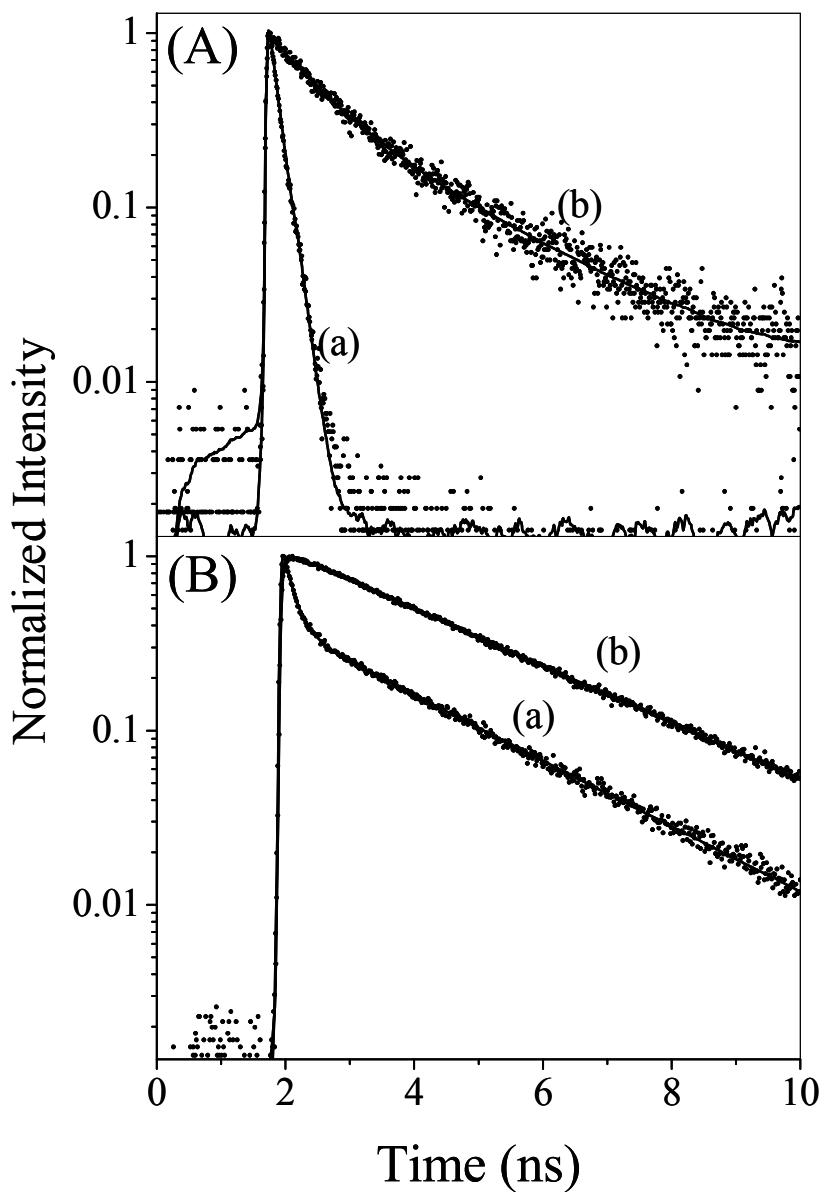


Figure 4.5. (A) Fluorescence decay traces of PRODAN in (a) n-heptane and (b) water, exciting at 266 nm. (B) Fluorescence decay traces of PRODAN in AOT/n-heptane/water ($w = 20$) exciting at (a) 266 nm and (b) 407 nm.

Table 4.1. Lifetime parameters of PRODAN in different environments

System	a_1	τ_1 (ns)	a_2	τ_2 (ns)
^a n-heptane	1.0	0.15	----	----
^a water	0.60	0.70	0.40	2.0
^a AOT/n-heptane/water (w = 20)	0.70	0.16	0.30	2.3
^b AOT/n-heptane/water (w = 20)	1.0	2.6	----	----

^a $\lambda_{\text{ex}} = 266 \text{ nm}$, $\lambda_{\text{em}} \geq 300 \text{ nm}$

^b $\lambda_{\text{ex}} = 407 \text{ nm}$, $\lambda_{\text{em}} \geq 425 \text{ nm}$

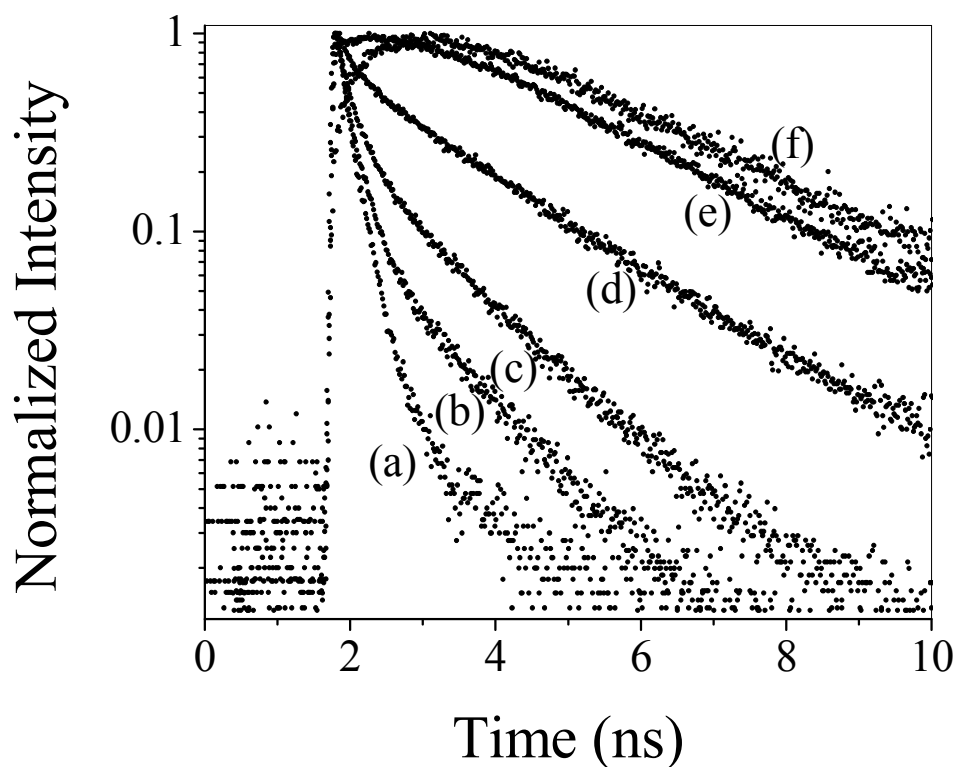


Figure 4.6. Representative wavelength-resolved decay traces of PRODAN in AOT/n-heptane/water (w = 20) at (a) 370 nm, (b) 400 nm, (c) 430 nm, (d) 460 nm, (e) 490 nm, and (f) 560 nm, exciting at 266 nm.

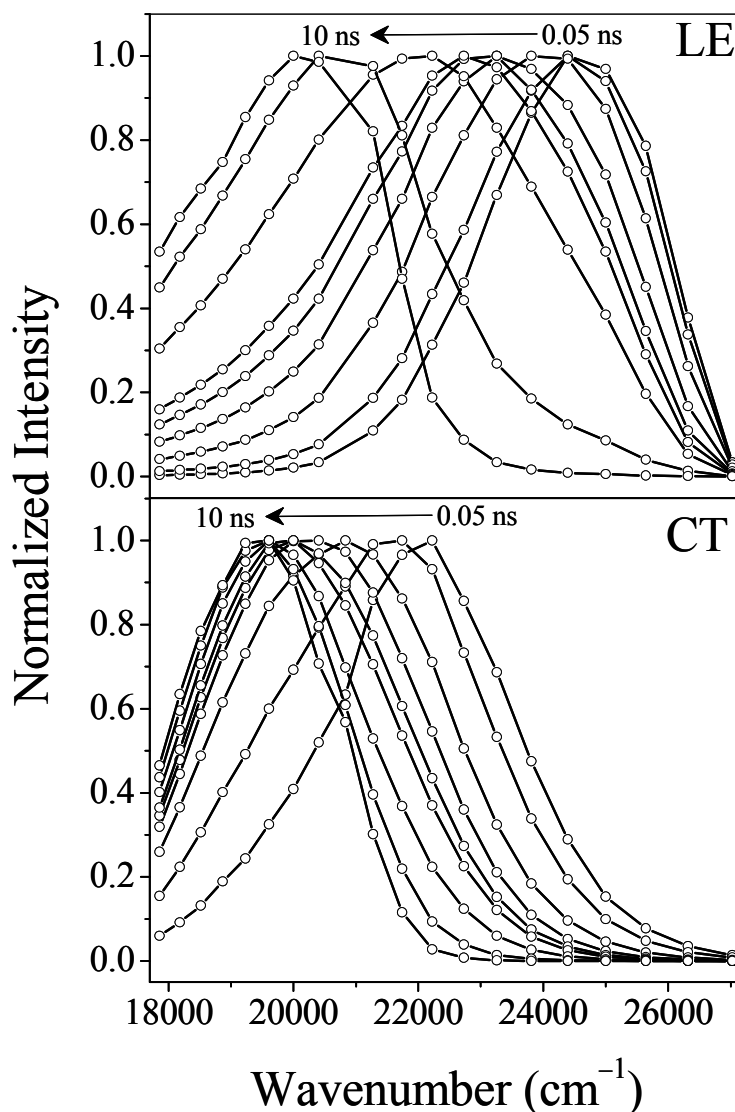


Figure 4.7. Representative normalized time-resolved emission spectra of the locally-excited state (LE) and the charged-transferred state (CT) at 0.05, 0.2, 0.4, 0.6, 0.8, 1.0, 2.0, 5.0, and 10.0 ns.

These results clearly demonstrate that the solvatochromic probe, PRODAN, can emit from different states in a heterogeneous environment and that, owing to the different natures of these states (i.e., charge-transferred or not), their solvation dynamics can occur on different time scales and they can have significantly different Stokes shifts. This,

consequently, introduces another level of complication into the interpretation of the data when fluorescence is observed from chromophores capable of emitting from more than one excited state. If the properties of each state are known, it is possible to take them into account. We have recently discussed and compared two methods of performing such an analysis.⁵⁵

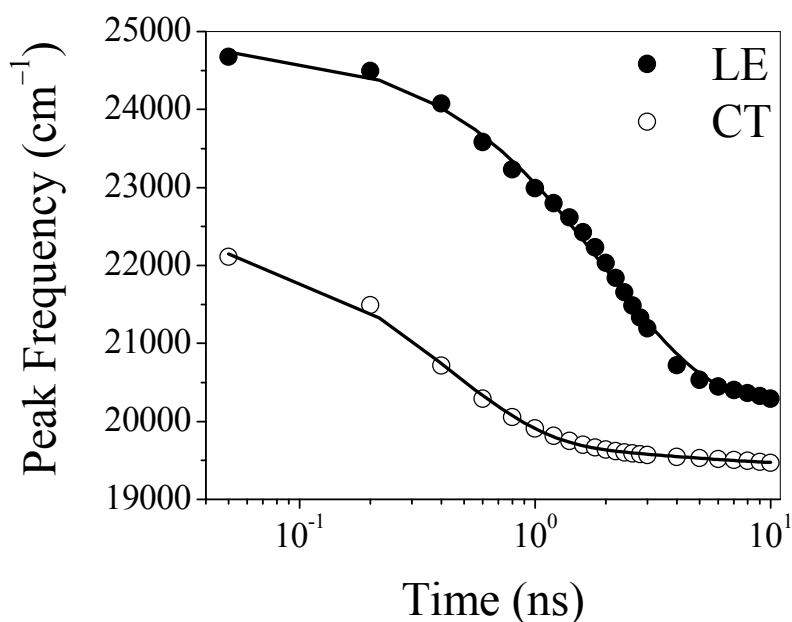


Figure 4.8. Plots of the maxima of the time-resolved emission spectra for the locally-excited (LE) state (solid circles) and the charge-transferred (CT) state (empty circles). Peak frequencies were obtained by fitting the time-resolved emission spectra to log-normal functions. The peak shift was fit to a single exponential of time constant 2.0 ns for LE and to two exponentials with time constants of 0.40 ns (91%) and 4.0 ns (9%) for CT.

There are other factors, however, that are more difficult to account for, namely the effects of slow conformational changes or aggregation, which is possible at the high concentrations (~ 1 mM)^{56,57} at which some of these experiments are performed. We now refer to a few examples. As illustrated in Figure 4.1, more elaborate fluorescent probes of biological systems are based upon the PRODAN chromophore, namely, DANCA⁵⁸ and,

more recently, a nonnatural amino acid analog, Aladan⁵⁹. Boxer and coworkers⁵⁶ have incorporated the latter at different buried and exposed sites of the immunoglobulin binding domain, B1, of protein G (GB1) and measured the time-dependent Stokes shift. All the sites showed a bimodal relaxation with an inertial ultrafast response of ~80-140 fs followed by a much slower relaxation on the timescale of several picoseconds to several nanoseconds, depending upon the location of the probe. This experimental work forms the basis for a good comparison with simulations performed by Golosov and Karplus.⁶⁰ In the context of their study, an interesting observation was that the time-resolved emission spectra of Aladan at fully and partially exposed sites of the protein showed a blue shift at long times (> 1 ns). The authors suggested that this blue shift could be attributed either to different chromophore populations having different lifetimes and solvation dynamics or to aggregation effects.

Based on our above results for the PRODAN photophysics and solvation dynamics, we suggest a model that can produce a blue shift of time-resolved spectra at long times. In this model we assume that the LE state is formed from CT states. *In particular, we assume a slow ground-state conformational change or aggregation that perturbs the environment of the chromophore in such a manner that CT states are no longer predominantly favored and thus increases the population of LE states.* As LE is gradually formed in this manner, it will undergo its characteristic solvation dynamics, which must be convoluted with the LE formation and decay in order to obtain the complete spectral response of this newly formed species. The spectrum at any given time will then have contributions from both CT and LE.

Thus, the time course of production and decay of LE, $L(t)$ is given by

$$L(t) = I_0 \left(e^{-\frac{t}{\tau_f}} - e^{-\frac{t}{\tau_{LE}}} \right) \quad (4.2)$$

where I_0 is fraction of the protein population that undergoes the conformational change discriminating against the formation of CT and instead favoring the production of LE. In our simulation, we took $I_0 = 0.1$ (~20% of the CT population, as given by the spectral decomposition of eq 4.1). The time of formation, τ_f , of LE from CT was chosen as 5.0 ns. The fluorescence lifetime of LE, τ_{LE} , was found experimentally to be 0.15 ns. The evolution of time-resolved spectra of LE is

$$I(\lambda, t) = Ae^{-\frac{1}{2} \frac{(\lambda - \lambda_m(t))^2}{\sigma^2}} e^{-\frac{t}{\tau_{LE}}} \quad (4.3)$$

where $A = 2.4$ and was obtained by spectral decomposition using eq 4.1 and $\sigma = 1280 \text{ cm}^{-1}$, as obtained from the time-resolved emission spectrum at the instrumental time-zero. The peak frequency of the time-resolved spectra is given by $\lambda_m = (\lambda_0 - \lambda_\infty)e^{-\frac{t}{\tau_{sol}}} + \lambda_\infty$, where λ_0 and λ_∞ were taken from the experimental data as 24675 cm^{-1} and 20292 cm^{-1} , respectively. The solvation time, τ_{sol} , of LE is 2.0 ns (Figure 4.8). The convolution of $L(t)$ with $I(\lambda, t)$ is

$$LE(\lambda, t) = \int_0^t L(t')I(\lambda, t - t')dt' \quad (4.4)$$

and yields the time-resolved emission spectrum induced by the slow conformational change or aggregation postulated above (Figure 4.9). The time-resolved spectra for LE and CT were then summed to generate the total time-resolved spectra. Those at $t = 0, 1.0, \text{ and } 10.0$ ns are shown in Figure 4.10. At $t = 0$ ns, there is virtually no contribution from LE in the total time-resolved spectrum; but with increasing time, LE contributes significantly to the total time-resolved spectrum. Other variations of this model are clearly possible.

Given, however, that the LE state was not accessed with 400 nm excitation (Table

4.1), the excitation wavelength used by Boxer and coworkers, and that their steady-state spectra showed no evidence of the LE state, the blue shift they observed is likely to have other origins. On the other hand, it is useful to consider three different investigations carried out to study the solvation response of myoglobin using various chromophores to replace the heme. These chromophores are: the PRODAN derivative, DANCA⁵⁸; another charge-transfer molecule capable of emitting from dual states, aniline-2-aminonaphthalene-6-dimethylsulfonamide (ANSDMA)⁶¹, and coumarin 153⁵⁷. Each probe of solvation dynamics exhibited a different response. DANCA yielded a complicated solvation response with significant contributions into the nanosecond regime. ANSDMA provided a single-exponential response of ~ 9 ns (although rapid components might have been neglected because of the time resolution of the experiment). Using coumarin 153, it was found that almost 60 % of the solvation is complete within the time resolution of the experiment (300 fs) and that this initial response is followed by a slower one. Most importantly, there was excellent agreement between the solvation correlation function, $C(t)$, from fluorescence upconversion experiments and those obtained from molecular dynamics simulations. While some of these differences may be attributed to how⁵⁵ or whether a solvation correlation function was actually constructed, it is legitimate to inquire whether some of the discrepancy might not also be attributed to the nature of the fluorescent probes employed. While DANCA and ANSDMA are both capable of charge transfer in the excited state, coumarin 153 is exquisitely inert, which is one of the reasons it has been so extensively employed as a probe of solvation.^{57,62-73} (The DANCA experiments used an excitation wavelength of 345 nm. Novaira et al. have observed that both LE and CT emission can be observed in reverse micelles at 330 nm. While the DANCA work⁵⁸ does not mention a blue-shift at long times,

it is feasible that some of the long-time dynamics observed are a result of the possible behavior we have suggested above.)

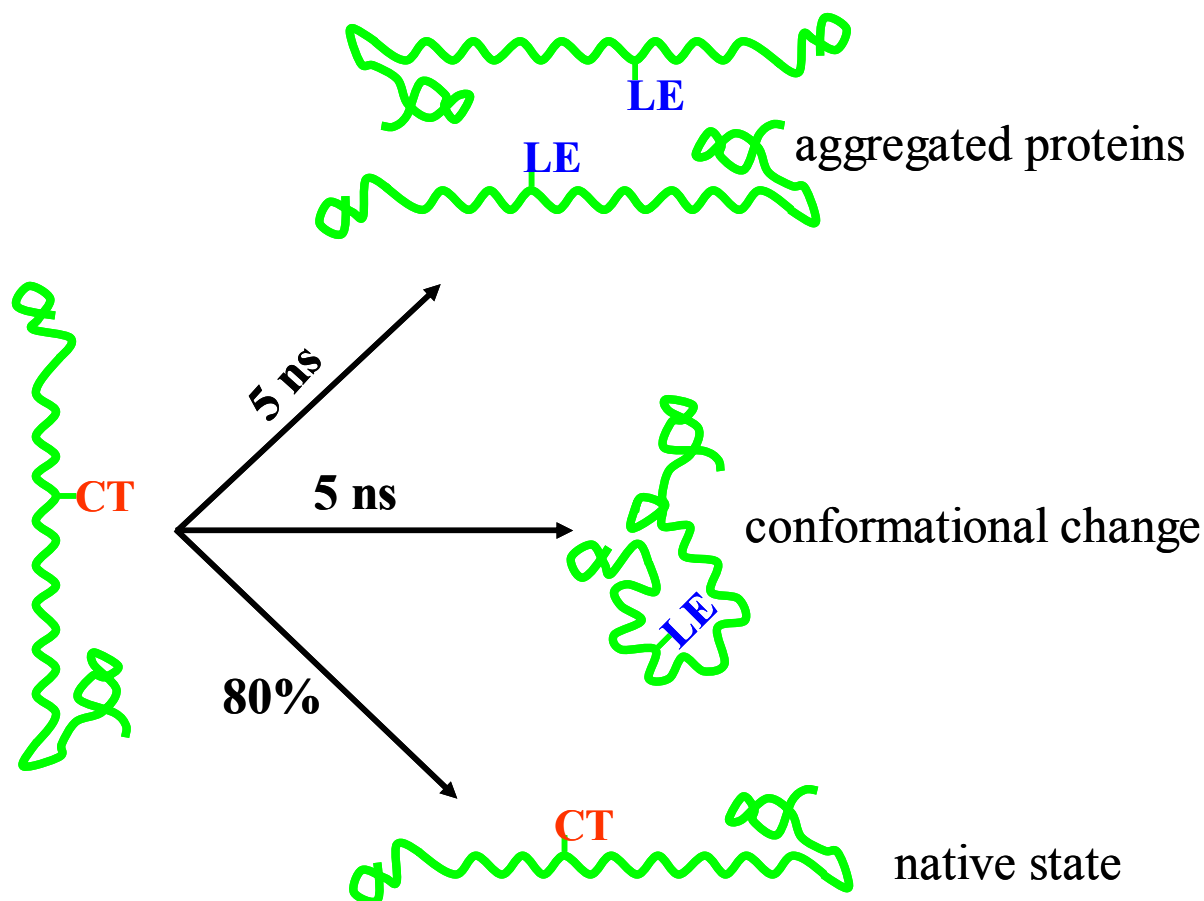


Figure 4.9. Schematic diagram illustrating the assumptions underlying the simulation described in the text. As noted in the Introduction and in the caption to Figure 4.2, it is generally agreed that in all cases, regardless of solvent or environment, the LE state is formed immediately upon excitation and that whether the LE state decays into the CT state does, however, depend on environment. The purpose of the simulation, whose results are illustrated in Figure 4.10, is to suggest a mechanism by which blue shifts in the dynamic Stokes shift may be observed at long times. We propose that they may arise from a system that emits completely from an ensemble of CT states initially, but that after several nanoseconds, for example, a small but nonnegligible population of protein assumes conformations where LE, not CT, is the emissive state. It must be noted that in the time required for the conformational change or aggregation to occur, the same protein sample is being used for the experiment (~ 2 hours for single wavelength decay measurement). It is not being suggested that the lifetime of CT is 5 ns, nor that there is an excited-state pathway converting CT to LE on this time scale.

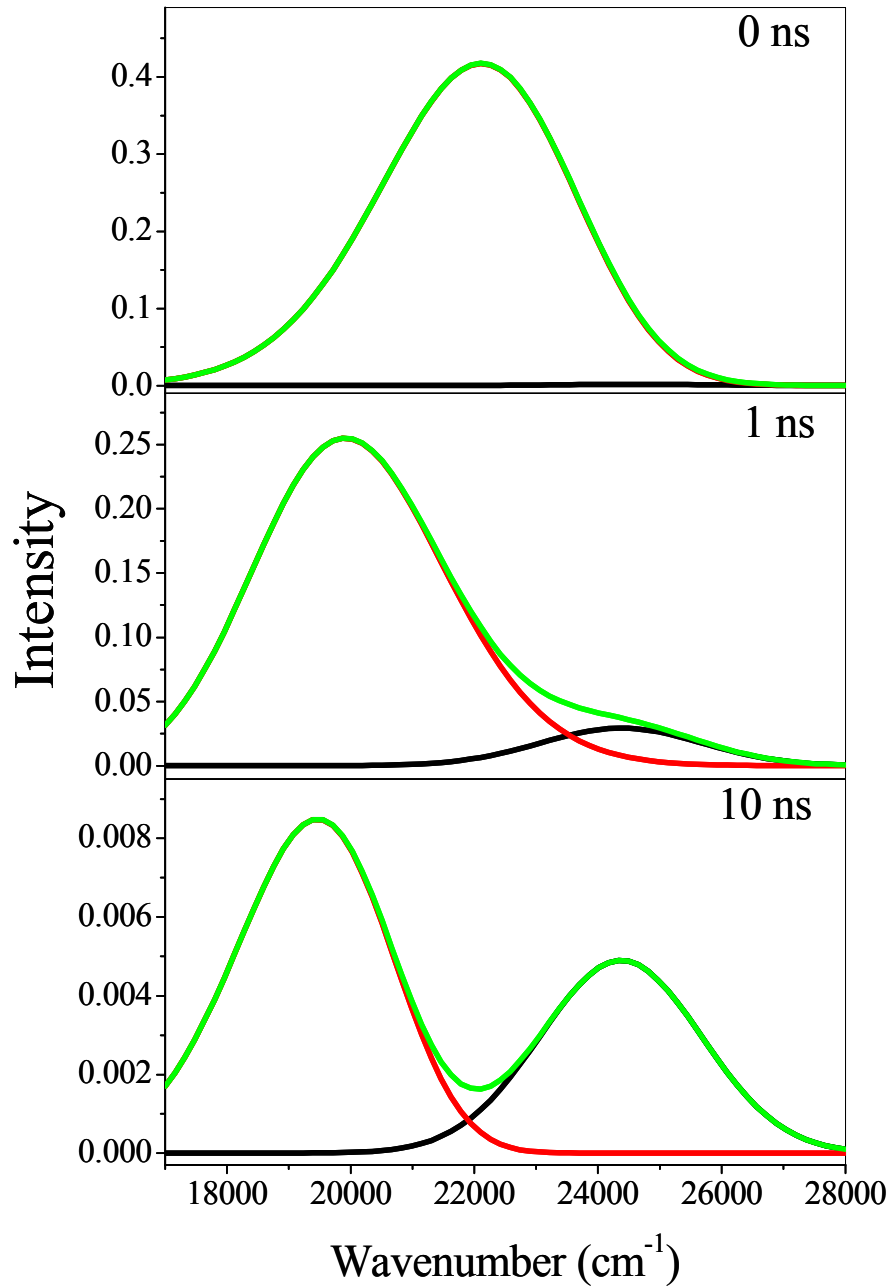


Figure 4.10. Simulation of the total time-resolved emission spectra at 0, 1, and 10 ns as described in the text. The black line is the time-resolved emission spectrum for LE; the red line, for CT. The sum of the two time-resolved spectra is shown in green. Note that the scale of the ordinate changes with time.

Conclusions

Stimulated by the work of Novaira et al.^{40,48}, we have studied the solvation dynamics of PRODAN in a heterogeneous environment (reverse micelles) that permits a distribution of the chromophores to emit from both the LE and the CT states. We have studied the solvation dynamics of both states and found them to be very different, as suggested by the work of Novaria et al. This result consequently leads to the question of whether PRODAN-based chromophores or, more generally, any chromophore capable of undergoing excited-state photochemistry, can induce artifacts into the interpretation of solvation dynamics in heterogeneous environments—in particular, those provided by biological systems such as proteins. Considerable care in choosing and characterizing the system is required in order to analyze the results fully.

References

- (1) Demchenko, A. P. *Luminescence and Dynamics of Protein Structure*; Nauka Dumka: Kiev, 1988.
- (2) Silvius, J. R. *Annu. Rev. Biophys. Biomol. Struct.* **1992**, *21*, 323.
- (3) Dobrestov, G. E. *Fluorescence Probes in Investigations of Cells, Membranes and Lipoproteins*; Nauka: Moscow, 1989.
- (4) Parasassi, T.; De Stasio, G.; Ravagnan, G.; Rusch, R. M.; Gratton, E. *Biophys. J.* **1991**, *60*, 179.
- (5) Viard, M.; Gallay, J.; Vincent, M.; Meyer, O.; Robert, B.; Paternostre, M. *Biophys. J.* **1997**, *73*, 2221.
- (6) Weber, G.; Farris, F. J. *Biochemistry* **1979**, *18*, 3075.
- (7) Moreno, F.; Cortijo, M.; Gonzalez-Jimenez, J. *Photochem. Photobiol.* **1999**,

69, 8.

(8) Lasagna, M.; Vargas, V.; Jameson, D. M.; Brunet, J. E. *Biochemistry* **1996**, *35*, 973.

(9) Rottenberg, H. *Biochemistry* **1992**, *31*, 9473.

(10) Bondar, O. P.; Rowe, E. S. *Biophys. J.* **1999**, *76*, 956.

(11) Bondar, O. P.; Rowe, E. S. *Biophys. J.* **1996**, *71*, 1440.

(12) Sommer, A.; Paltauf, F.; Hermetter, A. *Biochemistry* **1990**, *29*, 11134.

(13) Krasnowska, E. K.; Gratton, E.; Parasassi, T. *Biophys. J.* **1998**, *74*, 1984.

(14) Zeng, J. W.; Chong, P. L. *Biochemistry* **1991**, *30*, 9485.

(15) Chapman, C. F.; Fee, R. S.; Maroncelli, M. *J. Phys. Chem.* **1990**, *94*, 4929.

(16) Chapman, C. F.; Maroncelli, M. *J. Phys. Chem.* **1991**, *95*, 9095.

(17) Betts, T. A.; Zagrobelny, J.; Bright, F. V. *J. Supercrit. Fluids* **1992**, *5*, 48.

(18) Karmakar, R.; Samanta, A. *J. Phys. Chem. A* **2002**, *106*, 6670.

(19) Betts, T. A.; Zagrobelny, J.; Bright, F. V. *J. Am. Chem. Soc.* **1992**, *114*, 8163.

(20) Nowak, W.; Adamczak, P.; Balter, A.; Sygula, A. *J. Mol. Struct. THEOCHEM* **1986**, *32*, 13.

THEOCHEM **1986**, *32*, 13.

(21) Marks, D.; Proposito, P.; Zhang, H.; Glasbeek, M. *Chem. Phys. Lett.* **1998**, *289*, 535.

(22) Balter, A.; Nowak, W.; Pawelkiewicz, W.; Kowalczyk, A. *Chem. Phys. Lett.* **1988**, *143*, 565.

(23) Catalan, J.; Perez, P.; Laynez, J.; Garcia Blanco, F. *J. Fluoresc.* **1991**, *1*, 215.

(24) Parusel, A. B. J.; Schneider, F. W.; Kohler, G. *J. Mol. Struct. THEOCHEM* **1997**, *398-399*, 341.

- (25) Parusel, A. B. J.; Nowak, W.; Grimme, S.; Koehler, G. *J. Phys. Chem. A* **1998**, *102*, 7149.
- (26) Parusel, A. *J. Chem. Soc., Faraday Trans.* **1998**, *94*, 2923.
- (27) Ilich, P.; Prendergast, F. G. *J. Phys. Chem.* **1989**, *93*, 4441.
- (28) Heisel, F.; Miehe, J. A.; Szemik, A. W. *Chem. Phys. Lett.* **1987**, *138*, 321.
- (29) Bunker, C. E.; Bowen, T. L.; Sun, Y. P. *Photochem. Photobiol.* **1993**, *58*, 499.
- (30) Pal, S. K.; Mandal, D.; Bhattacharyya, K. *J. Phys. Chem. B* **1998**, *102*, 11017.
- (31) Lobo, B. C.; Abelt, C. J. *J. Phys. Chem. A* **2003**, *107*, 10938.
- (32) Samanta, A.; Fessenden, R. W. *J. Phys. Chem. A* **2000**, *104*, 8972.
- (33) Davis, B. N.; Abelt, C. J. *J. Phys. Chem. A* **2005**, *109*, 1295.
- (34) Mennucci, B.; Caricato, M.; Ingrosso, F.; Cappelli, C.; Cammi, R.; Tomasi, J.; Scalmani, G.; Frisch, M. J. *J. Phys. Chem. B* **2008**, *112*, 414.
- (35) Bakalova, S. M.; Kaneti, J. *Spectrochim. Acta Part A, Mol. Biomol. Spectrosc.* **2009**, *72*, 36.
- (36) Lakowicz, J. R.; Balter, A. *Biophys. Chem.* **1982**, *16*, 117.
- (37) Lakowicz, J. R.; Balter, A. *Biophys. Chem.* **1982**, *16*, 223.
- (38) Rollinson, A. M.; Drickamer, H. G. *J. Chem. Phys.* **1980**, *73*, 5981.
- (39) Nemkovich, N. A.; Baumann, W. *J. Photochem. Photobiol., A* **2007**, *185*, 26.
- (40) Novaira, M.; Biasutti, M. A.; Silber, J. J.; Correa, N. M. *J. Phys. Chem. B* **2007**, *111*, 748.
- (41) Sun, S.; Heitz, M. P.; Perez, S. A.; Colon, L. A.; Bruckenstein, S.; Bright, F. *V. Appl. Spectrosc.* **1997**, *51*, 1316.
- (42) Sengupta, B.; Guharay, J.; Sengupta, P. K. *Spectrochim. Acta, Part A* **2000**,

56A, 1433.

(43) Karukstis, K. K.; Frazier, A. A.; Martula, D. S.; Whiles, J. A. *J. Phys. Chem.* **1996**, *100*, 11133.

(44) Karukstis, K. K.; Frazier, A. A.; Loftus, C. T.; Tuan, A. S. *J. Phys. Chem. B* **1998**, *102*, 8163.

(45) Lissi, E. A.; Abuin, E. B.; Rubio, M. A.; Ceron, A. *Langmuir* **2000**, *16*, 178.

(46) Karukstis, K. K.; Zieleniuk, C. A.; Fox, M. J. *Langmuir* **2003**, *19*, 10054.

(47) Karukstis, K. K.; Suljak, S. W.; Waller, P. J.; Whiles, J. A.; Thompson, E. H. *Z. J. Phys. Chem.* **1996**, *100*, 11125.

(48) Novaira, M.; Moyano, F.; Biasutti, M. A.; Silber, J. J.; Correa, N. M. *Langmuir* **2008**, *24*, 4637.

(49) Chowdhury, P. K.; Halder, M.; Sanders, L.; Calhoun, T.; Anderson, J. L.; Armstrong, D. W.; Song, X.; Petrich, J. W. *J. Phys. Chem. B* **2004**, *108*, 10245.

(50) Lippert, E.; Lueder, W.; Moll, F.; Naegele, W.; Boos, H.; Prigge, H.; Seibold-Blankenstein, I. *Angew. Chem.* **1961**, *73*, 695.

(51) Lippert, E.; Lueder, W.; Boos, H. *Advances in Molecular Spectroscopy*; Pergamon Press Oxford, U.K., 1962.

(52) Tomin, V. I.; Hubisz, K.; Kwiek, P. *Opt. Spectrosc.* **2005**, *99*, 43.

(53) Changenet, P.; Plaza, P.; Martin, M. M.; Meyer, Y. H. *J. Phys. Chem. A* **1997**, *101*, 8186.

(54) Druzhinin, S. I.; Ernsting, N. P.; Kovalenko, S. A.; Lustres, L. P.; Senyushkina, T. A.; Zachariasse, K. A. *J. Phys. Chem. A* **2006**, *110*, 2955.

(55) Bose, S.; Adhikary, R.; Mukherjee, P.; Song, X.; Petrich, J. W. *J. Phys. Chem.*

B **2009**, *113*, 11061.

- (56) Abbyad, P.; Shi, X.; Childs, W.; McAnaney, T. B.; Cohen, B. E.; Boxer, S. G. *J. Phys. Chem. B* **2007**, *111*, 8269.
- (57) Halder, M.; Mukherjee, P.; Bose, S.; Hargrove, M. S.; Song, X.; Petrich, J. W. *J. Chem. Phys.* **2007**, *127*, 055101/1.
- (58) Pierce, D. W.; Boxer, S. G. *J. Phys. Chem.* **1992**, *96*, 5560.
- (59) Cohen, B. E.; McAnaney, T. B.; Park, E. S.; Jan, Y. N.; Boxer, S. G.; Jan, L. *Y. Science* **2002**, *296*, 1700.
- (60) Golosov, A. A.; Karplus, M. *J. Phys. Chem. B* **2007**, *111*, 1482.
- (61) Bashkin, J. S.; Mclendon, G.; Mukamel, S.; Marohn, J. *J. Phys. Chem.* **1990**, *94*, 4757.
- (62) Changenet-Barret, P.; Choma, C. T.; Gooding, E. F.; DeGrado, W. F.; Hochstrasser, R. M. *J. Phys. Chem. B* **2000**, *104*, 9322.
- (63) Maroncelli, M.; Fleming, G. R. *J. Chem. Phys.* **1987**, *86*, 6221.
- (64) Horng, M. L.; Gardecki, J. A.; Papazyan, A.; Maroncelli, M. *J. Phys. Chem.* **1995**, *99*, 17311.
- (65) Lewis, J. E.; Maroncelli, M. *Chem. Phys. Lett.* **1998**, *282*, 197.
- (66) Muhlfordt, A.; Schanz, R.; Ernsting, N. P.; Farztdinov, V.; Grimme, S. *Phys. Chem. Chem. Phys.* **1999**, *1*, 3209.
- (67) Jiang, Y.; McCarthy, P. K.; Blanchard, D. J. *Chem. Phys.* **1994**, *183*, 249.
- (68) Flory, W. C.; Blanchard, D. J. *Appl. Spectrosc.* **1998**, *52*, 82.
- (69) Palmer, P. M.; Chen, Y.; Topp, M. R. *Chem. Phys. Lett.* **2000**, *318*, 440.
- (70) Chen, Y.; Palmer, P. M.; Topp, M. R. *Int. J. Mass Spectrom.* **2002**, *220*, 231.

- (71) Agmon, N. *J. Phys. Chem.* **1990**, *94*, 2959.
- (72) Chowdhury, P. K.; Halder, M.; Sanders, L.; Arnold, R. A.; Liu, Y.; Armstrong, D. W.; Kundu, S.; Hargrove, M. S.; Song, X.; Petrich, J. W. *Photochem. Photobiol.* **2004**, *79*, 440.
- (73) Mukherjee, P.; Halder, M.; Hargrove, M.; Petrich, J. W. *Photochem. Photobiol.* **2006**, *82*, 1586.

**CHAPTER 5. EXCITED-STATE INTRAMOLECULAR HYDROGEN ATOM
TRANSFER AND SOLVATION DYNAMICS OF THE MEDICINAL PIGMENT
CURCUMIN**

A paper published in *The Journal of Physical Chemistry B*

Ramkrishna Adhikary,¹ Prasun Mukherjee,¹ Tak W. Kee^{2*} and Jacob W. Petrich^{1*}

Abstract

The potential use of the naturally occurring yellow-orange pigment curcumin as a photodynamic therapy agent is one of the most exciting applications of this medicinal compound. Although sub-nanosecond spectroscopy has been used to investigate the photophysical processes of curcumin, the time resolution is insufficient to detect important and faster photo-induced processes, including solvation and excited state intramolecular hydrogen atom transfer (ESIHT). In this study, the excited state photophysics of curcumin is studied by means of ultrafast fluorescence upconversion spectroscopy. The results show two decay components in the excited-state kinetics with time scales of 12-20 ps and ~100 ps in methanol and ethylene glycol. The resulting prominent isotope effect in the long component

Reprinted with permission from *The Journal Physical Chemistry B* 2009, 113(15), 5255-5261. Copyright (2009) American Chemical Society.

¹Department of Chemistry, Iowa State University, Ames, Iowa 50011-3111.

²School of Chemistry and Physics, University of Adelaide, Adelaide, South Australia, 5005, Australia.

* To whom correspondence should be addressed.

upon deuteration indicates that curcumin undergoes ESIHT in these solvents. The short component (12-20 ps) is insensitive to deuteration, and multi-wavelength fluorescence upconversion results show that this decay component is due to solvation of excited-state curcumin.

Introduction

Curcumin, 1,7-bis(4-hydroxy-3-methoxyphenyl)-1,6-heptadiene-3,5-dione, is a naturally occurring yellow-orange pigment derived from the rhizomes of *Curcuma longa* (turmeric). It has been traditionally used as a spice and food coloring in Indian cooking and medicine.¹ Currently, it is the subject of a large number of investigations in the fields of biology, medicine, and pharmacology owing to its profound effects on human health. Curcumin exhibits a variety of biological and photochemical properties, including antioxidant, anti-inflammatory, and anticancer activity.²⁻⁶ Recently, it was also established that curcumin has the ability to prevent protein aggregation in debilitating diseases such as Alzheimer's and Parkinson's.^{7,8} Curcumin has two tautomeric forms, namely the β -diketone and keto-enol. It has been shown that curcumin exists predominantly as a keto-enol tautomer in a number of solvents with various polarities using results from NMR spectroscopy.⁹ It follows that strong intramolecular hydrogen bonding is present in the keto-enol tautomer of curcumin, of which the chemical structure is shown in Figure 5.1, providing a favorable interaction for stabilization of this tautomeric form.

Recent research shows that curcumin has great potential to be an effective photodynamic agent.¹⁰⁻¹⁷ In particular, studies have demonstrated the use of curcumin to treat melanoma.¹⁸⁻²⁴ It was shown that the photodynamic action is greatly enhanced in the presence of light for destruction of tumor cells.¹⁵⁻¹⁷ It has been shown that stable

photoproducts are not responsible for the medicinal effects of curcumin.¹⁰ Photolytically produced active oxygen species such as singlet oxygen, hydroxyl radical, superoxide or hydrogen peroxide are mainly suggested for its activity.^{10,11,25-29} In addition, Slobodan et al. demonstrated that H-atom transfer is a preferred antioxidant mechanism of curcumin by laser flash photolysis and pulse radiolysis.³⁰ Currently, there are significant interests in developing a detailed level of understanding in the photophysics and photochemistry of curcumin in order to further exploit its medicinal effects.

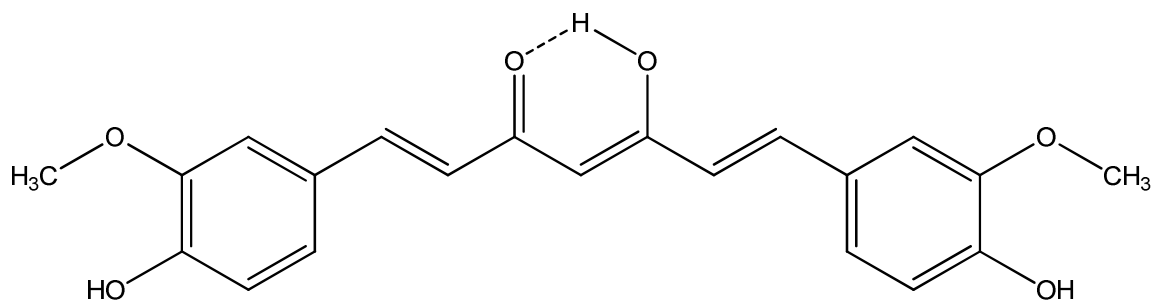


Figure 5.1. Structure of the keto-enol form of curcumin.

Several studies have focused on using time-resolved fluorescence spectroscopy to investigate the excited state photophysics of curcumin in organic solvents on the sub-nanosecond time scale, aiming to provide fundamental understanding to elucidate the medicinal properties of curcumin.^{12,18,31-33} In all cases, these studies focused on excited state intramolecular hydrogen atom transfer (ESIHT) of curcumin because this phenomenon has been associated with the medicinal properties of other pigment molecules, including hypericin and hypocrellin.³⁴⁻³⁸ For instance, two of these studies agree that the fluorescence lifetime of curcumin in methanol has a dominant component with a time constant of roughly 130 ps. This decay component, however, was assigned to different molecular processes, *i.e.* solvation³³ and ESIHT,³¹ in the two studies. Here, we perform ultrafast fluorescence

upconversion studies to address this issue in the literature. Using a time resolution of 300 fs and deuterated curcumin, we show unambiguously that ESIHT occurs with a time scale of approximately 100 ps. Furthermore, the similarity between the time scale of ESIHT and the measured fluorescence lifetime indicates that ESIHT is a major photophysical process in the deactivation of the excited state.

Owing to femtosecond time resolution of ultrafast fluorescence upconversion, in addition to the ESIHT component, a short-lived fluorescence decay component with a time scale of 12 ± 2 ps was also detected at 520 nm for curcumin in methanol. In ethylene glycol, the short-lived component has a time constant of 20 ± 3 ps. This fast decay component was previously unobserved because of the insufficient time resolution used. Solvation is expected to be present in the relaxation dynamics due to the substantial change in dipole moment reported for curcumin.³¹ In the present work, using results from multi-wavelength fluorescence upconversion measurements, we definitively assign this decay component to solvation dynamics. The solvation correlation function $C(t)$, which provides a quantitative measure of the time scale of solvation dynamics, has a fast component which is shorter than the instrument response function of 300 fs, and a slow component of 12 ± 2 ps in methanol and 30 ± 5 ps in ethylene glycol. These results strongly support the assignment of the 12 – 20-ps component observed in the fluorescence upconversion results to solvation.

Experimental Section

Materials. Curcumin (purity ~ 70% HPLC) was purchased from Sigma Aldrich and used without further purification. High purity curcumin ($\geq 98.5\%$) was obtained from Alexis Biochemicals. This highly purified product is virtually free of the other two closely related curcuminoids (~ 30%) which are also found in turmeric, namely demethoxy- and bis-

demethoxycurcumin. While the experiments performed in this work involved using curcumin from the first source, fluorescence upconversion and time correlated single photon counting measurements were repeated using high purity curcumin to ensure the roles of demethoxy- and bis-demethoxycurcumin are negligible. Methanol, ethylene glycol and chloroform were obtained from Fisher Scientific and used without further purification. In addition, chloroform was also dried over type 4A molecular sieves prior to use. Methanol- d_4 (purity 99.8%) and ethylene glycol $O,O-d_2$ (purity 98%) were purchased from Cambridge Isotope Laboratories, Inc. and used without further purification. For the experiments on curcumin in deuterated solvents, curcumin was allowed to equilibrate in these solvents for 48 hours to ensure complete exchange of the enolic hydrogen with deuterium.

Steady-state measurements. Steady-state absorption spectra were obtained on Hewlett Packard 8453 UV-visible spectrophotometer with 1-nm resolution. Steady state fluorescence spectra were obtained on a Spex Fluoromax-4 with a 3-nm bandpass and corrected for lamp spectral intensity and detector response. All the samples were excited at 407 nm for steady state fluorescence measurement. For both fluorescence and absorption measurements, a 5-mm path-length quartz cuvette was used. All experiments were done at room temperature.

Time-resolved measurements. The apparatus for fluorescence upconversion is described in detail elsewhere.³⁹ Briefly it is based on a homebuilt mode-locked Ti:sapphire oscillator producing femtosecond pulses at a fundamental wavelength of 814 nm with a repetition rate of 82 MHz. Frequency doubled pulses (407 nm) were used to excite the sample and the residual of the fundamental was used as the gate pulse to upconvert the fluorescence signal. First, the fluorescence signal was collected using a 10 \times objective lens.

Then, the gate pulse and fluorescence signal were focused onto a 0.4 mm type-I BBO crystal to generate the sum frequency light, which was detected by a photomultiplier tube mounted on a monochromator. The full-width-at-half-maximum (FWHM) of the instrument response function is 300 fs, obtained by the cross-correlation function of the frequency doubled and the fundamental light. A rotating sample cell was used and all experiments were performed at room temperature.

Solvation dynamics are analyzed and quantified by means of the solvation correlation function, $C(t)$,

$$C(t) = \frac{\nu(t) - \nu(\infty)}{\nu(0) - \nu(\infty)} \quad (5.1)$$

where $\nu(0)$, $\nu(t)$ and $\nu(\infty)$ denote the peak frequency of the emission spectra at time zero, t and infinity. The “zero time” emission spectrum has been approximated using the emission spectrum of curcumin in hexanes, according to the method of Fee and Maroncelli.⁴⁰ The $\nu(\infty)$ is taken as the peak frequency of the steady-state fluorescence spectrum. $\nu(t)$ is determined by taking the maxima from the log-normal fits as the time-resolved emission maximum which is constructed according to the procedure described by Fee and Maroncelli⁴¹ using steady-state emission spectrum and fitting parameters from wavelength-resolved decay traces. In most cases, however, the broad spectra result in uncertainty in the exact position of the emission maxima. Thus, using the signal-to-noise ratio and width of the spectrum (including “zero-time”, steady-state, or time-resolved emission spectrum) as guides, we have determined the typical uncertainties as follows: time-resolved emission ($\sim \pm 200 \text{ cm}^{-1}$), “zero-time” \sim steady-state ($\sim \pm 100 \text{ cm}^{-1}$). These uncertainties are used to compute error

bars for the $C(t)$. The fractional solvation at 300 fs was calculated using $f_{300\text{fs}} = 1 - C(t = 300 \text{ fs})$.

Time-resolved fluorescence lifetime anisotropy data were collected using the time-correlated single photon counting (TCSPC) technique. Our apparatus has been described elsewhere.³⁹ Recent modifications in the experimental set-up include the replacement of NIM-style electronics by the Becker & Hickl photon counting module Model SPC-630. With this modified system, the full-width-at-half-maximum of the instrument-response function is $\sim 40 - 45$ ps. The acquisition time window had a width of 3.33 ns with 1024 channels, corresponding to 3.25 ps per channel. All experiments were performed using 407 nm excitation obtained by frequency doubling of 814 nm fundamental light. For anisotropy measurements, 65,000 counts were collected at the peak channel for parallel polarization. A normalization factor was then applied to the TCSPC trace such that the maximum count was 10,000 due to requirement of the analysis software. A cuvette of 1-cm path length was used for the time-resolved anisotropy measurement. The anisotropy measurement involved collecting two fluorescence signals with polarizations parallel (I_{\parallel}) and perpendicular (I_{\perp}) to the excitation polarization in order to determine the anisotropy decay $r(t)$, as follows.

$$r(t) = \frac{I_{\parallel}(t) - I_{\perp}(t)}{I_{\parallel}(t) + 2I_{\perp}(t)} \quad (5.2)$$

The anisotropy data were obtained from simultaneous fitting of parallel and perpendicular decays.⁴² The decay of the anisotropy reflects the time scale of orientational relaxation.

Results and Discussions

UV-Vis absorption and fluorescence spectra of curcumin. Figure 5.2 illustrates the absorption and fluorescence spectra of curcumin in methanol, ethylene glycol, the

corresponding deuterated solvents, and chloroform. The spectra obtained in methanol and chloroform were found to be in agreement with the previous results with respect to the spectral shape and peak position.³² While the UV-Vis absorption spectra are relatively insensitive to the solvent used, the fluorescence spectra exhibit a strong solvent effect. The strong dependence of the Stokes shift on solvent polarity indicates that the excited state dipole moment of curcumin is considerably larger than that of its ground state. This property also implies that solvation dynamics play an important role in the excited state relaxation of curcumin, as will be discussed further.

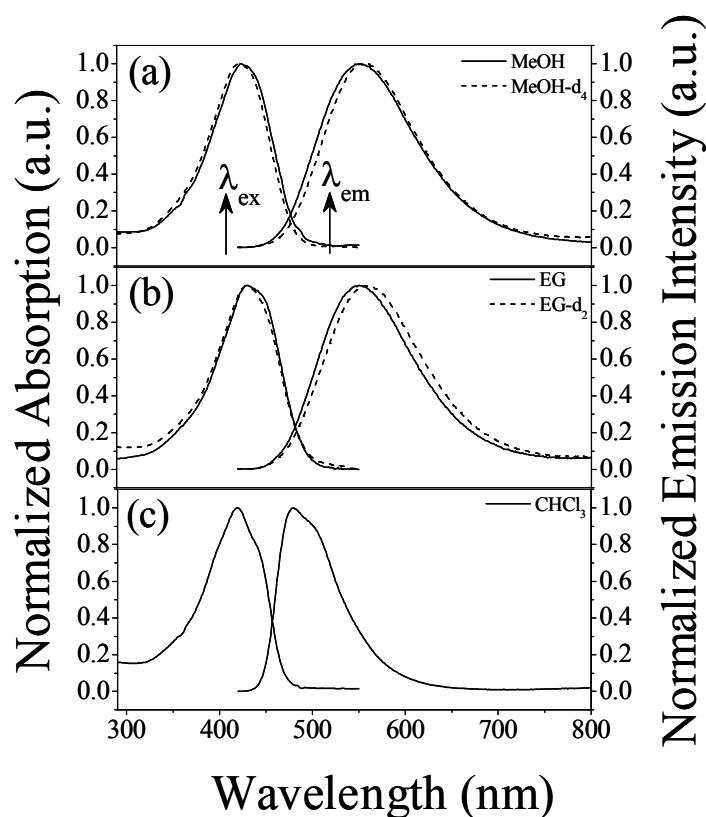


Figure 5.2. Normalized absorption and fluorescence spectra of curcumin in (a) methanol (MeOH), deuterated methanol (MeOH- d_4), (b) ethylene glycol (EG), deuterated ethylene glycol (EG- d_2) and (c) chloroform (CHCl_3).

Fluorescence upconversion and excited state intramolecular hydrogen atom transfer of curcumin. The excitation and probe wavelengths in the fluorescence upconversion experiments are 407 nm and 520 nm, respectively, as shown in Figure 5.2. While having the excitation wavelength at 407 nm efficiently promotes curcumin from the ground state to the excited state, monitoring the time resolved fluorescence at 520 nm, which is on the blue side of the fluorescence spectrum, provides the good signal-to-noise ratio and sensitivity to record early time events in the excited state relaxation process.

Figure 5.3a shows the fluorescence upconversion signals of curcumin in methanol and deuterated methanol as a function of time. The time-resolved fluorescence signal of curcumin in methanol (red) was fitted with a bi-exponential function with time constants of 12 ± 2 ps and 70 ± 10 ps with nearly equal amplitudes, see Table 5.1. In order to demonstrate the effect of deuteration, fluorescence upconversion of curcumin in deuterated methanol was investigated. In deuterated methanol (blue), while the first decay component remains identical within experimental error, a prominent isotope effect is observed in the second component. The decay time constant of this component is increased to 120 ± 20 ps upon deuteration. Fluorescence upconversion experiments were also performed with pure ($\geq 98.5\%$) curcumin in methanol and the same fast and slow components were obtained as mentioned above.

The appearance of this prominent isotope effect of 1.7 requires equilibration of curcumin in deuterated methanol for a period of approximately 48 hours. Exchange of the enolic hydrogen of curcumin with the deuterium of methanol- d_4 is expected to occur on this time scale, which is consistent with deuteration of a similar system.⁴³ In contrast, the inset of Figure 5.3a shows the fluorescence upconversion results of curcumin in methanol and

deuterated methanol with an equilibration time of only 15 minutes. The two traces are identical within experimental error, clearly showing the absence of an isotope effect at early equilibration time. The results shown in Figure 5.3a and the inset yield the following important insights. First, the observed isotope effect correlates with the enolic H/D exchange of curcumin, supporting the excited state hydrogen atom transfer character of the kinetics. Second, the lack of isotope effect at early equilibration time indicates that the hydrogen atom transfer process is intramolecular in nature, as opposed to a consequence of intermolecular hydrogen bonding with the surrounding solvent molecules. Additionally, this result also indicates that the observed isotope effect is unrelated to suppression of radiationless deactivation of excited state curcumin in deuterated methanol. Therefore, these results clearly indicate that ESIHT, which occurs with a time constant of 70 ps in methanol, is a major pathway of non-radiative decay in curcumin.

The effect of solvent on the fluorescence upconversion signal is shown in Figure 5.3b. In ethylene glycol (red), the time-resolved fluorescence signal also exhibits a bi-exponential decay, similar to methanol. However, the time scales of the decays are longer; the time constants of the decays are 20 ± 3 ps and 105 ± 15 ps, with nearly equal amplitudes. Deuteration of ethylene glycol produces a similar isotope effect, *i.e.*, the time constant of the short-lived decay component remains unchanged but that of the long-lived component is increased by a factor of 2.1, see Table 5.1. The presence of this notable effect further supports our assignment of the long-lived decay component to ESIHT. The ESIHT time constants of curcumin reported in this study are comparable to those of 7-azaindole in methanol.⁴⁴

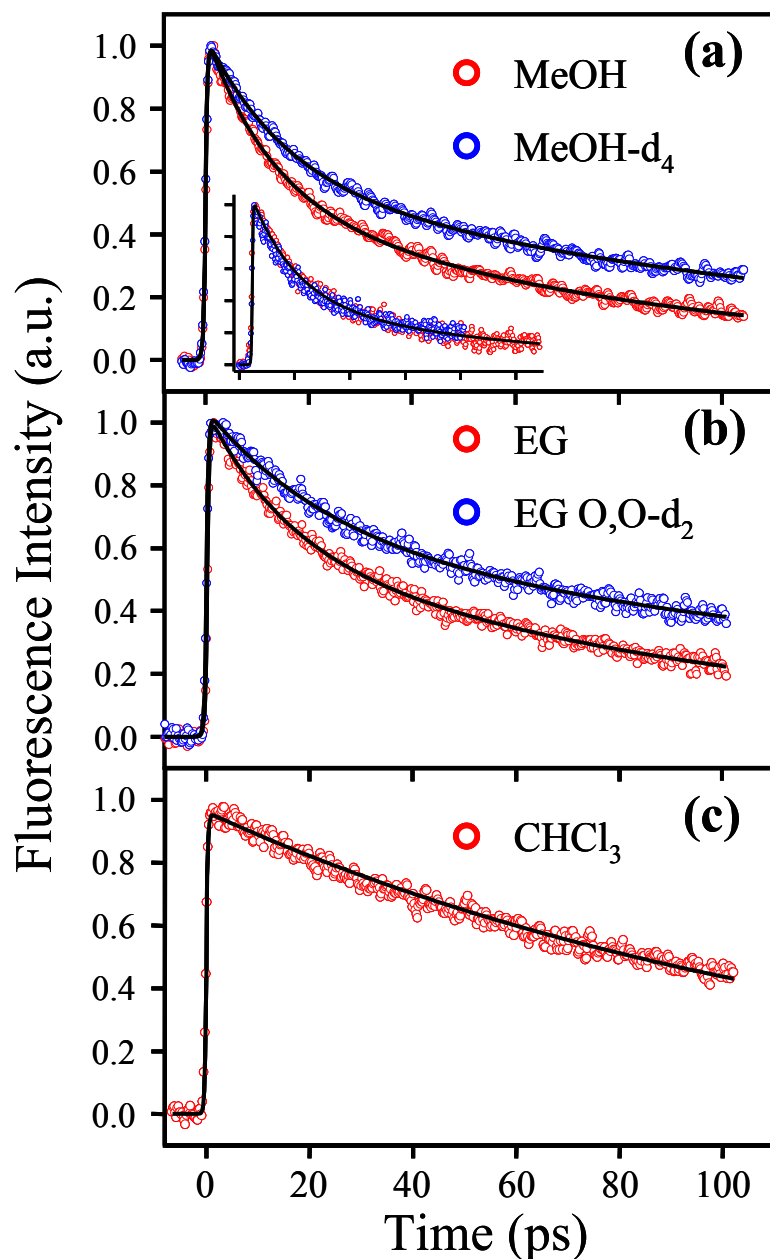


Figure 5.3. Fluorescence upconversion decays of curcumin in (a) methanol (MeOH), (b) ethylene glycol (EG) and (c) chloroform (CHCl_3); corresponding decays in the deuterated analogs in (a) and (b) show a prominent isotope effect. The inset in (a) shows the virtually identical traces prior to the H/D exchange (equilibration time of ~ 15 minutes), which indicates that the isotope effect observed after equilibration (48 hours) is independent of solvent effects. While the decays in (a) and (b) exhibit bi-exponential nature, the trace in (c) is single-exponential. All samples were excited at 407 nm and fluorescence was collected at 520 nm.

The ESIHT for curcumin in methanol and ethylene glycol occurs, within experimental error, on the same time scale: 70 ± 10 ps and 105 ± 15 ps, respectively (Table 5.1). While the solvent viscosity differs by a factor of ~ 30 between methanol and ethylene glycol (0.59 cP and 16.1 cP, respectively, at 20°C), the lack of dependence of the ESIHT time scale on viscosity indicates that ESIHT occurs through small amplitude molecular motions, which do not heavily involve the surrounding solvent molecules. In this regard, ESIHT in curcumin is similar to that in hypericin, for which the rate of ESIHT is uncorrelated to solvent viscosity.^{37,38} In another related species, 2-hydroxyacetophenone, it was determined that small amplitude molecular vibrations are responsible for the initial events in ESIHT and the O–H vibration is unaffected in this process.⁴⁵ Therefore, our results indicate that ESIHT in curcumin is similar to that of the systems in which ESIHT has a weak dependence on solvent viscosity.

Table 5.1. Fluorescence upconversion decay parameters for curcumin in different solvent systems^a

Solvent	a_1^b	τ_1 (ps)	τ_2 (ps)
Methanol	0.45	12	70
Methanol-d ₄	0.45	12	120
Ethylene glycol	0.45	20	105
Ethylene glycol O,O-d ₂	0.45	20	220
Chloroform ^c	1.0	130	-

^a The fluorescence upconversion traces, $f(t)$, were fitted with the multi-exponential function $f(t) = a_1 \exp(-t/\tau_1) + a_2 \exp(-t/\tau_2)$. The a_1 , a_2 and τ_1 were kept constant during the fitting process. All parameters have a relative error of $\pm 15\%$.

^b $a_1 + a_2 = 1$.

^c Chloroform was dried over molecular sieves prior to use. Water content was assessed with a coulometric Karl Fischer Titration (Mettler Toledo DL 36). % wt H₂O=0.002

Chloroform is a polar aprotic solvent with which curcumin is not involved in intermolecular H-bonding. Care was taken to exclude water in chloroform because it has

been reported that water quenches the fluorescence by forming a non-fluorescent stable complex with excited state curcumin.⁴⁶ In addition, the presence of a hydrogen-bonding impurity might complicate the excited state dynamics.⁴⁷ The fluorescence upconversion decay trace of curcumin in chloroform is shown in Figure 5.3c. The decay trace is best fitted with a single exponential decay function with a time constant of 130 ± 20 ps. This decay component is assigned to ESIHT for the following reasons. First, the decay trace is unrelated to solvation dynamics of curcumin in chloroform since solvation in chloroform occurs with time constants of 0.285 ps and 4.15 ps, as determined by Horng et al.⁴⁸ Consequently, because intermolecular hydrogen bonding with the solvent is impossible between curcumin and chloroform, the observed kinetics are attributed to an intramolecular interaction, which we assign to an intramolecular process, namely ESIHT. While the ESIHT time of a related molecule, 3-hydroxyflavone, is 240 fs in methylcyclohexane,⁴⁷ the absence of such a short component in Figure 5.3c indicates that ESIHT in curcumin does not occur as rapidly as in 3-hydroxyflavone. In fact, the 130-ps ESIHT time constant of curcumin in chloroform shows good agreement with those of curcumin in methanol and ethylene glycol.

Early time solvation dynamics. In addition to ESIHT, the fluorescence upconversion results also reveal that there is a short-lived component with a time scale of 12 ps in methanol, which is likely to be undetectable in TCSPC because of insufficient time resolution. Solvation, in addition to ESIHT, is expected to play a role in the excited state relaxation dynamics due to the significant dipole moment change reported for curcumin: $\Delta\mu = 6.1$ D.³¹ Such a $\Delta\mu$ is comparable to that of Coumarin 153 ($\Delta\mu \approx 8$ Debye),^{41,48} which is a standard probe molecule for solvation dynamics. Additionally the fluorescence spectra

exhibit a Stokes shift that is largely dependent on solvent polarity, implying that solvation may play a major role in the relaxation of the excited state in addition to ESIHT.

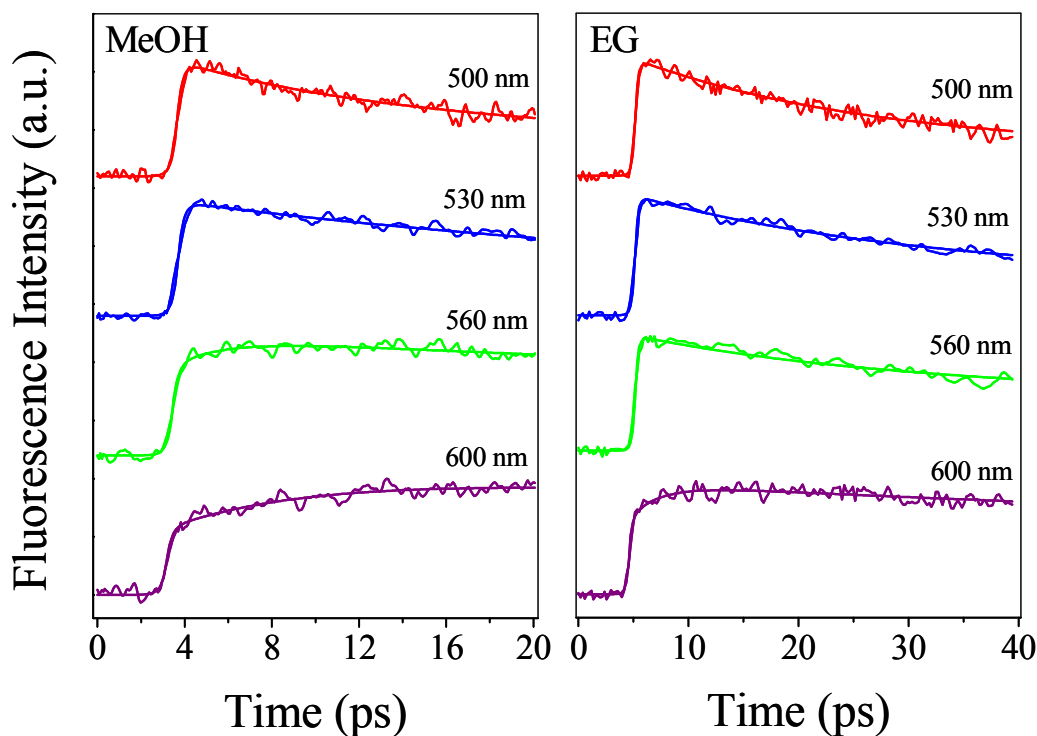


Figure 5.4. Representative normalized wavelength resolved fluorescence upconversion traces of curcumin in (a) methanol and (b) ethylene glycol. Time-resolved emission spectra were constructed by collecting upconversion traces over a range from 500 to 600 nm at intervals of 10 nm. The time resolved traces at the red end (600 nm) show a growing component, which is the signature of solvation dynamics.

To demonstrate the presence of solvation, we performed fluorescence upconversion experiments on curcumin at up to 11 wavelengths spanning the range of 500 – 600 nm in methanol and ethylene glycol. Representative decay traces are shown in Figure 5.4. For curcumin in methanol, all the transients are well fitted to a bi-exponential function with a fixed long decay component of 140 ps (fluorescence lifetime). In methanol, at the blue end of the emission spectrum (500 nm), the result shows a fast decay component of 10 ps (56%). At 530 nm, the time constant of the fast portion becomes 17 ps (41%). At 560 nm, a rising

components is observed with a rise time of 1.6 ps. The time constant of this rising component becomes 6.9 ps at 600 nm. The wavelength dependent behavior of the fast component is the signature of solvation dynamics. As shown in Figure 5.4, a similar behavior is also observed for curcumin in ethylene glycol, where the long decay component was also fixed at its lifetime of 210 ps. These results clearly indicate the major role of solvation in the relaxation of the excited state.

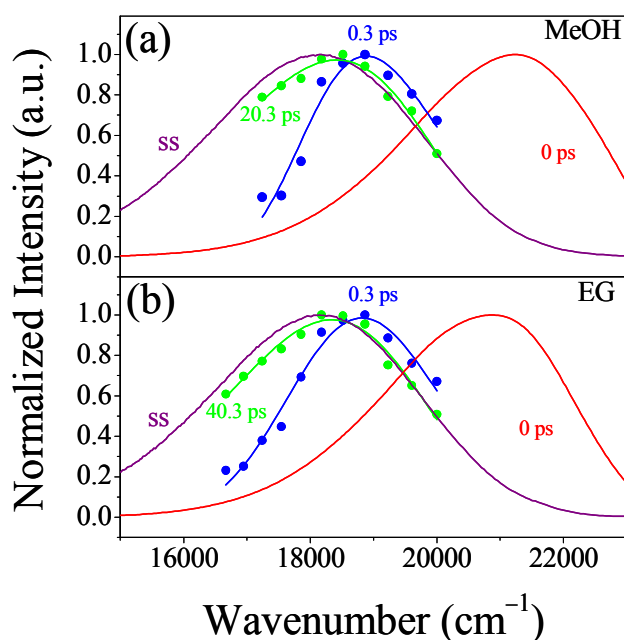


Figure 5.5. Normalized time resolved emission spectra of curcumin in methanol (MeOH) and ethylene glycol (EG). Steady-state (ss) and “zero-time” ($t = 0$ ps) spectra are included. Almost 70 % of the solvation is complete in both systems within the time resolution of our instrument (300 fs).

In Figure 5.5a, the emission spectra of curcumin in methanol at 0 ps, 0.3 ps, 20.3 ps and steady state ($t \rightarrow \infty$) are shown. For curcumin in ethylene glycol, the trend of emission spectral shift is similar to methanol but it occurs at a slower rate. For instance, it takes the

emission spectrum approximately 40 ps to almost fully recover to the steady state spectrum, as shown in Figure 5.5b.

Table 5.2. Solvation correlation function decay parameters for curcumin in different solvent systems

Solvent	$f_{300\text{fs}}^a$	a_1	$\tau_1(\text{ps})^b$	$\tau_2(\text{ps})$	$\langle\tau\rangle(\text{ps})$
Methanol	0.75 ± 0.04	0.71 ± 0.02	0.05	12 ± 2	3.5
Ethylene glycol	0.75 ± 0.05	0.73 ± 0.02	0.05	30 ± 5	8.2

^a $f_{300\text{fs}}$: fractional solvation at 300 fs

^b The faster component was fixed at 0.05 ps during fitting.

The $C(t)$ of methanol and ethylene glycol are presented in Figure 5.6 and the solvation parameters are shown in Table 5.2. In particular, the $f_{300\text{fs}}$ values show that more than 70% of solvation is completed in both the solvents within the time resolution (300 fs) of the instrument. The solvation correlation function shows an initial fast response (50 fs, fixed) followed by a slow response. As shown by previous studies on similar systems, this fast response is attributed to ultrafast librational motion of the solvents.⁴⁸⁻⁵⁰ The time constants of the other component are 12 ± 2 ps and 30 ± 5 ps in methanol and ethylene glycol respectively. These time scales are highly consistent to the fast component in the fluorescence upconversion results at 520 nm of curcumin in these solvents, see Figure 5.3 and Table 5.1. Based on the results from the studies on solvation dynamics, the short-lived component in the fluorescence upconversion results for curcumin in methanol and ethylene glycol at 520 nm has been assigned to solvation. In addition, the average solvation time in

methanol and ethylene glycol are 3.5 ps and 8.2 ps respectively, which are in excellent agreement with previous studies using Coumarin-153 as the probe molecule.⁴⁸

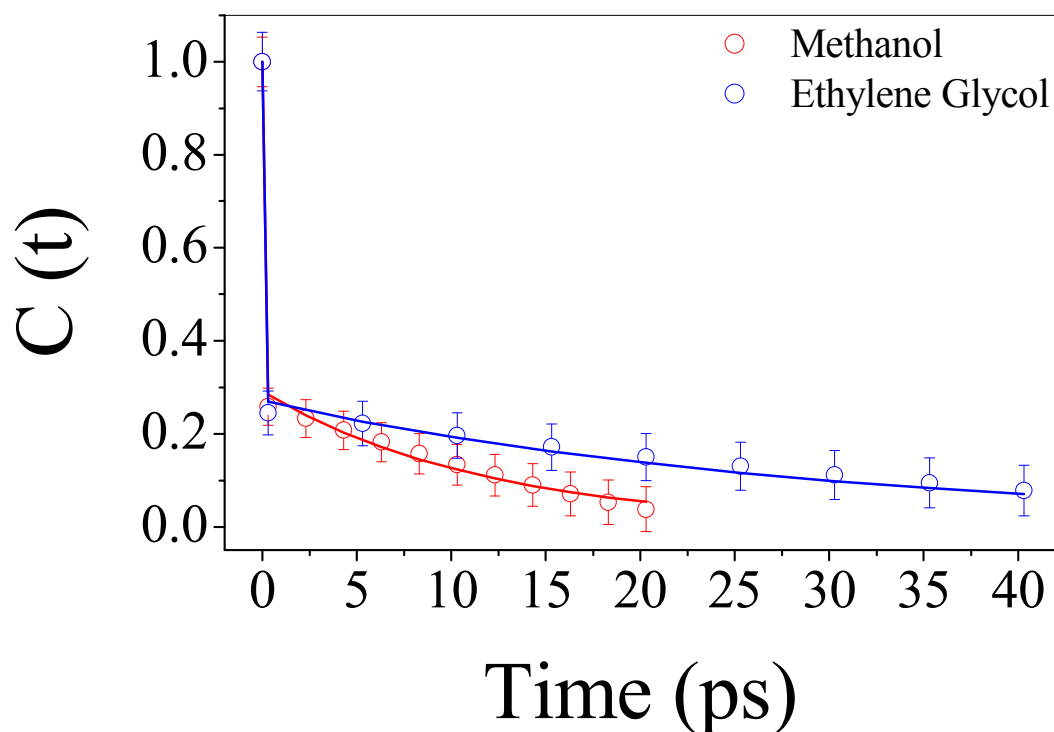


Figure 5.6. The solvation correlation function, $C(t)$ of curcumin in methanol and ethylene glycol obtained from fluorescence upconversion experiments. Solvation correlation function is fitted with bi-exponentials decay function. Both the solvent showed a same initial fast component of 50 fs but a different slow component of 12 ps (methanol) and 30 ps (ethylene glycol).

Fluorescence Anisotropy of Curcumin. The effects of solvation and ESIHT on the rotational motion of curcumin are examined with fluorescence anisotropy studies. To gain insight into the sensitivity of orientation of curcumin to the environment, anisotropy experiments were carried out in methanol and ethylene glycol. The anisotropy parameters are shown in Table 5.3; the anisotropy decays are single exponential, which are well described with the equation $r(t) = r_0 \exp[-t/\tau^{(r)}]$, where r_0 and $\tau^{(r)}$ are the initial anisotropy

value and molecular rotational time, respectively. The anisotropy results reveal that r_0 has values of 0.37 and 0.36 in methanol and ethylene glycol, respectively, very close to the theoretical limit of 0.4.

The anisotropy results also reveal that $\tau^{(r)}$ of curcumin is 200 ps in methanol and 5080 ps in ethylene glycol. The difference between the $\tau^{(r)}$ of methanol and ethylene glycol can be understood by taking into account the Debye-Stokes-Einstein relation, which states that $\tau_{\text{DSE}}^{(r)} = V\eta/k_{\text{B}}T$. Using $\eta_{\text{methanol}} = 0.59$ cP, $\eta_{\text{ethylene glycol}} = 16.1$ cP (with $T = 20^\circ\text{C}$) and the estimated hydrodynamic radius of curcumin of 8.5 \AA ,⁵¹ $\tau_{\text{DSE}}^{(r)}$ of methanol and ethylene glycol are estimated to be 375 ps and 10200 ps, respectively. Although the Debye-Stokes-Einstein relation overestimates $\tau^{(r)}$ of curcumin for both methanol and ethylene glycol, the ratio between the predicted $\tau^{(r)}$ agree very well with the experimental results, indicating, as expected, that viscosity is the determining factor for the molecular rotational time of curcumin.

The comparison between the time scales of molecular rotation and other processes including solvation and ESIHT can provide important insight into the coupling between molecular processes. In the case of curcumin in methanol, we have established that solvation and ESIHT occur on the time scales of 12 ps and 70 ps, respectively. Relative to the time scale of molecular rotation of 200 ps, the results indicate that the coupling between rotation and either of solvation and ESIHT is weak. On the other hand, the coupling is negligible for curcumin in ethylene glycol. This phenomenon is clearly demonstrated by comparing the molecular rotation time of 5080 ps to the time scales of solvation of 30 ps and ESIHT of 105 ps.

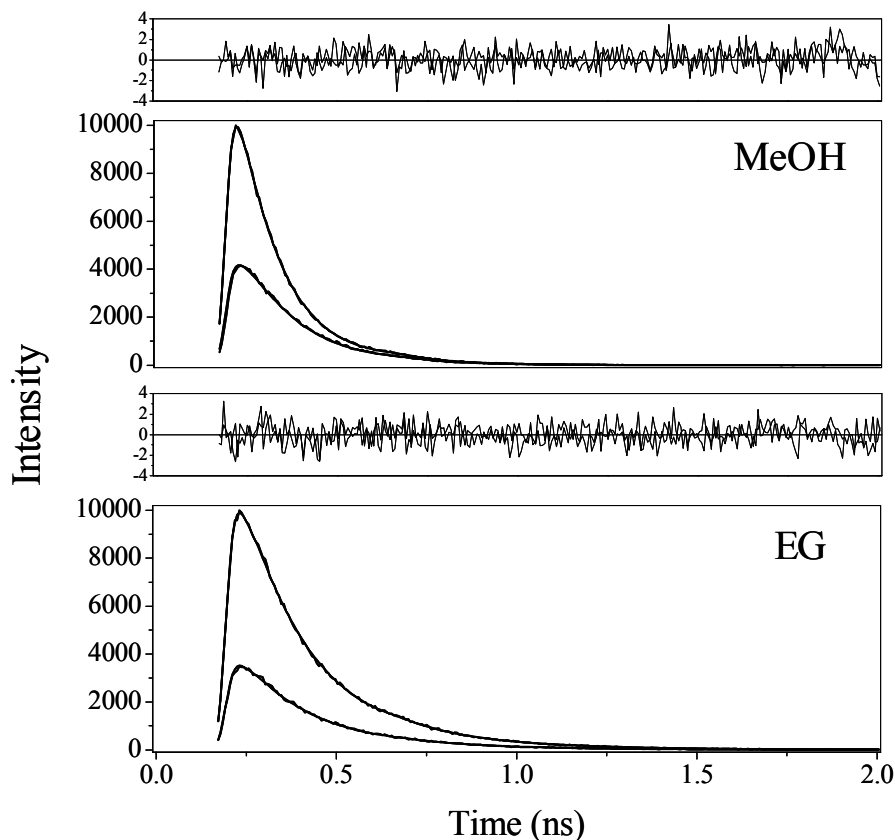


Figure 5.7. Polarized fluorescence traces and residuals of fits for curcumin in methanol (MeOH) and ethylene glycol (EG). Fitting parameters are given in Table 5.3. The upper trace represents that emission is collected parallel and the lower trace is collected perpendicular to the excitation polarization. $\lambda_{\text{ex}} = 407 \text{ nm}$, $\lambda_{\text{em}} \geq 500 \text{ nm}$.

Table 5.3. Time-resolved fluorescence anisotropy data of curcumin in different systems

System	r_0	$\tau^{(r)}$ (ps)	$\tau^{(r)}_{\text{calc.}}$ (ps)
Curcumin/MeOH ^a	0.37 ± 0.01	200 ± 20	375
Curcumin/EG ^a	0.36 ± 0.02	5080 ± 1100	10200

^a The errors are based on the average of three measurements. Fluorescence anisotropy decays are fit to the form: $r(t) = r_0 \exp[-t/\tau^{(r)}]$. In all cases $\chi^2 \leq 1.3$.

Conclusion

In summary, we have demonstrated with fluorescence upconversion that curcumin undergoes excited state intramolecular hydrogen atom transfer (ESIHT) and it plays a major role in the photophysics of curcumin. Photoexcitation of curcumin produces a fluorescence signal which decays with a bi-exponential fashion on the order of 12-20 ps and 70-105 ps. The long-lived signal, which exhibits a prominent isotope effect in deuterated solvents, is attributed to ESIHT. Additionally, the results show that ESIHT is insensitive to solvent viscosity, implying that only small amplitude motions are coupled to ESIHT of curcumin. We have also presented results from the studies on multi-wavelength fluorescence upconversion of curcumin. The results show that only decay components are present in the fluorescence upconversion signals on the blue side of the emission spectrum. A rising component, however, appears on the red side of the emission spectrum, clearly indicating the presence of solvation in the relaxation dynamics. We have shown that curcumin exhibits a long solvation component of ~12 ps in methanol and ~30 ps in ethylene glycol. Results from fluorescence anisotropy studies show that curcumin in methanol and ethylene glycol have $\tau^{(r)}$ of 200 ps and 5080 ps, respectively. By comparing the time scales of solvation and ESIHT with $\tau^{(r)}$, we conclude that the coupling between molecular rotation to other molecular processes is weak for curcumin in methanol. Additionally, in the case of curcumin in ethylene glycol, the coupling is essentially negligible.

Acknowledgment. TWK acknowledges a research grant from the Australian Research Council and National Health and Medical Research Council Network “Fluorescence Applications in Biotechnology and Life Sciences.”

Appendix

Origin (and Lack) of Isotope Effect

The kinetic isotope effect (KIE) arises from the difference in zero-point energies (*ZPE*) of the ground state and the transition state (TS) among the different isotopes.^{52,53} The *ZPE* is calculated by

$$ZPE = \frac{1}{2} h \nu \quad (5.3)$$

where h is the Planck constant and ν is the frequency of the vibrational mode being considered. The vibrational frequency can be estimated by using an equation that accounts the simple harmonic motion of the bond

$$\nu = \frac{1}{2\pi} \sqrt{\frac{k_f}{\mu}} \quad (5.4)$$

where the reduced mass, $\mu = m_1 m_2 / (m_1 + m_2)$. Eq 5.4 shows that ν is directly proportional to the square root of the force constant k_f and inversely proportional to the square root of the reduced mass, μ . As isotopic substitution has no effect on the electron density of the bond, k_f remains essentially same for both isotopic bonds. The vibrational frequency (ν) of the bond is lowered when a lighter atom is replaced by its heavier isotope because of the higher reduced mass μ and hence, the *ZPE* is lowered (Figure 5.8). If we consider transition state (TS) theory, it can easily be shown that the isotope effect originates from the exponentiated activation energies.⁵⁴ If we consider hydrogen (H) versus deuterium (D) transfer, the isotope effect can be expressed as⁵⁴

$$\frac{k_H}{k_D} \approx \exp[-(\Delta G_H^{TS} - \Delta G_D^{TS}) / RT] \quad (5.5)$$

where $\Delta G_H^{TS} - \Delta G_D^{TS} \approx ZPE_H^{TS} - ZPE_H^R - ZPE_D^{TS} + ZPE_D^R$. The reactant ZPE^R difference is larger for H than D, i.e., $(ZPE_D^{TS} - ZPE_D^R) > (ZPE_H^{TS} - ZPE_H^R)$. This type of KIE is $\sim 2-10$ at room temperature and follows the Arrhenius temperature dependence.

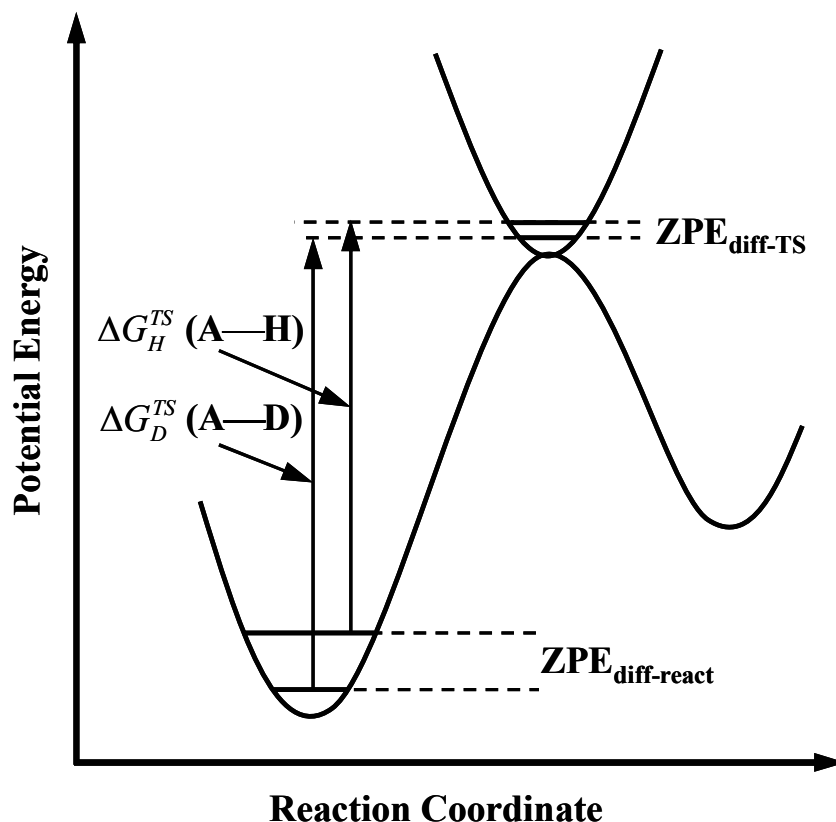


Figure 5.8. Different activation energies for H and D resulting from their different zero-point energies (ZPE) at the ground and transition state.

Sometimes a KIE of 50 or larger is observed for comparisons of H versus D.^{52,53} Such type of dramatic isotope effect has been attributed to quantum mechanical tunneling. A deviation of Arrhenius plot from linearity at low temperature is also a common observation for tunneling. Tunneling is the phenomena by which a particle transfers through the reaction barrier rather than over it due to its wave-like properties.^{53,55} The de Broglie wavelength is $\lambda = h/(2mE)^{1/2}$, where m is the particle's mass and E is its energy. This wavelength for

hydrogen with energy of 20 kJ/mol is thereby calculated to be 0.63 Å for ^1H (protium, H) and 0.45 Å for ^2H (deuterium, D).⁵⁵ These wavelengths are comparable to the molecular dimension. Uncertainty relation of Heisenberg ($|\Delta x||\Delta p| \approx \hbar$) predicts $|\Delta x| \approx \lambda/4\pi$, which is equivalent to saying that there is an appreciable probability of barrier penetration when λ becomes comparable with the width of the barrier.⁵⁵

Let us qualitatively discuss some useful concepts of tunneling for a collinear reaction $\text{A—H}\cdots\text{A} \leftrightarrow \text{A}\cdots\text{H—A}$, of proton transfer between two “heavy” atoms A taking place in condensed phase. We can generalize the proton transfer by considering transition between two harmonic oscillator’s potentials for two A—H. We will restrict our discussion on the ground state vibrational wavefunction of a covalently bound proton harmonic oscillator because the typical vibration quanta for A—H covalent bond is order of $\sim 3000\text{ cm}^{-1}$, while $kT \sim 200\text{ cm}^{-1}$ at room temperature.⁵⁶ The wavefunction at the ground state is represented by

$$\psi_0 = \frac{1}{\sqrt{a_0} \sqrt[4]{\pi}} \exp(-(1/2)(x/a_0)^2) \quad (5.6)$$

where x is the reduced coordinate and a_0 is the amplitude of the vibration. The tunneling transition probability is proportional to the resonance integral $\int \psi_i V_{if} \psi_f dv$, where ψ 's are the wavefunction of the initial (i) and final state (f), and V_{if} is the potential of their interaction.⁵⁶ This shows that the tunneling probability is higher for stronger overlap of the wavefunctions. When the oscillator’s reduced mass is small (for A—H) and the ZPE ($1/2 h\nu$) is large; correspondingly, the amplitude a_0 is large too, and the wave functions decay slowly. Therefore, the wave functions overlap is substantial already for the ground level, and the tunneling probability is high too (Figure 5.9). When the reduced mass of the oscillator (for

A—D) is higher, *ZPE* is lower, so the amplitude a_0 , and the overlap are poor and tunneling probability is low. Thus tunneling also results in a KIE. A similar concept also explains why the distance between the reactant and product wells affects the tunneling probability.

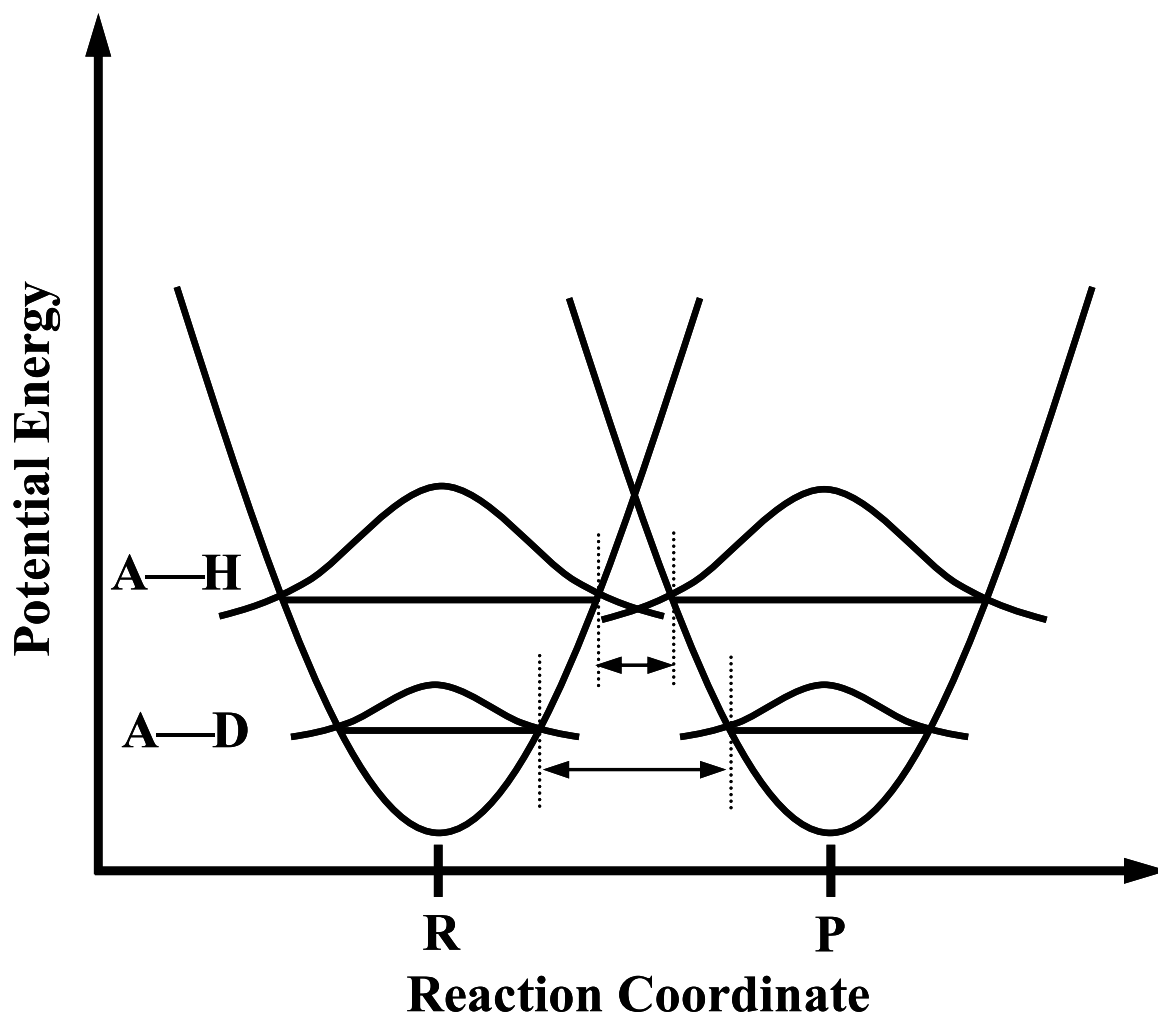


Figure 5.9. Schematic potential energy curves of A—H and A—D for ground-state nuclear tunneling. The wave function overlap is substantial for the A—H oscillator than that of A—D because of higher zero-point energy (*ZPE*). More overlap between the reactant and product wavefunctions results in higher tunneling probability.

It is important to note that tunneling becomes possible only in the case where the energy levels of initial and final states are equal because transition at this situation does not violate the energy conservation law. Electrostatic interactions through reorganization of

surrounding solvents with the proton plays an important role in order to equalize these levels, that, generally, are not equal from the beginning.⁵⁴

Influence of the Potential Energy Surface

Zero-point energy and the energy barrier are affected by the strength of the hydrogen bonds.⁵⁷⁻⁶⁰ Whether the zero-point energy is below or above the barrier in the proton coordinate is critically determined by the separation of the heteroatoms (A—A). The separation is dependent on the strength of the hydrogen bond.

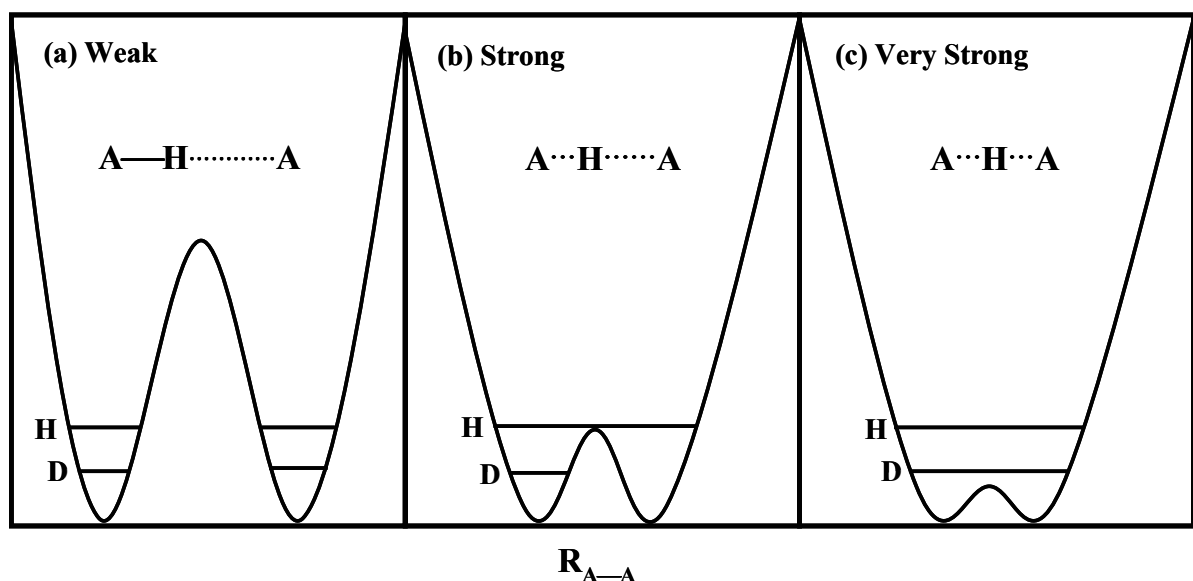


Figure 5.10. Zero-point energy and barrier height among three types of hydrogen bonds: (a) weak, (b) strong and (c) very strong.

Figure 5.10 illustrates how a zero-point energy and activation energy barrier changes for a weak, strong and very strong hydrogen bond. The potential energy of hydrogen-bonded complex, $A-H\cdots A$, can be represented by a symmetric double-well potential generated from the superposition of the potential wells of each species, $A-H$ and $H-A$. In a weak hydrogen bond (large $A-A$ distance, R_{A-A}), zero-point energies of hydrogen and deuterium lie near the bottom of the well and separated by a high barrier. When the hydrogen bond is

strong, the two heteroatoms are partially covalently bonded to the proton. In this case, the zero-point energy of the hydrogen is close or above the barrier but is lower when H is replaced by D and leads to an isotope effect. This hydrogen bond is categorized as the low-barrier hydrogen bond. In case of very strong hydrogen bond, the heteroatoms are so close to each other (small A—A distance, R_{A-A}) that they almost equally share the hydrogen resulting a very low barrier, and the zero-point energies of hydrogen and deuterium both lie well above the barrier. In this case, the zero-point energy effects do not support the same isotope effect but allow cross over and modestly opposite isotope effects.^{60,61}

Effect of Environment

Intermolecular interactions can also influence the potential of proton in a hydrogen-bonded system.⁵² The molecular complex $A-H\cdots B$ exhibits a small permanent electric dipole moment, which changes as it passes through a transition state $[A^{\delta-}\cdots H\cdots B^{\delta+}]^{\ddagger}$ to the product $A^-\cdots H-B^+$. This indicates that the reacting pair can interact with surrounding polar environment and the potential energy surface can be modulated. Proton potential energy curves with proton and solvent coordinates for a model symmetric proton transfer reaction in a linear hydrogen-bonded complex are shown in Figure 5.11. This shows how configurational changes in the surrounding environment distort potential from being initially asymmetric favoring residing the proton on A through the transition state where a proton symmetric double well is established, and on to an asymmetric potential now favoring the proton residing on B. The motion of the solvent is critical because of the coupling between the evolving charge distribution of the reacting pair and the polarization field of the solvent.

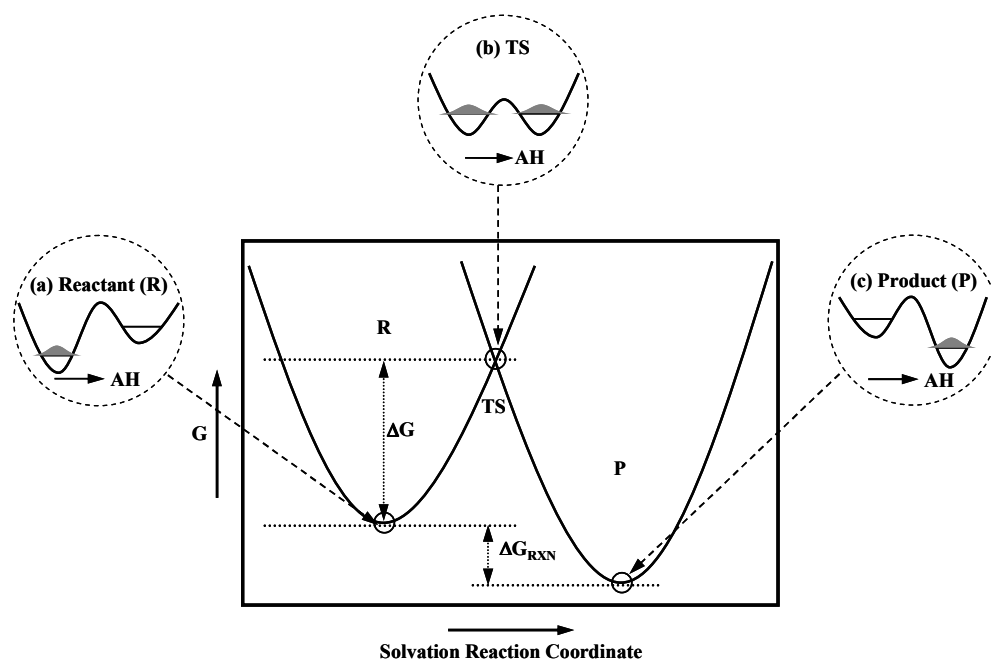


Figure 5.11. Illustration of proton potential energy curves with proton (in the circle) and solvent coordinates for a model symmetric proton transfer reaction in a linear hydrogen-bonded complex.

Adiabatic and Nonadiabatic Proton Transfer

Hynes and coworkers^{58,59} developed nontraditional theories on acid-base proton transfer reaction $A-H \cdots B \rightarrow A^- \cdots H-B^+$ in solution. The important nontraditional aspects are quantum mechanical character of proton's nuclear motion and solvent coordinate as the reaction coordinate. The two regimes for the proton's motion are adiabatic and nonadiabatic proton transfer. In the adiabatic proton transfer regime, the high frequency quantum proton vibration adiabatically follows the solvent fluctuations as the reaction proceeds from reactant to product, and at the transition state the zero-point level is above the barrier in the proton coordinate. Thus, the reaction coordinate is solvent coordinate rather than proton coordinate. This is in contrast to the common conception that if tunneling does not occur, there is classical motion of the proton over the barrier in the proton coordinate.

The second regime is nonadiabatic, where the lowest proton vibrational level is below the proton barrier when solvent has rearranged to establish a symmetric potential in the proton coordinate and the reaction is exclusively tunneling. Again the reaction coordinate is solvent. In adiabatic limit, an isotope effect is not obtained because lowest vibrational energy level of the proton stretch mode lies above the barrier whereas the opposite is true in nonadiabatic limit.

References

- (1) Goel, A.; Kunnumakkara, A. B.; Aggarwal, B. B. *Biochem. Pharmacol.* **2008**, *75*, 787.
- (2) Ruby, A. J.; Kuttan, G.; Babu, K. D.; Rajasekharan, K. N.; Kuttan, R. *Cancer Lett.* **1995**, *94*, 79.
- (3) Lantz, R. C.; Chen, G. J.; Solyom, A. M.; Jolad, S. D.; Timmermann, B. N. *Phytomedicine* **2005**, *12*, 445.
- (4) Aggarwal, B. B.; Kumar, A.; Bharti, A. C. *Anticancer Res.* **2003**, *23*, 363.
- (5) Shi, M.; Cai, Q.; Yao, L.; Mao, Y.; Ming, Y.; Ouyang, G. *Cell Biol. Int.* **2006**, *30*, 221.
- (6) Surh, Y.-J. *Food Chem. Toxicol.* **2002**, *40*, 1091.
- (7) Yang, F.; Lim, G. P.; Begum, A. N.; Ubeda, O. J.; Simmons, M. R.; Ambegaokar, S. S.; Chen, P. P.; Kaye, R.; Glabe, C. G.; Frautschy, S. A.; Cole, G. M. *J. Biol. Chem.* **2005**, *280*, 5892.
- (8) Masuda, M.; Suzuki, N.; Taniguchi, S.; Oikawa, T.; Nonaka, T.; Iwatsubo, T.; Hisanaga, S.-i.; Goedert, M.; Hasegawa, M. *Biochemistry* **2006**, *45*, 6085.
- (9) Payton, F.; Sandusky, P.; Alworth, W. L. *J. Nat. Prod.* **2007**, *70*, 143.

- (10) Tonnesen, H. H.; De Vries, H.; Karlsen, J.; Beijersbergen van Henegouwen, G. *J. Pharm. Sci.* **1987**, *76*, 371.
- (11) Dahl, T. A.; McGowan, W. M.; Shand, M. A.; Srinivasan, V. S. *Arch. Microbiol.* **1989**, *151*, 183.
- (12) Gorman, A. A.; Hamblett, I.; Srinivasan, V. S.; Wood, P. D. *Photochem. Photobiol.* **1994**, *59*, 389.
- (13) Chignell, C. F.; Bilski, P.; Reszka, K. J.; Motten, A. G.; Sik, R. H.; Dahl, T. A. *Photochem. Photobiol.* **1994**, *59*, 295.
- (14) Dahl, T. A.; Bilski, P.; Reszka, K. J.; Chignell, C. F. *Photochem. Photobiol.* **1994**, *59*, 290.
- (15) Chan, W.-H.; Wu, H.-J. *J. Cell. Biochem.* **2004**, *92*, 200.
- (16) Koon, H.; Leung, A. W. N.; Yue, K. K. M.; Mak, N. K. *J. Environ. Pathol. Toxicol. Oncol.* **2006**, *25*, 205.
- (17) Park, K.; Lee, J.-H. *Oncol. Rep.* **2007**, *17*, 537.
- (18) Barik, A.; Priyadarsini, I.; Mohan, H. *Orient. J. Chem.* **2002**, *18*, 427.
- (19) Iersel, M. L.; Ploemen, J.-P.; Struik, I.; Amersfoort, C. v.; Keyzer, A. E.; Schefferlie, J. G.; Bladeren, P. J. v. *Chem. Biol. Interact.* **1996**, *102*, 117.
- (20) Odot, J.; Albert, P.; Carlier, A.; Tarpin, M.; Devy, J.; Madoulet, C. *Int. J. Cancer* **2004**, *111*, 381.
- (21) Zheng, M.; Ekmekcioglu, S.; Walch, E. T.; Tang, C.-H.; Grimm, E. A. *Melanoma Res.* **2004**, *14*, 165.
- (22) Siwak, D. R.; Shishodia, S.; Aggarwal, B. B.; Kurzrock, R. *Cancer Lett.* **2005**, *104*, 879.

- (23) Lao, C. D.; Demierre, M.-F.; Sondak, V. K. *Expert Rev. Anticancer Ther.* **2006**, *6*, 1559.
- (24) Marin, Y. E.; Wall, B. A.; Wang, S.; Namkoong, J.; Martino, J. J.; Suh, J.; Lee, H. J.; Rabson, A. B.; Yang, C. S.; Chen, S.; Ryu, J.-H. *Melanoma Res.* **2007**, *17*, 274.
- (25) Sharma, O. P. *Biochem. Pharmacol.* **1976**, *25*, 1811.
- (26) Priyadarsini, K. I. *Free Radical Biol. Med.* **1997**, *23*, 838.
- (27) Khopde, S. M.; Priyadarsini, K. I.; Venkatesan, P.; Rao, M. N. A. *Biophys. Chem.* **1999**, *80*, 85.
- (28) Kunchandy, E.; Rao, M. N. A. *Int. J. Pharm.* **1989**, *57*, 173.
- (29) Kunchandy, E.; Rao, M. N. A. *Int. J. Pharm.* **1990**, *58*, 237.
- (30) Jovanovic, S. V.; Steenken, S.; Boone, C. W.; Simic, M. G. *J. Am. Chem. Soc.* **1999**, *121*, 9677.
- (31) Khopde, S. M.; Priyadarsini, K. I.; Palit, D. K.; Mukherjee, T. *Photochem. Photobiol.* **2000**, *72*, 625.
- (32) Barik, A.; Goel, N. K.; Priyadarsini, K. I.; Mohan, H. *J. Photosci.* **2004**, *11*, 95.
- (33) Nardo, L.; Paderno, R.; Andreoni, A.; Masson, M.; Haukvik, T.; Toennesen, H. H. *Spectroscopy* **2008**, *22*, 187.
- (34) Das, K.; English, D. S.; Petrich, J. W. *J. Phys. Chem. A* **1997**, *101*, 3241.
- (35) English, D. S.; Zhang, W.; Kraus, G. A.; Petrich, J. W. *J. Am. Chem. Soc.* **1997**, *119*, 2980.
- (36) Smirnov, A. V.; Das, K.; English, D. S.; Wan, Z.; Kraus, G. A.; Petrich, J. W. *J. Phys. Chem. A* **1999**, *103*, 7949.

- (37) Das, K.; English, D. S.; Petrich, J. W. *J. Am. Chem. Soc.* **1997**, *119*, 2763.
- (38) Petrich, J. W. *Int. Rev. Phys. Chem.* **2000**, *19*, 479.
- (39) Chowdhury, P. K.; Halder, M.; Sanders, L.; Calhoun, T.; Anderson, J. L.; Armstrong, D. W.; Song, X.; Petrich, J. W. *J. Phys. Chem. B* **2004**, *108*, 10245.
- (40) Fee, R. S.; Maroncelli, M. *Chem. Phys.* **1994**, *183*, 235.
- (41) Maroncelli, M.; Fleming, G. R. *J. Chem. Phys.* **1987**, *86*, 6221.
- (42) Cross, A. J.; Fleming, G. R. *Biophys. J.* **1984**, *46*, 45.
- (43) Fita, P.; Urbanska, N.; Radzewicz, C.; Waluk, J. Z. *Phys. Chem.* **2008**, *222*, 1165.
- (44) Moog, R. S.; Maroncelli, M. *J. Phys. Chem.* **1991**, *95*, 10359.
- (45) Peteanu, L.; Mathies, R. A. *J. Phys. Chem.* **1992**, *96*, 6910.
- (46) Bong, P.-H. *Bull. Korean Chem. Soc.* **2000**, *21*, 81.
- (47) Schwartz, B. J.; Peteanu, L. A.; Harris, C. B. *J. Phys. Chem.* **1992**, *96*, 3591.
- (48) Horng, M. L.; Gardecki, J. A.; Papazyan, A.; Maroncelli, M. *J. Phys. Chem.* **1995**, *99*, 17311.
- (49) Jimenez, R.; Fleming, G. R.; Kumar, P. V.; Maroncelli, M. *Nature* **1994**, *369*, 471.
- (50) Fleming, G. R.; Cho, M. H. *Annu. Rev. Phys. Chem.* **1996**, *47*, 109.
- (51) Zsila, F.; Bikadi, Z.; Simonyi, M. *Org. Biomol. Chem.* **2004**, *2*, 2902.
- (52) *Isotope Effects in Chemistry and Biology*; Kohen, A.; Limbach, H.-H., Eds.; Tylor & Francis: Boca Ratan, 2006.
- (53) Anslyn, E. V.; Dougherty, D. A. *Modern Physical Organic Chemistry*; University Science: Sausalito, California, 2006.

- (54) Kiefer, P. M.; Hynes, J. T. *J. Phys. Chem. A* **2003**, *107*, 9022.
- (55) Bell, R. P. *The proton in chemistry*, 2nd ed.; Cornell University Press: Ithaca, New York 1973.
- (56) Krishtalik, L. I. *Biochim. Biophys. Acta* **2000**, *1458*, 6.
- (57) Hibbert, F.; Emsley, J. *Adv. Phys. Org. Chem.* **1990**, *26*, 255.
- (58) Staib, A.; Borgis, D.; Hynes, J. T. *J. Chem. Phys.* **1995**, *102*, 2487.
- (59) Kiefera, P. M.; Hynesa, J. T. *Solid State Ionics* **2004**, *168*, 219.
- (60) *Ultrafast Hydrogen Bonding Dynamics and Proton Transfer Processes in the Condensed Phase* Elsaesser, T.; Bakker, H. J., Eds.; Kluwer Academic Publishers: Dordrecht ; Boston, 2002.
- (61) Frey, P. A.; Whitt, S. A.; Tobin, J. B. *Science* **1994**, *264*, 1927.

CHAPTER 6. EXCITED-STATE INTRAMOLECULAR HYDROGEN ATOM TRANSFER OF CURCUMIN IN SURFACTANT MICELLES

A paper published in *The Journal of Physical Chemistry B*

Ramkrishna Adhikary,¹ Philip J. Carlson,¹ Tak W. Kee^{2*} and Jacob W. Petrich^{1*}

Abstract

Femtosecond fluorescence upconversion experiments were performed on the naturally occurring medicinal pigment, curcumin, in anionic, cationic, and neutral micelles. In our studies, the micelles are composed of sodium dodecyl sulfate (SDS), dodecyl trimethyl ammonium bromide (DTAB) and triton X-100 (TX-100). We demonstrate that the excited-state kinetics of curcumin in micelles have a fast (3 – 8 ps) and slow (50 – 80 ps) component. While deuteration of curcumin has a negligible effect on the fast component, the slow component exhibits a pronounced isotope effect of ~ 1.6 , indicating that micelle-captured curcumin undergoes excited-state intramolecular hydrogen atom transfer. Study of solvation dynamics of curcumin in 10 ps time-window reveals a fast component (< 300 fs) followed by a 8, 6 and 3 ps component in the solvation correlation functions for TX-100, DTAB and SDS

Reprinted with permission from *The Journal Physical Chemistry B* 2010, 114 (15), 2997-3004. Copyright (2010) American Chemical Society.

¹Department of Chemistry, Iowa State University, Ames, Iowa 50011-3111.

²School of Chemistry and Physics, University of Adelaide, Adelaide, South Australia, 5005, Australia.

* To whom correspondence should be addressed.

micelles respectively.

Introduction

Curcumin, 1,7-bis(4-hydroxy-3-methoxyphenyl)-1,6-heptadiene-3,5-dione, has received considerable attention owing to its numerous medicinal properties.¹⁻⁹ Curcumin, whose structure is shown in Figure 6.1, is the major ingredient of the yellow pigments (curcuminoids) in the Indian spice plant turmeric. While curcuminoids are composed of approximately 77% curcumin, demethoxy curcumin (17%) and bisdemethoxy curcumin (3%) constitute most of the remaining portion. In addition, cyclocurcumin, which was isolated in 1993, is also present at a trace level.¹⁰ A large number of studies have shown that curcumin possesses anticancer,^{3,4} anti-Alzheimer,⁶ anti-cystic fibrosis,⁷ and other desirable medicinal benefits.^{1,8,9} Of particular interest are the prospects of curcumin or curcumin-like nontoxic agents to exhibit anticancer effects without side effects,^{3,4} unlike conventional chemotherapy drugs. Several clinical trials are either underway or have recently been completed with curcumin as the treatment agent.^{11,12} The preliminary results from these trials are highly promising.

Two major challenges in the application of curcumin as an effective treatment agent are lack of bioavailability and severely limited stability in aqueous environments. Because of the low aqueous solubility, curcumin tends to aggregate and precipitate in water, limiting its bioavailability.¹³⁻¹⁶ In addition, curcumin undergoes rapid degradation in water and buffer solutions, with a reaction half-life of 9.5 minutes at pH 7.2.¹⁷ It has been demonstrated that the degradation is mostly due to deprotonation of curcumin, producing the degradation products: vanillin, ferulic acid, and feruloyl methane.^{17,18} It is interesting that most of these products have medicinal properties as well. Previous studies have shown that encapsulation

of curcumin in surfactant micelles and binding to proteins resolve these two major issues.¹⁴⁻¹⁶

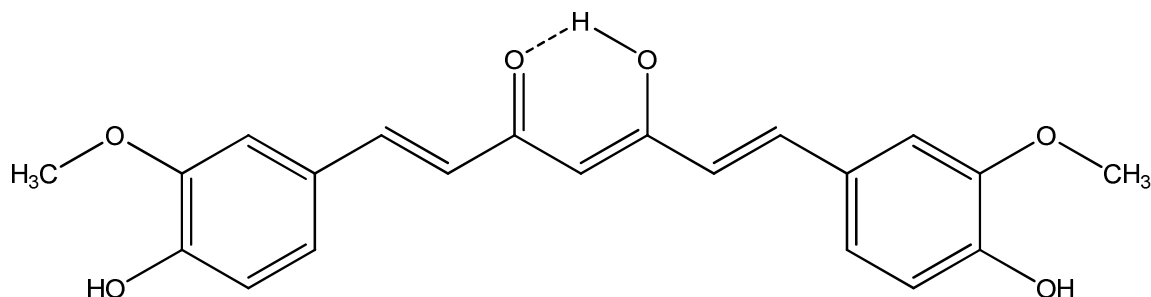


Figure 6.1. Structure of keto-enol form of curcumin.

Micellar systems may potentially play an important role in leading to improved clinical use of curcumin. It is established that micelle-captured curcumin is well dispersed in aqueous solutions, thereby increasing the bioavailability significantly.^{13,15,16} Moreover, curcumin is trapped in the regions of the micelle where the presence of free water molecules is relatively limited, preventing alkaline hydrolysis, which is the major mechanism for degradation.^{17,18} It is therefore plausible that association to micelles plays a considerable role in enabling curcumin to exhibit its medicinal characteristics. Apart from preventing degradation, micelles also serve as well defined model systems for biomembranes. It has been shown that a large portion of curcumin is membrane bound in a biological environment.¹⁹ Investigations on the behavior of curcumin in micelles may provide valuable insight into the properties of curcumin in biomembranes.

Curcumin exists predominantly as the keto-enol tautomer in a number of solvents.²⁰ It is capable of executing excited state intramolecular hydrogen atom transfer (ESIHT) due to the presence of strong intramolecular hydrogen bonding between the proton donor and the acceptor atom, as indicated in Figure 6.1. Although there is a general agreement that ESIHT is a major photophysical event of curcumin,²¹⁻²³ the exact time scale of this phenomenon was

not well established until our recent work.²³ Using deuteration of curcumin and time-resolved fluorescence upconversion as a technique for probing ESIHT, our work has shown that the time constant of ESIHT of curcumin is 70 ps in methanol and 120 ps in ethylene glycol.²³ It has been proposed that the presence of a labile hydrogen as a result of ESIHT plays a role in the medicinal effects of other naturally occurring pigments such as hypericin and hypocrellin.²⁴⁻³¹ As for curcumin, it is possible that ESIHT results in partial deprotonation, which induces fragmentation to yield the medicinal degradation products mentioned earlier. While ESIHT of curcumin in polar organic solvents has been established,²³ it remains unclear if micelle-captured curcumin also undergoes this photoinduced process. It is known that intramolecular proton transfer processes are affected in confined environment due to the structure, various interfaces and dynamics of the environment.³²

Here we present unambiguous results demonstrating that ESIHT is a major photophysical event of curcumin in micelles. The well studied micellar systems composed of sodium dodecyl sulfate (SDS), dodecyl trimethyl ammonium bromide (DTAB) and triton X-100 (TX-100), which are anionic, cationic and nonionic in nature, respectively, were chosen for our investigations. These micelles not only serve as model systems for biomembranes, but also enable photophysical investigations as a function of the polarity of the headgroup. By comparing the excited-state decay kinetics of the deuterated and nondeuterated species obtained by fluorescence upconversion spectroscopy, we show that the time constant of ESIHT of curcumin in these micelles ranges from 50 – 80 ps. In addition to ESIHT, a fast component of 3 – 8 ps was also observed. Results from multiwavelength studies reveal that the fast component is due to solvation dynamics of curcumin in the micellar media. In short,

the present studies offer the first insights into the photophysical events of curcumin in micelles, which may lead to further understanding of the behavior of curcumin in biomembranes.

Experimental Section

Materials. Curcumin (purity ~ 70% HPLC) and high purity curcumin ($\geq 98.5\%$) were purchased from Sigma Aldrich and Alexis Biochemicals, respectively. High purity curcumin was used for all experiments except in the solvation dynamics studies. We confirmed that curcumin from the two sources produces identical fluorescence upconversion results at 520 nm. Triton X-100 (TX-100, reduced), dodecyltrimethyl ammonium bromide (DTAB, ~99%) and sodium dodecyl sulfate (SDS, ~99%) were obtained from Sigma Aldrich and used without further purification. Tris- d_{11} solution (1 M in D_2O , 98 atom %D), deuterium chloride (35 wt% solution in D_2O , 99 atom %D) and D_2O (99.9 atom %D) were purchased from Sigma Aldrich. The nondeuterated tris (>99.8% purity) was acquired from AMRESCO. Methanol and Methanol- d_4 (purity 99.8%) were obtained from Fisher Scientific and Cambridge Isotope Laboratories, Inc., respectively, and used as received. All solutions were prepared with water from a Millipore Milli-Q NANOpure water system.

Sample preparation. A 20 mM buffer solution was prepared at either pH or pD = 7.4 for all the experimental work in these studies using tris or tris- d_{11} , respectively. The concentration of surfactant was maintained at 0.1 M, which is above the CMC for each of the micelles, in nondeuterated and deuterated tris buffer. Two stock solutions of curcumin in methanol and methanol- d_4 were used for steady-state, time-correlated single photon counting (TCSPC) measurements. A small quantity (2 μL) of the curcumin stock solution (4.5 or 1.5 mM) was transferred to the micellar solution to yield a solution with a curcumin

concentration of 3 or 1 μM for the UV-Vis or fluorescence spectra, respectively. Care was taken to keep the total methanol content of the final sample solution at $< 0.1\%$ for all solutions. The solutions were then allowed to equilibrate overnight in either the tris/ H_2O or tris- d_{11} / D_2O solution in the dark prior to the optical experiments. Equilibration was particularly important for curcumin in the D_2O micellar solutions to ensure a complete exchange of the enolic hydrogen of curcumin with deuterium, as indicated below. For the upconversion measurements, the required amount of curcumin (powder form) was directly added to the micellar solution to result in a curcumin concentration of 0.5×10^{-3} to 1×10^{-3} M. This solution was then sonicated for an hour in the dark. All the solutions for fluorescence upconversion measurements were allowed to equilibrate overnight. In addition, data collected with the deuterated samples that were equilibrated for 48 hours are identical to those with only overnight equilibration, indicating completion of H/D exchange.

Steady-state measurements. Steady-state UV-Vis absorption and emission spectra were acquired on a Hewlett Packard 8453 UV-visible spectrophotometer and Spex Fluoromax-4 with 1-nm resolution at room temperature. The emission spectra were corrected for lamp spectral intensity and detector response. The emission spectra were obtained with an excitation wavelength of 407 nm with 3-nm bandpass for all the samples. A 5-mm path-length quartz cuvette was used for all the absorption and emission measurements.

Time-resolved measurements. Excited-state lifetime measurements were performed using the TCSPC technique. A homebuilt mode-locked Ti:sapphire oscillator pumped by a Nd:VO₄ laser (Millennia, Spectra Physics) producing femtosecond pulses tunable from 780 to 900 nm with a repetition rate of 82 MHz was used as the laser source. The fundamental wavelength at 814 nm from the Ti-sapphire oscillator was modulated by a Pockels cell

(Model 350-160, Conoptics Inc.) to reduce the repetition rate to approximately 8.8 MHz and was subsequently frequency doubled by using a harmonic generator (Model TP-2000B, U-Oplaz Technologies). The resulting blue light, which had a central wavelength of 407 nm, provided the excitation source. The fluorescence was collected at a 90° geometry, and passed through an analyzer set at the magic angle (54.7°) with respect to excitation polarization. A half-wave plate before a vertical polarizer ensured the polarization of the excitation light. A 425 nm cut-off filter was placed in front of a multichannel plate, MCP (Hamamatsu). The detector output was amplified and fed to the Becker & Hickl photon counting module Model SPC-630. The full-width-at-half-maximum (FWHM) of the instrument response function is $\sim 40 - 45$ ps. All the measurements were made in a 3.33 ns time window with a total of 1,024 channels. A total of 65,000 counts were collected at the peak channel for all the lifetime measurements. A cuvette of 1-cm path length was used for all the lifetime measurements.

The apparatus for fluorescence upconversion is described in detail elsewhere.³³ In short, the laser source was also a homebuilt mode-locked Ti:sapphire oscillator. The fundamental wavelength and repetition rate of the femtosecond output were 814 nm and 82 MHz, respectively. The fundamental output from the oscillator was frequency-doubled by a type-I LBO crystal (2 mm). The frequency-doubled pulses (407 nm) were used to excite the sample and the residual of the fundamental was used as the gate pulse to upconvert the fluorescence signal. The polarization of the excitation pulse was at the magic angle relative to that of the gate pulses. First, the frequency-doubled blue pulses (407 nm) were focused onto a rotating cell containing the sample and the fluorescence signal was collected using a 10x objective lens. Then, the gate pulse and fluorescence signal were focused onto a 0.4 mm type-I BBO crystal to generate the sum frequency light, which was detected by a

photomultiplier tube mounted on a monochromator. The full-width-at-half-maximum (FWHM) of the instrument response function is 300 fs, obtained by the cross-correlation function of the frequency doubled and the fundamental light. All experiments were performed at room temperature. For most fluorescence upconversion experiments, a time window of 100 ps was used with a step size of 0.2 ps.

The solvation correlation function, $C(t)$, was used to analyze and quantify the solvation dynamics.

$$C(t) = \frac{\nu(t) - \nu(\infty)}{\nu(0) - \nu(\infty)} \quad (6.1)$$

The $\nu(0)$, $\nu(t)$ and $\nu(\infty)$ in eq 6.1 denote the peak frequency (typically in cm^{-1}) of the zero time, t and infinity emission spectra. Using the approach of Fee and Maroncelli,³⁴ the “zero time” emission spectrum was approximated by using the emission spectrum of curcumin in hexanes. As for $\nu(\infty)$, the peak frequency of the steady-state fluorescence spectrum was used. In these investigations, fluorescence upconversion measurements were performed at 15-16 wavelengths depending upon the system, ranging from 470 – 630 nm, with a time window of 10 ps to construct time-resolved emission spectra with sufficient data points to reflect the real spectra. Each of the time-resolved emission spectra was fitted with the log-normal function and the peak frequency $\nu(t)$ was obtained using the procedure outlined by Maroncelli and Fleming.³⁵ The relatively large width of the time dependent emission spectra typically results in uncertainty in the exact position of the maxima. Therefore, by using the signal-to-noise ratio and width of the spectrum (including “zero-time”, steady-state, or time-resolved emission spectrum) as sources of uncertainty, we determined the following typical uncertainties: time-resolved emission ($\sim \pm 200 \text{ cm}^{-1}$), “zero-time” and steady-state ($\sim \pm 100$

cm^{-1}). These uncertainties were used to compute error bars for the $C(t)$. Finally, the fractional solvation at 300 fs was calculated using $f_{300\text{fs}} = 1 - C(t = 300 \text{ fs})$.

Results and Discussions

UV-Vis absorption and emission spectra of curcumin in micelles. The spectral properties of curcumin in three different micelles were investigated systematically to examine the influence of micellar environments on spectral features. Figure 6.2 depicts the UV-vis absorption and emission spectra of curcumin in TX-100, DTAB and SDS micelles under deuterated (blue) and non-deuterated (red) condition at pD or pH = 7.4 in tris buffer. Curcumin exhibits a broad and intense absorption peak at 426 nm, 423 nm and 432 nm in the TX-100, DTAB and SDS micelles, respectively. A small shoulder in the absorption band is present at 445 nm and 442 nm in the TX-100 and DTAB micelles, whereas curcumin produces a featureless absorption band in the SDS micelle. The absence of vibronic structure in the absorption band of curcumin, as observed in the SDS micelle, is also observed for curcumin in water. This phenomenon indicates that curcumin may interact strongly with water molecules in the Stern layer of the micelle, which is the layer between the core/water interface and the hydrodynamic shear surface,³⁶ as will be discussed furthering more detail forthwith. Additionally, a broad spectral shoulder is present around 500 nm for curcumin in the DTAB micelle. This extra shoulder, which is absent in the other two micelles, is due to the presence of a small population of deprotonated curcumin at pH = 7.4.

As for the emission spectrum, curcumin shows a broad spectrum peaked at 501 nm, 498 nm and 548 nm in the TX-100, DTAB and SDS micelles, respectively. The peak positions of the UV-vis absorption and emission spectra of curcumin are affected by the isotopic substitution, as shown in Figure 6.2. While a 3-nm blue shift appears in the UV-vis

absorption of curcumin in both the TX-100 and DTAB micelles in D₂O, a red shift with the same magnitude in the emission maximum emerges in these micelles. As for the SDS micelle in D₂O, a 3 nm blue and ~10 nm red shift are found in the absorption and emission maxima, respectively. The changes in absorption and emission peak positions are possibly due to changes in zero-point energies in S₀ and S₁ induced by deuteration.^{37,38}

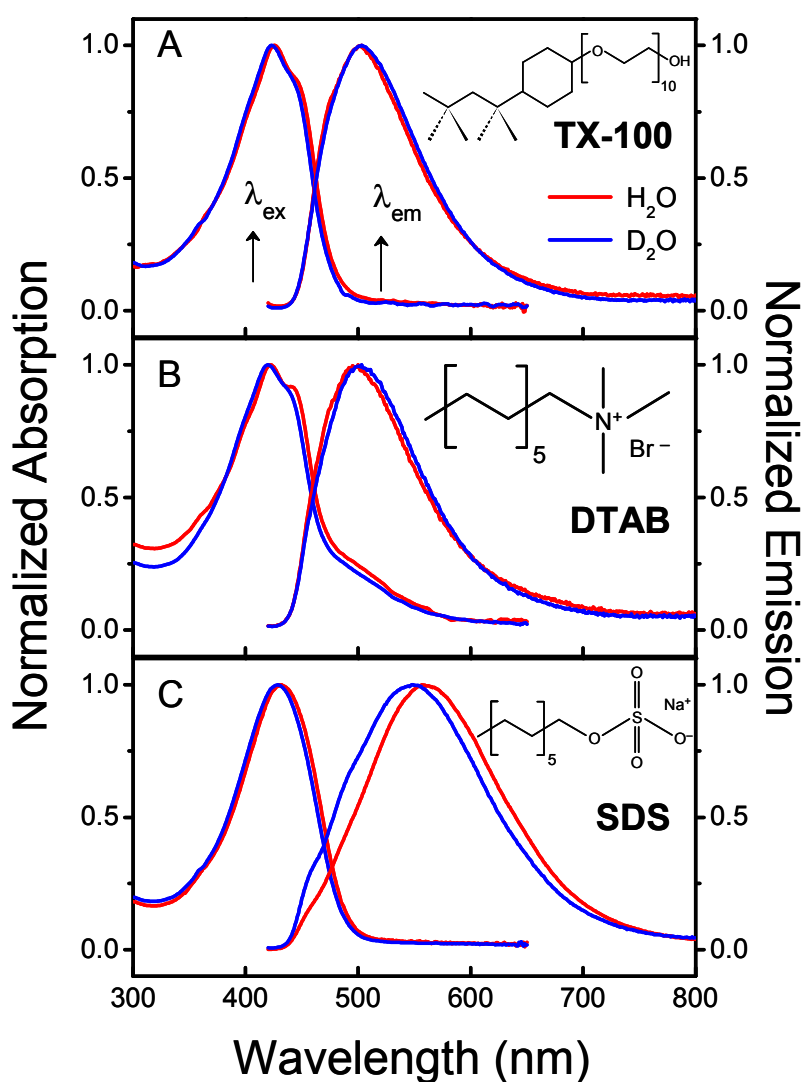


Figure 6.2. UV-Vis absorption and emission spectra of curcumin in (A) TX-100, (B) DTAB, and (C) SDS in H₂O (red) and D₂O (blue).

A comparison between the UV-vis absorption and emission spectra of curcumin in micelles with those in a number of organic solvents and water provides valuable insights. The UV-vis absorption spectra of curcumin in the TX-100 and DTAB micelles resemble those of curcumin in aprotic solvents, including chloroform and toluene,^{23,39} suggesting similarities between the environments. However, the emission spectra of curcumin in these micelles are red-shifted compared to those in the aprotic solvents, potentially due to interactions with water molecules at the interface and within the micelle,⁴⁰⁻⁴⁴ as will be discussed further in a later section. It is well established that curcumin exhibits a red-shifted emission spectrum in protic solvents including methanol and water, with an emission maximum around 550 nm. The overall results suggest that curcumin is likely to be located in the palisade layer of the TX-100 and DTAB micelles, which is consistent with results from another study.²² As for the SDS micelle, the positions of the UV-vis absorption and emission maxima are identical to those of curcumin in methanol and water, indicating that the micellar environment is analogous to the polar environment in these protic solvents. This suggests that curcumin is probably situated near the Stern layer of the SDS micelle, which facilitates strong interactions with bulk water.

The Stokes shifts of curcumin are 75 nm, 75 nm, and 116 nm in the TX-100, DTAB and SDS micelles, respectively. Interestingly, the value of the Stokes shift for TX-100 and DTAB micelles are similar to those measured for human and bovine serum albumin (HSA and BSA) bound curcumin.^{14,45-48} It is established that curcumin binds strongly in the hydrophobic pocket of these proteins. The similar Stokes shift values for TX-100 and DTAB micelles imply that the micellar environment is similar to the hydrophobic regions of HSA and BSA. In contrast, the sizeable Stokes shift observed in the SDS micelle is virtually

identical to that observed in a buffer solution, which reflects that the local environment of curcumin in the SDS micelle may have a significant bulk water content, which further supports that curcumin is located near the Stern layer of the micelle.

Fluorescence upconversion and excited-state intramolecular hydrogen atom transfer of micelle-captured curcumin. The fluorescence upconversion results of curcumin in the TX-100, DTAB and SDS micelles are shown in Figure 6.3. The fluorescence upconversion decay traces of curcumin in both nondeuterated and deuterated micellar environments at pH and pD =7.4, respectively, are illustrated in the figure. The decay kinetics were monitored at 520 nm with an excitation wavelength of 407 nm. Collection of time-resolved fluorescence at 520 nm for the SDS micelle provides early time excited-state relaxation information as this wavelength is on the blue side of the emission spectrum. In the case of curcumin in TX-100 and DTAB micelles, since 520 nm is on the red side of the emission peak maxima, relaxation processes including solvation could be pronounced as curcumin shows a strong solvatochromatic behavior. All the upconversion decays are well fitted with a biexponential function within the 100 ps time window and the results are summarized in Table 6.1. Curcumin in the TX-100/H₂O system shows a fast component of 8 ± 2 ps and a slow component of 80 ± 10 ps. Upon deuteration of curcumin in the same micelle, a biexponential decay with time constants of 8 ± 2 and 130 ± 20 ps is obtained. It is important to note that while the fast component remains identical within experimental error in the two results, the slow component shows a significant isotope effect of 1.6. The isotope effect on the slow component clearly indicates that ESIHT occurs with a time constant of 80 ps in TX-100. In DTAB/H₂O and SDS/H₂O, the time-resolved fluorescence also exhibited a distinct biexponential decay. The fast component has time

constants of 6 ± 2 and 3 ± 2 ps whereas in the slow component 50 ± 5 and 55 ± 3 ps are obtained for curcumin in the DTAB and SDS micelles, respectively. Deuteration of curcumin induces a similar isotope effect, *i.e.*, an identical fast component and lengthening of the slow component. The time constants of the long component are 80 ± 5 and 85 ± 6 ps in the DTAB/D₂O and SDS/D₂O media, respectively. The presence of an isotope effect of ~ 1.6 for curcumin in these two micelles reinforces our assignment of the long-lived component to ESIHT. As for the fast component observed in the results, further discussion will be given in the following section.

Several studies have shown that the ESIHT process in curcumin is highly sensitive to the presence of hydrogen bonding between curcumin and the solvent.²¹⁻²³ Nardo et al. and Khopde et al. independently reported that there is a ~ 50 ps decay component in the fluorescence lifetime (89 and 64 ps, as measured by the two groups, respectively) of curcumin in cyclohexane using TCSPC.^{21,22} This decay component is, however, limited by the time resolution of TCSPC apparatus. It is accepted that this fast decay component is due to ESIHT of curcumin.²² The ESIHT time constant of curcumin in this nonpolar solvent is shorter than that in methanol, which has a value of ~ 70 ps.²³ The results imply that the strength of the intramolecular hydrogen bond of curcumin is the determining factor in the rate of ESIHT. These authors, furthermore, suggest that in protic solvents, such as methanol and ethanol, the keto-enol group of curcumin forms strong hydrogen bonds with the solvent molecules, in addition to the intramolecular hydrogen bond within the keto-enol group.^{21,22} The interactions between curcumin and the protic solvent molecules interfere with the intramolecular hydrogen bond, weakening the bond effectively, thereby decreasing the rate of ESIHT. However, such perturbation in intramolecular hydrogen bonding is absent in

nonpolar solvents such as cyclohexane, enabling a strong intramolecular hydrogen bond in the keto-enol moiety of curcumin and facilitating a fast ESIHT.

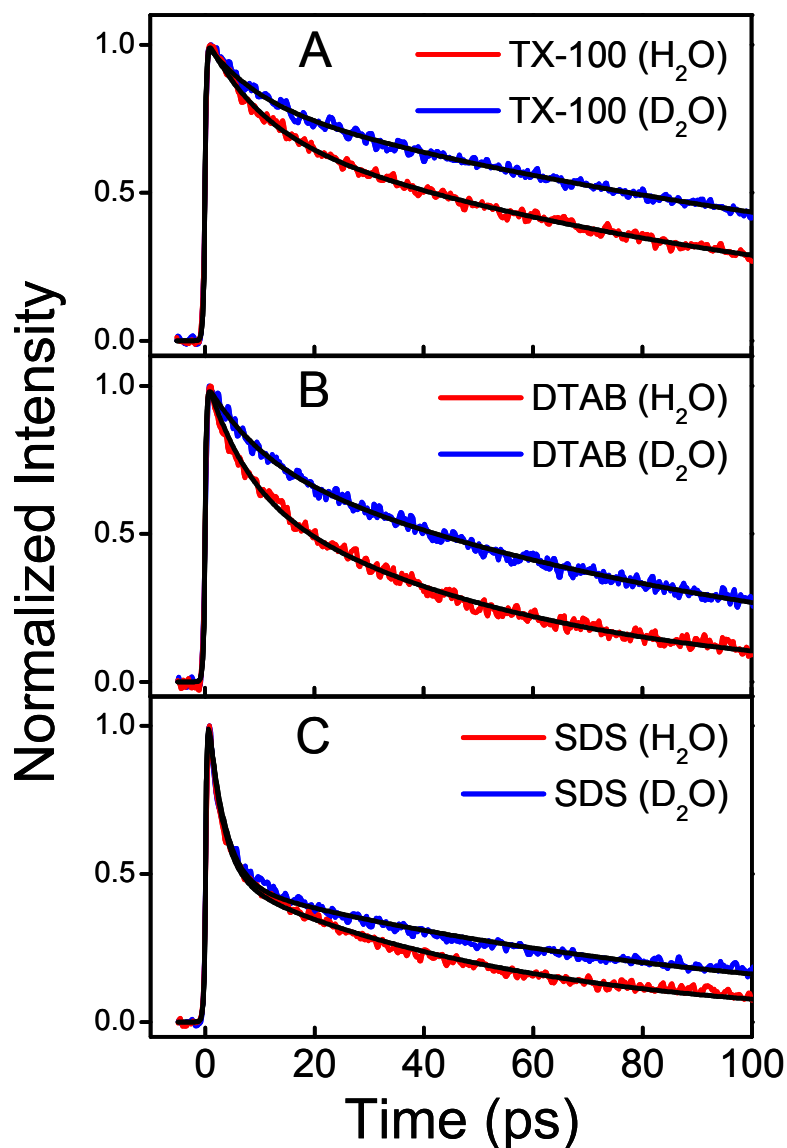


Figure 6.3. Fluorescence upconversion decays of curcumin collected at 520 nm in (A) TX-100, (B) DTAB and (C) SDS micelles at pH = 7.4 tris buffer (red) with an excitation wavelength of 407 nm. Corresponding upconversion decays in deuterated micellar environment at pD = 7.4 (blue) are also included. Curcumin shows a prominent isotope effect in all three micellar media.

The ESIHT time constant of curcumin in the TX-100 micelle, with a value of 80 ps as measured in this fluorescence upconversion study, is very similar to that of curcumin in methanol (70 ps), as reported in our previous study using the same technique.²³ Additionally, the ESIHT time constant of curcumin reported in this study is comparable to that of 7-azaindole in methanol.⁴⁹ The good agreement indicates a substantial level of curcumin-solvent and curcumin-surfactant intermolecular hydrogen bonding in the micelle. This result is consistent with a previous study, suggesting that curcumin is trapped in the palisade layer of the micelle,²² which is a relatively hydrophilic layer of the micelle.⁵⁰ In addition, studies have shown that the C–O groups in TX-100 interact favorably with water, which support that there is a substantial level of water in the micelle.^{51,52} Furthermore, curcumin may also have considerable hydrogen bonding with oxygens in the C–O groups in the TX-100 surfactants, as will be discussed below. In short, in the case of the TX-100 micelle, our results indicate that hydrogen bonding between curcumin and the micellar environment is similar to that between curcumin and bulk methanol, which is consistent with results from a previous report.²²

In the DTAB and SDS micelles, the ESIHT time constants are approximately 50 ps, as shown in Table 6.1. It appears that the fast ESIHT times observed in these micelles compare well with that in the nonpolar solvent cyclohexane.^{21,22} However, as indicated earlier, the ESIHT process of curcumin in cyclohexane is most likely faster than what was measured with TCSPC due to limited temporal resolution. In comparison to curcumin in the TX-100 micelle, the ESIHT process occurs faster in the DTAB and SDS micelles. It is obvious that there is a stronger curcumin intramolecular hydrogen bond, and a weaker curcumin-water and/or curcumin-surfactant interaction in these micelles compared to TX-

100. To gain insight into the higher rates of ESIHT in the DTAB and SDS micelles relative to that of TX-100, we first consider the water content of the micelles. Studies have suggested that the water contents are similar for the DTAB and TX-100 micelles but higher in the SDS micelle.⁵³ Therefore, it follows that the curcumin-water hydrogen bonding is likely to play a minor role in leading to a higher rate of ESIHT for curcumin in the DTAB and SDS micelles. An obvious difference between TX-100 and the other two surfactants is that the presence of a high number of C–O groups in the backbone of TX-100, which may interact with curcumin through hydrogen bonding. In contrast, the surfactant backbones of DTAB and SDS are composed of the dodecyl group, which only interacts with curcumin through weak van der Waals forces. It is likely that the presence of a considerable hydrogen bonding network for curcumin in the TX-100 micelle leads to a slower rate of ESIHT. In the DTAB and SDS micelles, however, the ESIHT rate is higher due to the absence of such hydrogen bonding network. While the results in this study are consistent with the notion of additional hydrogen bonding in the TX-100 micelles for curcumin, more work will be necessary to understand this effect fully.

Table 6.1. Fluorescence upconversion decay parameters for curcumin in different micellar systems^a

Micellar system	a_1	τ_1 (ps)	τ_2 (ps)
TX-100/H ₂ O	0.30 ± 0.04	8 ± 2	80 ± 10
TX-100/D ₂ O	0.23 ± 0.03	8 ± 2	130 ± 20
DTAB/H ₂ O	0.36 ± 0.03	6 ± 2	50 ± 5
DTAB/D ₂ O	0.22 ± 0.03	6 ± 2	80 ± 5
SDS/H ₂ O	0.57 ± 0.03	3 ± 2	55 ± 3
SDS/D ₂ O	0.57 ± 0.03	3 ± 2	85 ± 6

^a The fluorescence upconversion traces, $f(t)$, were fitted with the multi-exponential function $f(t) = a_1 \exp(-t/\tau_1) + a_2 \exp(-t/\tau_2)$, where $a_1 + a_2 = 1$.

Early time solvation dynamics in micelles. The fluorescence upconversion results in Figure 6.3 show that in addition to the component that is attributed to ESIHT, there is an early time decay component with a time constant significantly shorter than the ESIHT component. Table 6.1 summarizes the time constant of the fast component, showing that values of 8, 6 and 3 ps were obtained for curcumin in TX-100, DTAB, and SDS micelles, respectively. Interestingly, unlikely the ESIHT component which shows an isotope effect, the fast decay component is insensitive to deuteration of curcumin. As shown in Table 6.1, the τ_1 values are virtually identical for nondeuterated and deuterated curcumin in each of the micelles. In our previous study on curcumin in polar organic solvents, an isotope effect-free fast decay component was also observed and we demonstrated that the decay component is due to solvation of curcumin in these solvents.²³ Using the previous results as a guide, we conducted a series of fluorescence upconversion experiments with a time window of 10 ps. The results are shown in Figure 6.4. For curcumin in the TX-100 micelle (Figure 6.4A), the fluorescence upconversion traces show a clear decay at 470 nm (blue) and this decay slows down considerably at 540 nm (red). However, at 610 nm (green), the fluorescence decay vanishes and a rise component is observed. The presence of the decay and rise components as a function of fluorescence wavelength shown in Figure 6.4 is a key signature of solvation dynamics. As will be discussed further below, water molecules in the micellar structure play a major role in solvating curcumin. For curcumin in the DTAB micelle (Figure 6.4B), an almost identical trend in the fluorescence upconversion is shown, with a rise component observed at 610 nm. While a similar behavior of the multiwavelength fluorescence upconversion is shown by curcumin in the SDS micelle, the wavelengths at which the decays were recorded were set slightly to the red due to a larger Stokes shift observed for curcumin

in this micelle. In short, the results indicate the presence of solvation dynamics for curcumin in TX-100, DTAB and SDS micelles.

Using the method outlined in the experimental section, the solvation correlation function, $C(t)$, for curcumin in the three micelles were constructed from 15-17 wavelength-resolved decay traces depending upon the systems and are shown in Figure 6.5. First, it is clear that for curcumin in each micelle, $C(t)$ shows a rapid decay which is followed by a slow decay and an apparent constant offset. Curcumin shows a fractional solvation at 300 fs, f_{300} fs, of 0.25, 0.53, and 0.50, in the TX-100, DTAB, and SDS micelles, as summarized in Table 6.2. The $C(t)$ for curcumin in each of the micelles was fitted with a multiexponential function, of which the equation is shown as follows, and the fitting parameters are listed in Table 6.2.

$$C(t) = a_1 \exp(-t/\tau_1) + a_2 \exp(-t/\tau_2) \quad (6.2)$$

Initially, a fit to eq 6.2 was attempted by fixing the τ_2 component to 8, 6, and 3 ps for the TX-100, DTAB, and SDS micelles, respectively and excellent fits were obtained. For curcumin in the TX-100 micelle, the fast decay component in $C(t)$ has a time constant of 0.31 ps, which is as short as the instrument response function (IRF) of our apparatus, and an amplitude of 37%. In the DTAB and SDS micelles, however, the time constants of the fast component have values of 0.12 and 0.15 ps, respectively, which are shorter than the IRF of the instrument. These IRF-limited decay time constants have amplitudes of 56% and 54% in these two micelles. The fast component of $C(t)$ is followed by a slow decay component, of which the time constants are fixed as mentioned above. The amplitudes of this component are nearly the same in the three micelles, ranging from 20% to 26%. In addition to the fast (≤ 300 fs) and slow (3 – 8 ps) components of $C(t)$, it is obvious that solvation dynamics are

incomplete within the time window of the experiment, giving rise to a constant offset in the $C(t)$, as shown in Figure 6.5 and the a_3 term in the multiexponential equation in Table 6.2. Alternatively, a good fit to eq 2 can also be obtained by fixing the fast component to 0.1 ps for the three micelles. In this case, the slow component has a time constant of 1.8, 2.6, and 1.9 ps, respectively. The best-fit curves and fitting parameters are provided in the Supporting Information. The significance of the decay components of $C(t)$ are discussed below.

Solvation dynamics in micellar media is currently an intense area of research.^{40-43,54-62} Surfactant micelles are excellent model systems for more complex biomembranes and investigations on solvation dynamics in micelles provide critical insight into the behavior of small molecules in biomembranes. First of all, in our study, it is noteworthy that for each of the micelles the value of the time constant τ_2 of $C(t)$, as summarized in Table 6.2, is virtually identical within experimental error to that of the fast component of the fluorescence upconversion results shown in Figure 6.3 and Table 6.1. The excellent agreement strongly indicates that the fast component observed in the fluorescence upconversion results (Figure 6.3 and Table 6.1) is due to solvation dynamics of curcumin in micellar media. Second, the decay of $C(t)$ of curcumin in all micelles show a fast component with a time constant that is either as fast as the IRF (300 fs) or too short to be resolved with our apparatus. This fast decay component was also reported for the SDS and DTAB micelles in a study by Dey et al. using coumarin 480 as the probe molecule and a time constant of <300 fs was measured.⁵⁴ This fast component of solvation dynamics has been previously attributed to motions of labile or bulklike water molecules at the interface of the micelle.⁴⁰⁻⁴⁴ As for fast solvation dynamics in TX-100, Mandal et al. showed that the fastest component has a time constant of 2.1 ps,⁶⁰ which is somewhat longer than our measured value of ~300 fs. To our knowledge, a

~300 fs solvation dynamics component in the TX-100 micelle is previously unobserved, and our result is the first demonstration of ultrafast solvation dynamics of the TX-100 micelle. Third, it is apparent that curcumin has a shorter time constant of fast solvation dynamics in the SDS/DTAB micelles (<300 fs) than in the TX-100 micelle (~300 fs). This phenomenon is likely to originate from the level of interaction of curcumin with the bulklike water molecules at the aqueous/micelle interface. A previous study shows that the hydration layer of the SDS and DTAB-like micelles is substantially thinner (6 – 9 Å) than that of the TX-100 micelle (20 Å).⁴² This result indicates that curcumin is less shielded from the bulklike water molecules in the former two micelles than in the latter and hence faster solvation dynamics are observed in the SDS and DTAB micelles. Fourth, the slow component of $C(t)$, which has time constants of 8, 6 and 3 ps, respectively, in the TX-100, DTAB, and SDS micelles, shows reasonable agreement with results from previous studies,^{54,60} which has been assigned to solvation of water molecules that are bound to the surface of the micelle by hydrogen bonding or the head group-water interactions.⁴⁰⁻⁴⁴ Lastly, the constant offset observed in the $C(t)$ of curcumin in the three micelles, which is expressed as a_3 in Table 6.2, indicates the presence of a decay component with a time constant that is vastly longer than the 10 ps time window of the solvation dynamics studies. Although this decay component of $C(t)$ is too long to be resolved with our solvation dynamics investigations, it has been established in previous studies that $C(t)$ has a long lived component in micelles, with time constants ranging from 165 to 300 ps.^{54,60}

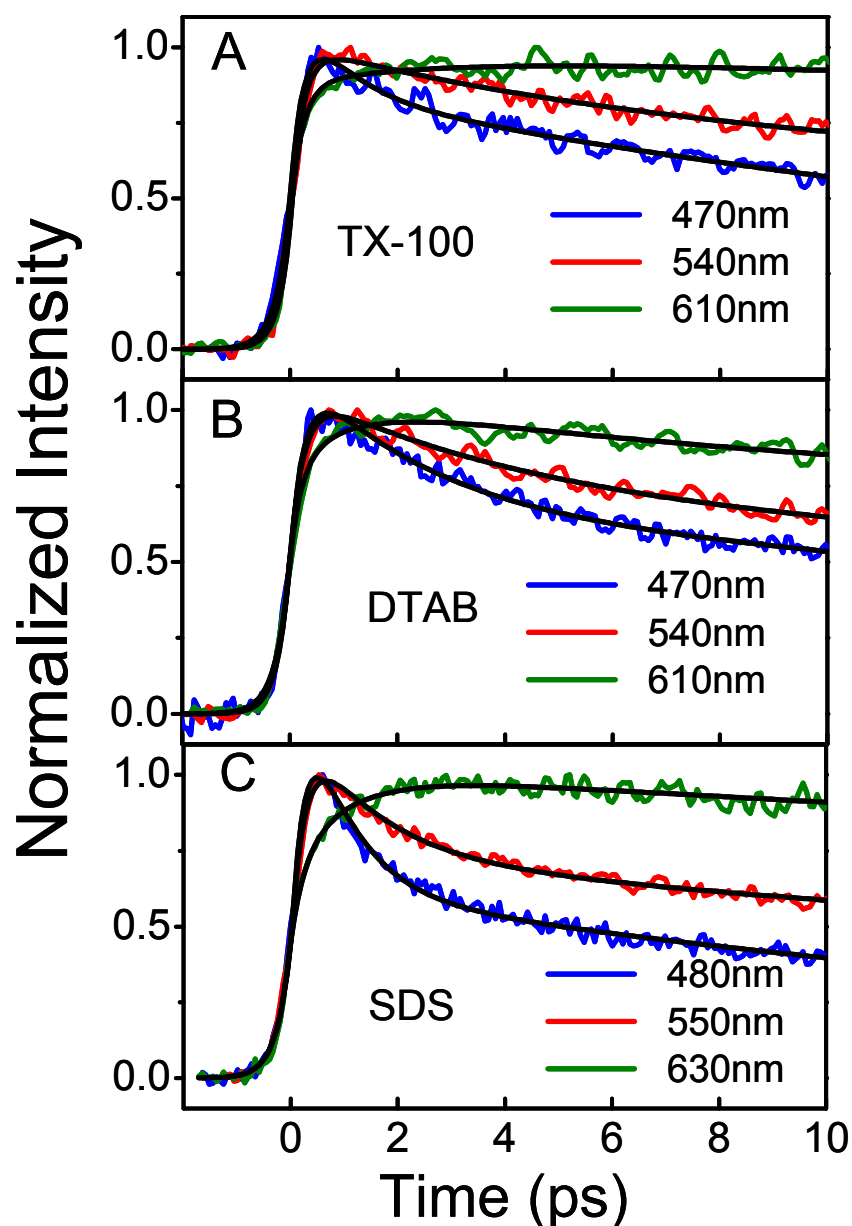


Figure 6.4. Representative normalized wavelength resolved fluorescence upconversion decay traces of curcumin at three different wavelengths in (A) TX-100, (B) DTAB, and (C) SDS micelles at pH = 7.4 tris buffer. The time-resolved traces at the red end (610 nm for TX-100 and DTAB and 630 nm for SDS micelles) show a rising component, clearly indicating the presence of solvation dynamics.

Table 6.2. Solvation correlation function, $C(t)$, decay parameters for curcumin in different micellar systems

Micellar system	$f_{300 \text{ fs}}^a$	a_1^b	τ_1 (ps)	a_2	τ_2 (ps) ^c	a_3
TX-100	0.25 ± 0.03	0.37 ± 0.02	0.31 ± 0.04	0.22 ± 0.03	8	0.41 ± 0.02
DTAB	0.53 ± 0.03	0.56 ± 0.02	0.12 ± 0.02	0.20 ± 0.02	6	0.24 ± 0.02
SDS	0.50 ± 0.03	0.54 ± 0.02	0.15 ± 0.02	0.26 ± 0.02	3	0.20 ± 0.01

^a $f_{300 \text{ fs}}$: fractional solvation at 300 fs.

^b The $C(t)$ was fitted with the multi-exponential function $C(t) = a_1 \exp(-t/\tau_1) + a_2 \exp(-t/\tau_2) + a_3$.

^c The τ_2 component was fixed at 8, 6, and 3 ps for the TX-100, DTAB, and SDS micelles, respectively to demonstrate the agreement with the results in Figure 6.3 and Table 6.1.

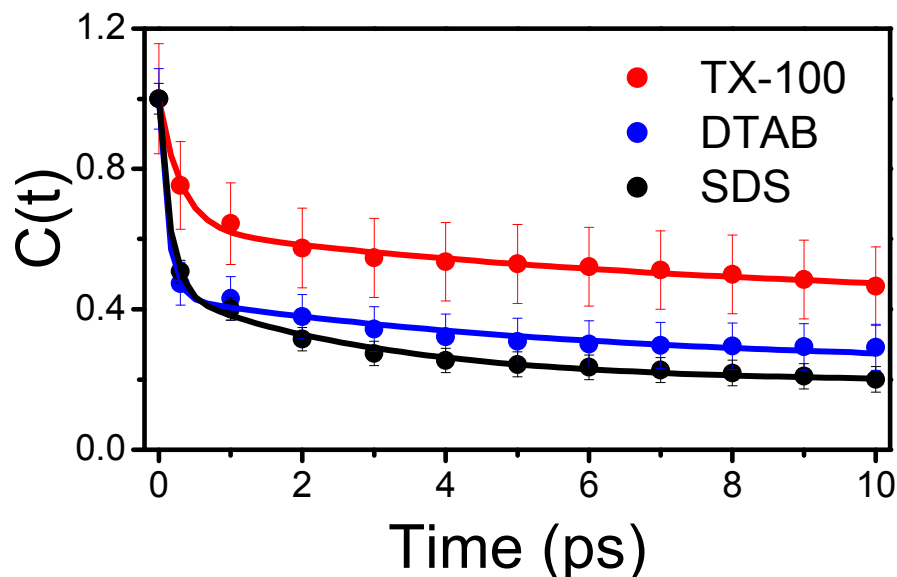


Figure 6.5. Solvation correlation function, $C(t)$, of curcumin in TX-100 (red), DTAB (blue), and SDS (black) micelles constructed from multiwavelength fluorescence upconversion results. The $C(t)$ is well fitted with a biexponential function. All three micelles show different fast and slow components, refer to Table 6.2. Note that the slow component in $C(t)$ for each micelle is identical to the fast component of the corresponding fluorescence upconversion decay at 520 nm within experimental error, see Figure 6.3 and Table 6.1.

Fluorescence Lifetime in Micelles. The excited-state kinetics of curcumin in micelles was also investigated using time-correlated single photon counting (TCSPC). Figure 6.6 shows the fluorescence decays of curcumin in the TX-100, DTAB and SDS micelles in tris (pH 7.4) and tris- d_{11} (pD 7.4) buffer with a 3 ns time window, in which curcumin produces an isotope effect in each of the micelles. The decays are multiexponential in nature and three exponential functions are necessary to fit the data well. The best fit parameters and the average fluorescence lifetimes are summarized in Table 6.3. Briefly, in H_2O , the fastest decay component has a time constant ranging from 50 – 60 ps,

which is followed a slower component of ~ 200 ps and then a long lived 400 – 900 ps component. In contrast, in D_2O , while the two slower components are essentially indistinguishable within experimental error, the fastest component increases to 70 – 85 ps, exhibiting an isotope effect of 1.4 in the three micelles.

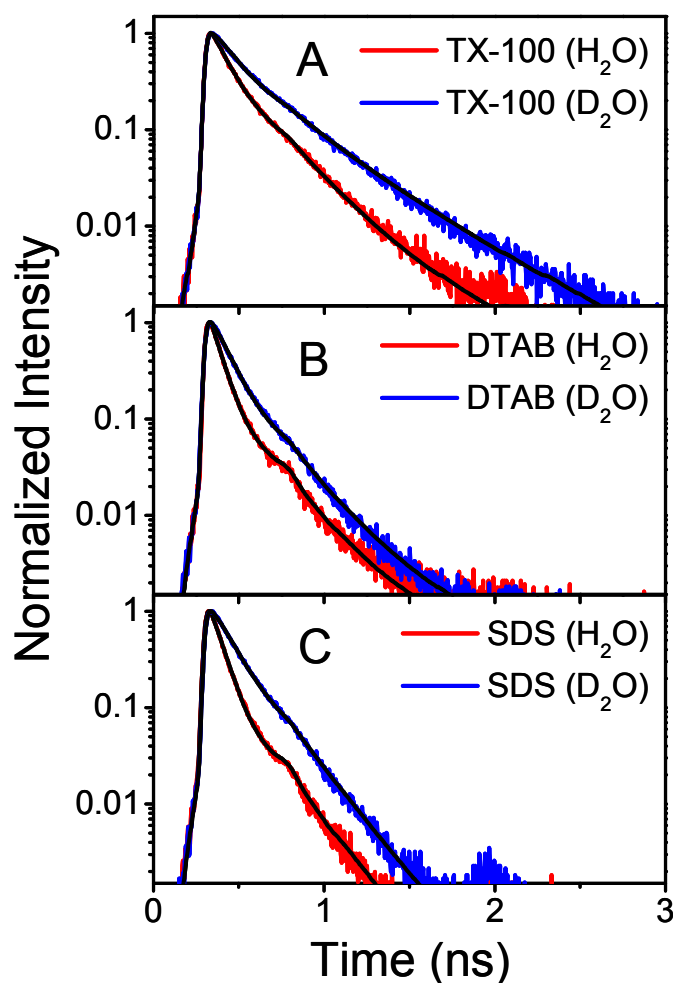


Figure 6.6. Fluorescence decays obtained with time-correlated single photo counting for curcumin in (A) TX-100, (B) DTAB and (C) SDS micelle at pH = 7.4 (red) and pD = 7.4 (blue) tris buffer. The decays were obtained at $\lambda_{\text{ex}} = 407$ nm and $\lambda_{\text{em}} \geq 425$ nm with a full time window of 3.33 ns. The decays are well fitted with a triexponential decay function. The lengthening of the shortest decay component in the deuterated media supports the assignment of this decay component to ESIHT, which shows excellent consistency with the fluorescence upconversion results.

Table 6.3. Fluorescence lifetime results of curcumin in different micellar systems

Micellar system	a_1^a	τ_1 (ps)	a_2	τ_2 (ps) ^b	τ_3 (ps)	$\langle \tau \rangle$ (ps)
TX-100/H ₂ O	0.68 ± 0.02	60 ± 5	0.30 ± 0.02	210 ± 30	510 ± 100	115 ± 15
TX-100/D ₂ O	0.48 ± 0.02	85 ± 5	0.32 ± 0.02	210 ± 30	430 ± 20	195 ± 12
DTAB/H ₂ O	0.88 ± 0.02	50 ± 5	0.11 ± 0.02	190 ± 50	900 ± 200	75 ± 12
DTAB/D ₂ O	0.72 ± 0.03	70 ± 5	0.27 ± 0.03	190 ± 50	730 ± 300	110 ± 17
SDS/H ₂ O	0.91 ± 0.01	55 ± 5	0.08 ± 0.01	185 ± 10	415 ± 80	70 ± 6
SDS/D ₂ O	0.55 ± 0.02	75 ± 5	0.44 ± 0.02	185 ± 10	405 ± 20	125 ± 8

^aThe fluorescence decay traces, $f(t)$, were fitted with the multi-exponential function $f(t) = a_1 \exp(-t/\tau_1) + a_2 \exp(-t/\tau_2) + a_3 \exp(-t/\tau_3)$, where $a_1 + a_2 + a_3 = 1$.

^bThe τ_2 values were limited to the range specified.

It is noteworthy that there is a close match between the time constants of the ESIHT component, as established in an earlier section on fluorescence upconversion, and the τ_1 component as measured by TCSPC, see Table 6.1 and 6.3. Furthermore, similar to the fluorescence upconversion results, this decay component experiences an isotope effect in the deuterated environment. Therefore, the results strongly indicate that the τ_1 component measured by TCSPC is due to ESIHT. Interestingly, the average fluorescence lifetimes of curcumin in the TX-100 micelle is close to that of curcumin in methanol (130 ps), suggesting the similarities of the two environments, as discussed in a previous section. The shorter average lifetimes of curcumin in the DTAB and SDS micelles imply a greater level of intramolecular hydrogen bonding but lesser extent of intermolecular hydrogen bonding, which was also discussed in the same section.

Conclusion

We have presented unambiguous results to demonstrate that excited-state intramolecular hydrogen atom transfer (ESIHT) is a major photophysical process of curcumin in the TX-100, DTAB and SDS micelles. The fluorescence upconversion transient of curcumin in each micelle shows a biexponential decay, with time constants of 3 – 8 ps (fast) and 50 – 80 ps (slow). The slow component exhibits a pronounced isotope effect, producing a decay time constant of 80 – 130 ps in the micelles, which is assigned to ESIHT. The ESIHT rate of curcumin in the TX-100 micelle is lower than those in the other two micellar system. The hydrogen bonding between curcumin and the TX-100 surfactant may contribute to this effect. The fast decay component, unlike the ESIHT process, is insensitive to deuteration of curcumin and has been attributed to solvation dynamics using results from multiwavelength fluorescence upconversion studies. The water molecules in the micellar

structure give rise to solvation dynamics of curcumin. The solvation dynamics observed in the micelles are due to water molecules at the micelle interface that are labile or bulklike and those that are bound to the surface of the micelles.

Acknowledgment. TWK acknowledges a research grant from the Australian Research Council and National Health and Medical Research Council Network “Fluorescence Applications in Biotechnology and Life Sciences.”

References

- (1) Ruby, A. J.; Kuttan, G.; Babu, K. D.; Rajasekharan, K. N.; Kuttan, R. *Cancer Lett.* **1995**, *94*, 79.
- (2) Lantz, R. C.; Chen, G. J.; Solyom, A. M.; Jolad, S. D.; Timmermann, B. N. *Phytomedicine* **2005**, *12*, 445.
- (3) Aggarwal, B. B.; Kumar, A.; Bharti, A. C. *Anticancer Res.* **2003**, *23*, 363.
- (4) Shi, M.; Cai, Q.; Yao, L.; Mao, Y.; Ming, Y.; Ouyang, G. *Cell Biol. Int.* **2006**, *30*, 221.
- (5) Yang, F.; Lim, G. P.; Begum, A. N.; Ubeda, O. J.; Simmons, M. R.; Ambegaokar, S. S.; Chen, P. P.; Kaye, R.; Glabe, C. G.; Frautschy, S. A.; Cole, G. M. *J. Biol. Chem.* **2005**, *280*, 5892.
- (6) Masuda, M.; Suzuki, N.; Taniguchi, S.; Oikawa, T.; Nonaka, T.; Iwatsubo, T.; Hisanaga, S.-i.; Goedert, M.; Hasegawa, M. *Biochemistry* **2006**, *45*, 6085.
- (7) Egan, M. E.; Pearson, M.; Weiner, S. A.; Rajendran, V.; Rubin, D.; Glockner-Pagel, J.; Canny, S.; Du, K.; Lukacs, G. L.; Caplan, M. J. *Science* **2004**, *304*, 600.
- (8) Jagetia, G. C.; Rajanikant, G. K. *J. Surg. Res.* **2004**, *120*, 127.
- (9) Maheshwari, R. K.; Singh, A. K.; Gaddipati, J.; Srimal, R. C. *Life Sci.* **2006**, *78*,

2081.

- (10) Kiuchi, F.; Goto, Y.; Sugimoto, N.; Akao, N.; Kondo, K.; Tsuda, Y. *Chem. Pharm. Bull.* **1993**, *41*, 1640.
- (11) <http://clinicaltrials.gov/ct2/show/NCT00094445>.
- (12) <http://clinicaltrials.gov/ct2/show/NCT00099710>.
- (13) Bisht, S.; Feldmann, G.; Soni, S.; Ravi, R.; Karikar, C.; Maitra, A.; Maitra, A. *J. Nanobiotechnol.* **2007**, *5*, 3.
- (14) Leung, M. H. M.; Kee, T. W. *Langmuir* **2009**, *25*, 5773.
- (15) Tønnesen, H. H. *Pharmazie* **2002**, *57*, 820.
- (16) Leung, M. H. M.; Colangelo, H.; Kee, T. W. *Langmuir* **2008**, *24*, 5672.
- (17) Wang, Y.-J.; Pan, M.-H.; Cheng, A.-L.; Lin, L.-I.; Ho, Y.-S.; Hsieh, C.-Y.; Lin, J.-K. *J. Pharm. Biomed. Anal.* **1997**, *15*, 1867.
- (18) Tønnesen, H. H.; Karlsen, J. Z. *Lebensm.-Unters. Forsch.* **1985**, *180*, 132.
- (19) Kunwar, A.; Barik, A.; Pandey, R.; Priyadarsini, K. I. *Biochim. Biophys. Acta, Gen. Subj.* **2006**, *1760*, 1513.
- (20) Payton, F.; Sandusky, P.; Alworth, W. L. *J. Nat. Prod.* **2007**, *70*, 143.
- (21) Nardo, L.; Paderno, R.; Andreoni, A.; Masson, M.; Haukvik, T.; Tønnesen, H. H. *Spectroscopy* **2008**, *22*, 187.
- (22) Khopde, S. M.; Priyadarsini, K. I.; Palit, D. K.; Mukherjee, T. *Photochem. Photobiol.* **2000**, *72*, 625.
- (23) Adhikary, R.; Mukherjee, P.; Kee, T. W.; Petrich, J. W. *J. Phys. Chem. B* **2009**, *113*, 5255.
- (24) Miskovsky, P. *Curr. Drug Targets* **2002**, *3*, 55.

- (25) Das, K.; English, D. S.; Petrich, J. W. *J. Phys. Chem. A* **1997**, *101*, 3241.
- (26) Das, K.; English, D. S.; Petrich, J. W. *J. Am. Chem. Soc.* **1997**, *119*, 2763.
- (27) English, D. S.; Das, K.; Ashby, K. D.; Park, J.; Petrich, J. W.; Castner, E. W., Jr. *J. Am. Chem. Soc.* **1997**, *119*, 11585.
- (28) English, D. S.; Zhang, W.; Kraus, G. A.; Petrich, J. W. *J. Am. Chem. Soc.* **1997**, *119*, 2980.
- (29) Petrich, J. W. *Int. Rev. Phys. Chem.* **2000**, *19*, 479.
- (30) Smirnov, A. V.; Das, K.; English, D. S.; Wan, Z.; Kraus, G. A.; Petrich, J. W. *J. Phys. Chem. A* **1999**, *103*, 7949.
- (31) Gai, F.; Fehr, M. J.; Petrich, J. W. *J. Am. Chem. Soc.* **1993**, *115*, 3384.
- (32) Zhong, D. P.; Douhal, A.; Zewail, A. H. *Proc. Natl. Acad. Sci. USA* **2000**, *97*, 14056.
- (33) Chowdhury, P. K.; Halder, M.; Sanders, L.; Calhoun, T.; Anderson, J. L.; Armstrong, D. W.; Song, X.; Petrich, J. W. *J. Phys. Chem. B* **2004**, *108*, 10245.
- (34) Fee, R. S.; Maroncelli, M. *Chem. Phys.* **1994**, *183*, 235.
- (35) Maroncelli, M.; Fleming, G. R. *J. Chem. Phys.* **1987**, *86*, 6221.
- (36) Stigter, D. *J. Phys. Chem.* **1975**, *79*, 1008.
- (37) Barik, A.; Goel, N. K.; Priyadarsini, K. I.; Mohan, H. *J. Photosci.* **2004**, *11*, 95.
- (38) Douhal, A.; Lahmani, F.; Zewail, A. H. *Chem. Phys.* **1996**, *207*, 477.
- (39) Chignell, C. F.; Bilski, P.; Reszka, K. J.; Motten, A. G.; Sik, R. H.; Dahl, T. A. *Photochem. Photobiol.* **1994**, *59*, 295.
- (40) Bagchi, B. *Chem. Rev.* **2005**, *105*, 3197.
- (41) Bhattacharyya, K. *Chem. Commun.* **2008**, 2848.
- (42) Bhattacharyya, K. *Acc. Chem. Res.* **2003**, *36*, 95.

- (43) Nandi, N.; Bhattacharyya, K.; Bagchi, B. *Chem. Rev.* **2000**, *100*, 2013.
- (44) Pal, S. K.; Zewail, A. H. *Chem. Rev.* **2004**, *104*, 2099.
- (45) Reddy, A. C. P.; Sudharshan, E.; Rao, A. G. A.; Lokesh, B. R. *Lipids* **1999**, *34*, 1025.
- (46) Barik, A.; Mishra, B.; Kunwar, A.; Priyadarsini, K. I. *Chem. Phys. Lett.* **2007**, *436*, 239.
- (47) Barik, A.; Priyadarsini, K. I.; Mohan, H. *Photochem. Photobiol.* **2003**, *77*, 597.
- (48) Mitra, S. P. *J. Surf. Sci. Technol.* **2007**, *23*, 91.
- (49) Moog, R. S.; Maroncelli, M. *J. Phys. Chem.* **1991**, *95*, 10359.
- (50) Silva, A. M. S.; Filipe, P.; Seixas, R.; Pinto, D.; Patterson, L. K.; Hug, G. L.; Cavaleiro, J. A. S.; Maziere, J. C.; Santus, R.; Morliere, P. *J. Phys. Chem. B* **2008**, *112*, 11456.
- (51) Kimura, N.; Umemura, J.; Hayashi, S. *J. Colloid Interface Sci.* **1996**, *182*, 356.
- (52) Wang, X.; Wang, J.; Wang, Y.; Chen, Z. Z.; Tang, B. *J. Photochem. Photobiol., A* **2007**, *186*, 194.
- (53) Melo, E. C. C.; Costa, S. M. B.; Maçanta, A. L.; Santos, H. *J. Colloid Interface Sci.* **1991**, *141*, 439.
- (54) Dey, S.; Sasmal, D. K.; Das, D. K.; Bhattacharyya, K. *ChemPhysChem* **2008**, *9*, 2848.
- (55) Pal, S.; Bagchi, B.; Balasubramanian, S. *J. Phys. Chem. B* **2005**, *109*, 12879.
- (56) Kumbhakar, M.; Nath, S.; Mukherjee, T.; Pal, H. *J. Chem. Phys.* **2004**, *121*, 6026.
- (57) Shirota, H.; Tamoto, Y.; Segawa, H. *J. Phys. Chem. A* **2004**, *108*, 3244.
- (58) Sen, P.; Mukherjee, S.; Halder, A.; Bhattacharyya, K. *Chem. Phys. Lett.* **2004**, *385*, 357.
- (59) Pal, S. K.; Peon, J.; Bagchi, B.; Zewail, A. H. *J. Phys. Chem. B* **2002**, *106*, 12376.

- (60) Mandal, D.; Sen, S.; Bhattacharyya, K.; Tahara, T. *Chem. Phys. Lett.* **2002**, 359, 77.
- (61) Balasubramanian, S.; Bagchi, B. *J. Phys. Chem. B* **2001**, 105, 12529.
- (62) Pal, S. K.; Sukul, D.; Mandal, D.; Sen, S.; Bhattacharyya, K. *Chem. Phys. Lett.* **2000**, 327, 91.

**CHAPTER 7. A NEW FLUORESCENCE BASED METHOD FOR THE REAL-TIME
DETECTION OF CENTRAL NERVOUS SYSTEM (CNS) TISSUES ON BOVINE
CARCASSES BASED ON LIPOFUSCIN**

A paper published in *Journal of Agricultural and Food Chemistry*

Holger Schönenbrücher[†], Ramkrishna Adhikary[‡], Prasun Mukherjee[‡], Thomas A. Casey[§],
Mark A. Rasmussen^{||}, Frank D. Maistrovich[‡], Amir N. Hamir[†], Marcus E. Kehrl, Jr.[†], Jürgen
A. Richt^{†*} and Jacob W. Petrich^{†*}

Abstract

The removal of Central Nervous System (CNS) tissues as part of Bovine Spongiform Encephalopathy (BSE) risk material is one of the highest priority tasks to avoid contamination of the human food chain with BSE. No currently available method enables the real-time detection of possible CNS tissue contamination on carcasses during slaughter. The fluorescent pigment lipofuscin is a heterogeneous, high-molecular weight material that has been shown to be enriched in high concentrations in neuronal tissues. In this study,

Reprinted with permission from *Journal of Agricultural and Food Chemistry* 2008, 56(15), 6220-6226. Copyright (2008) American Chemical Society.

[†]Virus and Prion Diseases of Livestock Research Unit, National Animal Disease Center, Agricultural Research Service, USDA, Ames, Iowa, 50010.

[‡]Department of Chemistry, Iowa State University, Ames, Iowa, 50011-3111.

[§]Pre-Harvest Food Safety and Enteric Disease Research Unit, National Animal Disease Center, Agricultural Research Service, USDA, Ames, Iowa, 50010.

^{||}SarTec Corp., Anoka, Minnesota, 55303.

* To whom correspondence should be addressed.

lipofuscin fluorescence was investigated as a marker for real-time detection of CNS contamination. Front-faced fluorescence spectra of brain and spinal cord samples from 11 cattle gave identical, reproducible fluorescence signal patterns with high intensities. The specificity of these spectra was assessed investigating 13 different non-CNS tissues enabling the differentiation of brain and spinal cord by signal intensity and structure of the spectra, respectively. Small quantities of bovine spinal cord were reliably detected in the presence of raw bovine skeletal muscle, fat, and vertebrae. The presented data are the fundamental basis for the development of a prototype device allowing real-time monitoring of CNS tissue contamination on bovine carcasses and meat cuts.

Introduction

Bovine spongiform encephalopathy (BSE) is a fatal, neurodegenerative transmissible spongiform encephalopathy (TSE) in cattle that is thought to be the cause of variant Creutzfeldt - Jakob disease (vCJD) in humans.¹ The oral route of infection is presumptively the most likely way of transmission of BSE to humans.^{2,3} Since most BSE cases were diagnosed in the United Kingdom and other European countries, the global nature of BSE was highlighted by detection of the disease in cattle in North America⁴⁻⁶ and Japan.⁷

Removal of bovine specified risk materials (SRMs, e. g. brain and spinal cord) from the human food chain is of critical importance for protecting consumers from BSE.^{8,9} Brain and spinal cord from BSE infected cattle have been shown to contain the highest infectivity titer of the causative agent of BSE, the abnormal prion protein PrP^{BSE}.⁸ As a consequence, many countries have banned bovine CNS tissues from meat and meat products. For instance, regulations regarding SRMs are constituted by the European commission in Annex V Commission Regulation (EC) No. 999/2001 and for the USA in Docket No. 03-025IF of the

USDA-Food Safety and Inspection Service (FSIS).

So far only laboratory methods for the detection of CNS tissues as part of the BSE risk material have been developed. These include immunochemical detection and enzyme-linked immunosorbent assays (ELISA)^{10,11}, gas chromatography-mass spectrometry (GC-MS)¹², Western blot analysis^{13,14}, immunohistochemical methods^{14,15} and a real-time reverse transcription (RT)-PCR assay.^{16,17} None of this method is suitable for the direct real-time monitoring of CNS contamination on bovine carcasses during slaughter. Real-time based detection of CNS tissue contamination would allow immediate trimming and removal of remaining SRM from the carcass before it enters the food chain. In addition, meat cuts could be monitored after boning to prevent possible contamination with SRM tissues.

Fluorescence spectroscopy has been commonly used in a variety of biological applications due to its high sensitivity and specificity (for a review see refs 18-22). In addition, members of our group have previously demonstrated the potential of fluorescence spectroscopy for the detection of fecal contamination on the surface of meat during slaughter.^{23,24} The pigment lipofuscin is a heterogeneous, high-molecular weight fluorescent material that has been shown to be enriched in high concentrations in neuronal tissues.²⁵⁻³⁰ Its exact chemical composition is controversial.²⁵ In previous steady-state, front-faced fluorescence experiments, spectral features consistent with lipofuscin were found in bovine brain and spinal cord.^{25,31} To investigate the applicability of fluorescence from lipofuscin for a real-time detection of brain and spinal cord, spectral shapes and intensities of these two most important SRM tissues were investigated and compared to 13 non-CNS tissues. Furthermore the detection sensitivity of bovine spinal cord in the presence of skeletal muscle, fat and vertebrae was assessed.

Materials and Methods

Collection of bovine tissue samples. CNS and non-CNS tissue samples were collected from healthy male (n=6) and female (n=5) cattle directly after slaughter at local abattoirs (n=9) or during necropsy of healthy control animals at the National Animal Disease Center (n=2). All samples were kept frozen at -20°C until processing. Breeds included Holstein (n=2), Simmental (n=2), and Angus cross breeds (n=7). Ages included 2 months (n=1), 5-6 months (n=2), 20-24 months (n=4), 48-72 months (n=4) as determined by dentition. Brain and spinal cord were investigated as CNS tissues. The 13 non-CNS tissues were adrenal gland, bone (vertebrae), bone marrow, dorsal root ganglia, fat, heart, kidney, liver, lung, lymph node (e.g. iliofemoral ln), peripheral nerve (e. g. sciatic nerve), skeletal muscle, and spleen.

Steady-State Measurements. Steady-state fluorescence spectra were obtained on a SPEX Fluoromax-2 (ISA Jobin-Yvon/SPEX, Edison, NJ) with a 5-nm band-pass and were corrected for lamp spectral intensity and detector response. Fluorescence spectra were collected in a front-faced orientation. To select the appropriate excitation wavelength, brain and spinal cord samples from cattle were excited at 350, 410, 470, and 520 nm. Excitation at 470 nm was determined to provide optimal measurements. Therefore, all samples were excited at 470 nm with an interference filter on the excitation side; and emission was collected at wavelengths greater than 505 nm using a cutoff filter before the detector to eliminate scattered light. Polarized fluorescence spectra were obtained using two polarizers, one on the excitation side and another one on the emission side with the appropriate excitation interference filter and cut-off emission filter. Fluorescence spectra were taken in horizontal-horizontal (HH) and horizontal-vertical (HV) orientations of the polarizers.

Statistical and graphical data analysis was performed by using Origin[®] V. 7 software (OriginLab Corporation, USA).

Investigation of fluorescence spectra of bovine brain, spinal cord and non-CNS tissues. Ten identically-sized cross and longitudinal sections (five of each) of identical regions of the frontal cortex and the cerebellum of each brain and ten spinal cord samples from each animal were prepared. Each sample was placed on a microscope slide and stored in a dark moist chamber at $\leq 7^{\circ}\text{C}$ for 120 minutes until collection of the fluorescence spectra at room temperature. Three cross sections were prepared for the measurement of the fluorescence signal from each of the cervical, the thoracic, the lumbar, and the sacral regions of the spinal cord from three different animals of 24 months (n=2) and 48 months (n=1) of age. Spinal cord samples from two different animals were kept at -20°C and used for collection of fluorescence spectra after 0, 5, 26, 30, 50, 56 hours, and 8 weeks. Longitudinal and cross sections of the non-CNS tissues were prepared as described above.

Sensitivity of detection of spinal cord by using the front-faced experiment. The lower limit of detection was determined for the optimized setup of the front-faced experiment by using spinal cord cross sections from two different animals. In general, the total surface area exposed with the excitation wavelength was 1.0 cm x 2.0 cm. Pieces of each spinal cord cross section were prepared in duplicate corresponding to surface areas of 0.4 cm x 0.4 cm and 0.1 cm x 0.2 cm and placed on microscope slides. For each sample, duplicate fluorescence spectra were collected and the experiment was repeated. The lower limit of detection is defined by convention as the smallest size of tissue, which could be detected typical spectra.

Sensitivity of detection of spinal cord in the presence of different background tissues. Bovine skeletal muscle, abdominal fat tissues and vertebrae of two different cattle were used for the assessment of the detection sensitivity of spinal cord in the presence of background signals. For the front-faced experiments, six sample sections of similar size and height were prepared from these tissues, and were placed on microscope slides. Skeletal muscle and fat were cut into pieces of ~0.2 cm x 0.2 cm. The slices from vertebrae were kept as one piece. Cross sections were prepared from the spinal cord collected from three different animals and prepared as described above. Fluorescence spectra of all background tissue samples and the spinal cord itself were collected. The surface area of the entire sample prepared was of similar size to the area exposed to excitation light. A piece of spinal cord was placed in between the skeletal muscle, fat or on top in case of vertebrae samples, respectively. The sample size of the spinal cord was adjusted to represent fractions of i) 10% and ii) 5% of the surface area of the entire sample. This corresponded to a spinal cord section of ~0.1cm x 0.1 cm for a surface area of 5%. All artificially spiked samples were prepared in duplicate and the experiment was conducted twice.

Semiquantitative measurement of the amount of spinal cord added to the different background tissues by means of real time-PCR. A comparative analysis using real-time PCR for the detection of ruminant glial fibrillary acidic protein (GFAP) mRNA was performed to i) show that fat and muscle samples used as background tissues were free of CNS and ii) show the reproducibility of our spiking experiments by using an alternative method as described previously.¹⁷ Briefly threshold cycle (Ct-values) obtained for the spiked samples were compared with Ct-values from standards of bovine minced meat artificially spiked with low amounts of bovine spinal cord to quantify the total amount of CNS tissue in

each sample.

Results

Selection of the excitation wavelength. Fluorescence spectra obtained using excitation wavelengths of 350 and 520 nm excitation were of low intensity and noisy, whereas excitation at 410 nm yielded high-intensity spectra containing few characteristic features -namely only one noticeable peak. On the other hand, by using 470 nm as the excitation wavelength, we were able to obtain structured fluorescence spectra with high signal-to-noise ratio from bovine brain and spinal cord. Therefore, we chose to use 470 nm as the excitation wavelength for all of the samples considered in this study. This is also consistent with the observations reported previously.³¹

Fluorescence spectra of bovine CNS and non-CNS tissues. The solid CNS and non-CNS tissues fluoresced over a broader range when excited at 470 nm. Characteristic overlaid front-faced fluorescence spectra for CNS (spinal cord and brain) and non-CNS (kidney, dorsal root ganglia, liver, lymph node, peripheral nerve, adrenal gland, lung, fat, heart, vertebrae, skeletal muscle, bone marrow and spleen) tissues are presented in Figure 7.1. Fluorescence spectra from brain and spinal cord exhibited three prominent peaks centered at ~ 525 nm, ~555 nm, and 585-600 nm. There were two small shoulders centered at ~625 nm and ~695 nm. To check whether the peaks shown by spinal cord were not caused by the light scattered from the sample, steady-state fluorescence anisotropy experiments using polarizing filters were undertaken. The HV spectra showed a structure very similar to that of the HH spectra (data not shown). This confirmed that the peaks found in spinal cord were not artifacts of the detection system. Similar results were obtained for brain and non-CNS tissues.

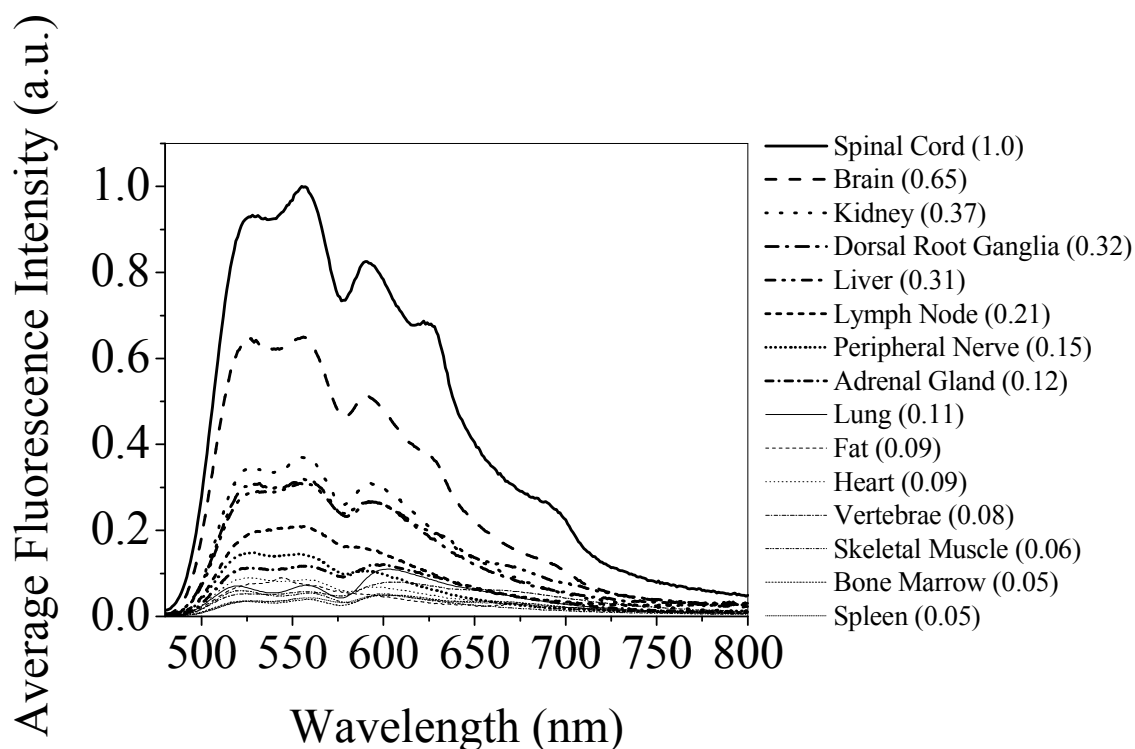


Figure 7.1. Representative overlaid fluorescence spectra of spinal cord, brain, kidney, dorsal root ganglia, liver, lymph node, peripheral nerve, adrenal gland, lung, fat, heart, vertebrae, skeletal muscle, bone marrow and spleen. The high fluorescence intensity from spinal cord enabled the detection of spinal cord in the presence of non-CNS tissue. All values were calculated with respect to the average fluorescence intensity of the spinal cord, which was arbitrarily taken as unity.

The spectral features of the CNS tissues were highly conserved in all samples studied regardless of age and breed. No differences in the structure and intensity were seen for brain samples taken from cerebrum or cerebellum as well as cervical, thoracic, lumbar and sacral spinal cord. The possible influence of the storage time and tissue consistency on the fluorescence signal was determined by measuring the fluorescence spectra at different time points and after homogenization, respectively. Reproducible results were obtained even after the storage of spinal cord sections for 0, 5, 26, 30, 50, 56 hours and 8 weeks at -20°C . A bead beater was used for mechanical homogenization of bovine spinal cord. This did not

affect the shape of the spectra, but resulted in decreased signal intensity (data not shown).

The most apparent difference between the two CNS tissues and all of the non-CNS tissues was the much higher fluorescence intensity obtained for spinal cord and brain tissues (Figure 7.1). This observation strongly suggests that fluorescence techniques can be exploited to differentiate these two tissues from non-CNS samples.

The normalized signal intensity obtained for bovine spinal cord was approximately three times higher than that from kidney and liver and eight-ten times higher than the intensity from skeletal muscle, fat and vertebrae. Standard errors in fluorescence intensity are shown in Figure 7.2. It is obvious that spinal cord can easily be detected in the presence of skeletal muscle, fat and vertebrae since the fluorescence intensity from these background tissues is very low. This might not be true in the presence of kidney, liver and lymph node tissues.

Based on the nature of their fluorescence spectra, the non-CNS tissues offered several other interesting findings. Peripheral nerves and dorsal root ganglia, both part of the peripheral nervous system, as well as the non-CNS tissues liver, kidney, heart, and lymph node showed strong similarities to the spectra of spinal cord (Figure 7.1). This included the localization of the three peaks with similar relative peak intensities. However, in these non-CNS tissues, the two small shoulders centered at ~625 and ~695 nm were rarely present. Non-CNS tissues like lung, adrenal gland, fat, skeletal muscle, bone marrow, vertebrae and spleen showed different fluorescence spectra with regard to relative peak intensity and also peak positions from CNS tissues (Figure 7.1). Lung tissue showed a quite different fluorescence spectrum with three peaks centered at ~520 nm, ~555 nm and a high intense peak at ~600- 610 relative to the first two peaks. This intense third peak was not observed in

CNS and PNS tissues. For adrenal gland and skeletal muscle, the spectra did show three peaks at similar peak maxima like CNS tissues, but the second and third peak had similar intensities. Fat tissue usually showed spectra with a single peak. A sharp peak at ~545 nm and sharp shoulder at ~675 nm were detected. Bone marrow showed the three peaks known from CNS tissues, but with a higher intensity for the third peak and an extra broad shoulder at ~655-665 nm. Spleen and vertebrae showed almost similar spectra as compared to that of bone marrow.

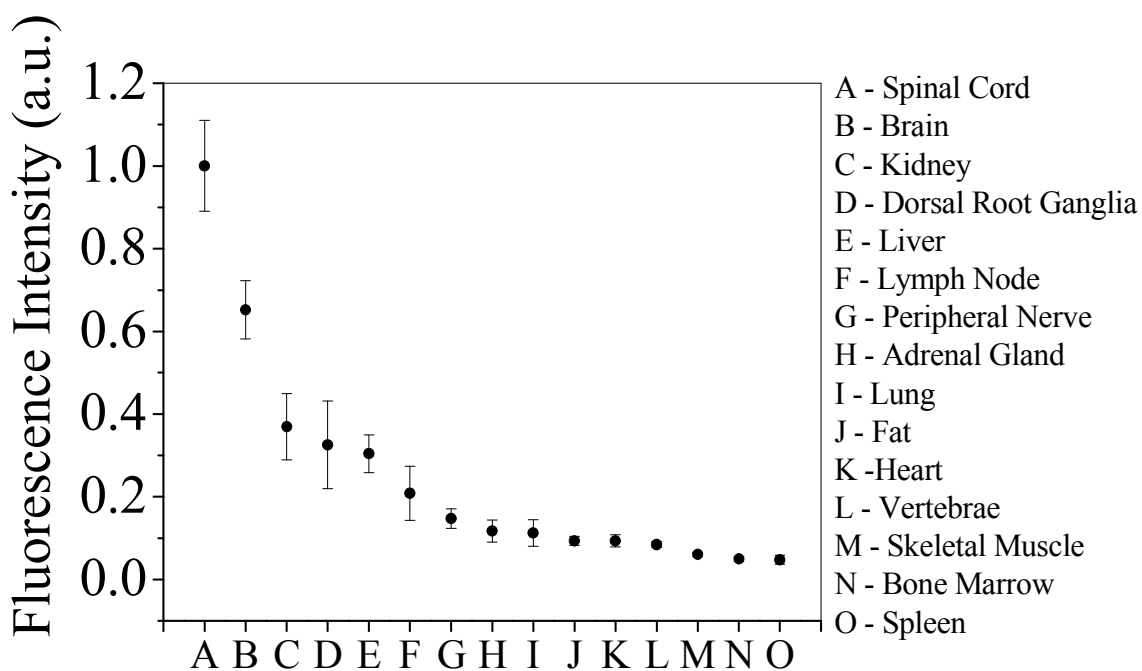


Figure 7.2. Average fluorescence intensities and corresponding standard errors of CNS and non-CNS tissues from cattle. Intensities were normalized with respect to the maximum average intensity of spinal cord. All values were calculated with respect to the average fluorescence intensity of the spinal cord, which was arbitrarily taken as unity.

Investigation of the detection sensitivity. The lower limit of detection for bovine spinal cord was addressed for the front-faced fluorescence experiment itself. In addition, the possible interference of the presence of skeletal muscle, fat, and vertebrae on the ability to detect CNS tissue was investigated. The front-faced experiment allowed reproducible collection of spectra described for spinal cord down to a surface area as small as ~ 0.1 cm x 0.1 cm. Regardless of the presence of skeletal muscle, fat or vertebrae 100% detection sensitivity was observed for all of the spinal cord samples representing 10% (n=36) of the entire surface area investigated. By using the experimental setup described above, 70% of all samples containing a 5% surface area of spinal cord in the background of fat (n=12) and skeletal muscle (n=12) as well as 80% of the samples in the presence of vertebrae (n=12) were identified correctly (Table 7.1). After the addition of 5% spinal cord, the fluorescence intensity was ~ 1.5 times higher and characteristic spectra for spinal cord in presence of background tissues were observed (Figure 7.3, Figure 7.4 A-C).

All fat and skeletal muscle samples used as background tissues for this experiment were shown to contain no CNS tissues by using real time-PCR analysis. Since solid vertebrae did not permit the possibility of obtaining a homogenous mixture with spinal cord, the outer surface of these bones was removed to assure that only a CNS free background was used. Comparative analysis of the fat and skeletal muscle samples containing a 5% surface area of spinal cord by real time-PCR detection of the GFAP mRNA gave concordant results for both consecutive experiments. The C_T values for skeletal muscle spiked with spinal cord were 25.53 (± 0.71). Spinal cord in the presence of fat showed C_T values of 21.46 (± 1.09) (Table 7.1).

Table 7.1. Detection sensitivity (% surface area) of bovine spinal cord in the presence of different background tissues investigated in two separate experiments for each background tissue.

Surface area (%) of spinal cord	Detection sensitivity (% [n]) in the presence of background tissues			C _T -values (± Standard deviations)	
	Skeletal muscle	Fat	Vertebrae	Skeletal muscle	Fat
10	100% (n=12)	100% (n=12)	100% (n=12)	n. d.	n. d.
5 ^a	70% (n=12)	70% (n=12)	80% (n=12)	25.53 (± 0.71)	21.46 (± 1.09)

^a The 5% surface area of bovine spinal cord tissue in muscle and fat corresponded to a total amount of 5 % (skeletal muscle) to 7% (fat) of spinal cord in the prepared samples as determined by RT real-time PCR amplification of the GFAP mRNA. Threshold cycle C_T-values are given for each of the two experiments conducted per tissue. Spinal cord in the background of solid vertebrae slices was not analyzed by real-time PCR since the solid bone did not result in a homogenous mixture the signal obtained from spinal cord would be overestimated.

n. d. not done

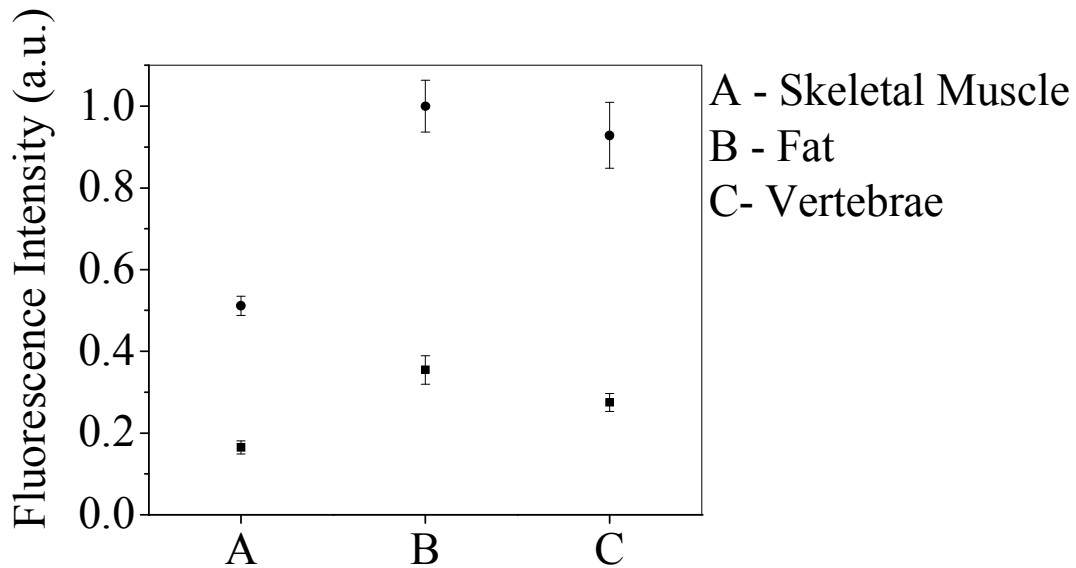


Figure 7.3. Fluorescence intensities obtained for the background tissues skeletal muscle fat, and vertebrae (■) and in the presence of 5% spinal cord (●). The error bars represent the standard errors associated with the measurements. Note that 5% spinal cord can be detected in presence of skeletal muscle, fat and vertebrae as background tissue.

Discussion

BSE is a zoonotic disease causally associated with vCJD in humans. BSE epidemic in various parts of the world had a severe impact on livestock and meat trade. Even 20 years after the first identification of the disease, the United Kingdom estimated costs in 2005 to 2006 for its BSE control measures including cohort culls and offspring cull compensation of approximately £265 million. Additional administrative costs for inspection and enforcement were estimated to be £64 million as reported for 1999-2000.³² In the U.S., beef exports decreased by over 80% in 2004 after the confirmation of only one BSE case and persist below pre-2004 levels.³³ Total U.S. beef industry losses arising from decreased beef and offal exports during 2004 ranged from \$3.2 billion to \$4.7 billion.³⁴ Resumption of beef exports depended on several restrictions made by the important trade partners Japan and

South Korea. This includes the removal of SRM (e.g. brain and spinal cord) and, in the case of South Korea, the acceptance of only boneless products, which represented an important export product for the South Korean market.³³

Consumer protection from the spread of BSE to the food chain is based on i) testing of cattle of particular minimal age for the presence of a BSE infection, ii) ban of SRM (in particular brain and spinal cord) from the food chain and iii) the ruminant feed ban. The materials identified as bovine SRM are the brain, skull, eyes, trigeminal ganglia, spinal cord, vertebral column (excluding the vertebrae of the tail, the transverse processes, and the wings of the sacrum), and dorsal root ganglia (DRG) from cattle of 30 months of age and older, and the distal ileum of the small intestine and the tonsils from all cattle.³⁵ The 30-month-and-older-age classification for SRMs is accepted by the U.S. and several other countries based on O.I.E (World Organisation for Animal Health, www.oie.int) requirements.

Current methods for detecting CNS tissues in meat and meat products are mainly based on ELISA and PCR techniques. The major drawback of the ELISA^{10,11} or real-time PCR^{16,17} methods are their high costs and the need for varying degrees of access to laboratory environments and equipment, making them unsuitable for on-site monitoring during the slaughter process. On the other hand, light-based spectroscopic techniques are rapid and noninvasive, requiring no sample preparation. For example, we have previously developed a method and apparatus for the real-time detection of fecal contamination on bovine carcasses using fluorescence-based detection of bovine feces containing undesirable bacteria, which has been proven to be a reliable technique^{23,24}; it is now being adopted in packing plants in the US and France. Using the same principles, we propose to use fluorescent lipofuscin as a marker of CNS tissue.³⁶

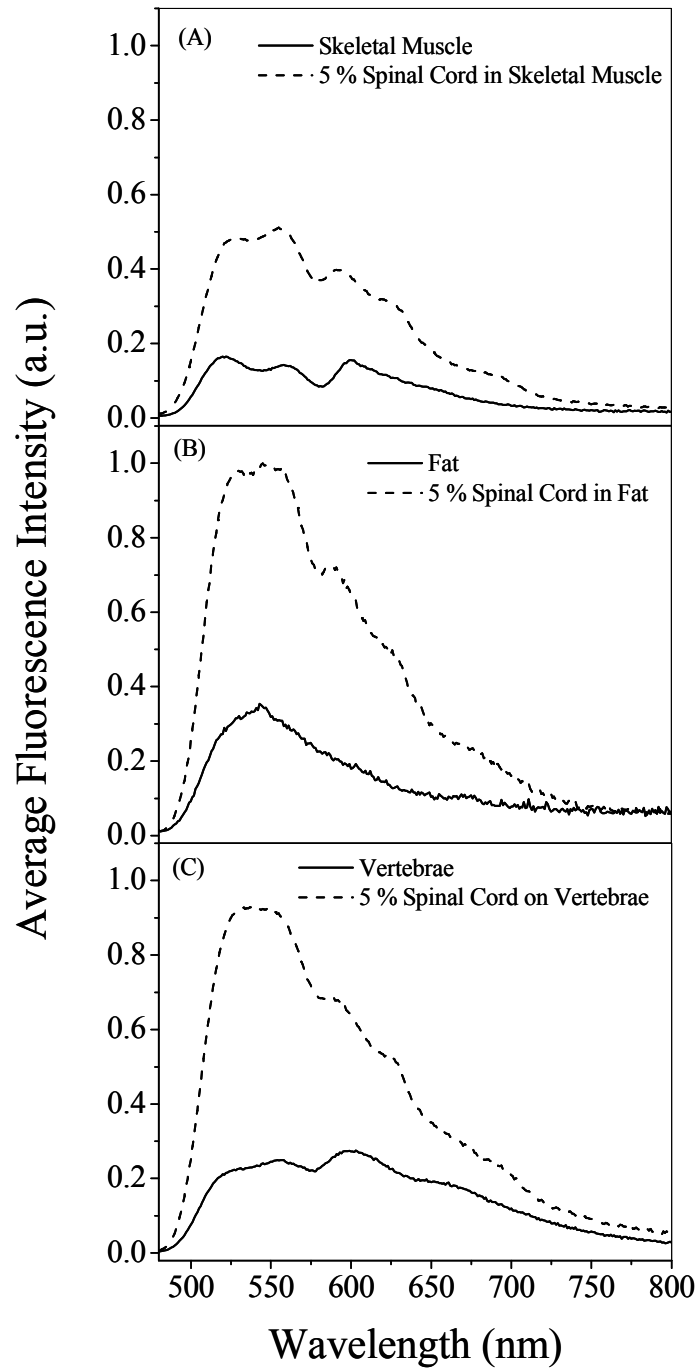


Figure 7.4. Assessment of the detection sensitivity of 5% surface area of bovine spinal cord in the presence of (A) skeletal muscle, (B) fat and (C) vertebrae. Excitation and emission conditions are as above. A surface area of 5 % spinal cord can be detected in presence of skeletal muscle, fat and vertebrae based upon fluorescence spectral shape and intensity. Detection sensitivity is given in table 7.1.

Lipofuscin is a high molecular weight granular yellow-brown substance which is believed to result from “oxidative stress” of many biomolecules particularly polyunsaturated fatty acids. It is heterogeneous, highly fluorescent and undergoes age-related progressive accumulation in animal cells, mainly in postmitotic cells, such as neurons, cardiac muscles and retinal epithelium. Lipofuscin is implicated in many aspects of normal health, including aging, oxidative stress, macular degeneration, lipid peroxidation, as well as some disease processes including atherosclerosis, dementia (Alzheimer’s Disease) and prion diseases.^{25-30,37-40}

We observed in this study, that spectra obtained from all solid bovine CNS and non-CNS tissue samples were not contaminated by the artifacts of scattered light. This was consistent with previous findings showing the occurrence of lipofuscin in high concentrations in brain and spinal cord.³¹ Our investigation included male and female cattle at the age of 2 to 72 months. Since 24-month-old bovines represent the largest contingent of slaughtered beef cattle in the U.S.⁴¹, special care was taken to include samples of animals of this age in every part of the validation studies. We conclude that the detectability of the fluorescence signal is not affected by nonhomogeneous distribution of lipofuscin that might be age or sex dependent or be observed in different anatomical regions. This is consistent with the chemical stability of lipofuscin.²⁵ To give a more detailed analysis of possible age related variations in signal intensity, experiments are underway investigating a large number of age, sex and breed matched samples. We also found that characteristic CNS tissue fluorescence spectra and intensities could be reliably detected after storage at -20°C for at least 8 weeks (data not shown) indicating that there is no significant alteration with regard to storage time. This observation is of special importance for the analysis of possible CNS contamination on

meat cuts processed from frozen beef.

The shape of the spectra collected from spinal cord and brain were not tissue specific, but could also be found in PNS tissues, liver, kidney, heart and lymph node. In contrast, lung, adrenal gland, skeletal muscle, bone marrow, spleen and vertebrae could be clearly distinguished with respect to relative peak intensity and in some cases also peak positions. However, the average fluorescence signal intensity of PNS and non-CNS tissues (except kidney and liver) is at least 4-5 times less than that in CNS tissues, offering the potential for the detection of low amounts of spinal cord and brain tissues on bovine carcasses based on different intensities. The presence of spinal cord on skeletal muscle, fat and vertebrae can also be determined by the different spectral features.

We focused on the detection sensitivity of spinal cord and the possible influence of different background tissues. Characteristic spectra of spinal cord were reliably detected down to a sample size of ~ 0.1 cm x 0.1 cm. It is noteworthy that this low detection sensitivity would also enable the detection of the small dorsal root ganglia and peripheral nerve cords. Dorsal root ganglia have been classified as SRM and peripheral nerves have been shown to contain low amounts of PrP^{BSE} in BSE affected cattle.^{42,43} During slaughter, spinal cord fragments are easily spread over skeletal muscle, fat and vertebrae, making those tissues the most important non-CNS tissues that had to be included in the present study. It should be noted that the fluorescent signal collected from 5% surface area of spinal cord and detected in 70% (skeletal muscle, fat) or 80% (vertebrae) of the samples, respectively, was not caused by the entire amount of fluorescent substances present in the sample, but only the amount in the two-dimensional (2D) area exposed to the excitation light. This method does not allow the comparison with CNS percentage values, which are usually used for semi-

quantitative measurements by ELISA or real time-PCR methods. The latter test systems refer to the amount of target material contained in the total initial weight and use the three-dimensional (3D) analysis of the entire sample. Therefore, the real time-PCR based detection of GFAP mRNA^{16,17} was selected to investigate the quality of the artificially contaminated samples. This method had previously shown its accuracy and robustness in a multi-center trial.⁴⁴ Its high tissue specificity and the potential for accurate quantification of CNS tissues were proven recently in direct comparison with two commercially available ELISAs.⁴⁵ Since all skeletal muscle and fat tissues were free of CNS tissues as confirmed by PCR analysis, it was proven that the spectra obtained from these tissues were not due to CNS contamination. As indicated by the C_T values all artificially spiked samples were homogenous preparations containing an entire amount of spinal cord ranging from 5% in muscle to 7% in fat. In comparison, semi-quantitative measurements of spinal cord contamination on bovine carcasses varied from 0.5%⁴⁶ to more than 1% (data not shown). Since the front-faced experiment collects the fluorescence of the CNS tissue located only on a sample surface, the detection sensitivity obtained by fluorescence spectroscopy is actually lower than the detection sensitivity reported by real time PCR analysis.

The fluorescence spectra of fat and vertebrae not only differed in signal intensity, but also in shape. As a consequence, the potential to lower the detection sensitivity can be easily achieved. Similarly, the sensitivity for detection of spinal cord in the presence of skeletal muscle can possibly be increased by comparing the fluorescence signal intensity ratio between the second and the third peak. The third peak always gave lower signal intensity in spinal cord, but a higher intensity in skeletal muscle.

The present study revealed the potential of fluorescent marker substances, such as

lipofuscin, for the real-time detection of spinal cord on bovine carcasses and processed meat cuts including bone-in or boneless products. The front-faced experiments were conducted with a well standardized, but technologically simple setup that allowed the detection of small amounts of bovine spinal cord in the presence of fat, skeletal muscle and vertebrae. Our future work will focus on the development of industrial prototypes such as a hand-held device or entire carcass imaging. Future focus will be on complex mixtures of CNS tissues with background tissues obtained from skeletal muscle, fat and sawdust of vertebrae and other bones. Real-time monitoring for possible CNS contamination during slaughter would provide an additional, science-based tool for sanitation procedures for the removal of SRM at the abattoir. A benefit to the beef producing industry would be improved product quality assurance and would result in increased consumer protection.

Acknowledgment

Disclaimer: Mention of trade names or commercial products in this article is solely for the purpose of providing specific information and does not imply recommendation or endorsement by the U.S. Department of Agriculture. The support of local slaughterhouses and the Iowa State University Meat Laboratory in sample collection is gratefully acknowledged. We thank Hannah Polashek for technical assistance with the real time-PCR analysis.

References

- (1) Ironside, J. W. *Brain Pathol.* **1996**, *6*, 379.
- (2) Cousens, S.; Smith, P. G.; Ward, H.; Everington, D.; Knight, R. S.; Zeidler, M.; Stewart, G.; Smith-Bathgate, E. A.; Macleod, M. A.; Mackenzie, J.; Will, R. G. *Lancet* **2001**, *357*, 1002.

- (3) Comer, P. J.; Huntly, P. J. *Stat. Methods Med. Res.* **2003**, *12*, 279.
- (4) Richt, J. A.; Kunkle, R. A.; Alt, D.; Nicholson, E. M.; Hamir, A. N.; Czub, S.; Kluge, J.; Davis, A. J.; Hall, S. M. *J. Vet. Diagn. Invest.* **2007**, *19*, 142.
- (5) Erratum. *J. Vet. Diagn. Invest.* **2007**, *19*, 454.
- (6) Stack, M. J.; Balachandran, A.; Chaplin, M.; Davis, L.; Czub, S.; Miller, B. *Can. Vet. J.* **2004**, *45*, 825.
- (7) Giles, J. *Nature* **2001**, *413*, 240.
- (8) (EFSA), E. F. S. A. "Quantitative Assessment of the Residual BSE Risk in Bovine-Derived Products, EFSA QRA Report 2004 - working document," 2005.
- (9) Cohen, J. T.; Gray, G. M.; Harvard center of Risk Analysis, Harvard School of Public Health, 2005, access at http://www.fsis.usda.gov/Science/Risk_Assessments/, 2005.
- (10) Schmidt, G. R.; Hossner, K. L.; Yemm, R. S.; Gould, D. H.; O'Callaghan, J. P. *J. Food Prot.* **1999**, *62*, 394.
- (11) Schmidt, G. R.; Yemm, R. S.; Childs, K. D.; O'Callaghan, J. P.; Hossner, K. *L. J. Food. Prot.* **2001**, *64*, 2047.
- (12) Biedermann, W.; Lücker, E.; Porschmann, J.; Lachhab, S.; Truyen, U.; Hensel, A. *Anal. Bioanal. Chem.* **2004**, *379*, 1031.
- (13) Villmann, C.; Sandmeier, B.; Seeber, S.; Hannappel, E.; Pischetsrieder, M.; Becker, C. M. *J. Agric. Food Chem.* **2007**, *55*, 7114.
- (14) Lücker, E. H.; Eigenbrodt, E.; Wenisch, S.; Failing, K.; Leiser, R.; Bülte, M. *J. Food Prot.* **1999**, *62*, 268.
- (15) Wenisch, S.; Lücker, E.; Eigenbrodt, E.; Leiser, R.; Bülte, M. *Nutr. Res. (N.Y.)* **1999**, *19*, 1165.

- (16) Schöenbrücher, H.; Abdulmawjood, A.; Bülte, M. *Fleischwirtschaft* **2004**, 84, 114.
- (17) Abdulmawjood, A.; Schöenbrücher, H.; Bülte, M. *J. Mol. Diagn.* **2005**, 7, 368.
- (18) Christensen, J.; Nørgaard, L.; Bro, R.; Engelsen, S. B. *Chem. Rev.* **2006**, 106, 1979
- (19) Wold, J. P.; Mielnik, M. *J. Food Sci.* **2000**, 65, 87.
- (20) Olsen, E.; Vogt, G.; Ekeberg, D.; Sandbakk, M.; Petterson, J.; Nilsson, A. *J. Agric. Food Chem.* **2005**, 53, 338.
- (21) Olsen, E.; Vogt, G.; Veberg, A.; Ekeberg, D.; Nilsson, A. *J. Agric. Food Chem.* **2005**, 53, 7448.
- (22) Wold, J. P.; Mielnik, M.; Pettersen, M. K.; Aaby, K.; Baardseth, P. *J. Food Sci.* **2002**, 67, 2397.
- (23) Ashby, K. D.; Casey, T. A.; Rasmussen, M. A.; Petrich, J. W. *J. Agric. Food Chem.* **2001**, 49, 1123.
- (24) Ashby, K. D.; Wen, J.; Chowdhury, P.; Casey, T. A.; Rasmussen, M. A.; Petrich, J. W. *J. Agric. Food Chem.* **2003**, 51, 3502.
- (25) Yin, D. *Free Radical Biol. Med.* **1996**, 21, 871.
- (26) Boellaard, J. W.; Schlote, W.; Tateishi, J. *Acta Neuropathol.* **1989**, 78, 410.
- (27) Terman, A.; Brunk, U. T. *Acta Pathol., Microbiol., Immunol.* **1998**, 106, 265.
- (28) Tsuchida, M.; Miura, T.; Aibara, K. *Chem. Phys. Lipids* **1987**, 44, 297.
- (29) Curtis, H. J. *Biological Mechanisms of Aging*; Charles C. Thomas: Springfield, IL, 1966.

- (30) Strehler, B. L. *Time, Cells, and Aging*; Academic Press: San Diego, 1977.
- (31) Chowdhury, P. K.; Halder, M.; Choudhury, P. K.; Kraus, G. A.; Desai, M. J.; Armstrong, D. W.; Casey, T. A.; Rasmussen, M. A.; Petrich, J. W. *Photochem. Photobiol.* **2004**, *79*, 21.
- (32) BSE General Question and Answer; Department for Environment, Food, and Rural Affairs. Animal Health and Welfare, 2007; pp <http://www.defra.gov.uk/animalh/bse/index.html>.
- (33) Vandever, M. *Amber Waves* **2007**, *5*, 28.
- (34) Coffey, B.; Mintert, J.; Fox, J. A.; Schroeder, T.; Valentin, L. In *The Economic Impact of BSE on the U.S. Beef Industry: Product Value Losses, Regulatory Costs, and Consumer Reactions*; Kansas State University Agricultural Experiment Station and Cooperative Extension Service. MF-2678, 2005; pp available at <http://fss.k>.
- (35) Prohibition of the use of specified risk materials for human food and requirements for the disposition of non-ambulatory disabled cattle; Prohibition of the use of certain stunning devices used to immobilize cattle during slaughter (9 CFR Parts 309, 310, and 318 [Docket No. 03-025F]). In *Fed. Regist.*; Food Safety and Inspection Service, 2007; pp 38700.
- (36) Casey, T. A.; Rasmussen, M. A.; Gapsch, A. H.; Flick, R. L.; Petrich, J. W. Real-time monitoring of age pigments and factors relating to transmissible spongiform encephalopathies and apparatus. USA, 2004.
- (37) Sohal, R. S. *Age Pigments*; Elsevier: Amsterdam, 1981.
- (38) Terman, A. *Redox Rep.* **2001**, *6*, 15.
- (39) Mata, N. L.; Weng, J.; Travis, G. H. *Proc. Natl. Acad. Sci. USA* **2000**, *97*,

7154.

(40) Boulton, M.; Docchio, F.; Dayhaw-Barker, P.; Ramponi, R.; Cubeddu, R. *Vision Res.* **1990**, *30*, 1291.

(41) Lawrence, T. E.; Whatley, J. D.; Montgomery, T. H.; Perino, L. J. *J. Anim. Sci.* **2001**, *79*, 1683.

(42) Iwata, N.; Sato, Y.; Higuchi, Y.; Nohtomi, K.; Nagata, N.; Hasegawa, H.; Tobiume, M.; Nakamura, Y.; Hagiwara, K.; Furuoka, H.; Horiuchi, M.; Yamakawa, Y.; Sata, T. *Jpn. J. Infect Dis.* **2006**, *59*, 100.

(43) Masujin, K.; Matthews, D.; Wells, G. A.; Mohri, S.; Yokoyama, T. *J. Gen. Virol.* **2007**, *88*, 1850.

(44) Abdulmawjood, A.; Schönenbrücher, H.; Bülte, M. *J. AOAC Int.* **2006**, *89*, 1335.

(45) Schonenbrücher, H.; Abdulmawjood, A.; Göbel, K. A.; Bülte, M. *Vet. Microbiol.* **2007**, *123*, 336.

(46) Lücker, E.; Schlottermüller, B.; Martin, A. *Berl. Munch. Tierarztl. Wochenschr.* **2002**, *115*, 118.

CHAPTER 8. FLUORESCENCE SPECTROSCOPY OF THE RETINA FOR DIAGNOSIS OF TRANSMISSIBLE SPONGIFORM ENCEPHALOPATHIES

A paper published in *Analytical Chemistry*

Ramkrishna Adhikary[†], Prasun Mukherjee^{†,‡}, Govindarajan Krishnamoorthy^{†,§}, Robert A. Kunkle^{||}, Thomas A. Casey^{||}, Mark A. Rasmussen^{||,⊥}, Jacob W. Petrich^{+*}

Abstract

The feasibility of exploiting fluorescence spectra of the eye for diagnosis of transmissible spongiform encephalopathies (TSEs) was examined. Retinas from scrapie-positive sheep were compared with scrapie-negative sheep using fluorescence spectroscopy and distinct differences in the fluorescence intensity and spectroscopic signatures were observed. The characteristic fluorescent signatures are thought to be the result of an accumulation of lipofuscin in the retina. It appears that the eye, in particular the retina, is a useful tissue for noninvasive examination of some neurological pathologies such as scrapie.

Reprinted with permission from *Analytical Chemistry*, 2010, 82(10), 4097-4101. Copyright (2010) American Chemical Society.

[†] Department of Chemistry, Iowa State University, Ames, Iowa, 50011, USA.

[‡] Current Address: Department of Chemistry, University of Pittsburgh, PA 15260, USA.

[§] Current Address: Department of Chemistry, Indian Institute of Technology, Guwahati, 781039, India.

^{||} National Animal Disease Center, ARS-USDA, 1920 Dayton Avenue, Ames, Iowa 50010, USA.

[⊥] Current Address: Center for Veterinary Medicine, U.S. FDA, 8401 Muirkirk Rd, Laurel, MD 20708, USA.

*To whom correspondence should be addressed.

The development of procedures based on examinations of the eye that permit the detection of neurological disorders in animals holds great promise.

Introduction

Neurological disorders of the central and peripheral nervous system are caused by a disease, trauma, or injury to the nervous system. They can be difficult to treat and often are debilitating. Transmissible spongiform encephalopathies (TSEs) are one of many other well known neurological disorders such as Parkinson's disease, Alzheimer's disease, Huntington's disease, systematic amyloidosis and maturity-onset diabetes that involve accumulation of extracellular aggregates leading to tissue damage and disease.¹⁻⁴ TSEs are slowly progressive, insidiously degenerative diseases that affect the central nervous system (CNS) of both humans and animals and are usually accompanied by the production of "spongiform" changes in the brain. TSEs are believed to be transmitted by abnormal proteins, which are resistant to enzymatic degradation, called prions and in the case of scrapie, designated as PrP^{sc}.⁵

The TSE of most concern for the food supply is bovine spongiform encephalopathy (BSE), a fatal neurodegenerative transmissible disease in cattle. It is thought to be associated with variant Creutzfeldt-Jakob disease (vCJD) in humans.⁶ The oral route of infection is considered to be the most probable path for transmission of BSE to humans.^{7,8} In order to reduce the risk of human exposure, specified risk material (SRM, e.g. brain and spinal cord) from cattle is removed during slaughter and processing. Prohibition of SRM in the human food chain is considered of critical importance for protection of consumers from BSE.^{9,10} Regulations regarding SRM have been promulgated by the European Commission (Annex V Commission Regulation (EC) No. 999/2001) and for the United States by the Food Safety

and Inspection Service (99 CFR 310.22). Many other countries have also banned bovine CNS tissues from meat products and its presence is cause for import rejection and international trade disputes. Developing technology for monitoring CNS tissue in meat and other food products as well as for diagnosing animals for TSEs will be increasingly important in securing the safety of the world's food supply.

Fluorescence spectroscopy has been commonly used in a variety of biological applications, and its feasibility for the detection of fecal contamination by exploiting fluorescent chlorophyll metabolites on meat during slaughter has been previously reported.¹¹ Instruments developed for this application are currently being used to screen carcasses in real time at beef processing plants in the United States and France. A similar approach can be applied to CNS detection by exploiting lipofuscin, a highly fluorescent, heterogeneous, high-molecular weight material that has been shown to accumulate in high concentrations in neural tissues.¹²⁻¹⁷ Our previous work has shown that brain and spinal cord samples display highly conserved spectral characteristics and these characteristics have potential for use in meat processing applications.¹⁸⁻²⁰ We have investigated the spectra and spectral intensities of the two most important SRM tissues (brain and spinal cord) and compared the data to non-CNS tissues. Based upon a study of the spectral signatures of CNS tissue, we have previously suggested the development of devices for detecting CNS tissue in meat products by the rapid monitoring of fluorescence spectra.¹⁹ It is known that the amount of fluorescent lipofuscin in CNS tissue increases as a result of spontaneous and experimentally induced Creutzfeldt-Jakob's disease (CJD). Boellaard et al. have demonstrated a relationship between lipofuscin production, a decline in autophagocytosis activity, and the experimental induction of CJD in mice.¹³ Furthermore, there is substantial documentation linking

neurological disease produced by TSEs to eye damage and the accumulation of lipofuscin.^{13,21-28}

In this work, we investigate the use of fluorescence spectroscopy of the retina to identify scrapie, which we use as a model for TSEs. Scrapie is the most widespread TSE affecting sheep and goats worldwide. It is characterized by a gradual onset; and advanced cases show typical disease characteristics including unthriftiness, compulsive itching, balance and ambulatory abnormalities, convulsions, and eventual death. The disease has been observed for centuries. At present, it is incurable and the most common form of control is quarantine, euthanasia, and proper disposal of the carcass. Scrapie is not considered to be infectious to humans.

While several research groups are actively involved in developing spectral examinations of the eye to assess the extent of macular degeneration and other abnormalities²⁷⁻³⁵, to our knowledge, few have reported on the use of the retinal scans for this particular pathological application.^{25,26,36,37} The objective of this work is to find spectral signatures of intrinsic fluorescent markers of eye that can provide a nonlethal and noninvasive means of determining if a living animal is infected with a TSE. Our experiments were designed to address the following questions: 1. Can spectra obtained from the eye be used for identification of neurological disease? 2. Can the effects of neurological disease observed in the eye be distinguished from those associated with normal aging? 3. Can images of the eye be obtained that report on neurological disease? With these questions in mind we have now extended previous work and investigated fluorescence spectroscopy of the retina for potential diagnosis of neurological disease. Our investigations, which have focused on scrapie-positive and scrapie-negative sheep, suggest that the retina is a most promising part of the

eye for revealing spectroscopic signatures indicative of neurological disease.

Materials and Methods

Materials. DAKO™ Target Retrieval Solution and biotinylated anti-mouse IgG (made in horse) were obtained from DAKO Corp., Carpinteria, CA and Vector Laboratories, Burlingame, CA respectively. Basic Alkaline Phosphatase Red Detection Kit and NexES IHC modules were acquired from Ventana Medical Systems, Inc., Tucson, AZ. All other chemicals used for pathological procedures were obtained from Sigma Aldrich.

Animal tissue samples. Tissue samples from both scrapie-positive and scrapie-negative sheep were obtained from several sources. Samples from 73 sheep were collected for the study for a total of 140 eyeballs. In some cases only one eye was collected from the animals sampled. Both positive and negative tissue samples were harvested according to a standardized necropsy procedures from sheep identified through the National Scrapie Surveillance Plan administered by the Animal and Plant Health Inspection Service (APHIS), United States Department of Agriculture (USDA).³⁸ Samples were also obtained from the Caine Veterinary Teaching Center, University of Idaho, Caldwell, ID. The identity of individual producers if known has been withheld. Scrapie-negative tissue samples were also obtained locally from sheep at the National Animal Disease Center (NADC), Ames, IA. All procedures relating to the care and experimental use of live sheep used on site at NADC were approved by the NADC Institutional Animal Care and Use Committee. Information regarding breed, age, and sex was also obtained for each tissue sample used in this study (see Table S-1 in the supporting information).

Disease diagnosis. All animals were diagnosed for scrapie infection status using conventional pathological methods. To obtain brain tissue, the disarticulated heads of sheep

were split near sagittal midline with a bandsaw. Each half of the brain was carefully removed from the calvarium and one of the halves was immersion fixed in 10% neutral buffered formalin for 2-3 weeks. The formalin-fixed brain was cut into 2-4 mm wide coronal sections at four levels: 1) brainstem at the obex, 2) cerebellum at mid-level lateral lobe, 3) midbrain at the rostral colliculus, and 4) hippocampus and adjacent cerebral cortex. The tissue blocks were placed in histopathology cassettes, dehydrated, and embedded in paraffin wax. Paraffin-embedded tissues were sectioned to 5 µm thickness, affixed to charged glass slides, and stained with hematoxylin and eosin (HE) for examination by light microscopy or left unstained for immunohistochemistry (IHC) processing.

An automated IHC method for detection of infectious prion protein (PrP^{Sc}) was used as described previously.³⁹ In brief detail, following deparaffinization in xylene and rehydration through gradations of alcohol to water, tissue sections were autoclaved (121°C, 1.38 x 10⁵ Pa) for 30 minutes in an antigen retrieval solution and labeled with an indirect avidin biotin system designed for an automated immunostainer. The primary antibody was a cocktail of 2 monoclonal antibodies, F89/160.1.5⁴⁰ and F99/97.6.1⁴¹, each used at a concentration of 5 µg/ml, and incubation was carried out at 37°C for 32 min. The secondary antibody was biotinylated anti-mouse, diluted 1:200. The preparation was incubated for 8 min at 37°C.

Sample preparation. The eyeballs collected were stored frozen until use. After thawing, the eyeballs were dissected; and the retina or other eye tissue was removed and placed on a plain glass microscope slide (25 x 75 x 1 mm). The retina, in particular was oriented as a thin layer on the microscope slide enabling the entire area of the sample to be exposed to the excitation light.

Steady-State measurements. Steady-state fluorescence spectra were obtained on a SPEX Fluoromax-2 (ISA Jobin-Yvon/SPEX, Edison, NJ) with a 5-nm band-pass unless otherwise specified and corrected for lamp spectral intensity and detector response. Fluorescence spectra were collected in the front-faced orientation. For the experiments reported in this study, the samples were excited at $\lambda_{\text{ex}} = 470$ nm with an interference filter on the excitation side, and emission was collected at $\lambda_{\text{em}} \geq 505$ nm using a cutoff filter before the detector to eliminate scattered light. Polarized fluorescence spectra were obtained using two polarizers, with one on the excitation side and another on the emission side with the appropriate excitation interference and cut-off emission filters. Fluorescence spectra were obtained using horizontal-horizontal (HH) and horizontal-vertical (HV) orientations of the polarizers.

Hyperspectral fluorescence imaging microscopy. The hyperspectral images were captured on a system located in the Roy J. Carver Laboratory for Ultrahigh Resolution Biological Microscopy, Iowa State University. This system was based on a NIKON ECLIPSE TE 2000-E microscope. The illumination source was an X-Cite 120 PC from EXFO. Samples were excited at 470 nm using an interference filter, and fluorescence was collected at ≥ 500 nm with a longpass filter and a Nikon Plan Fluor 10X/0.30 PH1-DL objective. The collected fluorescence was dispersed using a Spectral-DV spectrometer from Optical Insights and captured by a Photometrics Cascade 512 B CCD camera (Roper Scientific). Software used for image capture was Mélange V3.7.

Results and Discussion

We studied a total of 140 sheep eyeballs from 73 animals obtained from several sources. Thirty five of the animals were scrapie-positive and 38 of the animals were scrapie-

negative. In the sheep identified as scrapie-negative, there was no evidence of spongiform change or other significant lesions, as assessed by microscopic examination of hemotoxylin and eosin stained brain sections. Likewise, there was no labeling indicative of PrP^{sc} seen in brain tissue sections examined following IHC (immunohistochemical) processing. Conversely, in sheep diagnosed as scrapie-positive, the observation of both lesions and IHC labeling confirmed a positive diagnosis for scrapie.

Fluorescence spectra from various parts of the sheep eye (cornea, iris, lens layer, lens gel, lens, vitreous humor, retina, tapetum, optic nerve, and sclera) were obtained at different excitation wavelengths using a fluorometer in a front-faced geometry. The retina (and the sclera) show large differences in spectral features when comparisons are made between scrapie-negative and scrapie-positive samples. The sclera is the protective tissue that covers the entire eyeball except the cornea. The retina is the preferred part of eye for noninvasive diagnosis of TSE affected animal because it can be directly accessed by light to excite the pigments, in contrast with the sclera. Front-faced fluorescence spectra of solid retina samples from scrapie-negative and scrapie-positive sheep excited at 470 nm are presented in Figure 8.1. The data indicate that fluorescence spectra from eyes (especially the retina) are very rich and vary considerably with excitation wavelength (λ_{ex}). When $\lambda_{ex} = 470$ nm, the fluorescence intensity of the scrapie-positive retinas is significantly greater than that of scrapie-negative sheep. The spectra from scrapie-positive samples were also more structured and displayed two intense peaks at ~560 and ~600 nm with a shoulder at ~525 nm. The scrapie-positive samples also displayed a minimum at ~575 nm. The literature indicates that TSE is caused by an accumulation of protease-resistant prions in central nervous system tissues such as brain, spinal cord, and eye.⁵ It is also known that lipofuscin accumulation

occurs in diseased eye (e.g., in retinal pigment epithelium).⁴²⁻⁴⁸ The spectral differences in scrapie-positive retinas compared to scrapie-negative retinas can be attributed to the result of altered or increased lipofuscin owing to prion infection.

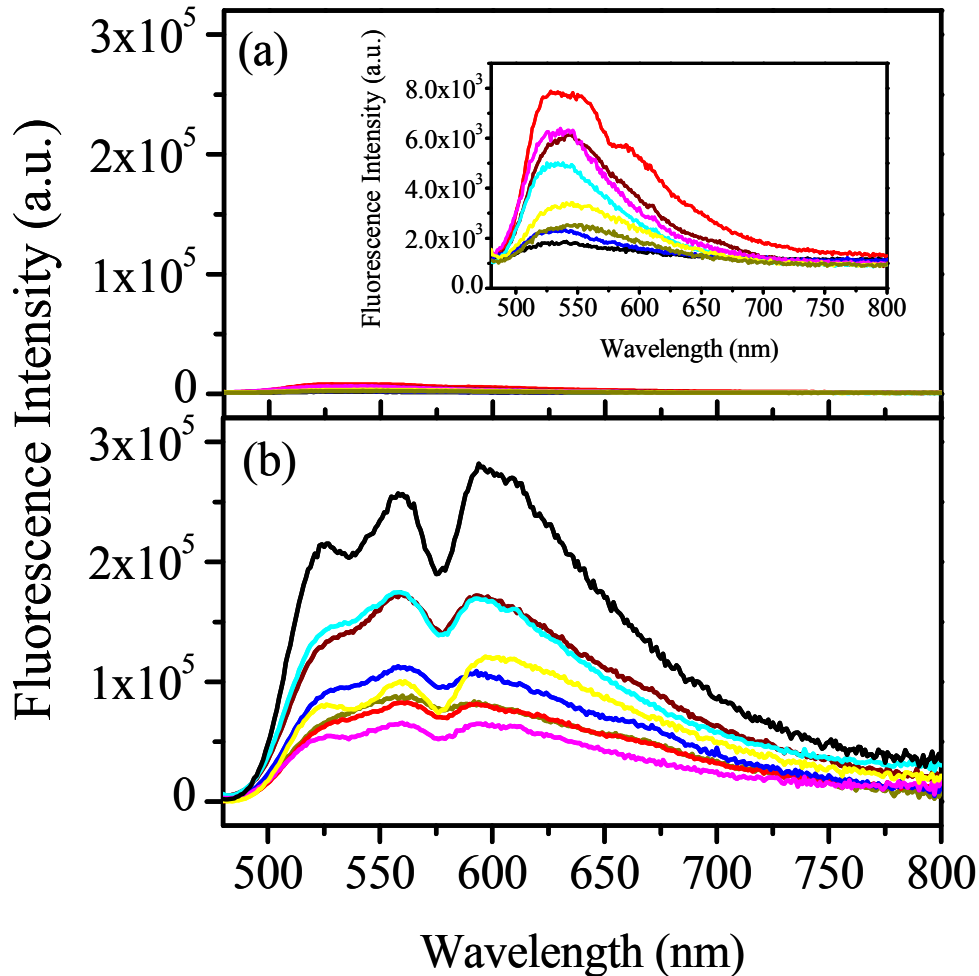


Figure 8.1. Fluorescence spectra of the retina from scrapie-negative and scrapie-positive sheep. Comparison of (a) scrapie-negative and (b) scrapie-positive sheep retinas at $\lambda_{\text{ex}} = 470$ nm. Representative, different, front-faced fluorescence spectra from eight individual retinas are shown for each scrapie-negative and scrapie-positive animal. Note that the intensity values are in the same range for both data sets on the primary graphs. The inset graph for the scrapie-negative data uses an expanded ordinate. Significant differences of fluorescent intensity exist between the two data sets.

Given the pronounced structural differences observed in the spectra of the scrapie-positive tissue, additional control experiments were undertaken to ensure that these data were not an experimental artifact, since spectra were collected from solid samples, which may have contributed to excessive light scattering. Although spectral structure was not pronounced in the scrapie-negative samples, it was necessary to determine that the results were independent of the polarization of the excitation radiation. The data in Figure 8.2 demonstrate that the spectra observed were, indeed, independent of polarization. We suggest that these spectral differences are the result of neurological disease or in this case, scrapie.

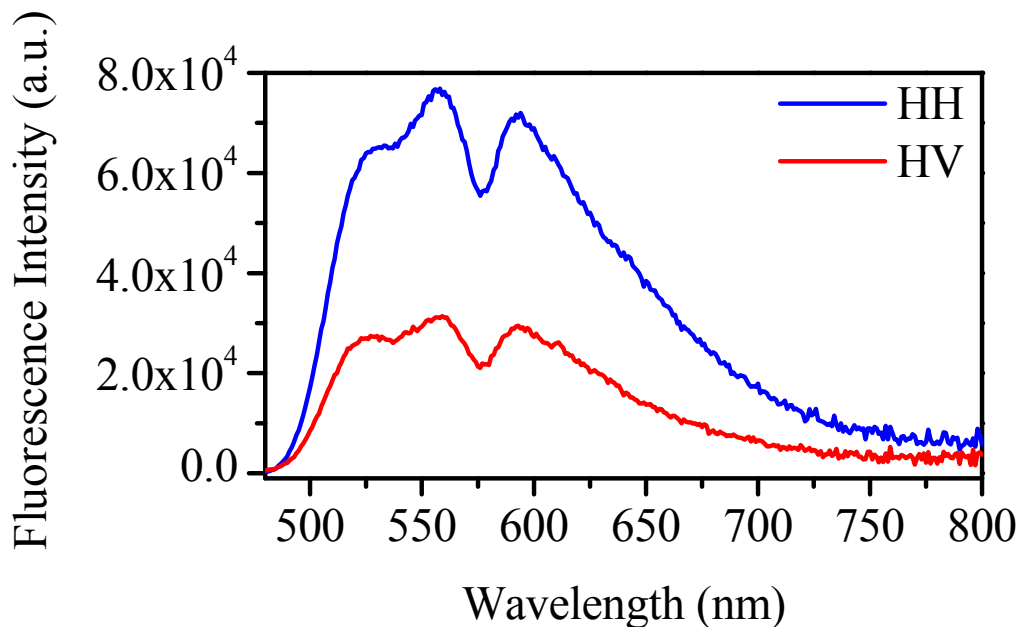


Figure 8.2. Polarized fluorescence spectra from a scrapie-positive sheep. Spectra were collected in a front-faced orientation. Samples were excited at 470 nm with an interference filter in the excitation light path, and fluorescence was collected after 505 nm with a long pass filter. In order to determine whether the observed structure is due to scattered light, the experiments were conducted with two polarizers in either of two positions: HH (horizontal excitation/horizontal emission) or HV (horizontal excitation/vertical emission). The data indicate that the spectral structure observed is authentic and not an artifact.

It has been reported that the intracellular fluorescent pigment lipofuscin accumulates in the retina with increasing age.⁴⁹⁻⁵¹ It is important to distinguish the spectral differences arising from scrapie with respect to those arising from normal aging. A plot of integrated fluorescence intensity obtained from both scrapie-positive and scrapie-negative sheep retinas as a function of age is shown in Figure 8.3. Samples were obtained from sheep up to 9 years of age. The data indicate clear differences, with the scrapie-positive retinas being more fluorescent than those from the scrapie-negative retinas. The differences in total fluorescence due to disease status greatly exceed any differences that result from other factors, such as age.

In addition, hyperspectral fluorescence microscopy was used to compare images of retinas with respect to disease status. Representative images from different regions of sex- and age-matched retinas for scrapie-negative and scrapie-positive sheep are displayed in Figure 8.4. The scrapie-positive retina shows significantly higher fluorescence intensity as opposed to the scrapie-negative retina, as indicated by the grayscale intensity gradient of the images. This result is also consistent with the data presented in Figures 8.1 and 8.3 indicating that the scrapie-positive retinas are more fluorescent than those of scrapie-negative retinas. The scrapie-positive images also contain aggregates of fluorescent material, as indicated by the arrows in Figure 8.4 and are more heterogeneously fluorescent. In contrast the scrapie-negative tissue is more homogeneous and is weakly fluorescent. This further supports our observations from front-faced fluorescence spectra that scrapie-positive retinas show higher fluorescence with prominent structure. From this comparison of age-matched retinas, we conclude that the scrapie-positive retinas contain very bright regions of highly fluorescent material, which is suggestive of neurological damage as a result of disease.

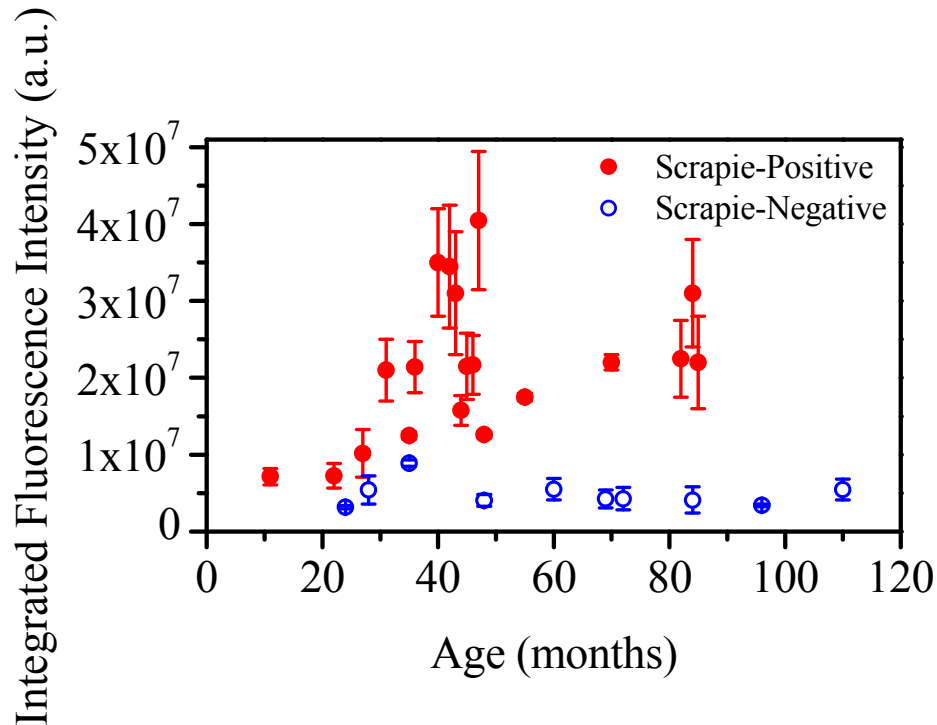


Figure 8.3. Plot of the integrated fluorescence intensity from scrapie-positive and scrapie-negative sheep retinas as a function of age. All points represent multiple spectroscopic determinations with standard error bars. Those with visible error bars are an average of 4-12 experimental replications. The remaining data points with error bars smaller than the symbol are with $N = 2$. Fluorescence spectra were collected as described in a front-faced orientation. For all experiments, samples were excited at 470 nm with an interference filter in the excitation light path, and fluorescence was collected at wavelengths greater than 505 nm to eliminate scattering. Note that the differences in total fluorescence due to disease status greatly exceed any differences that result from age.

Others have reported observations that support this current research. Recently Smith et al. have shown that the function and morphology of retinas are altered in TSE-infected cattle and sheep infected with scrapie.^{25,26} Hortells et al. concluded that PrP^{sc} in the retina was highly correlated with the occurrence of scrapie²⁷ whereas Rubenstein et al. used ultraviolet fluorescent spectroscopy to detect different forms of PrP^{sc} in the eye.²⁸ Fundus autofluorescence has also been investigated for possible diagnostic use in a large number of

retinal diseases^{33,35} including the “conformational diseases” caused by accumulation of proteinaceous aggregates.³⁴ Autofluorescence has also been used to map lipofuscin distribution in the retina of humans.³³ In this study we have not determined the specific structures that are responsible for the fluorescence but others have suggested that lipofuscin and other macromolecular aggregates are responsible.^{27,34}

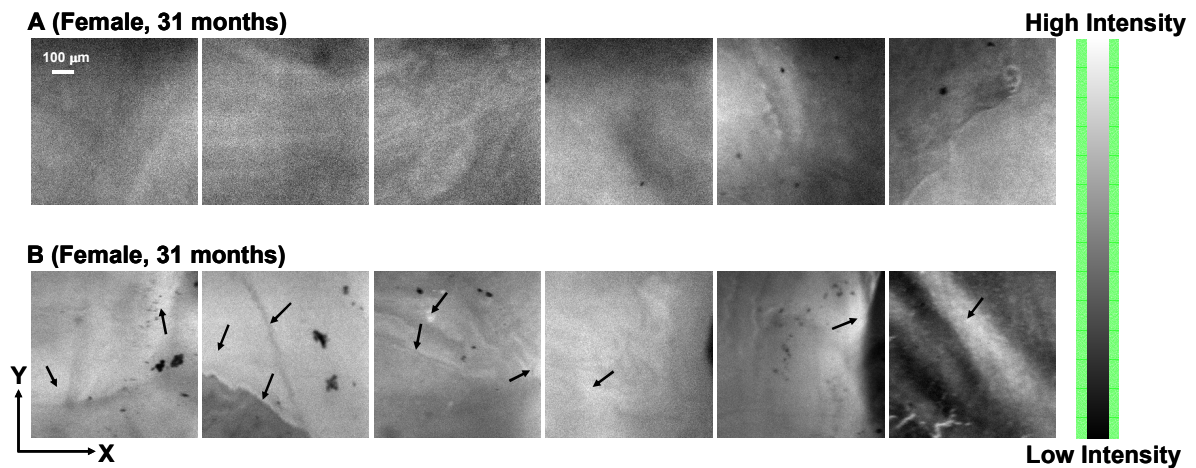


Figure 8.4. Hyperspectral fluorescence images of the retina of sheep. Representative images from different regions of sex- and age-matched (31 months) (A) scrapie-negative and (B) scrapie-positive sheep retinas. The samples were excited at 470 nm using an interference filter, and fluorescence was collected at wavelengths greater than 500 nm using a long-pass filter. The images shown are 800 microns by 800 microns. All images were captured under identical conditions. High intensity is represented by white; low intensity, by black on a grayscale gradient. Note the more intense fluorescence and aggregation of fluorescent material in the scrapie-positive images.

Conclusion

Given our results, we suggest that the distinct differences in the spectral signatures of the retina are diagnostic of animals naturally infected with scrapie. We further suggest that the eye, and in particular the retina, will be a useful tissue for noninvasive determination of neurological pathologies such as scrapie.

Acknowledgement

We thank Dr. Michelle Crocheck, Matt Inbody, Bob Morgan, Deb Lebo, Bob Doyle, Curtis Mosher and Dr. Eric Nicholson for their assistance in obtaining and analyzing the animal tissue samples. Part of this work was supported by DOD contract DAMD17-03-1-0460.

References

- (1) Kelly, J. W. *Structure* **1997**, 5, 595.
- (2) Tan, S. Y.; Pepys, M. B.; Hawkins, P. N. *Am. J. Kidney Dis.* **1995**, 26, 267.
- (3) Sunde, M.; Serpell, L. C.; Bartlam, M.; Fraser, P. E.; Pepys, M. B.; Blake, C. C. F. *J. Mol. Biol.* **1997**, 273, 729.
- (4) Conway, K. A.; Harper, J. D.; Lansbury, P. T. J. *Biochemistry* **2000**, 39, 2552.
- (5) Prusiner, S. B. *Proc. Natl. Acad. Sci. USA* **1998**, 95, 13363.
- (6) Ironside, J. W. *Brain Pathol.* **1996**, 6, 379.
- (7) Cousens, S.; Smith, P. G.; Ward, H.; Everington, D.; Knight, R. S.; Zeidler, M.; Stewart, G.; Smith-Bathgate, E. A.; Macleod, M. A.; Mackenzie, J.; Will, R. G. *Lancet* **2001**, 357, 1002.
- (8) Comer, P. J.; Huntly, P. J. *Stat. Methods Med. Res.* **2003**, 12, 279.
- (9) (EFSA), E. F. S. A. "Quantitative Assessment of the Residual BSE Risk in Bovine-Derived Products, EFSA QRA Report 2004 - working document," 2005.
- (10) Evaluation of the Potential for Bovine Spongiform Encephalopathy in the United States, 2001; Harvard Center of Risk Analysis, Harvard School of Public Health, and Center of Computational Epidemiology, College of Veterinary Medicine, Tuskegee University, 2001; Vol. 2001; available at

http://www.fsis.usda.gov/Science/Risk_Assessments/.

- (11) Ashby, K. D.; Wen, J.; Chowdhury, P.; Casey, T. A.; Rasmussen, M. A.; Petrich, J. W. *J. Agric. Food Chem.* **2003**, *51*, 3502.
- (12) Yin, D. *Free Radical Biol. Med.* **1996**, *21*, 871.
- (13) Boellaard, J. W.; Schlote, W.; Tateishi, J. *Acta Neuropathol.* **1989**, *78*, 410.
- (14) Terman, A.; Brunk, U. T. *Acta Pathol., Microbiol., Immunol.* **1998**, *106*, 265.
- (15) Tsuchida, M.; Miura, T.; Aibara, K. *Chem. Phys. Lipids* **1987**, *44*, 297.
- (16) Curtis, H. J. *Biological Mechanisms of Aging*; Charles C. Thomas: Springfield, IL, 1966.
- (17) Strehler, B. L. *Time, Cells, and Aging*; Academic Press: San Diego, 1977.
- (18) Chowdhury, P. K.; Halder, M.; Choudhury, P. K.; Kraus, G. A.; Desai, M. J.; Armstrong, D. W.; Casey, T. A.; Rasmussen, M. A.; Petrich, J. W. *Photochem. Photobiol.* **2004**, *79*, 21.
- (19) Schöenbrücher, H.; Adhikary, R.; Mukherjee, P.; Casey, T. A.; Rasmussen, M. A.; Maistrovich, F. D.; Hamir, A. N.; Kehrli, M. J.; Richt, J.; Petrich, J. W. *J. Agric. Food Chem.* **2008**, *56*, 6220.
- (20) Adhikary, R.; Schonenbrucher, H.; Rasmussen, M. A.; Casey, T. A.; Hamir, A. N.; Kehrli, M. E.; Richt, J. A.; Petrich, J. W. *Photochem. Photobiol.* **2009**, *85*, 1322.
- (21) Foncin, J. F.; Gaches, J.; Le Beau, J. *Rev. Neurol. (Paris)* **1964**, *111*, 507.
- (22) Jacobson, S.; Koenig, H.; Ross, E. *J. Neuropathol. Exp. Neurol.* **1967**, *22*, 152.
- (23) Kirschbaum, W. R. *Jakob-Creutzfeldt disease*; Elsevier: Amsterdam, New York, 1968.

- (24) Miyashita, M.; Stierstorfer, B.; Schmahl, W. *J. Vet. Med. B* **2004**, *51*, 209.
- (25) Smith, J. D.; Greenlee, J. J.; Hamir, A. N.; Richt, J. A.; Greenlee, M. H. W. *Vet. Pathol.* **2009**, *46*, 810.
- (26) Smith, J. D.; Greenlee, J. J.; Hamir, A. N.; Greenlee, M. H. W. *Vet. Rec.* **2009**, *165*, 179.
- (27) Hortells, P.; Monzon, M.; Monleon, E.; Acin, C.; Vargas, A.; Bolea, R.; Lujan, L.; Badiola, J. J. *Brain Res.* **2006**, *1108*, 188.
- (28) Rubenstein, R.; Gray, P. C.; Wehlburg, C. M.; Wagner, J. S.; Tisone, G. C. *Biochem. Biophys. Res. Commun.* **1998**, *246*, 100.
- (29) Holz, F. G.; Bellman, C.; Staudt, S.; Schutt, F.; Volcker, H. E. *Invest. Ophthalmol. Vis. Sci.* **2001**, *42*, 1051.
- (30) Smith, R. T.; Nagasaki, T.; Sparrow, J. R.; Barbazetto, I.; Koniarek, J. P.; Bickmann, L. J. *J. Biomed. Opt.* **2004**, *9*, 162.
- (31) Delori, F. C. *Arch. Biochem. Biophys.* **2004**, *430*, 156.
- (32) Schweitzer, D.; Hammer, M.; Schweitzer, F.; Anders, R.; Doebbecke, T.; Schenke, S.; Gaillard, E. R. *J. Biomed. Opt.* **2004**, *9*, 1214.
- (33) Schmitz-Valckenberg, S.; Holz, F. G.; Bird, A. C.; Spaide, R. F. *Retina J. Retinal Vitreous Dis.* **2008**, *28*, 385.
- (34) Surguchev, A.; Surguchov, A. *Brain Res. Bull.* **2010**, *81*, 12.
- (35) Smith, R. T.; Gomes Nuno, L.; Barile, G.; Busuioc, M.; Lee, N.; Laine, A. *Invest. Ophthalmol. Vis. Sci.* **2009**, *50*, 3907.
- (36) Smith, J. D.; Greenlee, J. J.; Hamir, A. N.; West Greenlee, M. H. *J. Comp. Pathol.* **2008**, *138*, 12.

- (37) Greenlee, J. J.; Hamir, A. N.; Greenlee, M. H. W. *Vet. Pathol.* **2006**, *43*, 733.
- (38) National Scrapie Surveillance Plan; APHIS, USDA, 2008; access at http://www.aphis.usda.gov/vs/nahss/sheep/national_scrapie_surveillance_plan_08192008.pdf.
- (39) Hamir, A. N.; Kunkle, R. A.; Richt, J. A.; Miller, J. M.; Cutlip, R. C.; Jenny, A. L. *J. Vet. Diagn. Invest.* **2005**, *17*, 3.
- (40) O'Rourke, K. I.; Baszler, T. V.; Miller, J. M.; Spraker, T. R.; Sadler-Riggelman, I.; Knowles, D. P. *J. Clin. Microbiol.* **1998**, *36*, 1750
- (41) O'Rourke, K. I.; Baszler, T. V.; Besser, T. E.; Miller, J. M.; Cutlip, R. C.; Wells, G. A. H.; Ryder, S. J.; Parish, S. M.; Hamir, A. N.; Cockett, N. E.; Jenny, A.; Knowles, D. P. *J. Clin. Microbiol.* **2000**, *38*, 3254.
- (42) Gaillard, E. R.; Atherton, S. J.; Eldred, G.; Dillon, J. *Photochem. Photobiol.* **1995**, *61*, 448.
- (43) Docchio, F.; Boulton, M.; Cubeddu, R.; Ramponi, R.; Barker, P. D. *Photochem. Photobiol.* **1991**, *54*, 247.
- (44) Dillon, J.; Zheng, L.; Merriam, J. C.; Gaillard, E. R. *Exp. Eye Res.* **2004**, *79*, 753.
- (45) Mata, N. L.; Weng, J.; Travis, G. H. *Proc. Natl. Acad. Sci. USA* **2000**, *97*, 7154.
- (46) Boulton, M.; Docchio, F.; Dayhaw-Barker, P.; Ramponi, R.; Cubeddu, R. *Vision Res.* **1990**, *30*, 1291.
- (47) Gaillard, E. R.; Zheng, L.; Merriam, J. C.; Dillon, J. *Invest. Ophthalmol. Vis. Sci.* **2000**, *41*, 1454.

- (48) Glickman, R. D. The Origin of Photo-Oxidative Stress in the Aging Eye. In *Progress in Brain Research*; Ripps, K. H. H., Wu, S., Eds., 2001; pp 699.
- (49) Wing, G. L.; Blanchard, G. C.; Weiter, J. J. *Invest. Ophthalmol. Vis. Sci.* **1978**, *17*, 601.
- (50) Delori, F. C.; Staurenghi, G.; Arend, O.; Dorey, C. K.; Goger, D. G.; Weiter, J. J. *Invest. Ophthalmol. Vis. Sci.* **1995**, *36*, 2327.
- (51) Mukherjee, P.; Bose, S.; Hurd, A. A.; Adhikary, R.; Schöenbrücher, H.; Hamir, A. N.; Richt, J. A.; Casey, T. A.; Rasmussen, M. A.; Petrich, J. W. *Photochem. Photobiol.* **2009**, *85*, 234.

CHAPTER 9. GENERAL CONCLUSIONS

Hypericin is a natural photosensitizing pigment which displays virucidal activity against several types of viruses as well as antiproliferative and cytotoxic effects in many tumor cell lines. It has minimal dark toxicity, tumor selectivity and high clearance rate from the host body. All these properties make hypericin a very promising photodynamic drug for the treatment of cancer and virus diseases. Serum proteins primarily LDL binds with hypericin when it is administered in the blood. Since hypericin is aggregated in aqueous solution at physiological pH, interactions with the serum proteins help it to solubilize into its monomeric form that is crucial for its biological activity. Literatures also show that photosensitizers mixed with LDL before administration lead to an increase in photodynamic efficiency in comparison with the administration of photosensitizers alone. The precise knowledge of the interaction of hypericin with LDL is important in improving the efficiency of hypericin in therapeutic applications. In chapter 3 we have shown results of interaction of hypericin with LDL from steady-state and time-resolved fluorescence spectroscopy. Our results indicate that multiple hypericins can penetrate considerably deeply into the LDL molecule. Very inefficient fluorescence quenching of hypericin by Γ^- ions in 1:1 LDL-hypericin complex shows that hypericin is not exposed to the surface of LDL. Fluorescence anisotropy data indicate that a single hypericin is rigidly held, and thus probably resides fairly deeply in LDL. Fluorescence energy transfer from tryptophans in apoB-100 to hypericin is efficient. The R_0 for the hypericin-LDL complex is $\sim 27\text{\AA}$. This distance suggests that hypericin can be moderately close to the surface, where apoB-100 is located. Upon increasing the hypericin concentration, the fluorescence lifetime and quantum yield of hypericin decreases drastically after 1:20 LDL-hypericin, suggesting most likely the self

quenching of aggregated hypericin. This indicates that up to ~ 20 nonaggregated hypericin molecules can enter one LDL. The accommodation of multiple hypericins in LDL should not be surprising considering the diameter of LDL ($\sim 220 \text{ \AA}$) and the dimensions of hypericin: major axis, 10.5 \AA ; minor axis, 9.6 \AA .

PRODAN is a highly fluorescent hydrophobic molecule that has been used to probe biological system because its absorption and emission spectra are strongly dependent upon the polarity of its environment. It has also been exploited to study solvation dynamics in polar liquids, ionic liquids, and supercritical fluids. PRODAN based chromophores have been also used to probe the solvation dynamics in protein environments. PRODAN is a charge-transfer chromophore that produces a substantial change in its excited-state dipole moment upon photoexcitation owing to the presence of an electron-donating and –withdrawing group. It can also emit from dual excited states (CT and LE) depending upon the polarity of its surrounding environment. It has already been reported that PRODAN in a heterogeneous environment like reverse micelles emit from both the LE and the CT states due to the distribution of the chromophores to different polarity region of the reverse micelle. Protein environment is highly heterogamous in nature because of presence of polar, nonpolar and charged residues. Our goal is to find if any chromophore capable of undergoing excited-state photochemistry can induce artifacts into the interpretation of solvation dynamics in heterogeneous environments, such as a protein. In chapter 4, we have studied the solvation dynamics of PRODAN in the heterogeneous environment provided by reverse micelles formed by sodium 1,4-bis-(2-ethylhexyl) sulfosuccinate (AOT)/*n*-heptane/water, and separated the contributions of the LE and CT states of to its solvation dynamics. We have found that the LE and CT states of PRODAN solvate on different time scales in reverse

micelles (2 and ~ 0.4 ns, respectively), and have concluded that PRODAN's use as a probe of heterogeneous environments must be used with caution.

Curcumin is the subject of a large number of investigations in the fields of biology, medicine, and pharmacology owing to its profound effects on human health. It has been shown that the curcumin can act as photodynamic agent particularly for the treatment of skin cancers, and its photodynamic action is greatly enhanced in the presence of light. In order to further exploit its medicinal effects, it is important to gain a detailed level of understanding in the photophysics and photochemistry of curcumin. Curcumin exists predominantly as a keto-enol tautomer in a number of solvents with various polarities. It follows that curcumin is capable of executing excited-state intramolecular hydrogen atom transfer (ESIHT) owing to the presence of strong intramolecular hydrogen bonding. In chapter 5, we have demonstrated that curcumin undergoes excited state intramolecular hydrogen atom transfer (ESIHT) in methanol and ethylene glycol using ultrafast time-resolved fluorescence spectroscopy. Fluorescence upconversion decay traces of curcumin in methanol and ethylene glycol are best described with a biexponential function. In methanol it shows ~ 12 ps and ~ 70 ps component with nearly equal amplitudes. Curcumin in ethylene glycol also exhibits biexponential fluorescence decay with time constants ~ 20 ps and ~ 105 ps. However, the longer components in methanol and ethylene glycol show a prominent isotope effect. The longer time constants are assigned as ESIHT time in the respective solvents. Solvation, in addition to ESIHT, is expected to play a role in the excited-state relaxation dynamics due to the significant dipole moment change reported for curcumin: $\Delta\mu \sim 6.1$ D. Multiwavelength fluorescence upconversion results show that the short component (12-20 ps) insensitive to deuteration is due to solvation of excited-state curcumin.

The major challenges in the application of curcumin as an effective treatment agent are the lack of bioavailability and severely limited stability in aqueous environments. Encapsulation of curcumin in surfactant micelles and binding to proteins resolve these major issues. It is established that micelle-captured curcumin is well-dispersed in aqueous solutions, thereby increasing the bioavailability and stability significantly. Apart from preventing degradation, micelles also serve as well-defined model systems for biomembranes. It has been shown that a large portion of curcumin is membrane-bound in a biological environment. In chapter 6 we have studied the ESIHT of curcumin in the TX-100, DTAB and SDS micelles. The fluorescence upconversion transient of curcumin in each micelle shows a biexponential decay, with time constants of 3 – 8 ps (fast) and 50 – 80 ps (slow). The slow component exhibits a pronounced isotope effect, producing a decay time constant of 80 – 130 ps in the micelles, which is assigned to ESIHT. The ESIHT rate of curcumin in the TX-100 micelle is lower than those in the other two micellar system. The hydrogen bonding between curcumin and the TX-100 surfactant may contribute to this effect. The fast decay component, unlike the ESIHT process, is insensitive to deuteration of curcumin and is attributed to solvation dynamics using results from multiwavelength fluorescence upconversion studies.

Transmissible spongiform encephalopathies (TSEs) are slowly progressive, insidiously degenerative diseases that affect the central nervous system (CNS) of both humans and animals. The TSE of most concern for the food supply is bovine spongiform encephalopathy (BSE). It is thought to be associated with variant Creutzfeldt-Jakob disease (vCJD) in humans. The removal of central nervous system (CNS) tissues as part of BSE risk material is one of the highest priority tasks to avoid contamination of the human food chain

with BSE. No currently available method enables the real-time detection of possible CNS tissue contamination on carcasses during slaughter. In chapter 7 we investigate the fluorescence lipofuscin as a marker for the real-time detection of CNS contamination. We have studied front-faced fluorescence of brain and spinal cord, and compared with 13 different non-CNS tissues. A comparison between the spectral intensity of CNS and various non-CNS tissues clearly indicates that the fluorescence intensity from brain and spinal cord is higher than that found for non-CNS tissues. We have also demonstrated that small quantities of bovine spinal cord can be reliably detected in the presence of raw bovine skeletal muscle, fat, and vertebrae. These data form the fundamental basis for the development of a prototype device allowing real-time monitoring of CNS tissue contamination on bovine carcasses and meat cuts.

There are also no current methods which can detect TSE disease in live animals. Only post-mortem examinations and laboratory tests can confirm if the animal has been suffering from TSE disease. Any technique which is capable of testing a live animal for TSE disease is of great interest. Scrapie is the most widespread TSE affecting sheep and goats worldwide. In chapter 8 we present the results from fluorescence spectroscopic studies of healthy and scrapie eye parts to identify scrapie, which we use as a model for TSEs. Our data indicate that the fluorescence spectra from scrapie-positive retinas are more structured and intense compared to the scrapie-negative retinas. The difference in the spectral properties can be attributed to the result of altered or increased lipofuscin owing to prion infection. We suggest that the distinct differences in the spectral signatures of the retina are diagnostic for noninvasive examination of some neurological pathologies such as scrapie.

VITA

NAME OF AUTHOR: Ramkrishna Adhikary

DATE AND PLACE OF BIRTH: January 1, 1981, Bangalji, Nadia, India

DEGREES AWARDED:

B.S. in Chemistry, Ramakrishna Mission Vidyamandira, University of Calcutta, 2003

M. S. in Physical Chemistry, Indian Institute of Technology, Bombay, 2005

HONORS AND AWARDS:

National Merit Scholarship, Government of West Bengal, India, 1999

Madhav Pandey Fellowship, Indian Institute of Technology, Bombay, India, 2004-2005

National Eligibility Test (NET) for Lectureship in Chemical Science, India, 2005

Iowa State University Teaching Excellence Award, 2010

The Alpha Chi Sigma Award for Outstanding Research, Iowa State University, 2010

PROFFESIONAL EXPERIENCE:

Teaching and Research Assistant, Department of Chemistry, Iowa State University, 2005-2010

PROFESSIONAL PUBLICATIONS:

1. Mishra PP, **Adhikary R**, Lahiri P, Datta A. Chlorin p6 as a Fluorescent Probe for the Investigation of Surfactant-Cyclodextrin Interactions. *Proceedings of SPIE* **2006**, 6097, 609708/1-10.
2. Mishra PP, **Adhikary R**, Lahiri P, Datta A. Chlorin p6 as a Fluorescent Probe for the Investigation of Surfactant-Cyclodextrin Interactions. *Photochem. Photobiol. Sci.* **2006**, 5, 741-7.
3. Mukherjee P, Crank JA, Sharma PS, Wijeratne AB, **Adhikary R**, Bose S, Armstrong DW, Petrich JW. Dynamic Solvation in Phosphonium Ionic Liquids: Comparison of Bulk and Micellar Systems and Considerations for the Construction of the Solvation Correlation Function, C(t). *J. Phys. Chem. B* **2008**, 112, 3390-6.
4. Mukherjee P, **Adhikary R**, Halder M, Petrich JW, Miskovsky P. Accumulation and Interaction of Hypericin in Low-density Lipoprotein—a Photophysical Study. *Photochem. Photobiol.* **2008**, 84, 706-12.
5. **Adhikary R**, Bose S, Mukherjee P, Thite A, Kraus GA, Wijeratne AB, Sharma PS, Armstrong DW, Petrich JW. Influence of Chiral Ionic Liquids on the Excited-State Properties of Naproxen Analogs. *J. Phys. Chem. B* **2008**, 112, 7555-9.
6. Schönbrücher H, **Adhikary R**, Mukherjee P, Casey TA, Rasmussen MA, Maistrovich FD, Hamir AN, Kehrl ME, Jr. Richt JA, Petrich JW. Fluorescence-Based Method, Exploiting Lipofuscin, for Real-Time Detection of Central Nervous System Tissues on Bovine Carcasses. *J. Agric. Food. Chem.* **2008**, 56, 6220-6.

7. Mukherjee P, Bose S, Hurd AA, **Adhikary R**, Schöenbrücher H, Hamir AN, Richt JA, Casey TA, Rasmussen MA, Petrich JW. Monitoring the Accumulation of Lipofuscin in Aging Murine Eyes by Fluorescence Spectroscopy. *Photochem. Photobiol.* **2009**, *85*, 234-8.
8. **Adhikary R**, Mukherjee P, Kee TW, Petrich JW. Excited-state Intramolecular Hydrogen Atom Transfer and Solvation Dynamics of the Medicinal Pigment Curcumin. *J. Phys. Chem. B* **2009**, *113*, 5255-61.
9. Bose S, **Adhikary R**, Mukherjee P, Song X, Petrich JW. Considerations for the Construction of the Solvation Correlation Function and Implications for the Interpretation of Dielectric Relaxation in Proteins. *J. Phys. Chem. B* **2009**, *113*, 11061-8. (Feature Article, Cover Page)
10. **Adhikary R**, Schöenbrücher H, Rasmussen MA, Casey TA, Hamir AN, Kehrli ME, Richt JA, Petrich JW. A Comparison of the Fluorescence Spectra of Murine and Bovine Central Nervous System and other Tissues. *Photochem. Photobiol.* **2009**, *85*, 1322-6.
11. **Adhikary R**, Barnes CA, Petrich JW. Solvation Dynamics of the Fluorescent Probe PRODAN in Heterogeneous Environments: Contributions from the Locally Excited and Charge-transferred States. *J. Phys. Chem. B* **2009**, *113*, 11999-2004.
12. **Adhikary R**, Carlson PJ, Kee TW, Petrich JW. Excited-State Intramolecular Hydrogen Atom Transfer of Curcumin in Surfactant Micelles. *J. Phys. Chem. B* **2009**, *114*, 2997-3004.
13. **Adhikary R**, Bose S, Casey TA, Gapsch A, Rasmussen MA and Petrich JW. Applications of Fluorescence Spectroscopy to Problems of Food Safety: Detection of Fecal Contamination and of the Presence of Central Nervous System Tissue and Diagnosis of Neurological Disease. *Proceedings of SPIE* **2010**, *7576*, 757617/1-15 (Invited Paper).
14. **Adhikary R**, Mukherjee P, Krishnamoorthy G, Kunkle RA, Casey TA, Rasmussen MA, Petrich JW. Fluorescence Spectroscopy of the Retina for Diagnosis of Transmissible Spongiform Encephalopathies. *Anal. Chem.* **2010**, *82*, 4097-4101.
15. Bose S, **Adhikary R**, Barnes CA, Fulton B, Hargrove MS, Song X, Petrich JW. Comparison of the Dielectric Response obtained from Fluorescence Upconversion Measurements and Molecular Dynamics Simulations for Coumarin 153-apomyoglobin Complexes and Structural Analysis of the Complexes by NMR and Fluorescence Methods. *J. Phys. Chem. A* **2010** (In Press, Special Issue).
16. **Adhikary R**, Mukherjee P, Schöenbrücher H, Casey TA, Rasmussen MA, Petrich J W. Real Time Detection of Central Nervous System Tissues on Bovine Carcasses using Fluorescence Spectroscopy. *Am. Lab.* **2010**, *3*, 8-14.
17. **Adhikary R**, Trampel RL, Kee TW, Petrich JW. Cis-Trans Isomerization of Cyclocurcumin. **2010** (In Preparation).
18. Zhao L, Pang X, **Adhikary R**, Petrich JW. Lin, Zhiquan Semiconductor Anisotropic Nanocomposites via Directly Coupling Conjugated Polymers with Quantum Rods. **2010** (Submitted).